Order Number 9312750

Surface freezing and surface induced ordering in liquid crystal films

Swanson, Brian Douglas, Ph.D.

University of Washington, 1992

U·M·I
300 N. Zeeb Rd.
Ann Arbor, MI 48106

Surface Freezing and Surface Induced Ordering in Liquid Crystal Films

by

Brian D. Swanson

A dissertation submitted in partial fulfillment of the requirements for the degree of

Doctor of Philosophy

University of Washington

1992

Approved by L B Sorensen

(Chairperson of Supervisory Committee)

Program Authorized
to Offer Degree Physics

Date 8/14/92

In presenting this dissertation in partial fulfillment of the requirements for the Doctoral degree at the University of Washington, I agree that the Library shall make its copies freely available for inspection. I further agree that extensive copying of this dissertation is allowable only for scholarly purposes, consistent with "fair use" as prescribed in the U.S. Copyright Law. Requests for copying or reproduction of this dissertation may be referred to University Microfilms, 1490 Eisenhower Place, P.O. Box 975, Ann Arbor, Michigan 48106, to whom the author has granted "the right to reproduce and sell (a) copies of the manuscript in microform and/or (b) printed copies of the manuscript made from microform."

Signature Brian Swanson

Date 12/18/92

University of Washington

Abstract

Surface Freezing and Surface Induced Ordering in Liquid Crystal Films

by Brian D. Swanson

Chairperson of Supervisory Committee: *Professor Larry B. Sorensen*
Department of Physics

Polarized-video-microscopy has been used to study the layer-by-layer surface freezing transitions found in four liquid crystal materials: 9O.4, 4O.7, 7O.7 and $\overline{14}$S5. The functional form for the growth of the frozen surface layer thickness versus temperature, $l(t)$, depends on the dominant intermolecular forces in the system. Examples of surface freezing, with long-range van der Waals forces and with short-range exponential forces, have been found for the first ten surface freezing transitions in $L \approx 64$ layer thick films. For the surface freezing of 9O.4, the appearance of the first ten surface layers is described very well by the simple power-law form predicted for a system with long-range van der Waals forces. The surface freezing of 4O.7 and 7O.7 is described by the simple logarithmic form predicted for surface freezing in a system with short-range exponential forces. The surface freezing of $\overline{14}$S5 is described equally well by either long-range van der Waals or short-range exponential force models. After the first ten transitions, there is a systematic slowdown in the appearance of subsequent surface freezing transitions and $l(t)$ deviates from the initial power-law or logarithmic divergence. To study this slowdown, we have measured the influence of film thickness on the surface freezing in two LC materials, 4O.7 and 7O.7, for film thicknesses ranging from 17 about a thousand layers. A remarkable variation with film thickness has been observed which can be explained with a single effective interfacial potential. From this model-independent effective interfacial potential, the shape of the repulsive potential responsible for the finite-size effects can been deduced.

A new method is described to make model-independent determinations of the in-

terlayer density profile of freely suspended liquid crystal films by directly inverting grazing incidence x-ray scattering data. Although, in general, the measured scattering intensities determine only the magnitude of the scattering amplitudes, in the special case of one-dimensional centrosymmetric freely suspended films, the phases can be determined by inspection. The direct inversion analysis is a completely new method for solving the phase problem that does not depend on intensity relationships between different Bragg peaks used by direct methods, but instead uses the directly measured zeros of the primary and subsidiary maxima of the structure factor to determine the phase of each "Bragg peak" (primary maximum) and of each subsidiary maximum. An experimental demonstration of this method is presented for the evolution of smectic ordering in smectic-G and smectic-I/C films of 7O.7 for thicknesses from three to 15 molecular layers.

TABLE OF CONTENTS

LIST OF FIGURES

LIST OF TABLES

ACKNOWLEDGMENTS

This work could not have been completed without the help and encouragement of many people. I wish to express my gratitude to my advisor Larry Sorensen for his assistance, guidance, and for giving me the opportunity to work on many projects over the years. His knowledge and love of physics, enthusiasm and friendship have made this time very enjoyable. I thank Oscar Vilches for his assistance and enthusiasm which helped motivate me to pursue this Ph.D. I especially thank Cecilia Bitz, Doug Tweet, and Hans Stragier for help in taking the data presented in this thesis. I will always appreciate the original experience of building the lab together with Larry, Doug and Hans. During this time I very much enjoyed our many physics discussions. I thank Heinz Guldenmann, Ron Musgrave, and Bob Morley for help building the equipment used in these and other experiments. I thank Julie Cross for her cartoons and help, Dennis Yee and Tiaming Zhang for assistance in the experiments. And I thank all the gang of graduate student friends, Georg, Doug, Guille, Patri, Jose and all the others who hiked, cajoled and even sanded on the boat together during those first few years of graduate school. I thank my family for the gifts of optimism and a sense of humor without which this project and life in general would be so much more difficult. I thank Eulah Laucks for her support and encouragement which was of enormous help in so many ways. Most of all I thank my wife, Mary, who has assisted in final figure-making and editing of an early version of this thesis. Her love, constant support, and encouragement have sustained me throughout this project.

To Mary

Within the earth, wood grows:
The image of pushing upward.
Thus the superior man of devoted character
heaps up small things
In order to achieve something high and great.

- I CHING

Chapter 1

INTRODUCTION

Scientific research can reduce superstition by encouraging people to think and survey things in terms of cause and effect. Certain it is that a conviction, akin to religious feeling, of the rationality or intelligibility of the world lies behind all scientific work of a higher order.

- Albert Einstein

Freely suspended liquid crystal films are remarkable systems since they display critical behavior and structure intermediate between two and three dimensions. Two-dimensional phase transitions are different than those in ordinary three-dimensional systems due to the interplay of defects, fluctuations and surface tension. The influence of surfaces in semi-infinite systems can have an interesting effect on phase transitions in these systems. In semi-infinite systems, universal second-order surface critical behavior has been observed and due to the surface, the first-order 3D phase transition, without any universal critical exponents, is sometimes converted into an 'apparently critical' surface-induced first-order phase transition, i.e., surface freezing. For liquid crystal (LC) films in particular, the quenched fluctuations at the surfaces are important in the nucleation of surface freezing transitions. LC films are uniquely suited for studying surface-induced phase transitions since the surface to volume ratio, usually 1 part in 10^8 for typical bulk systems, can be made very large for a two layer film. LC films are decoupled from any effects of an underlying substrate and the complication of substrate-induced order, seen in 2D melting and dimensional crossover studies of other quasi-two-dimensional systems, is absent [1, 2].

Some of the questions that will be discussed in this thesis are: Chapter 2: What is a surface freezing transition? Why does the surface freeze? What is the effective interfacial potential for a LC film? What are the effects of film thickness (finite-size) on the surface freezing transitions? How does the interfacial potential change as the phase transition moves into the film? Chapter 3: How can the crystallographic phase problem be solved for systems with 1D centrosymmetric densities? How can a model independent determination of the interlayer structure of LC films be obtained? What is the structure of thin LC films and what is the influence of the surface on this structure? How does the interlayer structure vary with film thickness? What model-independent information can be obtained about the electron density and center-of-mass density of LC films? Chapter 4: How does the surface tension affect the fluctuations near the surface and is there an interlayer fluctuation profile in thin smectic films? Does this fluctuation profile change with the thickness of the film? What is the nature of the smectic layers themselves, and how is the divergence of the smectic layer fluctuations quenched in thin films? How is the surface freezing transition related to the interlayer structure of the film? What is the relation between the effective interfacial potential, electron density, and the order parameter profile of the film?

1.1 Thesis Organization and Outline

This thesis describes two experiments: a polarized-video microscopy study of layer-by-layer surface freezing and an x-ray diffraction study of the surface-induced order found in the interlayer structure of thin films. Both experiments measure the influence of surfaces on phase transitions and the structure of freely-suspended liquid crystal (FSLC) films.

This chapter contains a four-part introduction and overview of surface freezing and the structure of LC films. Section 1.2 presents the basics of LC phases and LC films. Section 1.3 describes traditional surface freezing theory which is compared in Chapter 2 to data from four different LC materials to determine the dominant forces in these systems. Section 1.4 previews the results obtained using the methods developed in Chapter 3 to make a model-independent determination of the interlayer structure of LC films.

Chapter 2 contains the results from the polarized video microscopy measurements

of layer-by-layer surface freezing at the LC-vapor interface. These measurements are analyzed using the traditional mean-field surface melting theory based on the competition between the bulk and surface energies in a semi-infinite system. In this theory, the functional form of the frozen surface layer thickness versus temperature depends on the dominant characteristic forces in the LC material. The measurements show the behavior predicted for the two kinds of forces expected in LC materials, long-range van der Waals and short-range exponential forces. The complete model-independent effective interfacial potential versus temperature and film thickness is derived from this data.

Chapter 3 gives a description of a new method for determining the interlayer density of LC films from x-ray diffraction measurements. This method involves solving the crystallographic phase problem in this special case where the interlayer structure is centrosymmetric. The interlayer density and corresponding center-of-mass density are determined and are compared with those found using a forward model.

In Chapter 4, a new quenched-fluctuation-induced surface freezing theory is compared with the experimental surface freezing results presented in Chapter 2. This theory developed by Hołyst [19] is based on the Kosterlitz-Thouless 2D melting theory coupled to the surface-tension-quenched fluctuations at the film's surfaces. This method of analysis connects the surface freezing results, described in Chapter 2, with the interlayer structural measurements, described in Chapter 3. Chapter 4 also contains a discussion of the order parameter profile during the surface freezing transition.

1.2 Liquid Crystal Films

Liquid crystals are rich and interesting systems for phase transition studies and this section describes the molecular structure and in-plane molecular orientations of the various smectic LC phases [3]. The thermotropic liquid crystals used in the two experiments described here are highly anisotropic rod-like organic molecules with thermodynamically stable phases intermediate between liquid and solid phases [4]. The structure of one of the compounds, 4-n-heptyloxybenzylidene-4-n-heptylaniline (7O.7), discussed in Chapters 2 and 3, is shown in Fig. 1.1a. The structure consists of two rigidly linked benzene rings with hydrocarbon chains extending on either end. In the high temperature phases, the approximately planar shaped molecules rotate freely about the long axis and the phases can be understood in terms of the packing of

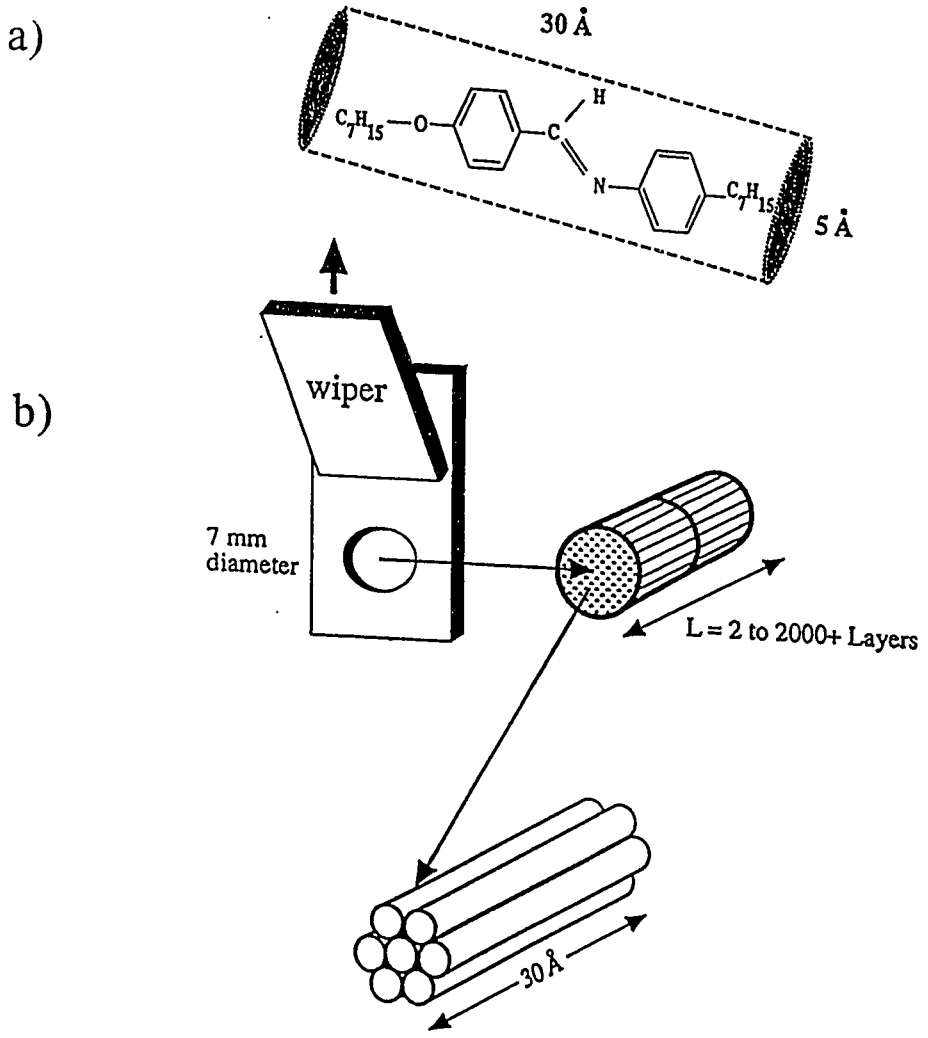

Figure 1.1: 7O.7 Structure and Smectic Films. a) The structure of 7O.7 consists of two rigidly linked benzene rings with a 7 member hydrocarbon chain on either end. The molecule rotates freely at high temperatures and can be approximated as a 5 Å diameter by 30 Å long rigid rod.

b) A smectic film is formed, like a soap bubble, when the LC material in a 2D liquid phase is drawn across an aperture. The smectic layers form parallel to the plane of the film surface with the in-plane order of the layers either liquid, hexatic, or solid. Films can be made from two to thousands of layers thick.

semi-rigid rods about 30 Å in length and 5 Å in diameter. LC films [5], illustrated in Fig. 1.1b, are produced by placing a small amount of LC material around the edge of a planar aperture, heating the material to a liquid smectic phase, and drawing a wiper across the aperture. The film is stabilized by its smectic structure and the smectic layers form parallel to the surface of the film. The thickness of the film can be easily changed from about 60 Å to several microns by varying the amount of liquid crystal, the wiping speed, and the temperature. Smectic phases are 1D crystals organized into layers. The 'alphabet soup' of smectic phases is shown in Fig. 1.2 where the distinct mesophases are characterized by the symmetries and orientations of the molecules. As the temperature of the film is raised (or lowered), the film typically makes a sharp first-order transition to a less (or more) ordered phase. However, as will be seen in Chapter 2, there are at least four LC systems in which the phase transition starts at the surface of the film and procedes inward one monolayer at a time.

In the study of surface freezing transitions described in Chapter 2, all four materials, 9O.4, 4O.7, 7O.7, and $\overline{14}$S5, are in the smectic-A phase before the surface freezing transitions start. The smectic-A phase consists of a one-dimensional stack of equidistant two-dimensional liquid layers with the average molecular axis called the director, $\hat{n}$, normal to the smectic layers. Each surface freezing transition involves an increase in the in-plane order of a single molecular layer. In these four systems, the surface frozen phase is a biaxial phase in which the director makes a finite angle with respect to the smectic layers. Optical microscopy suggests that all these surface frozen phases are either hexatic smectic-I or smectic-F phases. The smectic-I and smectic-F phases both have in-plane six-fold hexatic symmetry, and are distinguished by their molecular tilt directions as shown in Fig. 1.2b.

The thickness dependent phase diagram for 7O.7 is shown in Fig. 1.3. This LC was chosen for both the x-ray diffraction and optical microscopy studies since the thickness dependence of its phase diagram had been well studied [6, 7, 8]. As with many LC materials, significant changes in the phase transition temperatures and even in the phase sequence can be seen in films several hundred layers thick. Except for the smectic-F to smectic-G transition in thin films, the transition temperatures consistently increase from the bulk values as the film thickness decreases. The surface freezing transitions observed for 64 layer thick films appear at the points marked by triangles. Note that in this system, the surface-frozen phase is a surface stabilized

a)

	ORDER	NOT TILTED	TILTED	
			FACE	CORNER
LIQUID	Z : 1D SOLID X-Y: 2D LIQUID	A	C	
HEXATIC	ORIENTATIONALLY ORDERED Z: 1D SOLID X-Y: 2D LIQUID	HEX B	F	I
SOLID	3D PLASTIC SOLID	CRY B	G	J
	3D FROZEN SOLID	E	H	K

b)

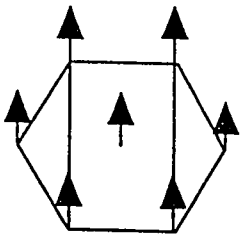

F, G, H

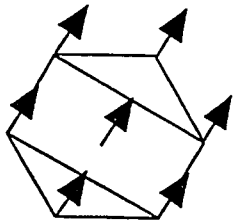

I, J, K

Figure 1.2: Smectic Liquid Crystal Phases. a) The ordering of these 3D phases is as follows: The A, C, Hex B, F, and I phases have short-range 2D liquid-like in-plane positional order and the Cry B, G, J, E, H, and K have long-range 3D crystalline positional and bond orientational order. The A and C have short-range 2D liquid-like in-plane bond orientational order while the Hex B, F, and I have long-range 3D hexatic in-plane bond orientational order. All the tilted phases have long-range tilt orientational order. The surface freezing transitions in the four LC systems studied here are from untilted to tilted phases.

b) Arrows indicate the molecular tilt directions with respect to the in-plane structure for the tilted smectic phases.

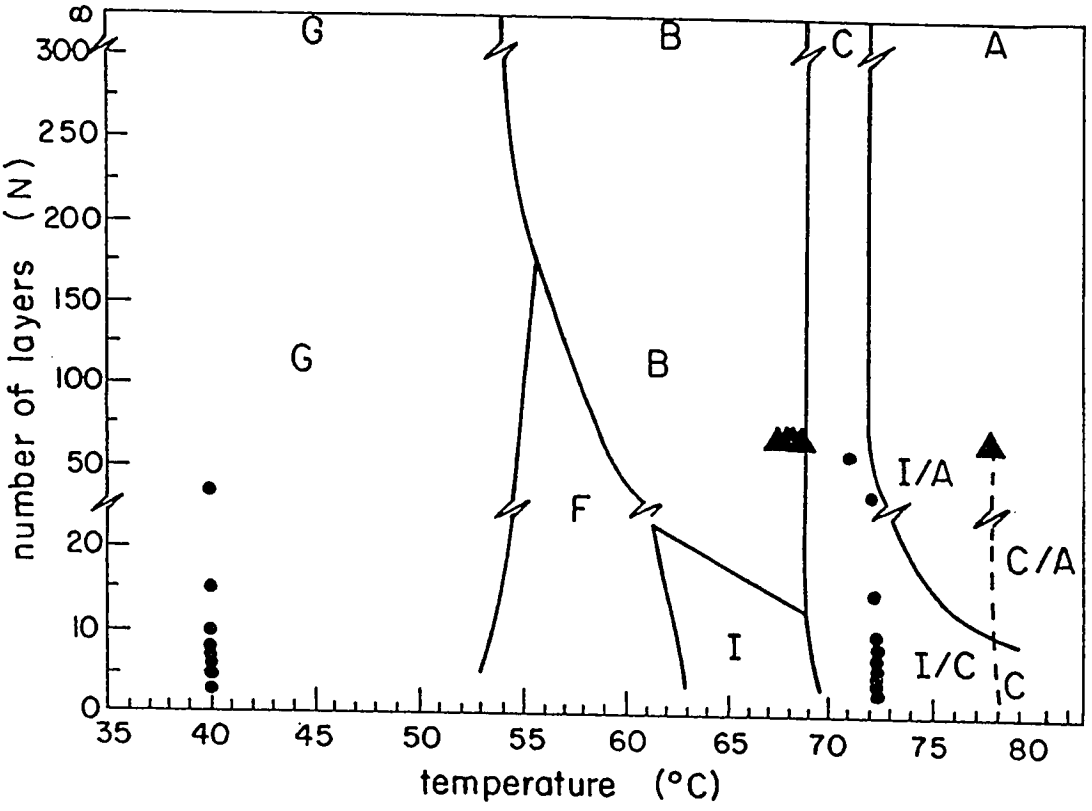

Figure 1.3: 7O.7 Thickness Dependent Phase Diagram [6]. For bulk samples, the phase sequence with decreasing temperature is (A) smectic-A, (C) smectic-C, (B) smectic-B, and (G) smectic-G. The smectic-B phase exhibits numerous restacking transitions which for simplicity have not been shown. In thinner films, the smectic-B region is replaced by (I) the hexatic smectic-I and (F) the hexatic smectic-F phase. A monolayer of surface-frozen hexatic smectic-I present on the interior smectic-C or smectic-A is indicated by (I/C) and (I/A). A monolayer of tilted smectic-C on interior smectic-A is indicated by (C/A). The surface freezing transitions observed for 64 layer thick films are indicated by triangles (▲). The x-ray measurements analyzed by the direct inversion method described in Chapter 3 were performed for the films indicated by dots (•).

tilted phase appearing at the smectic-B to smectic-C boundary. The x-ray measurements and the subsequent direct inversion analysis, described in Chapter 3, were performed on the films indicated by dots. For the x-ray measurements, two LC phases were studied: a monolayer surface-frozen phase denoted smectic-I/C, which consists of monolayer 2D hexatic smectic-I surface layers on a 2D fluid smectic-C interior [6, 7, 8, 9], and the crystalline smectic-G phase. The smectic-I/C phase was chosen to measure the effects of a monolayer surface-frozen phase on the structure of the films. Measurements were made of the crystalline smectic-G phase for comparison.

1.3 Surface Melting and Surface Freezing

At a surface, a first-order 3D phase transition without any universal critical exponents can be converted into a surface-induced first-order phase transition which manifests an 'apparent criticality' with universal critical behavior [10]. A standard first-order phase transition is illustrated in Fig. 1.4a which shows a first-order 3D bulk transition for a system without surfaces. As the temperature approaches the bulk melting point, T_o, a discontinuity occurs in the thermodynamic variables corresponding to first derivatives of the free energy and the crystal symmetry of the solid abruptly changes between the crystalline and the liquid states. Fig. 1.4b indicates the 'apparent' first-order critical behavior evident in a semi-infinite system undergoing a surface melting transition. As the temperature of the system is raised, instead of abruptly melting the system develops a melted liquid layer on the surface of thickness, l, which grows as the temperature approaches T_o. The reduced temperature, t, dependence of the growth of the melted layer thickness, $l(t)$, depends on the dominant intermolecular forces in the system, the detailed behavior of $l(t)$ depends on both the range of the interactions and on whether the interfaces are rough or smooth. Previous experimental surface melting studies of metals and physisorbed rare gases have shown a logarithmic growth of the thickness of the surface layer indicating the dominant interactions in these systems are short-range exponential forces, and continuous rather than layer-by-layer melting transitions indicating the interfaces are rough. All four LC systems shown in Chapter 2 demonstrate layer-by-layer surface freezing originating at the two LC-vapor interfaces. The fact that in all four LC systems the surface freezing appears layer-by-layer indicates the interface between the frozen surface phase and the liquid interior is smooth. The dominant interactions in these four systems exhibit the two types of

forces expected in liquid crystals: long-range van der Waals forces and short-range exponential forces.

The Lindemann melting criterion [11] provides a simple estimate of T_o based on the ansatz that a crystal melts when the mean-squared displacement, $\langle u^2 \rangle$, due to thermal motion is a significant fraction ($\sim$ 20%) of the lattice constant. Diffraction experiments directly measure the mean-squared displacement, $\langle u^2 \rangle$, since thermal motion attenuates the diffracted beam intensities via the Debye-Waller factor, $\exp(-q^2\langle u^2 \rangle/4)$, where q is the magnitude of the momentum transfer. Some previous experiments have compared surface versus bulk scattering to relate the relative amplitudes of the thermal motions for the surface and bulk [12]. Chapter 3 describes a new technique for determining the spatial dependence of the thermal motions of different layers of molecules in smectic LC films. Instead of separating the surface layer from the interior scattering, this new technique solves the crystallographic phase problem and allows the direct inversion of the total scattering from the film to reveal the thermal amplitudes for each individual layer.

A naive application of the Lindemann criterion suggests that surface atoms disorder at temperatures below the bulk melting temperatures since a surface atom experiences a smaller restoring force than a bulk atom. This is the basis for a phenomenological model for surface melting [14]. In this model, the second layer will melt at a slightly higher temperature, but still below T_o, since the surface layer exerts an intermediate restoring force. Consequently, each subsequent interior layer melts when its local Lindemann criterion is met and the interface propagates into the crystal as the temperature approaches T_0. This simple Lindemann model for surface melting, which links the melting temperatures to vibrational amplitudes within solids, is incorrect since it fails to predict the actual variations found in real systems and it cannot account for the surface freezing found in LC systems. A thermodynamically correct description of surface melting and surface freezing is obtained by considering the interfacial wetting of a melt liquid (or frozen solid) on its own crystalline (or liquid) substrate. In this case, both surface melting and surface freezing are predicted to have identical universal critical behavior which depends only on the range of the interactions in the particular system and whether the interface between the surface phase and the interior is rough or smooth [10, 15, 16].

Figure 1.4: First-Order Phase Transitions. a) The top panel pictures a bulk system undergoing a 3D first-order phase transition, where at T_o the system exhibits a discontinuity and changes from solid to liquid.
b) The lower panel illustrates a surface melting transition where a melted liquid layer of thickness, l, develops on the surface of the semi-infinite system as $T \rightarrow T_o$. The thermodynamics of surface melting of a semi-infinite liquid involves competition between the energy cost of converting the layer of solid to liquid and the energy gained by exchanging the liquid-vapor interface with liquid-solid and solid-vapor interfaces. The transition is predicted to be either continuous or layer-by-layer depending upon whether the solid-liquid interface is rough or smooth.

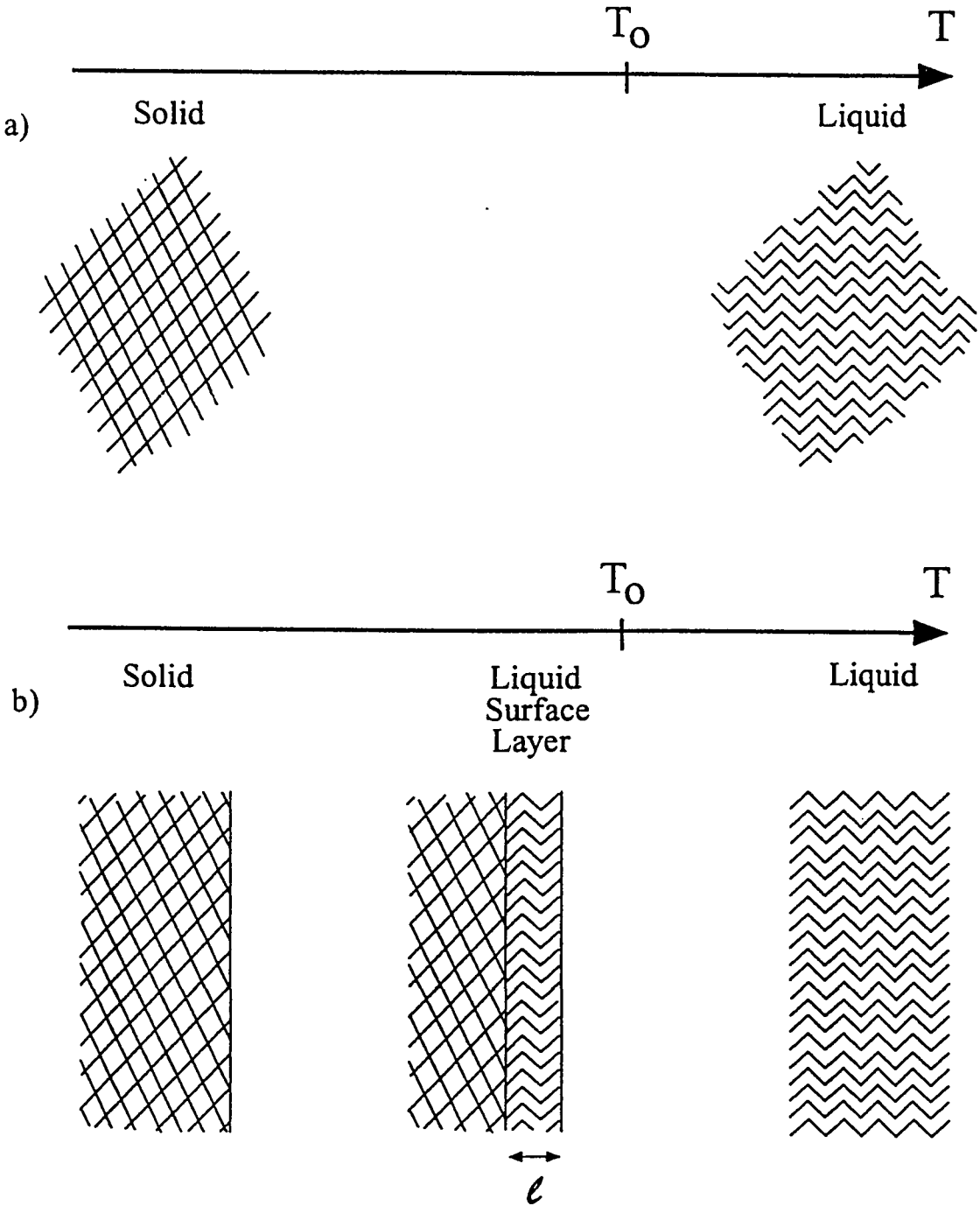
a)
T_o
T
Solid
Liquid
b)
T_o
T
Solid
Liquid
Surface
Layer
Liquid
ℓ

1.3.1 Surface Melting Mean-Field Theory

The traditional mean-field description of surface melting requires defining the effective interfacial potential which is the free energy difference between the two states of the system. Surface melting is a case of interfacial wetting and results from a competition between the bulk free energy and the surface free energy of the system. Below the bulk melting temperature, the simple thermodynamic surface melting argument goes as follows [17]: The equilibrium state of a bulk semi-infinite system in equilibrium with its vapor is determined by the minimum of the total free energy. If a thin solid layer of thickness l is converted from solid to liquid below the bulk melting point temperature, then the free energy per unit area will increase by the phase conversion cost, proportional to the chemical potential difference between the solid and liquid, and will decrease by interface-interface interaction energy term which depends upon the interfacial free-energy difference in the liquid layer now on the surface of the system. In the surface melting process, the system replaces the original solid-vapor interface with a liquid-vapor and a solid-liquid interface. This reduces the free energy per unit area and depends on both the difference between these interfacial free energies and the range of dominant interactions in the system. Since the bulk term is zero at the bulk melting point temperature, T_o, the chemical potential difference can be expanded in terms of the reduced temperature, $t = \frac{|T_o - T|}{T_o}$, and the location of the interface between the surface induced coexisting liquid and solid is given by $l(t)$ and can be obtained by minimization the total free energy. This results in $l = l_o + \xi \ln(1/|t|)$ for short-range exponential forces and $l \propto t^{-1/3}$ for long-range van der Waals forces. Both types of forces are found in the LC systems studied here.

An attempt by Holyst [19] to make a specific microscopic surface freezing/melting theory is discussed in Chapter 4. This theory relates the interlayer structure of the film to the surface freezing behavior by considering the first stage of the Kosterlitz-Thouless defect-mediated melting theory [20, 21] in which disclination pairs unbind at the liquid-hexatic transition. Holyst argues that the surface in-plane ordering is induced by quenched out-of-plane fluctuations caused by the surface tension and notes that the surface freezing transitions start at the surface where the fluctuation amplitudes are smallest. The direct x-ray measurements of the center-of-mass densities for all thickness liquid films show quenched interlayer fluctuations at the surface. Holyst tries to relate these measured quenched fluctuations to the surface freezing transition.

Measurements of the fluctuation profile, shown in Chapter 3 using both the direct inversion and forward model analysis methods, allows predictions of the functional form for the surface freezing. A detailed comparison between Holyst's theory and another simpler phenomenological theory with the surface freezing measurements is made in Chapter 4.

Both the simple thermodynamic description and the Landau-Ginzburg mean-field description predict the same functional form for the temperature dependence of the frozen surface layer but the Landau-Ginzburg theory makes explicit predictions about the order-parameter profile [10, 13]. The Landau-Ginzburg formulation is discussed in Chapter 4 and the order parameter profile, $M(z)$, derived from the experimentally determined electron density, $\rho(z)$, is presented there.

1.3.2 Effective Interfacial Potential and Finite-Size Effects

The effective interfacial potential for LC films has been determined versus film thickness for the surface freezing of three materials. Experimentally, it is found that after about the first ten surface freezing transitions on each surface, the freezing transitions for additional layers slowdown and deviate from the original power-law or logarithmic divergence. A beautiful systematic variation of the slowdown of the surface freezing transitions with film thickness, L, has been observed. This systematic divergence is described by a finite-size model, $t = \beta \exp(-l/\xi) - \beta' L/(L - \varepsilon l)$, which is similar to finite-size effects found in other systems where the transition temperature shift, $\Delta T \sim 1/L$, where L is the size of the system. This finite-size behavior provides evidence for a new effective force in these materials and a new finite-size dependent term in the effective interfacial potential. Without taking up the question of whether or not this finite-size model is correct, this model provides an excellent parameterization of the data which has been used to make a model independent determination of the complete effective interfacial potential and to demonstrate the existence of a new contribution to the effective interfacial potential which describes all LC films measured. A second parameterization provides indistinguishable effective interfacial potentials.

1.4 Model-Independent Interlayer Structure Determination

The interlayer structure of freely suspended liquid crystal (FSLC) films has not been studied until very recently [22, 23]. Surface-induced tilt angle changes [24, 25], monolayer surface-induced phases [9], and surface freezing, are all influenced by the surface-tension-quenched fluctuations at the surfaces of FSLC films. The importance of surface tension, finite-film thickness and the presence of monolayer surface-frozen layers on the interlayer structure of LC films has been studied using x-ray diffraction.

Chapter 3 describes a new model-independent method to determine the interlayer structure by directly inverting the measured diffraction intensity. The direct inversion analysis involves removing the instrumental broadening from the measured diffraction intensity by deconvolution and then explicitly solving the one-dimensional crystallographic phase problem to yield the interlayer electron density. Three facts allow the crystallographic phase assignments for the scattering from thin FSLC films to be made by inspection. The electron density is real, positive, and centrosymmetric and anomalous scattering effects are negligible at the x-ray wavelength used in this study so the scattering amplitude is real and even. The measured thin film x-ray diffraction patterns reveal the zero-crossings or phase changing points of the scattering amplitude. Finally, the phase angles switch between 0 or π in a well-defined way since the zeros in the scattering amplitude are due to the product of the molecular form factor and the 'N-slit' interference factor.

With the help of the above observations the direct inversion analysis consists of six steps: 1) Adding a $q_z = 0$ patch to the experimental data in the unmeasured region near $q_z = 0$ to produce an extended measured intensity, $M(q_z)$, which begins at $q_z = 0$. 2) Removing the instrumental broadening from $M(q_z)$ to produce the intrinsic intensity, $I(q_z)$. 3) Making scattering corrections and taking the square-root of $I(q_z)$ to give the magnitude of the scattering amplitude, $|S(q_z)|$. 4) Hand phasing $|S(q_z)|$ to give the scattering amplitude, $S(q_z)$. 5) Back-transforming $S(q_z)$ to give the electron density, $\rho(z)$. 6) Removing the molecular form factor from $\rho(z)$ to give the center-of-mass density, CM(z).

Forward model analysis creates a model for the interlayer density, which is then Fourier transformed and squared to calculate the model scattering intensity. This model scattering intensity is convolved with the measured resolution function and a non-linear least-squares fit is made to the measured scattering intensity. The fit

involves varying parameters in the model interlayer density. The direct inversion method, as described above, makes a model-independent determination of the interlayer structure by directly inverting the measured diffraction intensity.

Both the forward modeling and the direct inversion analysis techniques have some inherent questions and problems associated with them. In the case of the forward model, the following questions may be asked: What are the measurement errors and is the resulting χ^2 from the fit a reasonable value? Even if the model fits with a reasonable χ^2, is it correct? Is this model a unique parameterization of the measured intensity? Are the model parameters correlated? The direct inversion method has inherent 'noise' associated with extracting a signal in the presence of measurement errors using Fourier transforms which is discussed in detail in Chapter 3. In the case of the FSLC film data analyzed here using both techniques, the diffraction intensity could not be measured all the way to $q_z = 0$ due to occlusion of the x-ray beam by the LC film holder. This means that any Fourier components in the density with reciprocal length scales between 0 and q_{min} (where q_{min} is the magnitude of the smallest scattering vector measured) are not accounted for in the forward model best-fit parameters or the direct inversion density. The direct inversion analysis is particularly sensitive to this problem since fast Fourier transform algorithms are used which require data all the way to $q_z = 0$. The direct inversion analysis substitutes the forward model intensity into this region, but as will be seen, the shape of the substituted model intensity does have an effect on the resulting density. By applying these two techniques to the same data, it is hoped that they will provide complementary information about the interlayer structure of these films.

Comparisons are made of the interlayer structure versus film thickness extracted from the diffraction intensities using these two methods. The forward modeling results have been reported elsewhere [22, 26]. Comparisons are made in Sec. 3.9 between the densities obtained from the forward model and those obtained using the direct inversion analysis. The electron densities and the center-of-mass densities from both the direct inversion and forward model analysis have many similar features: The center-of-mass densities for thick smectic-G films have uniform height and the center-of-mass distribution of each layer have equivalent FWHM's throughout the film. The center-of-mass densities for the smectic-I/C films show enhanced density at the surface of the film. For all films, the density modulations are well described by 'Gaussian'

layers with surface enhanced order in sharp contrast to the usual uniform sinusoidal density wave models for bulk smectics. There are also some interesting differences between the forward model and direct inversion results: The forward model center-of-mass densities are flatter in the smectic-G phase than the direct inversion center-of-mass densities. And, in general, the direct inversion FWHM's of the interlayer positions are wider than those resulting from the forward model analysis.

Chapter 2

SURFACE FREEZING TRANSITIONS OF LIQUID CRYSTAL FREE FILMS

Liquid crystals are beautiful and mysterious;
I am fond of them for both reasons.

- P.G. de Gennes

2.1 Introduction

There has been considerable recent interest in the influence of surfaces on the general properties of matter, and on phase transitions, in particular. Many experiments have studied the surfaces of materials to determine if the surface order is the same as the structure found in the bulk. In this study, polarized-video-microscopy has been used to study the influence of intermolecular forces on surface freezing transitions in freely suspended liquid crystal (LC) films of four LC materials: 9O.4, 4O.7, 7O.7, and $\overline{14}$S5. Theory predicts that the form of the divergence of the surface freezing (SF) transition temperatures indicates the dominant intermolecular forces in the system. LC films are held together by some combination of steric, van der Waals, hydrogen-bonding, and chemical-bonding forces; the most important being either the long-range van der Waals interactions or the short-range exponential interactions [27, 28]. In addition to discovering that these four LC materials undergo layer-by-layer surface freezing transitions, the measurements have been used to determine the dominant forces in these four systems. The power-law growth with reduced temperature, t, of the frozen surface layer thickness, $l = l_o t^{-1/3}$, characteristic of long-range van der Waals forces, was found in 9O.4 and these results were previously briefly reported [29]. This thesis presents the first report of surface freezing with layer-by-layer logarithmic growth. The surface freezing transitions in 4O.7 and 7O.7 are described by the logarithmic

form, $l = l_o' + \xi \ln(1/|t|)$, characteristic of short-range exponential forces. Surface freezing transitions in $\overline{14}S5$ exhibit growth of the frozen surface layer consistent with both van der Waals and exponential forces.

These results show that FSLC films exhibit two of the four universality classes of surface freezing; layer-by-layer power-law growth and layer-by-layer logarithmic growth [29, 30]. Surface freezing (SF) is a novel phase transition, originating at the LC-vapor interface, in which the film undergoes a series of first-order monolayer freezing transitions all the way to the center of the film. In general, the SF transition is expected to be either layer-by-layer or continuous depending upon whether the transition occurs above or below the roughing temperature. All four liquid crystal systems discussed here exhibit layer-by-layer surface freezing indicating that the frozen layer-vapor interface is smooth. For all film thicknesses studied, the layer-by-layer transitions continue until the entire film is frozen.

After the first ten SF transitions, as the SF continues to the center of the film, there is a systematic slowdown of the appearance of additional surface-frozen layers from the original power-law or logarithmic divergence. To study this slowdown, the film thickness-dependence of the SF transitions have been measured in two systems, 9O.4 and 7O.7, for freely suspended films 17 to $\sim$ 1000 layers thick. A beautiful systematic variation of the SF with the thickness of the film has been observed. This variation can be explained with a single complete effective interfacial potential for all the film thicknesses studied. The finite-size influenced surface freezing is found to obey the relation $t = \beta \exp(-l/\xi) - \beta' L/(L - \varepsilon l)$ where L is the thickness of the film and $1.2 < \varepsilon < 1.6$. This result is similar to finite-size effect results found in other systems, with a characteristic size L, where the shift in transition temperature $\Delta T \sim 1/L$. Whether this model is appropriate remains an open question, but this finite-size parameterization allows a model-independent construction of the complete effective interfacial potential for these films and provides evidence for a new effective force not seen before in LC films.

2.2 Phase Transitions and the Primary Intermolecular Forces in LC Films

2.2.1 The Effect of Surfaces on Phase Transitions

Over a century ago the suggestion was made that melting should start at the surface since the surface is a "natural defect" in the order of the crystal [31]. Surface melting has been proposed to explain a number of puzzles in nature such as, why liquids can be super-cooled but not super-heated, how ice skating is possible, and how crystals grow and sinter. The reduction of the melting temperature for an uncoupled 2D layer on the surface of a 3D system is not surprising from dimensionality considerations alone since the shifts in the triple point temperature often follows the rule that $T_{2D} \sim 2/3 T_{3D}$. However, in quasi-two-dimensional systems like liquid crystals, the transition temperature shifts are not expected to be as large.

The influence of a surface on first- and second-order phase transitions can be seen both theoretically and experimentally by comparing the phase diagrams of bulk and semi-infinite systems [32]. A standard first-order phase transition in a bulk system appears as a discontinuity in the thermodynamic variables as the temperature approaches the bulk melting point T_o and the crystal symmetry of the solid abruptly changes. The bulk order parameter makes a discontinuous jump at the transition temperature, T_o, with no critical exponents. In a semi-infinite systems with second-order bulk transitions, universal surface critical behavior has been observed, and in semi-infinite systems with first-order 3D phase transitions without any universal critical exponents there can be a surface-induced first-order phase transition which exhibits an "apparent criticality" [10]: The surface order parameter diverges continuously approaching the transition temperature as $|T - T_o|^{\beta'}$, with a universal critical exponent, β', which depends only on the spatial dimensionality of the system, and on the form of the microscopic interactions. When a surface phase wets the interior phase, a surface layer can intervene between the bulk phase and the vapor, and an interface delocalization transition can occur as $T \rightarrow T_o$. This leads to a surface-induced phase transition where the thickness of the liquid layer diverges as the bulk transition temperature is approached. The functional form for the growth of the interfacial layer thickness depends on the form of the dominant interactions in the system.

For a second-order phase transition in semi-infinite system, it has been shown that while the bulk order parameter diverges at the critical temperature, T_c, according to

$|T - T_c|^{\beta}$ as $T \rightarrow T_c$ from below, the surface order parameter also has a power-law divergence, $|T - T_c|^{\beta_s}$, but with a different surface critical exponent, β_s, than the bulk exponent, β. From direct hysteresis measurements, the surface freezing transitions described in this thesis are clearly first-order phase transitions.

Surface melting is the formation of a stable liquid on the surface of its solid at a temperature below the bulk melting point and surface freezing is the formation of a stable solid on the surface of its liquid at a temperature above the bulk freezing point. Surface freezing and surface melting are predicted to have identical universal critical behavior which depends only upon the range of the interactions and whether the interface is smooth or rough [10, 15, 16]. If an intermediate disordered phase wets the interface between the ordered phase and vapor, then it is possible that this intermediate phase will intervene between the bulk and the vapor interfaces in a transition called surface-induced disordering (SID). On the other hand, if an intermediate ordered phase wets the interface between the disordered phase and vapor, then it is possible that this intermediate phase will intervene between the bulk and the vapor interfaces in a transition called surface-induced ordering (SIO). Conventional surface melting, an example of SID, occurs when the liquid phase wets the solid-vapor interface and conventional surface freezing, an example of SIO, occurs when the solid phase wets the liquid-vapor interface. For both surface melting and surface freezing, the relative magnitudes of the solid-vapor, solid-liquid and liquid-vapor interfacial energies determine whether SIO or SID transitions can occur. In the surface freezing experiments described in this chapter, the surface and interior phases are neither liquid nor solid; both are smectic LC phases with either 2D liquid or 2D hexatic intralayer order. Liquid crystals surface freeze rather than surface melt since a more ordered surface LC phase forms on the less ordered LC interior. A microscopic understanding of why some surfaces melt below the bulk melting temperature and other surfaces freeze above the bulk melting temperature is not presently available; the thermodynamic model shows this must depend on the microscopics of the interfacial free-energies of the system.

2.2.2 The Dominant Intermolecular Forces in Liquid Crystals

Aside from the discovery of surface freezing at the LC-vapor interface, the next most important result from this study is the determination of the dominant forces in the

four LC systems studied. The two most important forces in liquid crystal systems are long-range van der Waals forces and steric short-range exponential forces [27, 28]. The temperature dependence of the LC surface freezing transitions reveals which of these two simple forces are dominant between the molecules in the film.

The attractive van der Waals forces between electrically neutral non-polar molecules is due to their quantum mechanically induced fluctuating dipole moments. At small separations, r, this interaction potential has, to leading order, the form $V(r) \propto r^{-6}$ [33, 34]. To calculate the interactions between a surface frozen layer and the underlying bulk, all the van der Waals forces in the semi-infinite system are summed resulting in an attractive potential $V(l) \propto l^{-2}$, where l is the separation of the two interfaces [1]. For unretarded van der Waals forces, the thickness l of the surface frozen layer is predicted to follow a power-law divergence, $l \propto t^{-1/3}$, where, $t = |T - T_o|/T_o$, is the reduced temperature.

The other forces expected to be important in these systems are short-range and have the exponential form, $f(l) \propto \exp(-l/\xi)$, with the corresponding potential $V(l) \propto \exp(-l/\xi)$. In contrast to the exponential forces in metals, which are due to screening of the long-range interactions by the conduction electrons, the exponential forces in liquid crystals are due to steric forces [27]. For LC's dominated by their short-range exponential interactions, the divergence of the surface frozen layer is predicted here to be logarithmic , $l = l'_o + \xi \ln(1/|t|)$ [10, 15]. Since both forces should be present, in a system originally dominated by exponential interactions there is predicted to be a crossover from the exponential short-range forces to the long-range dispersion forces [36] when the frozen surface layer grows larger than a few exponential decay lengths. As will be discussed later, no evidence is found for this crossover form below 300Åcorresponding to the first ten surface freezing transitions.

Results from the four liquid crystals studied show that these systems represent both classes of layer-by-layer surface-induced ordering transitions: systems with long-range van der Waals and systems with short-range exponential forces.

---

[1] Assuming the sharp-kink approximation at the interface and that all the forces are pair-wise additive [35].

2.3 *Principles of Surface Freezing*

The discussion of surface freezing in this section is organized to answer the following three important questions: 1) Why does the surface layer freeze? 2) How does the frozen surface layer grow? 3) Why do the transitions occur layer-by-layer instead of continuously?

2.3.1 *Why Does the Surface Layer Freeze?*

Traditional surface melting is the formation of a thin film of surface melted liquid at temperatures below the bulk melting point, T_o on some faces of the crystal surface. Traditional surface freezing is the formation of a thin film of surface frozen solid at temperatures above the bulk melting point. Both the thermodynamic [17], Landau-Ginzburg, [10] and density-functional theory [37] result in the same functional form for the temperature dependence of the thickness of the frozen or melted surface layer, but the essential ideas are most easily seen by considering the simple mean-field theory which is presented in this section for surface freezing in the same terms as the simple thermodynamic surface melting description [17].

The equilibrium state of a bulk semi-infinite system in equilibrium with its vapor is determined by the minimum of the total free energy. This free energy per unit area is composed of the bulk term, $\mu N/A$, and a surface term, γ, where μ is the chemical potential and γ is the surface tension. Surface freezing is a case of interfacial wetting which results from a competition between the phase conversion cost and the interfacial energy gain of the system. If the solid (or more ordered phase) wets its own liquid-vapor interface (or its own less ordered interior phase-vapor interface), then the system can lower its total free energy whenever the interfacial energy gain, $\Delta\gamma$, is greater than the phase conversion cost. Here $\Delta\gamma = \gamma_{lv} - \gamma_{sv} + \gamma_{sl}$ is the interfacial free energy savings of the system produced by replacing the liquid-vapor interface by a solid-vapor and a solid-liquid interface. The result of replacing the original solid-vapor interface with a liquid-vapor and a solid-liquid interface is shown in Fig. 2.1. The phase conversion cost, when a thin solid layer of thickness l is converted to liquid below the bulk triple-point temperature, increases the free energy per unit area by the amount,

$$\delta F_{Conversion} = (\mu_l - \mu_s)l. \tag{2.1}$$

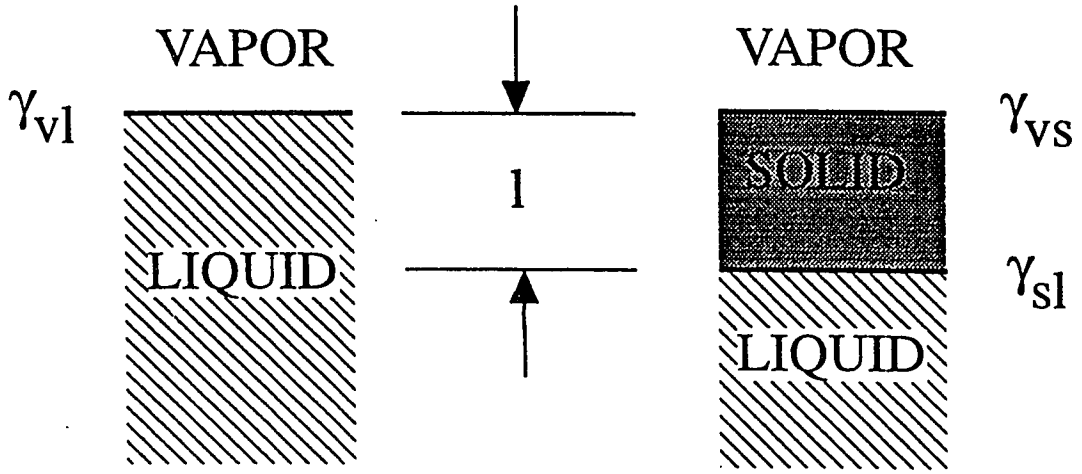

Figure 2.1: Thermodynamics of Surface Freezing. The thermodynamics of surface freezing of a semi-infinite liquid involves competition between the energy cost of converting the layer of liquid to solid and the energy gained by exchanging the liquid-vapor interface, having an interfacial energy γ_{lv}, with the combination of a liquid-solid and a solid-vapor interface having an energy $\gamma_{ls} + \gamma_{sv}$ neglecting interactions. The simple effective interfacial potential, δF, is the sum of the phase conversion cost and the interfacial free energy difference.

Since the interfaces are maintained a distance l apart, and the interfacial energy saving, $\Delta\gamma$, is reduced by the summation of the intermolecular forces over the system. For a system with short-range exponential forces, $V(l) = \lambda \exp(-l/\xi)$, with characteristic length ξ, the interfacial free energy difference per unit area is given by,

$$\delta F_{Interface} = (\gamma_{lv} + \gamma_{sl} - \gamma_{sv})(1 - \lambda e^{-l/\xi}). \tag{2.2}$$

For a system with long-range van der Waals forces, $V(l) = \lambda l^{1-n}$, where $n = 3$, the interfacial free energy difference per unit area is given by,

$$\delta F_{Interface} = (\gamma_{lv} + \gamma_{sl} - \gamma_{sv})(1 - \lambda l^{1-n}). \tag{2.3}$$

In both cases λ is a constant of order 1. Since the phase conversion term is zero at the bulk melting temperature, T_o, the chemical potential difference can be expanded in terms of the reduced temperature, $t = |T - T_o|/T_o$, and the conversion energy is given by Ctl to convert the liquid layer of thickness l to a metastable solid phase layer [38] (C is a constant). In this, the simplest of models, all temperature dependence has been lumped into this linear in t phase conversion term. The total free energy difference between the two states, δF, is also the simple effective interfacial potential, $V_{Simple}(l) \equiv \delta F[l]$, and is given for a system with short-range exponential forces by,

$$\delta F = \delta F_{Conversion} + \delta F_{Interface} = Ctl + (\gamma_{lv} + \gamma_{sl} - \gamma_{sv})(1 - \lambda e^{-l/\xi}) \tag{2.4}$$

and for a system with long-range van der Waals forces by,

$$\delta F = Ctl + (\gamma_{lv} + \gamma_{sl} - \gamma_{sv})(1 - \lambda l^{1-n}). \tag{2.5}$$

Two graphical representations of the simple effective interfacial potential are given in Fig. 2.2 for a semi-infinite system. The simple effective interfacial potential shown, corresponds to Eq. 2.5 and governs the growth of the frozen surface layer during the first ten surface freezing transitions in 9O.4 films which are dominated by long-range van der Waals forces. This potential is the sum of two terms, the phase conversion cost and the interface-interface interaction energy. The position of the interface is given by the minimum of this potential; note that as $t \to 0$ the surface frozen layer thickness grows, $l \to \infty$. The growth of the surface frozen layer can be either continuous

(top panel) or layer-by-layer (bottom panel) depending upon whether the effective interfacial potential displays the molecular periodicity of the material. If the interface is to rough, the average position of the interface is not well defined, and the growth will appear continuous. If the interface is smooth enough that it is well defined, the surface freezing will jump from minimum to minimum of the effective interfacial potential [39] and the transitions will appear layer-by-layer. Surface freezing transitions in all four LC systems described in this chapter exhibit this layer-by-layer growth of the frozen surface phase.

The Landau-Ginzburg theory and its explicit connection with the order-parameter profile of the film is discussed in Sec. 4.7; the predicted order parameter profile is also compared with the interlayer density profile extracted using the direct inversion analysis described in Chapter 3.

2.3.2 How Does the Frozen Surface Layer Grow?

The location of the interface between the surface-induced coexisting liquid and solid is given by $l(t)$ which is the functional relationship between the reduced temperature, t, and the thickness of the frozen surface layer, l. The functional form of $l(t)$ depends on the intermolecular forces in the system and can be obtained by minimization, $\delta F/\delta l = 0$, giving

$$t = \beta e^{-\frac{l}{\xi}} \tag{2.6}$$

for short-range exponential forces, and

$$t = \alpha l^{-n} \tag{2.7}$$

for long-range van der Waals forces. These simple equations fit the first ten transitions in the four materials studied very well. Inverting these relations, the thickness, l, of the surface frozen layer, in terms of the reduced temperature, t, is given by $l = l_o' + \xi \ln(1/|t|)$, for short-range exponential forces, and by $l = l_o t^{-\nu}$, with $\nu = 1/n = 1/3$, for long-range van der Waals forces. The value of the exponential force coefficient β has not been predicted by theory but the van der Waals coefficient, l_o, is given by $l_o = [(2\Delta\gamma\lambda)/(CT_o n(\partial(\Delta\mu))/(\partial T))]^{1/3}$, where n is the surface density of the liquid phase and $\Delta\mu = \mu_s - \mu_l$ is the solid-liquid chemical potential difference. For a system governed by van der Waals forces, the exponent $\nu = 1/3$. For exponential force

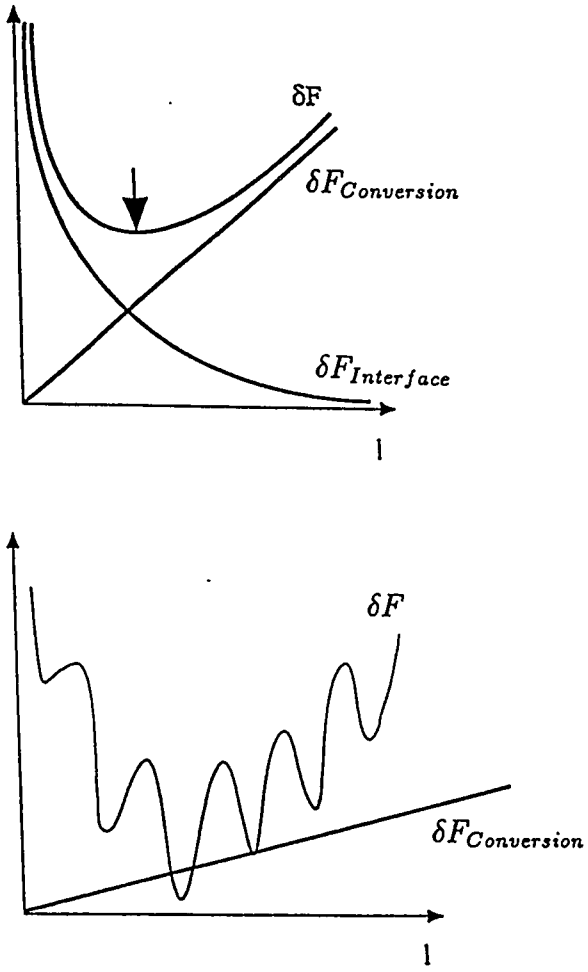

Figure 2.2: Simple Effective Interfacial Potential. A schematic illustration of the simple effective interfacial potential, δF, correct for the first ten SF transitions in thicker films. δF is the sum of the interface-interface interaction, $\delta F_{Interface} = \Delta\gamma(1 - \lambda l^{-2})$, and the phase conversion energy, $\delta F_{Conversion} = Ctl$. The effective interfacial potential will be smooth (top panel) if the system has a rough interface and surface freezing transitions will be continuous. For a smooth interface (bottom panel), δF will display the molecular periodicity of the system and the system will exhibit layer-by-layer surface freezing transitions. For all four liquid crystal systems discussed in this chapter, the interface is smooth and the transitions appear layer-by-layer.

systems, the characteristic length, ξ, should be about one molecular layer, $\xi \approx 1$, since the exponential forces describe short-range steric interactions. The values of ν and ξ produced from the data analysis fits are compared to these predicted physical constraints to determine whether the fit is physically reasonable.

For surface freezing in a finite film of total thickness L, the derivation of $t(l)$ is somewhat different than the standard semi-infinite derivation since the finite system has two solid-vapor interfaces and two solid-liquid interfaces as shown in Fig. 2.3. By symmetry, there will be frozen surface layers on both film-vapor interfaces. The results from the summation of the intermolecular forces throughout the film then give,

$$t = \begin{pmatrix} Interface- \\ NearVapor \\ Term \end{pmatrix} + \begin{pmatrix} Interface- \\ FarVapor \\ Term \end{pmatrix} + \begin{pmatrix} Interface- \\ Interface \\ Term \end{pmatrix}, \qquad (2.8)$$

again using the sharp kink approximation, and assuming pair-wise additive intermolecular forces throughout the film. For exponential forces, where $V(l) = \lambda \exp(-l/\xi)$,

$$t = \beta e^{-\frac{l}{\xi}} - \beta e^{\frac{-(L-l)}{\xi}} + \beta' e^{\frac{-(L-2l)}{\xi}}, \qquad (2.9)$$

and for long-range non-retarded van der Waals forces, where $V(l) = \lambda l^{1-n}$,

$$t = \alpha l^{-n} - \alpha(L-l)^{-n} + \alpha'(L-2l)^{-n} \qquad (2.10)$$

with $n = 3$. In these two equations, the first two terms correspond to the interface-near vapor and the interface-far vapor interactions, respectively. The third term corresponds to interactions between the two interior interfaces. For the first ten transitions of 64-layer films, the two interior interfaces are always very far apart, $\geq$ 1200Å, and the interior interface-interior interface interactions and the interior interface-far vapor interface terms are very small. The interaction coefficients α and α' vary as the refractive index difference (the density difference, to first order) between the interacting phases, so $\alpha >> \alpha'$ [33, 34]. For these reasons, the second and third terms in Eq. 2.9 are expected and found experimentally to be negligible for all four materials for films thicker than about 30 layers. Therefore, Eq. 2.6 for short-range exponential forces and Eq. 2.7 for long-range van der Waals forces provide a good description of the first ten surface freezing transitions in films with thickness $L \geq 30$

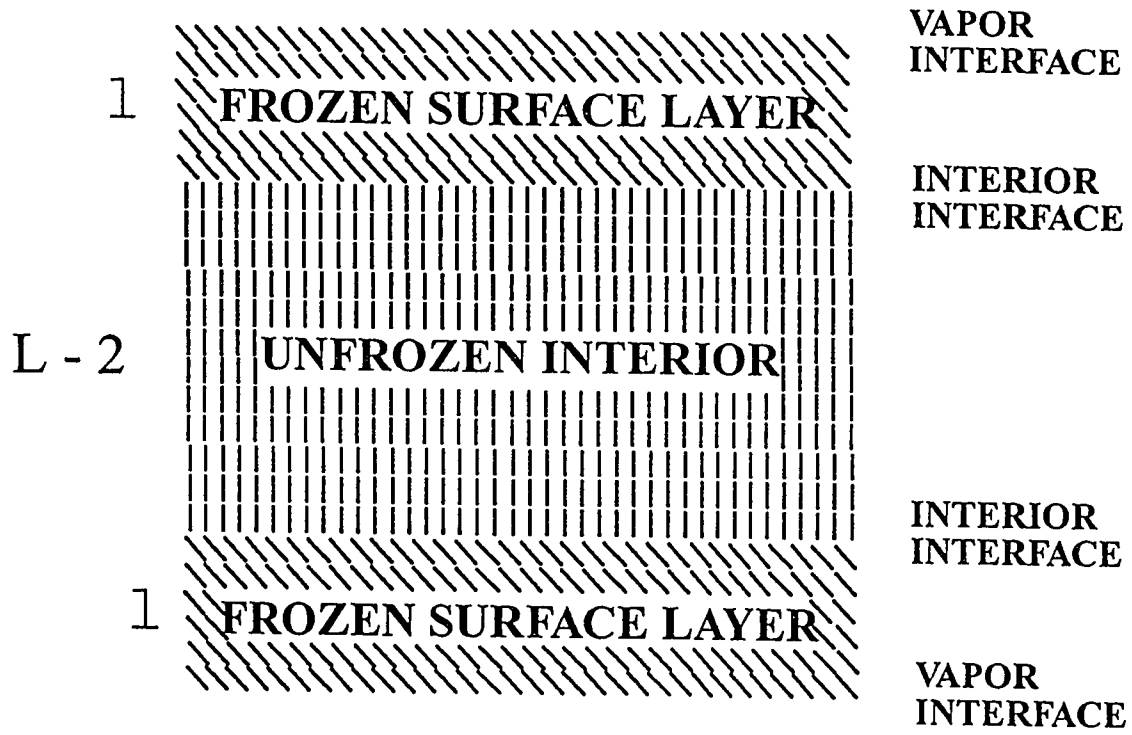

Figure 2.3: Thermodynamics of Surface Freezing in Films. Surface frozen layers of thickness l form on both surfaces of the liquid crystal film during the surface freezing transition. Therefore, a film with total thickness L has two frozen surface layer-unfrozen interior layer interfaces, called interior interfaces, and two frozen surface layer-vapor interface, called vapor interfaces. The effective interfacial potential involves the interaction of each interface with the other three, as shown in Eq. 2.9 and 2.10 but only the interior interface-near vapor interface interactions are important for films thicker than about 30 layers. In the simple thermodynamic picture of surface freezing, if the frozen surface layer wets the initially unfrozen vapor interface, the system will surface freeze when the interfacial energy gain is greater than the phase conversion cost. For smooth interfaces, the surface freezing transition is layer-by-layer.

layers. For films thinner than $L \sim 30$ layers, the interior interfaces are sufficiently close that it is necessary to take into account their interaction.

The thermodynamic theory presented above is equivalent to the mean-field description [10] and ignores fluctuations. This is valid if the physical dimension of the system is greater than the upper marginal dimensionality. When the dimensionality of the system is larger than the upper marginal dimensionality, the properties and phase transitions are not affected by thermal fluctuations and the critical exponents will have mean field values. If the dimensionality is equal to the upper marginal dimensionality, then there are logarithmic corrections to the exponents near the phase transition. The upper marginal dimensionality, d^*, satisfies the hyper-scaling relation, $\nu d^* = 2 - \alpha$, with classical values for the critical exponents, ν and α. For surface melting at interfaces in three dimensions governed by van der Waals forces [35, 40], $d^* = 2$ and classical exponents are expected. For surface melting governed by short-range exponential interactions, $d^* = 3$ [41] and logarithmic corrections very near the transition temperature are expected. A search for these logarithmic corrections in the short-range exponential force LC systems is planned. The four LC systems described in this thesis seem to exhibit mean-field behavior, although the observed finite-size effects may be partially due to scaling corrections.

2.3.3 Why Do the Transitions Occur Layer-by-Layer Instead Of Continuously?

The character of surface melting and surface freezing transitions also depends on whether the interface between the surface phase and the interior phase is rough or smooth. For conventional surface melting, this depends upon whether the solid-vapor interface is above or below the roughening temperature, T_r. If $T > T_r$, then the interface is rough, and the growth of a wetting layer at this interface is predicted to be continuous [16] since the roughness washes out the natural atomic periodicity in the effective interfacial potential. For $T < T_r$, the solid-vapor interface will be smooth and the transition is predicted to proceed layer-by-layer. In the four LC systems studied here, surface freezing always occurred layer-by-layer indicating that the effective interfacial potential retains the natural periodicity of one molecular layer [39]. This provides indirect evidence that the layers in these systems are well defined; direct x-ray evidence for the relatively high quality of the layering is given in Chapter 3.

Surface melting and surface freezing are special cases of interfacial wetting [16, 42] in which the surface melted or frozen layer wets its own solid/vapor or liquid/vapor interface, respectively. Wetting behavior can be nonwetting, incomplete wetting , or complete wetting. Most LC surface freezing transitions are nonwetting since the entire film freezes abruptly. Many FSLC films exhibit incomplete (monolayer) wetting in which the two surface monolayers freeze about ten degrees above the bulk freezing transition temperature and the rest of the interior layers freeze at the bulk transition temperature. Monolayer incomplete wetting has been studied for crystalline smectic-B monolayers on smectic-A films [43, 44] and for smectic-I monolayers on smectic-C films [9]. In all four LC systems studied here, the surface frozen phase is surface stabilized, since it does not appear in the bulk phase diagram. The surface freezing transitions in these systems all proceeded in a layer-by-layer fashion until the entire film was frozen. Technically, this surface freezing still corresponds to incomplete wetting, because the surface frozen phase is not in the bulk phase diagram; the surface stabilized phase for a semi-infinite system would always have a finite thickness. The importance of surfaces in stabilizing non-bulk phases has not been fully appreciated. LC systems are typically described by their bulk phase diagrams which only provide a partial description of their behavior. It is still an interesting and unsolved question as to why all the surface freezing transitions in these four systems have surface-stabilized, bulk-thermodynamically-unstable, surface-frozen phases.

The relation between wetting, roughening and surface ordering is apparent both in the surface freezing of LC films and in the layering transitions observed in rare-gas films adsorbed on uniform homogeneous substrates [31, 42]. Physisorbed rare gas layers on graphite [45] exhibit layering during the formation of liquid or solid layers with increasing chemical potential. If the temperature remains constant and $T < T_t$, where T_t is the triple point temperature, then adsorption isotherms exhibit either continuous or stepwise increases in surface coverage as the pressure of the 3D gas is increased. If the two components of the system wet one another, then the system grows all the way to bulk. The mode of growth, either continuous or layer-by-layer, depends on whether the interface is rough or smooth; whether the system is above or below the roughening temperature, T_r. In the layer-by-layer growth mode, the isotherm steps locate liquid-vapor or liquid-solid transitions. At higher temperatures, after a substantial number of distinct layer steps, the sharp steps disappear

when passing through the roughening transition which occurs near 0.8 T_t [46]. In very thick LC films, a roughening transition might be induced by increased capillary wave amplitudes at the surface of the film and enhanced thermally induced smectic fluctuations near the center of the film. Layer-by-layer transitions have been observed in LC films from 17 to about a thousand layers thick and no evidence has been seen for a crossover to continuous growth indicating a roughening transition.

2.4 Four Classes of Surface Freezing and Surface Melting

The classification of systems according to their intermolecular interactions and the character of the their interfaces, produces four universality classes of surface freezing and surface melting: systems can be either dominated by long-range van der Waals forces or short-range exponential forces and the transitions can proceed either layer-by-layer or in a continuous manner. These four possible classes of universal surface freezing and melting behavior are then: (1) continuous power-law, (2) continuous logarithmic, (3) layer-by-layer logarithmic, and (4) layer-by-layer power-law. Table 2.1 lists these four universality classes and provides examples of each class. The LC systems studied here fall into two classes: 9O.4 exhibits a layer-by-layer transition with power-law growth and 4O.7 and 7O.7 exhibit layer-by-layer transitions with logarithmic growth. The surface freezing of $\overline{14}$S5 is consistent with both classes of layer-by-layer transitions. This is the first report of logarithmic and power-law layer-by-layer growth at the LC-vapor interface which continues until the entire (albeit finite) film is frozen.

2.5 Finite-Size Effects

Freely-suspended-liquid-crystal (FSLC) films are wonderful systems in which to measure finite-size effects since they are substrate-free and the thickness of the film can be continuously changed from two to thousands of molecular layers. In fact changes in structure and in the phase transitions have been noticed during the crossover from two to three dimensions [6, 43, 44, 51].

The effect of finite system size on phase transitions has been extensively studied theoretically [32, 47, 48, 49, 50, 52, 53]. For a second-order phase transition in a finite-size system, scaling relations describe the modification of the bulk critical ex-

Table 2.1: The Four Classes of Surface Freezing and Melting. Illustrated below are the four universality classes of surface freezing and surface melting and some experimental examples. The experimental techniques used to study the various systems are: Proton back-scattering [64], heat capacity [68], neutron diffraction [69], polarized microscopy [29, 30], and x-ray diffraction [65, 78, 79]. The four systems studied here, **9O.4**, **4O.7**, **7O.7**, and **$\overline{14}$S5**, exhibit surface freezing transitions which occur layer-by-layer. Examples of both long-range van der Waals and short-range exponential force systems have been discovered. The results for $\overline{14}$S5 are consistent with either long-range van der Waals or short-range exponential force models.

	Power-Law	Logarithmic
Continuous	Ne/Gr, Ar/Gr [68] Pb [65]	Pb [110] [64] O_2/Gr [69]
Layer-by-Layer	**9O.4** [29] **$\overline{14}$S5** [30]	**4O.7** [30] **7O.7** [30] **$\overline{14}$S5** [30] 8CB [78] 12CB [79]

ponents very near the critical point. As the critical point is approached for a wetting transition, the correlation length increases and the thickness of the wetting layer diverges with the longitudinal correlation length until cut off by the finite-size limit imposed by the film thickness [52]. For first-order bulk transitions in a finite-size systems, the thermodynamic singularities are rounded and finite-size scaling theory [49, 53] describes the crossover from the analytic behavior in finite systems to the singular behavior in bulk. Only recently has the finite-size scaling (FSS) behavior of the wetting transition been calculated for first-order transitions [47] and transition temperature shifts have been predicted for first-order transitions in short-range exponential and long-range van der Waals interaction systems where additional densities (e.g. impurities) are required to fully describe the system [48].

For systems undergoing a first-order transition in a confined geometry, the transition temperature is shifted from that found in the unconfined bulk. In the liquid-gas system, the chemical potential $\mu(L)$ at which the transition occurs in a film of thickness L is given by the Kelvin equation [54], $\mu(L) - \mu(\infty) = (2\Delta\gamma)/(L\Delta\rho)$, where $\mu(\infty)$ is the chemical potential for the infinite system at saturation, $\Delta\gamma$ is the liquid-gas surface energy difference, and $\Delta\rho$ is the density difference at the transition. A similar result has also been proposed to explain physisorption of rare gases in capillaries [54]. In addition, an analogous relation has been derived for the shift in transition temperature for thin LC films at the nematic-isotropic transition [55],

$$T_{NI}(L) = T_{NI}(\infty)\left(1 - \frac{2(\gamma_I - \gamma_N)}{Ll_o}\right) \tag{2.11}$$

where l_o is the latent heat per unit volume. This temperature shift functional form, $\Delta T \propto 1/L$, has been derived for general first-order transitions [56]. Previous experiments studying finite-size effects in LC materials have primarily studied confined nematics in porous silica [57] and porous membranes [58]; both systems exhibit shifts in the transition temperatures and pore-size dependent effects.

Although no theories have been proposed for the finite-size effects in first-order surface freezing transitions in smectic films, the analogy with the systems described above would suggest a transition temperature shift, ΔT, with the form $\Delta T \propto 1/L$. In the case of a film initially in a liquid phase with total thickness L, before surface freezing, the thickness of the liquid region is equal to the total thickness of the film. After the formation of surface frozen layers of thickness l on each vapor interface,

the thickness of the interior liquid layer is $L - 2l$. The transition temperature shift, proportional to the thickness of the intermediate liquid region of the film would then be $\Delta T \propto 1/(L - 2l)$. This would modify the simple effective interfacial potential described above by adding an additional "finite-size term". The resulting modified effective interfacial potential, called the "complete" effective interfacial potential, is given by $V_C = Ctl + \Delta\gamma(1 - \lambda \exp) - l/\xi)) - (\beta'/2)\ln(L - 2l)$ for a system dominated by short-range exponential forces. The three terms in V_C correspond to the phase conversion cost, the interface-interface interaction, and the finite-size shift, respectively. This form of the complete effective interfacial potential results in a transition temperature shift proportional to the reciprocal of the liquid thickness and changes with each surface freezing transition as the thickness of the interior liquid layer changes. Minimizing this free energy, and solving for the reduced temperature, yields $t = \beta \exp(-l/\xi) - \beta'/(L - 2l)$ for short-range exponential interactions, and the analogous derivation yields $t = \alpha l^{-n} - \beta'/(L - 2l)$ for long-range van der Waals forces.

The form of the finite-size temperature shift, ΔT, must also be modified if the overall film thickness changes due to the SF transitions. For the LC materials measured, the surface freezing transitions are from untilted to tilted phases and the total film thickness does change due to the molecular tilt of the tilted phase. As shown in detail in Sec. 2.9, the results from all three LC systems where the finite-size effects were studied are fit very well with a phenomenological finite-size temperature shift ΔT, with the functional form $\Delta T \propto 1/(L - \varepsilon l)$. Here ε is a temperature and film thickness-independent fitting parameter. The $t(l)$ relations are now, for short-range exponential forces, given by,

$$t = \beta e^{-\frac{l}{\xi}} - \frac{\beta' L}{L - \varepsilon l}, \tag{2.12}$$

and for long-range van der Waals forces

$$t = \alpha l^{-n} - \frac{\beta' L}{L - \varepsilon l}. \tag{2.13}$$

The corresponding complete effective interfacial potential, $V_C(l)$, for a system dominated by short-range exponential forces is now,

$$V_C = Ctl + \Delta\gamma(1 - \lambda e^{-\frac{l}{\xi}}) - \frac{\beta' L}{\varepsilon} \ln(L - \varepsilon l) \tag{2.14}$$

and for long-range van der Waals force systems,

$$V_C = Ctl + \Delta\gamma(1 - \lambda l^{1-n}) - \frac{\beta' L}{\varepsilon} \ln(L - \varepsilon l). \tag{2.15}$$

The experimental results indicate that $\beta' \sim 0.3$ and that $\varepsilon \sim 1.2$ for all thickness 4O.7 and 7O.7 films. For these materials, ε is less than the value predicted by the simple confinement model where $\varepsilon = 2$.

2.6 Previous Experimental Results

The termination of translational symmetry imposed by a surface often causes considerable spatial order in both solids and liquids. This termination of the spatial periodicity also induces a surface potential and produces special electrical properties at the surfaces and interfaces of metals and semiconductors. Numerous metal and semiconductor interface reconstructions and e.g., the order-disorder surface transition in Cu_3Au [59], are well known examples of surface-induced order (SIO) in the transverse direction, whereas the layering of rare gases physisorbed at crystal-vapor interfaces [45] and liquid metals [60] are examples of SIO in the longitudinal direction. A general successful microscopic theory which describes how surfaces induce both transverse and longitudinal order does not exist.

The influence of surfaces on phase transitions has generated much interest with numerous experimental observations of both surface melting and surface freezing. Numerical simulations [18, 85] demonstrate the importance of surfaces in initiating both disordering and ordering. The surfaces of 3D crystals show enhanced order rather than disorder far below the melting temperature, but as the temperature is raised, many surfaces disorder before the bulk. The importance of the surface in nucleating melting is clearly demonstrated in work studying coated metal particles [61] where melting of the internal material is inhibited and the coated materials can be heated well above the normal melting temperatures.

2.6.1 Surface Melting

The suggestion that melting begins at a surface came from early observations of the melting of ice [31]. Ellipsometric [62], regelation [63] and polarized reflectivity [33] studies contain reports of the presence of a liquid layer on some facets of ice below 0°

C, but detailed atomic measurements of the growth of the liquid layer have not been made.

Surface melting has been predicted to occur in many systems and a number of experiments [33, 62]–[71] have attempted to measure the thickness of the melted layer below the bulk melting transition temperature. Recent studies of the surface melting of Pb crystals [64, 65, 66, 67] and of rare gases physisorbed on graphite [68, 69, 70] give clear experimental demonstrations of the influence of surfaces on phase transitions. Surface melting studies of the [110] Pb crystal surface using proton backscattering [64] and LEED [67] show a logarithmic temperature dependence of the melted layer thickness, a screening length of about three atomic distances, and an atomically sharp liquid-solid interface, but no layer-by-layer steps. This result was supported by thin-film Pb TEM studies [66]. However, more recent x-ray diffraction studies of bulk Pb [65] show a power-law functional form for the growth and anisotropy [67, 71] between surface melting on the $[1\bar{1}0]$ and the [001] Pb directions. Calorimetric studies of thick physisorbed films of both Argon and Neon [68] on graphite foam below the triple point show a continuous power-law behavior, $l \propto t^{-1/3}$, for the growth of melted layers. The interpretation of these results has been complicated by ellipsometric isotherm [72] measurements, which indicate that capillary condensation occurs for intermediate coverages in these high surface area graphite substrates. Neutron diffraction experiments of thin O_2 films [69] on graphite have reported a logarithmic divergence of the surface melted layer and quasi-elastic neutron scattering measurements of methane on MgO [70] have also indicated the presence of a liquid layer below T_o. Consequently, the functional form of the surface melting in these systems remains somewhat controversial since both logarithmic [64, 69] and power-law [65, 68] behavior has been reported. Note that these systems show continuous surface-melting transitions which indicates they have either rough interfaces or some other system inhomogeneities. A further complication is that, unlike free standing LC films, the physisorbed systems all involve a solid substrate. Consequently, the analysis of their behavior is complicated by questions about the polarizability of the substrate [33] and about surface-induced longitudinal ordering of the overlayer.

2.6.2 Surface-Induced Order and Surface Freezing in Liquid Crystals

Liquid crystals surface freeze rather than surface melt and exhibit surface enhanced positional, orientational, and longitudinal order at LC-solid and LC-vapor interfaces [73]. Orientational anchoring [74, 76], nematic ordering [74, 75, 77], and smectic layering in bulk [78, 79, 80] and in FSLC films [29, 82] have all been studied.

Considerable work has been done studying the surface ordering at bulk LC-solid interfaces. Studies of the anisotropic substrate-molecule interactions and surface treatments have shown that various forms of orientational order are induced [74, 76, 83] at the substrate surface and that this order is usually different than that found away from the surface. Surface orientational and anchoring configurations in nematics [73] have also been studied and are technologically important due to the requirement for controlled molecular alignment at the surfaces of LC display devices. Longitudinal ordering at the LC-solid interface is often observed since smectic alignment is sterically favored. It has also been well established that the orientational wetting properties do depend on the alkyl chain length [84]. Logarithmic growth of nematic ordering [77] and of smectic layering [79] has been found at solid-isotropic interfaces. X-ray reflectivity studies of (10-12)CB on alkylsilane-coated Si (100)[79] showed induced homotropic orientation at the surface and layer-by-layer growth of the smectic layering into the isotropic phase, but with fewer layering transitions than the same system at the LC-vapor surface.

The SIO of the LC-vapor interface in bulk samples has also been studied extensively both theoretically and experimentally [9, 26, 30, 73, 85]–[90]. Lattice models [85], density functional theories [87], and generalized mean-field [88] theories for surface-induced smectic order predict partial wetting at the isotropic-vapor interface. Polarized microscopy experiments [80] have demonstrated smectic order at the vapor interface of LC droplets. Landau-de Gennes theory [74] has predicted and ellipsometry experiments [89] have measured the presence of nematic order at an isotropic-vapor interface. X-ray reflectivity measurements [78, 90] of the isotropic-vapor interfaces of (9.5 - 12)CB and (12 - 16)OCB show partial wetting by smectic-A layers, and 12CB exhibits layer-by-layer logarithmic growth of smectic-A layers into the bulk isotropic phase. X-ray reflectivity studies [90] of mixtures of 9CB and 10CB observed smectic order at the nematic-vapor interface which decays exponentially into the bulk. Finally, layer-by-layer formation of smectic layers has even been reported

during the compression of LC monolayers on water [91].

In this chapter, results are presented for four LC systems that exhibit layer-by-layer surface freezing with logarithmic and power-law growth of the frozen surface layer [29, 30]. Freely-suspended liquid crystal (FSLC) films [6, 9, 25, 43, 44] often exhibit monolayers of non-bulk tilted phases at the LC-vapor interface. The appearance of ordered phases on films is not surprising since the transition from a untilted to a tilted smectic phase increases the areal density at the surface and because the surface tension quenches the layer fluctuations [22]. Incomplete wetting has been observed previously for crystalline smectic-B monolayers on 2D-liquid smectic-A films [43, 44], tilted 2D-liquid smectic-C monolayers on 2D-liquid smectic-A films [25], and tilted hexatic smectic-I monolayers on tilted 2D-liquid smectic-C films [9]. Some very recent heat capacity studies of thin films have also shown monolayer [81] and a few layers [82] of surface freezing transitions. A new feature in the four LC systems described in this chapter is that the surface freezing transitions continue in a layer-by-layer manner all the way to the center of the film.

2.7 Experimental Apparatus and Method

The experimental apparatus consists of a temperature-regulated film oven mounted in a vacuum chamber. Uniform thickness circular LC films were illuminated with polarized white light and the specular reflected light passing through a second polarizer was monitored with a video camera. Due to a radial temperature gradient provided by the film oven, the monolayer freezing transitions appeared as interfaces moving radially outward from the center of the film as the temperature of the film was lowered.

The experimental apparatus is shown schematically in Fig. 2.4. The 10 mm diameter LC films were created using a spring loaded stainless steel wiper which was drawn across the 0.13 mm thick stainless steel film holder. The film holder was mounted axially passing through the center of the 55 mm diameter by 125 mm long film oven. The oven was mounted on a rotatable vacuum seal inside of a vacuum chamber. During most experimental runs, the chamber was first evacuated and then backfilled with 300 torr of dry N_2 gas to inhibit film degradation, to maintain a strong thermal link between the film and the oven, and to prevent Rayleigh-Benard convection of the N_2 since it disturbs the film temperature. The film oven was heated using two

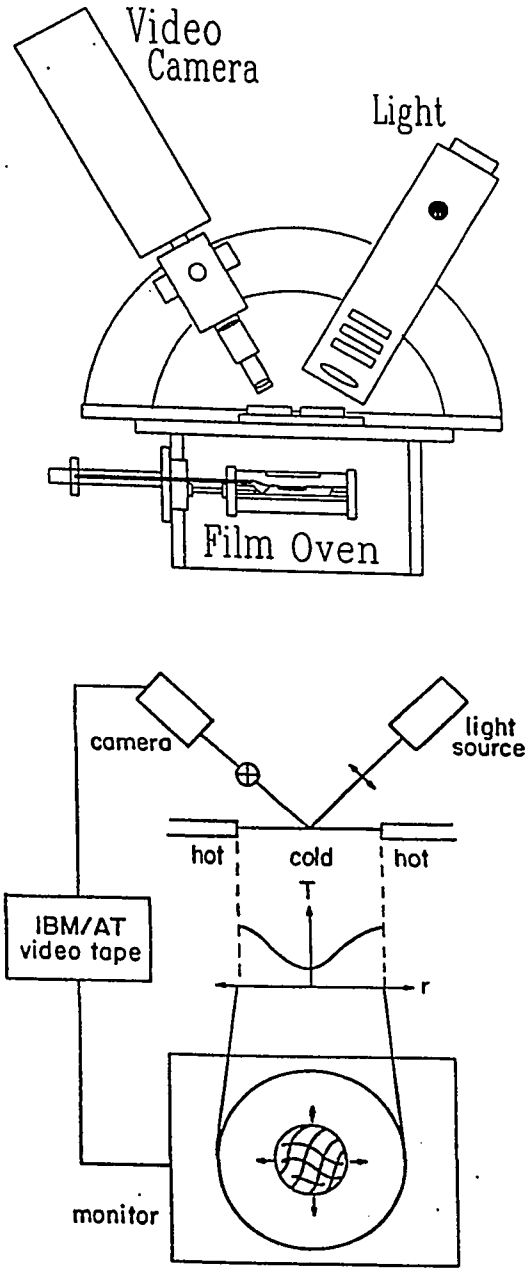

Figure 2.4: Experimental Apparatus. Two illustrations are shown of the experimental setup. The film is illuminated by polarized white-light and viewed by a video camera through a crossed polarizer. The liquid crystal film oven provides a radial temperature gradient, so the surface freezing transitions originate at the center of the 10 mm diameter film and move radially outward as the temperature of the oven is lowered.

50 ohm foil heaters. Control and sense thermistors were located directly under one of the heaters and on the film support plate, about 10 mm from the film, respectively. The sensitivity of these thermistors was 900 Ω/degree at 60° C. The oven and sample temperatures were continuously monitored using 5 1/2 digit voltmeters interfaced via IEEE488 to an IBM AT computer. The temperature stability, provided by a home-built computer-controlled proportional-integral-differential temperature controller [125], was maintained to better than ± 1 mK/hour. This temperature controller was interfaced via its single-board computer, to the RS232 port of the IBM AT computer used to control the experiment and monitor the temperature.

Optical access to the film was provided through a Plexiglas window mounted on the flat top of the vacuum chamber and through a slot cut in the top of the film oven. A semi-circular optical rail (see Fig. 2.4), mounted on top of the vacuum chamber, allowed adjustment of the video camera and the light assembly . The film was illuminated by an air cooled 240W quartz-halogen lamp focused onto the film by an 85 mm focal length lens. To prevent excessive film heating, the infrared was filtered out using a heat reflecting mirror and two heat absorbing filters. A polarizer was placed before and after reflection from the film. The video images from the specularly reflected light were magnified by about a factor of 50 with a zoom lens. The images are computer-contrast enhanced by a frame grabber board and image enhancement software to increase visibility since the optical contrast change corresponding to a single molecular layer transition is very small. The signal from the camera is contrast-enhanced using a saw-tooth look-up table; this table expanded the dynamic range of the intensity by a factor of about five before it was written on video tape. The saw-tooth look-up table mapped the 8-bit digitized camera intensity onto the 0-255 scale of output intensity by folding over the input intensity five times: the inputs from 0-50 were mapped onto outputs from 0-255 and the inputs from 51-100 were mapped on to 254-0, etc. To obtain the maximum sensitivity, the camera had to be aligned with the specular reflection direction and the film oven had to be rotated axially to uniformly illuminate the film. The incident light was roughly polarized, and the output polarizer was slightly uncrossed to maximize the light intensity at the camera without saturation.

The liquid crystals used in this study are rod-like organic molecules which have phases intermediate between liquid and solid [4]. The distinct LC mesophases are

characterized by the symmetries and orientations of the LC molecules (see Chapter 1). All the phases studied here are smectics, meaning they are 1D crystals with the LC molecules organized into layers. LC films which have been formed across a planar aperture [5] are stabilized by their planar smectic structure and form with the smectic layers parallel to the film surface. Liquid crystal films with thicknesses from about 60 Å to several microns can be produced easily. All the surface freezing transitions studied here probably began in the smectic-A phase, which consists of 2D liquid layers with the average molecular axis normal to the layers. The surface freezing phase transition involves a change in the in-plane order of the LC molecules and the surface frozen phase in all four cases is a tilted phase in which the molecular axis makes a finite angle with respect to the smectic layers. Because the tilted liquid crystal phases are very birefringent, monolayer freezing transitions can be observed optically through crossed polarizers [6]. The present identification of the surface phases as either smectic-I or smectic-F phases, which are both hexatic phases with six-fold symmetry distinguished by the molecular tilt direction relative to the near neighbor directions, was based on the observed textures. In-plane x-ray scattering measurements are planned to determine all these surface frozen phases.

During the experiment, the computer-enhanced film image is displayed on a monitor and simultaneously recorded on video tape. The film temperature was also recorded on the video tape by encoding it on the audio channel using a homemade 1200 baud modem. The modem details are described in Appendix A. Subsequent re-analysis of the data used the video-taped images and temperatures. During the experiment, the temperature of the oven was typically lowered by 0.5 mK/sec. As the temperature of the oven was lowered, the surface freezing transitions appeared as waves of enhanced contrast starting at the center of the film and preceding radially outward. Fig. 2.5 shows a computer-enhanced image of a surface freezing transition. A video tape of representative surface freezing experimental data has been submitted with this thesis. The actual experimental data was obtained by recording the transition temperature as each layer froze. A key driven computer program was used to record the temperature of each surface freezing transition by playing back the video tape and visually observing the freezing waves. Data for films thicker than 100 layers usually had one or two regions of very poor optical contrast which produced gaps of some transitions where the surface freezing transitions could not be observed. These

data sets were splined to replace the missing transitions. During the data-taking process, these small breaks in the data were obvious and the spline simply replaced the missed transitions. Care was taken to make sure this procedure did not modify the results or the best-fit parameters.

2.7.1 Temperature Profile of a LC Film

The film oven provided a small radial temperature gradient, with the center of the film being the coldest and the circular support of the film being the warmest, and equal to the temperature of the oven. The equilibrium temperature profile of the film can be understood by solving the heat equation subject to the boundary conditions that the edge of the film is at the oven temperature, T_{oven}, and that the sum of the heat flows from radiation, gas, and film conduction are zero in equilibrium. After linearization, the equilibrium temperature profile is given by $T(r,z) = T_{oven} - A\mathrm{J_o}(ar)\mathrm{Cosh}(az)$, with the first zero of the Bessel function, J_o, at $ar_o = 2.405$ and the film radius, $r_o = 5$ mm. For a 64-layer film, the temperature difference in the z direction between the surface layer and the center layer is negligible, $\Delta T_z = 6 \times 10^{-5}$ K, since the film is so thin, 1800 Å. Both the pressure of the N_2 in the oven and the intensity of the light source influenced the magnitude of the radial temperature gradient. We found that the optimal pressure was about 300 torr: the N_2 gas started to have Rayleigh-Benard convection creating film convection at higher N_2 pressures, and equilibration times were too long if the pressure was much lower. At 300 torr N_2, the radial gradient, ∂T/∂r, was about 10 mK/mm near the center of the film (where the surface freezing measurements were made). Fig. 2.6 displays the experimentally measured temperature profiles of a 64-layer 7O.7 film at 79° and 69° C. These temperature profile measurements were made by noting the SF interface position as the oven temperature, T_{oven}, was stepped below the phase transition temperature. As can be seen in Fig. 2.6, the temperature profile is steeper in the intermediate region (between the center and the edge of the film) and flatter near the center of the film. The LC film met the circular film holder at $r = 5$ mm. The temperature difference between the holder and the center of the film for phase transitions at 79° and 69° was 0.73° and 0.5°, respectively. Preliminary analysis indicates that this small change in the profile with oven temperature, due to the coupling of the LC film via the N_2 with the vacuum chamber wall at T_{room}, does not affect the surface freezing and finite-size

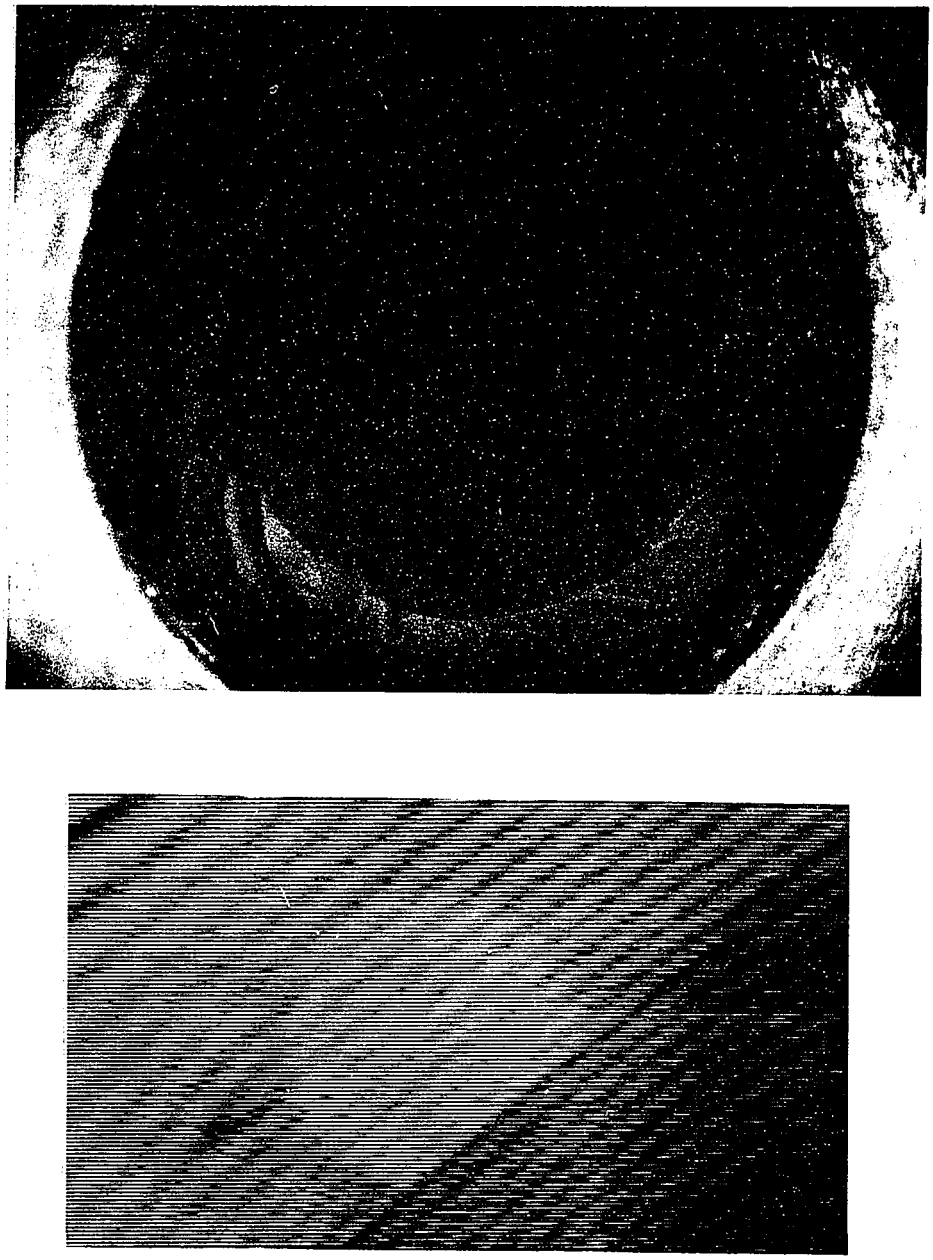

Figure 2.5: Image of a Surface Freezing Transition. The upper panel shows a magnified and image-enhanced picture of a 9O.4 surface freezing transition (the circular region in the center of the film) in a 64-layer film. Surface freezing transitions in these birefringent liquid crystal phases appear as a region of enhanced contrast since the transition is from a untilted to a tilted phase. The stripped texture results from the various tilt domains of earlier surface freezing transitions. The lower panel shows a color picture of a 64-layer 7O.7 film during the smectic-I/A to smectic-I/C transition.

results reported here.

2.7.2 LC Film Thickness Determination and Material Degradation

The LC film thickness was determined by comparing the thickness calculated from the film color [6] and from the total number of observed surface freezing transitions. For FSLC films with thicknesses in the range of 25 to 200 layers, the color of the film when viewed with reflected white light is one of the best ways of determining the thickness. The expected color of a film of thickness, l, can be computed from the intensity reflection coefficient, $I_\lambda(l)$, for wavelength, λ, given the layer spacing, the index of refraction, and the angle of incidence [92]. Fig. 2.7 is a plot of the C. I. E. coordinates and the film color for the liquid crystal 7O.7 [6, 93]. After some practice, turquoise-blue films, $L \sim 64$ layers thick (± 1 layer), could be made reproducibly and film thickness nonuniformities within one layer could be detected. After 200 layers, it is difficult to determine the thickness from the color alone and film thickness determination was made by counting the total number of surface freezing transitions. The number of surface freezing transitions and the film color corresponded quite well for thinner films. Multiple SF measurements made on the same 64-layer film produced the same value for the total number of surface freezing transitions to within ± 5 % and agreed with the thickness of the film calculated from the color to within the ± 10 % accuracy of the color method. Fig. 2.8 shows apparent variations in film thickness found from counting the number of surface freezing transitions during multiple measurements of the surface freezing from a blue 64-layer and a very thick whitish $L \sim 480$-layer 9O.4 film. All of these data sets display nearly the same number of SF transitions and the film appeared the same color visually both before and after these measurements. For thick films, multiple measurements of the number of surface freezing transitions of a film gave a value for the total number of transitions which varied by about ± 10 %. This value was used as the total film thickness, L, in the fits.

Fig. 2.8 also shows transition temperature variations for multiple measurements of the surface freezing from the same film. The numbers next to each data set indicate the time sequence of the repeated measurements. The 64-layer film exhibited some small variations in shape of the SF transitions with repeated measurement, but the largest feature was the uniform shift of all the SF transition temperatures to

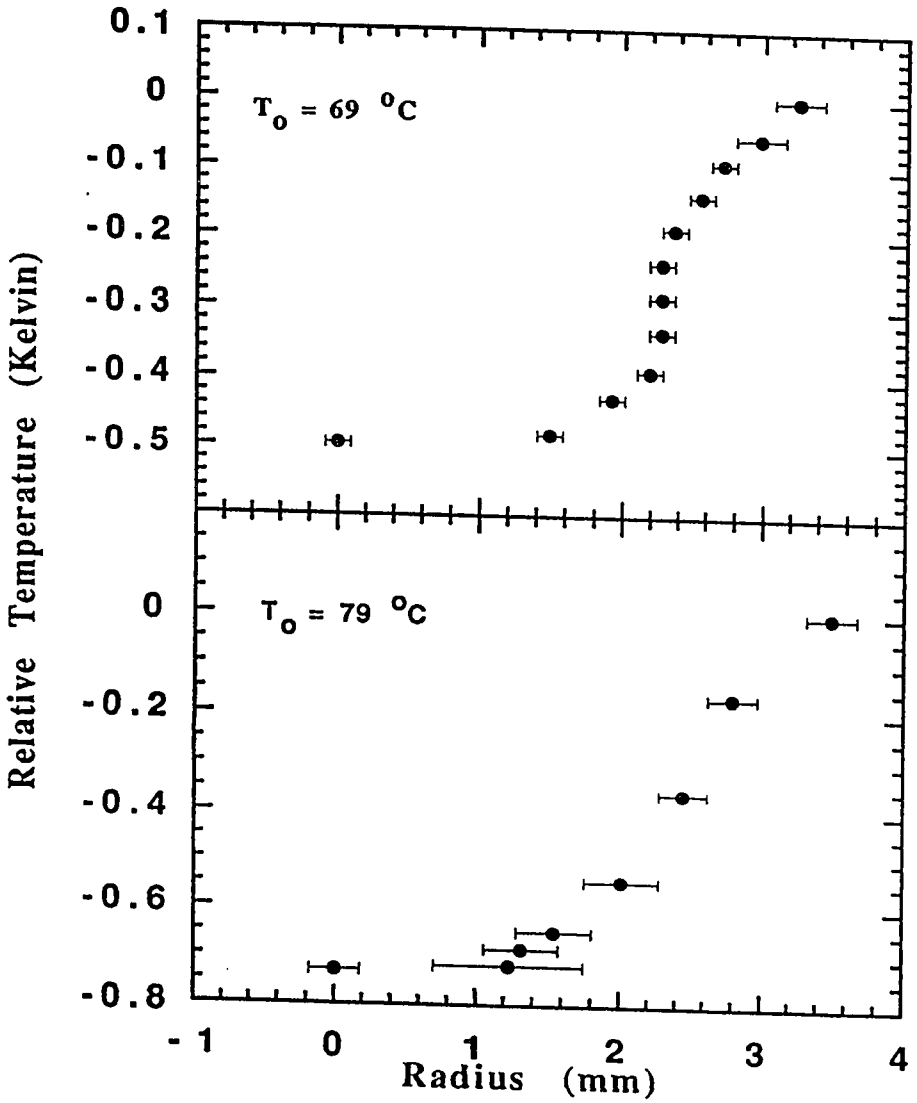

Figure 2.6: Radial Temperature Profile of the Film. The experimentally measured radial temperature profile of a 64-layer 7O.7 film determined for temperatures around the first two surface freezing transitions by stepping the oven temperature away from the transition and measuring the interface position. Note that the profile for the smectic-I/C to smectic-2I/C at 69° is much steeper and about 0.3° shallower than that found for the smectic-A to smectic-I/A transition at 79°.

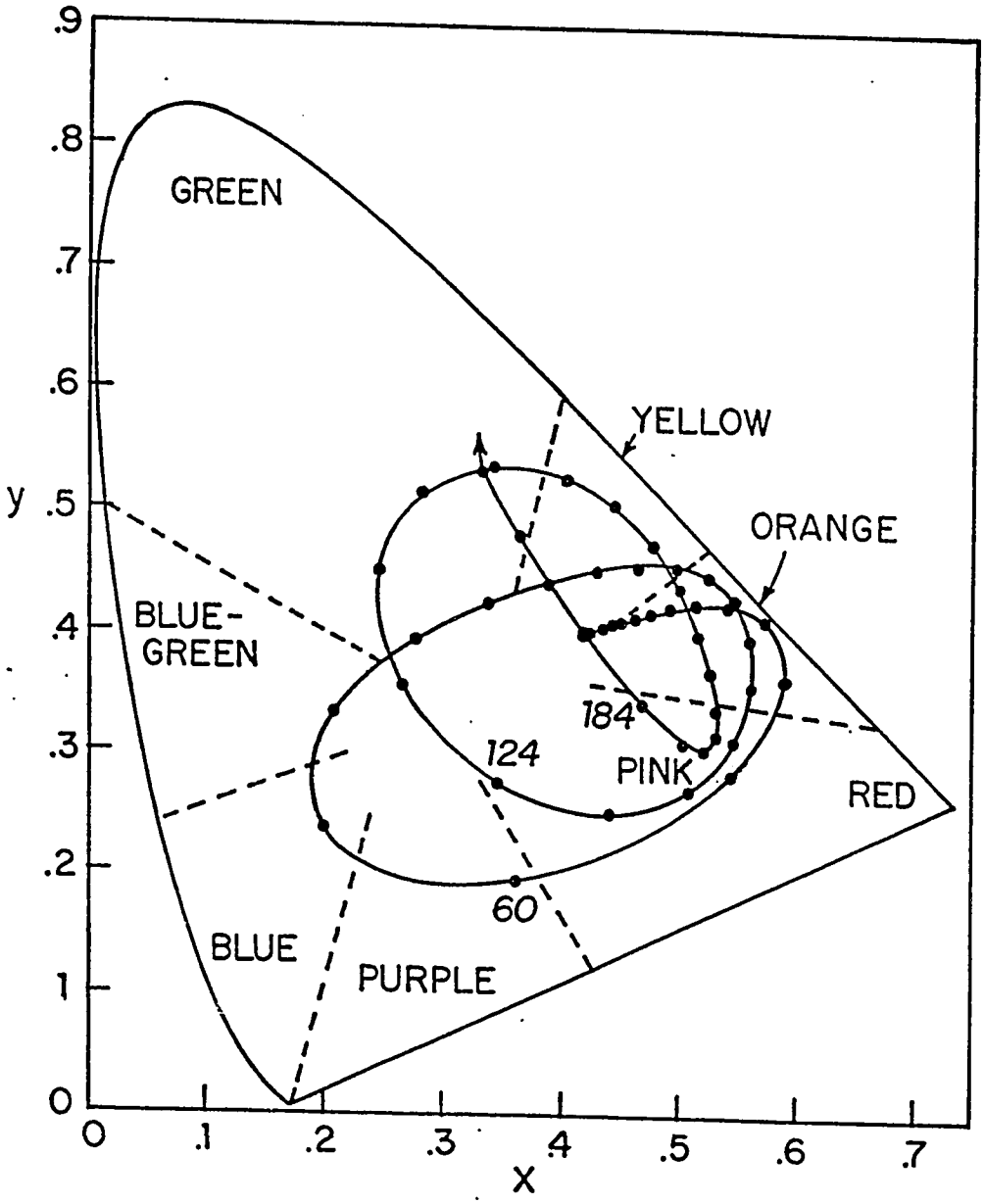

Figure 2.7: Chromaticity Diagram for Film Thickness Determination. The C. I. E. chromaticity diagram with the thickness curve calculated for the liquid crystal 7O.7 [6, 93]. The dots along the curve are the film thicknesses noted every four layers. Near the minimum in X corresponding to the color blue, the film thickness could be accurately determined to within a single layer. The surface freezing results were from films with this turquoise-blue color, $L \sim 64$ layers thick.

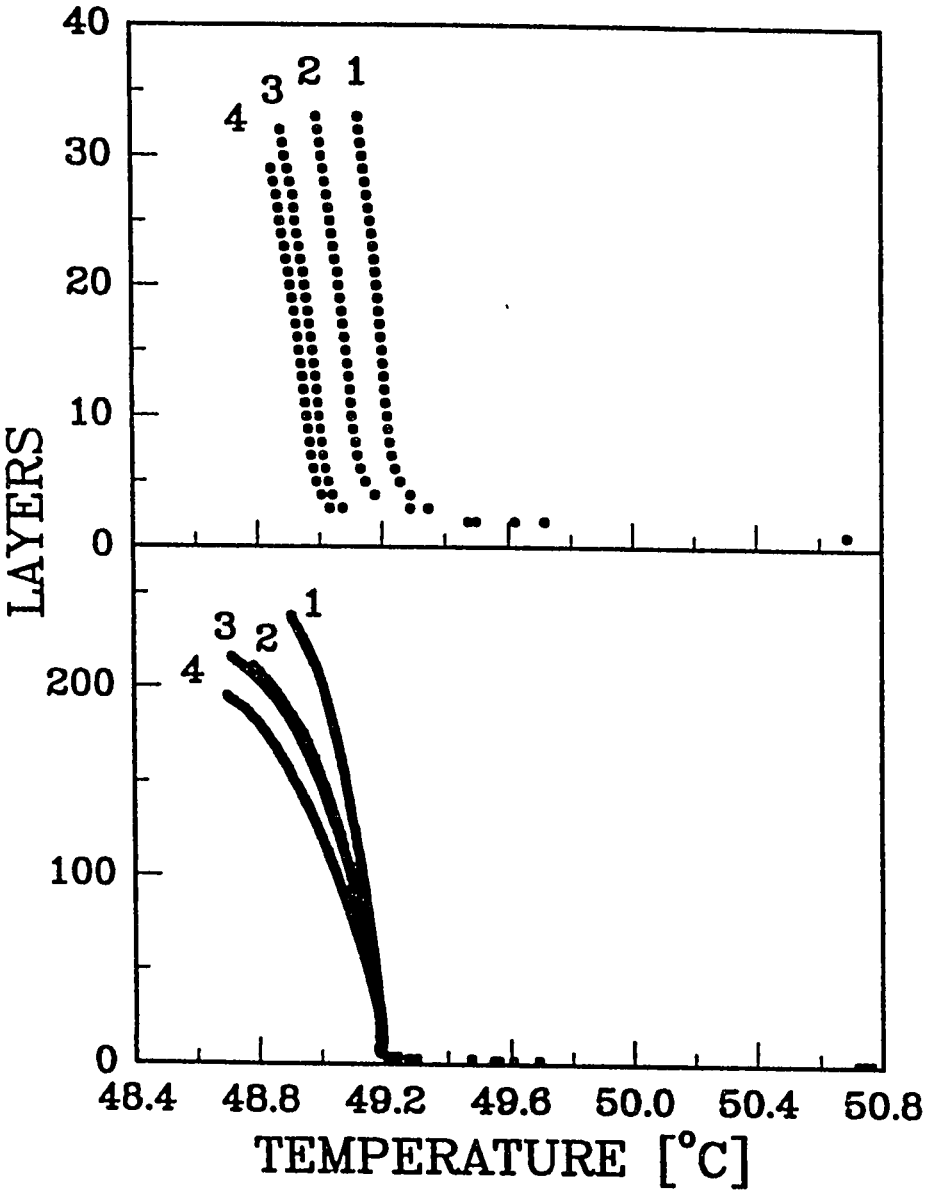

Figure 2.8: Transition-Temperature Variations. Repeated measurements from a single $L \sim 64$-layer and a single $L \sim 480$-layer 4O.7 film. Note the systematic variation of transition temperature with time due to material degradation. The numbers indicate the order of the data sets with 1 being the first data taken on the film. The data sets for both films consisted of successive heating and cooling temperature ramps. The apparent thickness change may be due to deteriorating optical contrast during the repeated data runs. No change in film color, indicating thickness change, was noticed between runs.

lower T as the film aged. The variations displayed here did not affect the critical behavior and only resulted in different T_o values for each data set. For the 480-layer film, the measured surface freezing layer thickness versus temperature decreased with time; runs 1, 2, 3, and 4 were taken starting at 0, 80, 200 min, and 12 hours later, respectively. This decreased SF rate was probably due to film degradation. First-order transition temperature shifts to lower temperature with film age have been observed previously in the LC homologue 7O.7 [6]. All the data sets analyzed in this thesis for the 64-layer and finite-size studies were first run data sets taken on freshly made films. The size of the transition temperature variations shown in Fig. 2.8 for the 480-layer film do not significantly change the finite-size model fitting parameters and are also much smaller than the systematic decrease versus film thickness in SF rate shown in Fig. 2.17. For all thickness films in the finite-size study, the variations between different thickness films were much larger than the variations seen between multiple measurements of the same thickness film.

For the nO.m's, it is well established that the transition temperatures slowly degrade with time due to the spontaneous decomposition of the liquid-crystal molecules. The resulting impurities lower the transition temperature, but typically do not affect the critical behavior aside from the shift in temperature. To test for the possible effects of impurities, we deliberately produced large temperature shifts by keeping some samples for weeks, but no change in the critical behavior was observed. It is interesting to note for the nO.7 homologue series the tilted smectic-C phase appears between the smectic-A and the smectic-B phase in the phase diagram beginning with 5O.7. This is the region of the phase diagram where surface freezing is observed in 4O.7 and 7O.7. Since surface freezing is observed in both 4O.7 and 7O.7, it would be interesting to look for surface freezing in 5O.7 and 6O.7.

Tentative identification of the phase of the surface frozen layers was done by comparing the observed tilt domain patterns to those from known phases [94]. The texture of the smectic-I and smectic-F phases are different than all the untilted phases and can be distinguished from smectic-C phases because they do not shimmer. Multiple surface freezing measurements were taken for all four materials, and only uniform single-thickness films with clearly visible surface freezing transitions originating at the center of the film were used.

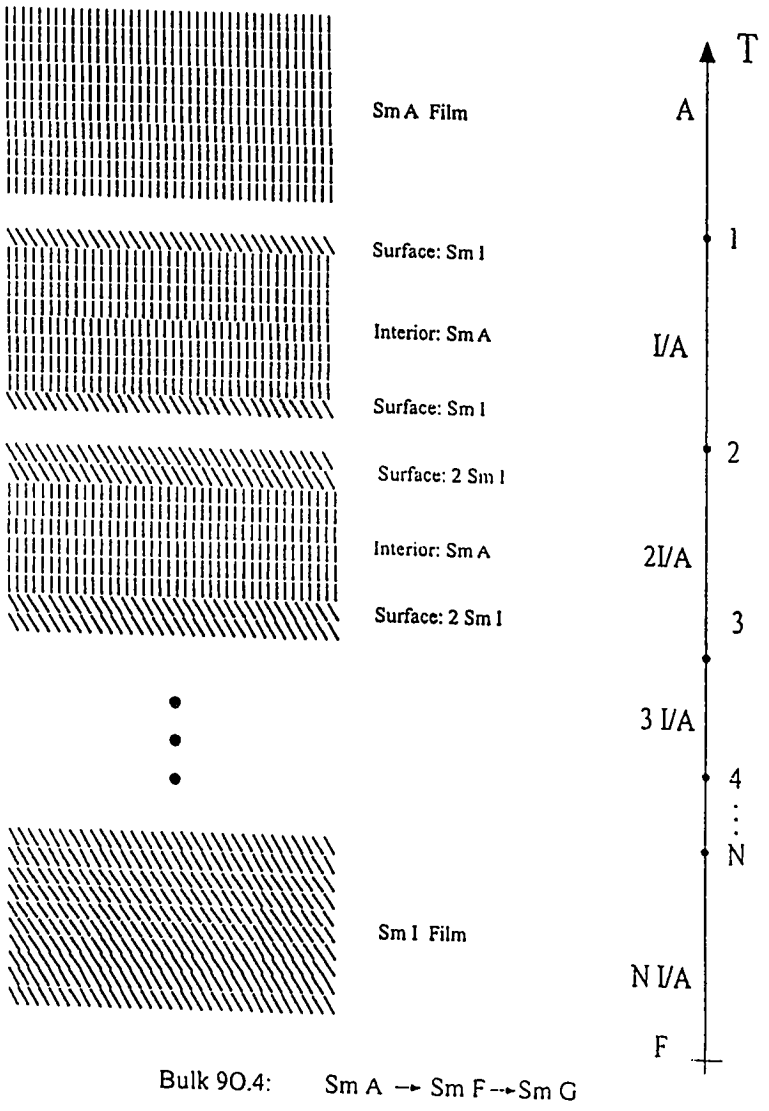

Figure 2.9: Schematic Representation of 9O.4 Surface Freezing. The figure illustrates, for simplicity, the behavior of a ten-layer film; the actual film thickness studied was 64 layers. Surface freezing in a 9O.4 film involves a transition from an uniform untilted smectic-A phase at high temperature to a stratified film with monolayers of tilted smectic-I on each surface. As the temperature is lowered, the film makes sequential layer-by-layer transitions to a film with one monolayer, two monolayers, three monolayers, etc. of surface frozen smectic-I on *each* vapor interface. This layer-by-layer surface freezing continues until the whole film is smectic-I. At a lower temperature, the film makes a sudden first-order transition to the smectic-F phase.

2.7.3 Surface Freezing Observations: 9O.4

Fig. 2.9 illustrates, for simplicity, the process of surface freezing in a ten-layer 9O.4 LC film; the actual film thickness studied was 64 layers. The vertical axis on the right of the illustration indicates the temperatures and phases of the film. At high temperatures, the entire film is in the smectic-A phase. As the temperature is lowered the film becomes stratified. At the first surface freezing transition both surfaces of the film surface freeze producing a monolayer of smectic-I at each film-vapor interface while the center of the film remains smectic-A. As the film temperature is lowered further, the film makes a second surface freezing transition at each of the internal interfaces producing two monolayers of smectic-I on each surface of the stratified film. The thickness of the surface layer grows layer-by-layer as the temperature is lowered until the entire film is surface frozen. The film then remains smectic-I for a small temperature interval before there is an abrupt first-order transition to the smectic-F phase. The film is observed to make a transition to the smectic-G phase with further lowering of the temperature. The appearance of the smectic-F and the smectic-G phases, occur at about the same transition temperatures they do in bulk 9O.4 [29, 30]. The bulk phase sequence [95] for 9O.4 is Isotropic–Smectic-A–Smectic-F–Smectic-G. In 9O.4, the surface freezing transition is surface-induced and the surface frozen smectic-I phase is a surface-stabilized phase: the smectic-I phase does not appear in the bulk phase diagram.

The inset of Fig. 2.10 shows the surface freezing transition temperatures for the first few layers on both film surfaces for a blue 64-layer 9O.4 film. In this figure, the temperature at which each surface freezing transition occurs is plotted versus the transition number. Above 76.1° C the entire film is in an untilted and untextured smectic-A phase. At about 76.1° C a pair of transitions occur corresponding to the freezing of the two outside layers of the film. This pair of transitions, $\sim$ 5 mK apart, corresponds to transitions on the two outside surfaces of the film. In this way the film is stratified with monolayer surface frozen tilted hexatic smectic-I layers on each surface and untilted liquid smectic-A in the interior of the film[2]. The first

[2] This identification of the surface phase as a Smectic-I is based on the observed texture which indicates either a smectic-I or a smectic-F phase. Since the surface frozen phase to smectic-F transition is observed in the film at the same temperature as the bulk smectic-A to smectic-F transition, we infer indirectly that the surface phase is a surface-induced smectic-I. In-plane x-ray

surface freezing transition appears as a textured region, corresponding to different tilt domains, moving radially out on the originally untextured smectic-A film.

The small time separation between the freezing of the top and bottom surface corresponds to an apparent transition-temperature difference of $\sim$ 5 mK. Observations of surface freezing for all four systems studied indicated a small time separation between the transitions from the top and bottom surfaces for the first few transitions. The experimental evidence for freezing inward from the surface consists of the optical observation of overlapping tilt domains; adjacent frozen layers at the center of the film would not have overlapping domains. Freezing inward from the surface is also the theoretically expected behavior and is consistent with recent direct interlayer x-ray observations of frozen smectic-I surface layers in films of the homologue, 7O.7 [9, 22, 26] described in Chapter 3.

At about 70.3° C, a second pair of transitions occurs in 9O.4 films corresponding to an additional monolayer of surface frozen smectic-I on each surface. These subsequent layer transitions appear as waves of slightly increasing contrast spreading radially outward from the center of the film. The second, third and fourth freezing transitions also appear as well resolved pairs of transitions from the top and bottom of the film with similar $\sim$ 5 mK apparent transition-temperature separations. After about the fourth pair, the temperature separation between adjacent pairs becomes comparable to the separation within the pairs. The layer-by-layer freezing continues until the entire film is smectic-I. For films that were measured to be 64 layers thick, $64\ ^{+0}_{-3}$ surface freezing transitions were observed. The entire film remains smectic-I from 69.2° to 68.8° C where there is an abrupt first-order transition to smectic-F. The transition to the smectic-F phase looks very different than the surface freezing waves; it appears as a slowly moving interface spreading out from the center of the film.

Fig. 2.10 shows the number of frozen surface layers at a single vapor interface versus the reduced temperature, t, for six different turquoise 64-layer 9O.4 films. Only the first ten surface freezing transitions at a single vapor interface are shown. The surface freezing transitions have been assumed to alternate between the top and the bottom interfaces in the film so that the data set shown consists of every other transition corresponding to transitions at one vapor interface. The SF results for all four materials were independent of which set of transitions were chosen. As will be

---

measurements to verify this assignment are planned.

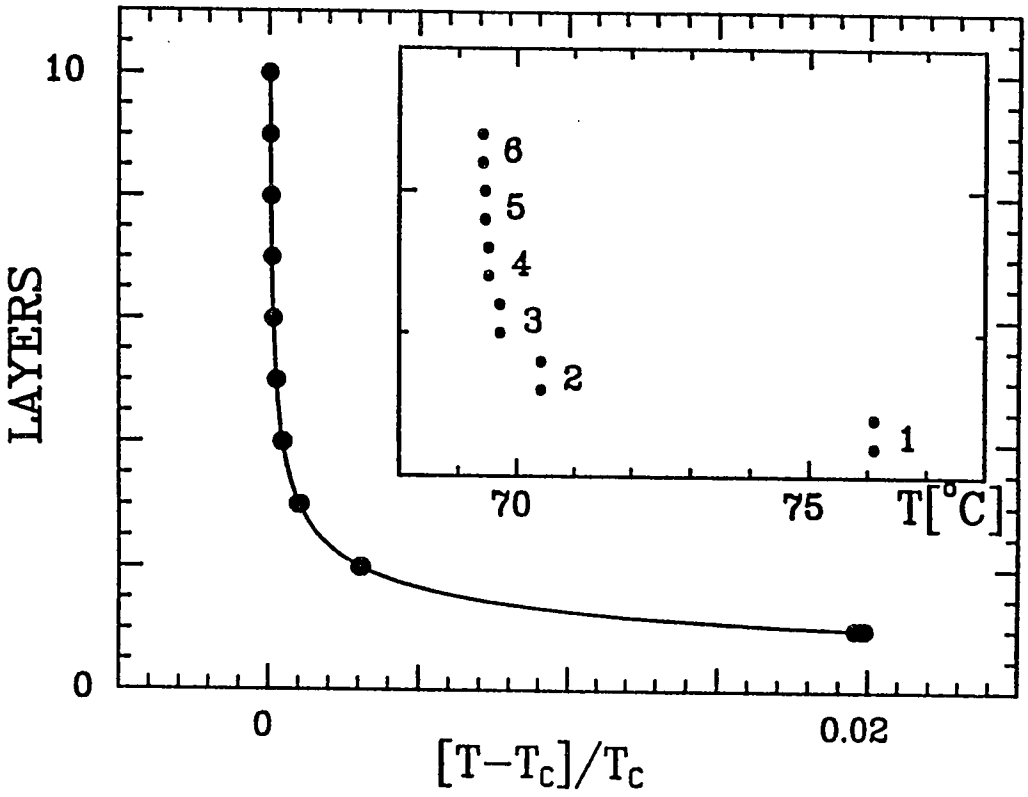

Figure 2.10: 9O.4 Surface Freezing: Linear Plot. A plot of the number of frozen surface layers at each vapor interface versus the reduced temperature, t, for six different turquoise 64-layer 9O.4 films. Only the first ten surface freezing transitions (on each interface) are shown. The layer-by-layer surface freezing transitions continue until the entire film is frozen. The first ten transitions are fit quite well by the power-law form $l = l_o t^{-\nu}$, with exponent $\nu = 0.373$, consistent with $\nu \approx 1/3$ expected for a system dominated by long-range van der Waals forces. The solid line indicates the corresponding power-law fit. The data from the six films agree very well, with most points indistinguishable. The inset shows both the top and bottom surface freezing transition temperatures for the first six pairs of transitions in a single film. The first four frozen surface layers on each surface occur as clearly resolved pairs, indicating that the top and the bottom layers freeze at very nearly the same temperature.

discussed in detail below, for 9O.4 films, the first ten transitions are fit quite well by the simple power-law form $l = l_o t^{-\nu}$, with the measured exponent $\nu \approx 1/3$ consistent with behavior expected for a system dominated by long-range van der Waals forces.

2.7.4 Surface Freezing Observations: 4O.7

Surface freezing transitions were also observed in many different thickness 4O.7 films. The phase diagram for 4O.7 [95] indicates the bulk phase sequence is: Isotropic–Nematic–Smectic-A–Crystalline-B. The thickness dependent phase diagram for 4O.7 has not been measured yet. For 4O.7 films, the entire film is smectic-A above about 50.6° C and the film appears untextured. At 50.6°, a pair of surface freezing transitions appear as regions of increased contrast emerging from the center of the film indicating that the two outside layers have frozen. With this pair of transitions, the film becomes stratified with a tilted hexatic monolayer of either smectic-I or smectic-F, appearing at each of the two vapor interfaces[3]. As the temperature is decreased, the next few transitions also appear as well resolved pairs due to SF transitions at the top and bottom of the film. As in 9O.4, after about the fourth pair, the temperature separation between adjacent pairs becomes comparable to the separation within pairs. Again, the layer-by-layer surface freezing continues until all the layers of the film are surface frozen into the hexatic phase. At 48.5° C, a transition to the untilted smectic-B phase occurs. This transition generally appears first near the center of the film as a uniform untextured region which slowly moves radially outward.

2.7.5 Surface Freezing Observations: 7O.7

Surface freezing transitions were also observed in 7O.7 at the smectic-I/C to smectic-B phase boundary. The bulk [95] and thickness-dependent [6] phase diagram are well known for 7O.7. The thickness-dependent phase diagram shown in Fig. 1.3, displays large shifts in the phase boundary transition temperatures versus film thickness for the smectic-I–smectic-B, smectic-B–smectic-I/C, and smectic-I/C–smectic-I/A phase transitions. For films 64 layers thick, the phase sequence is Isotropic–Nematic–Smectic-A–Smectic-C/A –Smectic-I/A–Smectic-C–Smectic-B–Smectic-G. The surface

[3] This identification of the surface phase as a smectic-I or smectic-F is based on the observed texture which indicates a non-shimmering (not smectic-C) tilted phase.

freezing transitions for this film are shown in Fig. 1.3. Surface freezing waves were not seen in previous studies of 7O.7 FSLC films, although the smectic-I monolayer surface phases have been studied on the smectic-A and smectic-C phase [6, 9]. As the $L \approx$ 64-layer 7O.7 films are cooled, a pair of surface freezing transitions occurs at about 79°C and the film makes a transition from the smectic-C/A phase, a phase having monolayer tilted smectic-C surface layers on the liquid smectic-A interior, to the smectic-I/A phase, a phase with monolayer 2D hexatic smectic-I surface layers on the smectic-A interior. This pair of surface freezing waves appear as sharp textured circular interfaces emerging from the center of the film. At about 72°C, the interior of the film makes a first-order transition to the smectic-C phase. The film is now in the smectic-I/C phase with a monolayer of smectic-I on each surface of the film and the interior in the smectic-C phase. The second pair of surface freezing transitions occur at about 69.4° C, and surface freezing transitions continue as the film is cooled further. Again, these surface freezing transitions appear as pairs of transitions corresponding to the top and bottom surfaces of the film, until the transition temperature separation between pairs becomes a few mK and the pairs are no longer distinguishable. The SF transitions continue until the film is completely smectic-I[4]. The film remains smectic-I until 68.6°C, when an untextured patch of untilted smectic-B phase appears near the center of the film and slowly grows out to cover the film.

2.7.6 Surface Freezing Observations: $\overline{14}S5$

Surface freezing was also observed in $\overline{14}$S5 films. Bulk $\overline{14}$S5 has a well studied phase diagram [96] with a bulk phase sequence of Isotropic–Smectic-A–Smectic-B in the temperature region of interest. For $L \sim$ 64-layer royal blue films above 73.9° C, the entire film is in an untextured smectic-A phase. As the film is cooled, at about 73.9° textured patches on the untextured smectic-A appear. As the film is cooled further, transitions appear as waves with slightly overlapping domains expanding outward from the center of the film. As with the other materials, the first few transitions

[4] This identification of the surface phase as a smectic-I is based on the observed texture with indicates a tilted phase. From the optical observation of the texture alone, this phase could also be smectic-F, but previous x-ray measurements have confirmed the existence of smectic-I/C for thin 7O.7 films [9]. In-plane x-ray diffraction measurements are planned to check this phase assignment for thicker films.

appear as pairs corresponding to transitions from the top and bottom surfaces of the film. The SF transitions continue until at 69.5° a transition is made to the smectic-B phase. The smectic-B transition is seen as a distinct boundary of an untilted phase which slowly moves out to cover the film. The tilted surface freezing phase remains unidentified, but is assumed to be either smectic-I or smectic-F since the phase does not appear to shimmer like the smectic-C phase. X-ray experiments are planned to identify the phases in all four of these LC systems.

2.8 Surface Freezing Results for $L \approx 64$ Layer Thick Films

In this section, SF results are presented based on measurements of the first ten surface freezing transitions in $L \sim 64$ layer thick films of four different LC materials: 9O.4, (4-(n-Nonyl)oxybenzylidene-4-(n-Butyl)aniline), 4O.7 (4-(n-Butyl)oxybenzylidene-4-(n-heptyl)aniline), 7O.7, (4-(n-heptyl)oxybenzylidene-4-(n-heptyl)aniline) , and $\overline{14}$S5 (4-n-pentylbenzenethio-4-n-tetradecyloxybenzoate). In all four systems, the surface freezing transitions appear to continue until the entire film is surface frozen. Only the first ten transitions on each vapor interface will be considered in this section; the thickness dependence is discussed in Sec. 2.9. This film thickness (about 64 layers) was chosen because the color for this thickness films determines the relative film thickness very precisely. As will be shown, for the first ten SF transitions in these intermediate thickness films, the two interior interfaces remain sufficiently far apart that the interior interface-interior interface interactions can be neglected. The finite-size effects will be discussed in Sec. 2.9. In this section, careful measurements of the surface freezing transition temperatures at each vapor interface for the first ten layers will be used to answer the following question: What are the dominant forces acting in each of these LC systems?

Long-range van der Waals and short-range exponential forces are expected to be the two forces present in LC systems, and the surface freezing transitions should be described by either Eq. 2.7 or 2.6. For the first ten transitions in these intermediate thickness films, $L \sim 64$ layers, the interior interface-near vapor interface interaction dominates over interactions due to the other interface-interface interactions. The experimental criterion adapted here for a van der Waals long-range force system is that the three free-parameter fit to Eq. 2.7 of the first ten layer transitions agree with the predicted exponent $\nu = 1/n = 1/3$. The corresponding experimental criterion

for an exponential short-range force system is that the three free-parameter fit to Eq. 2.6 must result in a physically reasonable value for the characteristic range of the interaction, $\xi \approx 1$ molecular layer. The van der Waals force prediction that the exponent $\nu \approx 1/3$ within the experimental errors is very explicit. Since the exponential force model does not make very precise predictions for the magnitude of ξ, fits with $0.1 < \xi < 1$ layer will be considered acceptable indicators of steric short-range exponential force systems.

2.8.1 9O.4 Results

Fig. 2.10 shows that the first ten SF transitions from six different $L \sim 64$-layer 9O.4 films are well described by the solid line indicating the best-fit van der Waals power-law form, $l = l_o t^{-\nu}$, for the number of surface layers, l, versus the reduced temperature, t. Only the first ten layer transitions are shown but the layer-by-layer freezing continues until the entire film is frozen. The 6 independent data sets agree well; once they are corrected for their T_o shifts most of the points are indistinguishable in the linear plot. The transition-temperature variations shown in the figure are random, there is no systematic variation for different films, and the random variation of each point is about ± 8 mK. The surface freezing data from each film shown in Fig. 2.10 was fit separately to the power-law form, $l = l_o t^{-\nu}$, to determine the free parameters l_o, T_o and ν. The average best-fit parameters were then calculated from the 6 independent determinations. The solid line indicates the best-fit power-law for the combined data set with corresponding parameters $l_o = 0.24 \pm 0.01$ and $\nu = 0.373 \pm 0.015$. A theoretical calculation of l_o can be made knowing the Hamaker constants for the system [34]. Future measurements of these Hamaker constants for 9O.4 will allow an independent determination of l_o which can be compared with the above value. The critical exponent determined from the power-law fit is consistent with the exponent, $\nu = 1/3$, predicted for simple van der Waals forces at the three-standard-deviation level [29]. The log-log plot in Fig. 2.11 of the same data plotted in Fig. 2.10, shows that this data is described very well by this best-fit power-law form over about three decades in reduced temperature.

An attempt has been made to describe the 9O.4 data using the exponential form, $t = \beta \exp(-l/\xi)$, predicted for short-range exponential forces. The solid line in Fig. 2.12 shows the best-fit exponential and power-law forms fit to the surface freez-

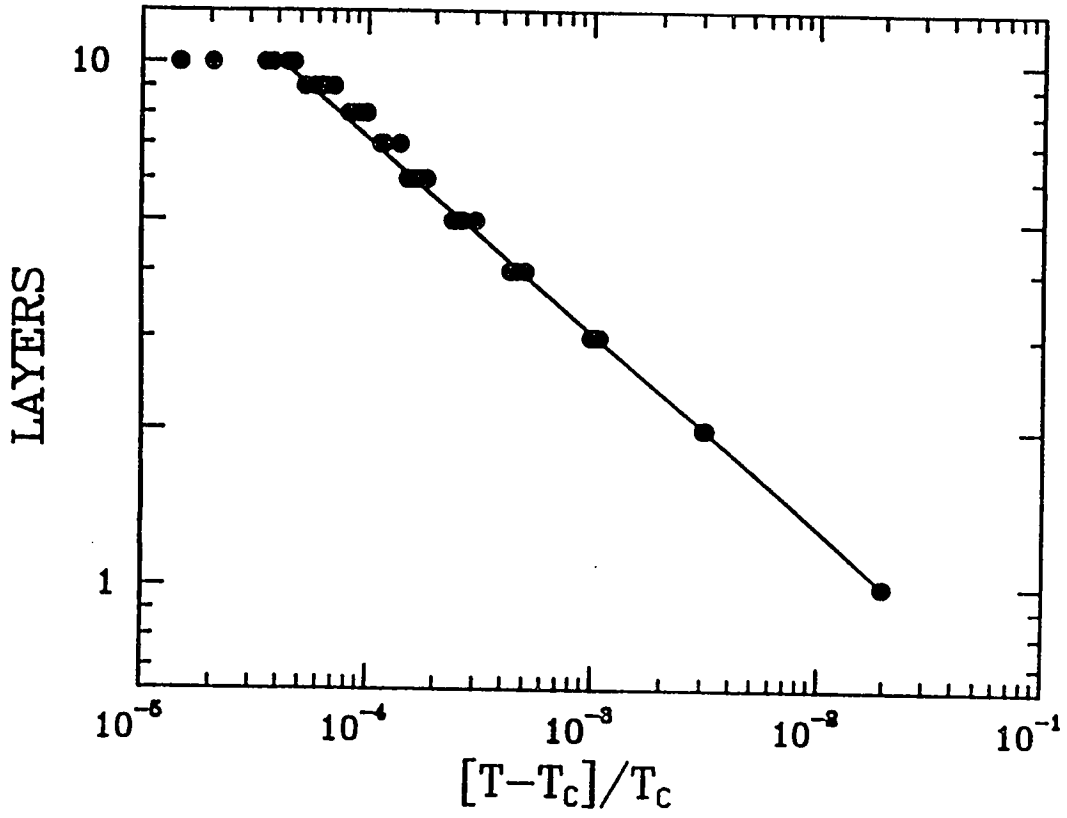

Figure 2.11: 9O.4 Surface Freezing: Log-Log Plot. Log-Log plot of the number of frozen surface layers on each vapor interface versus the reduced temperature, t, for six different 64-layer 9O.4 films. Only the first ten surface freezing transitions are shown. The layer-by-layer surface freezing transitions continue until the entire film is frozen. The first ten transitions are fit quite well by the power-law form $l = l_o t^{-\nu}$, with the exponent $\nu \sim 1/3$ expected for van der Waals forces. The solid line indicates the power-law best-fit.

Figure 2.12: 9O.4 Surface Freezing. Plots of the number of frozen surface layers on each surface versus temperature for six different 64-layer 9O.4 films. The upper panel indicates the results from a fit to the van der Waals force power-law model, $l = l_o t^{-\nu}$. The best-fit parameters are $\nu = 0.373$ and $l_o = 0.24$. The lower panel displays the fit to the short-range exponential force model $t = \beta e^{-l/\xi}$. The best-fit parameters are $\beta = 43.3$ and $\xi = 0.54$. Each data set was fit separately to determine the model parameters and the solid line in each panel displays the best-fit parameters to the respective model for the combined data set. The exponential model displays significant deviations from the data. These deviations are much larger than the random errors and indicate that model does not fit. The size of the random errors are indicated by the spread of the overplotted data from the six different films. Note for some points these errors are smaller than the circles in the plot. The power-law fit agrees within the random errors and has $\nu = 0.373$ in reasonable agreement with $\nu = 1/3$ expected for van der Waals interactions.

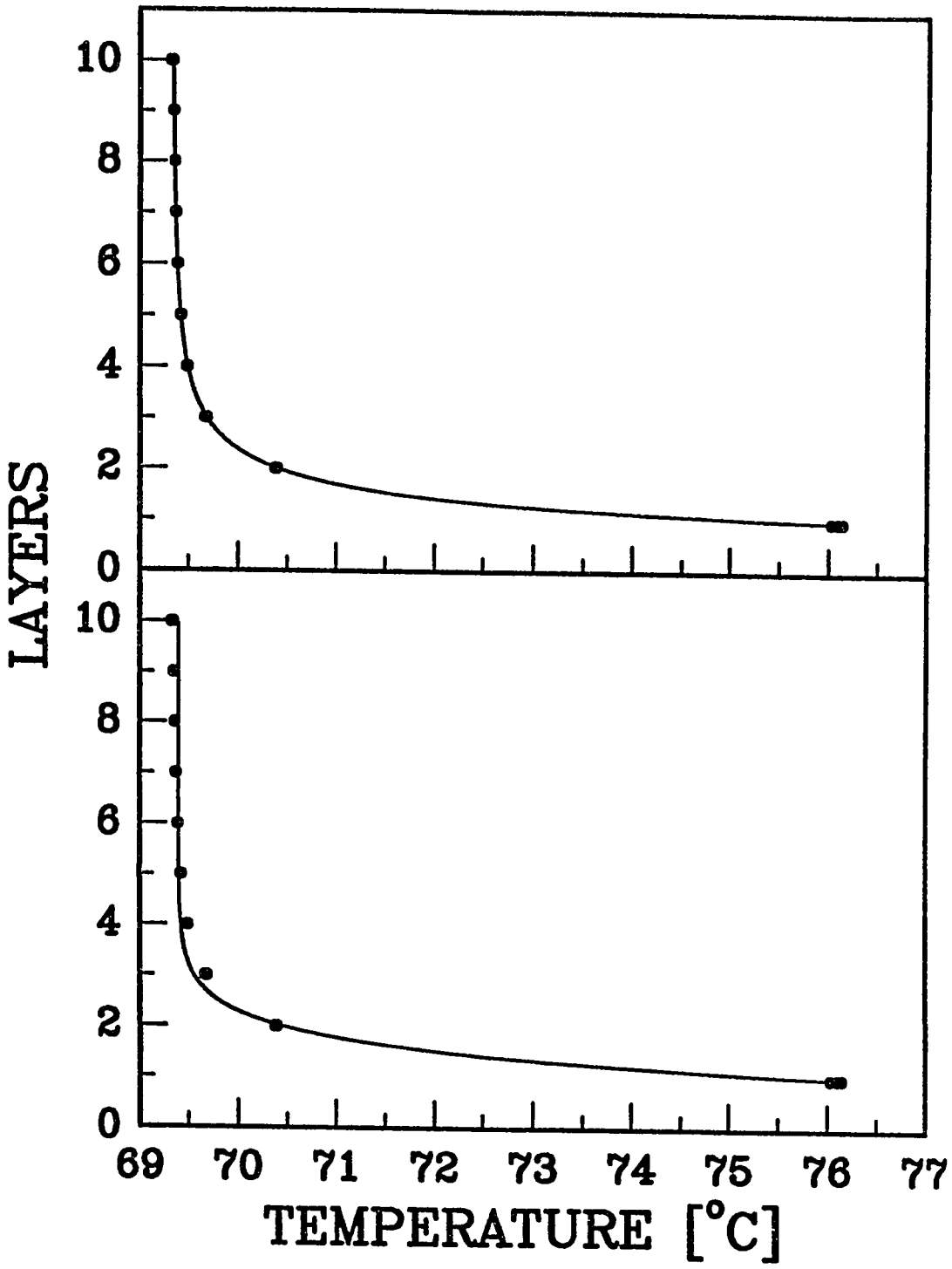
LAYERS
10
8
6
4
2
0
10
8
6
4
2
0
69
70
71
72
73
74
75
76
77
TEMPERATURE [°C]

ing data from the six different 64-layer 9O.4 films. The best-fit parameters for the exponential form are $\beta = 5.4 \pm 0.8$ and $\xi = 0.82 \pm 0.06$. However, the small deviations visible in Fig. 2.12 show that the exponential force model is not consistent with the data quantitatively, because these deviations are much larger than the superb reproducibility of the data for this system. The data for 9O.4 was the most reproducible of the four systems studied here.

Hysteresis measurements were made for the first few surface freezing transitions in 64-layer 9O.4 films to check the reversibility of the surface freezing transitions and the order of the phase transition. Multiple measurements of the transition temperatures for waves one through eight indicate a first-order transition with a 40 mK shift of the transition temperature between heating and cooling. Multiple measurements were required to remove the overall transition temperature drift due to material degradation. To make these measurements, the light intensity was strobed quickly to modulate the film temperature without changing the temperature of the oven or the film holder. These experiments demonstrated that the observed hysteresis is due to the film and not to the oven. The surface freezing appears reversible as long as the film has not made a transition to the smectic-F phase; many waves move back in from the edge of the film as the temperature is raised. However, after the film makes the smectic-F transition, only a few waves are visible when the film is reheated into the smectic-I phase. The first eight SF transition temperatures measured heating the film were nearly indistinguishable from those measured cooling the film except for the overall $\sim$ 40 mK temperature shift. After the eighth transition, 'on heating' SF measurements were difficult due to the nearby smectic-F phase.

2.8.2 4O.7 Results

Fig. 2.13 shows data from the first ten surface freezing transitions from five different $L \sim$ 64-layer thick 4O.7 films. As shown, the first ten surface freezing transitions are fit acceptably well by the exponential force form and marginally by the power-law form. Each data set shown was fitted separately to both the exponential and power-law forms to determine l_o, ν, β, ξ, and T_o. The solid line in each panel indicates the best-fit values of the power-law and exponential models to the combined data sets. For the power-law model, $t = \alpha l^{-n}$, the corresponding best-fit parameters are $n = 1.81 \pm 0.14$ and $\alpha = 1.62 \pm 0.10$. Unlike 9O.4, fits to the power-law model result

in an exponent, $\nu = 1/n = 0.56 \pm 0.04$, which is not consistent with the predicted van der Waals exponent, $\nu = 1/3$, within the experimental errors indicated by the spread of the data from the separate data sets. The short-range exponential force model, $t = \beta e^{-l/\xi}$, gives an acceptable fit with best-fit parameters $\beta = 5.4 \pm 0.8$ and $\xi = 0.82 \pm 0.06$. This value for ξ is acceptable since the characteristic-length predictions for a short-range force only constrain ξ to be about one layer. By the criteria adopted above, 4O.7 is therefore an example of a LC system dominated by short-range exponential forces and this discovery shows that LC systems exhibit both types of expected forces; long-range van der Waals (9O.4) and short-range exponential (4O.7) forces.

2.8.3 7O.7 Results

Fig. 2.14 shows the number of frozen surface layers at each vapor interface versus temperature for three 64-layer thick 7O.7 films. The two panels display the results from fits to both the long-range van der Waals and short-range exponential force models. The first ten surface freezing transitions in 7O.7 films are fit very well by both models. Each data set shown was fit separately to both models to determine the respective model parameters and the solid line in each panel of Fig. 2.14 indicates the best-fit parameters from the combined data set. The best-fit parameters for the van der Waals force model, $l = l_o t^{-\nu}$, are $l_o = 1.45$ and $\nu = 0.16 \pm 0.02$ and for the exponential force model, $t = \beta \exp(-l/\xi)$ are $\beta = 6.8 \pm 2.9 \times 10^2$ and $\xi = 0.24 \pm 0.02$. Although the data fits both models equally well, the best-fit power-law exponent is inconsistent with the predicted exponent $\nu = 1/3$ for a system dominated by van der Waals forces. Within the experimental errors, indicated by the spread in the data from the different data sets, the simplest form of the van der Waals force model, with $\nu = 1/3$, is not consistent with the data. The exponential force model gives a good fit with a physically reasonable characteristic length. Again, by the criteria adopted above, 7O.7 is also an example of a LC system dominated by short-range exponential forces.

2.8.4 $\overline{14}S5$ Results

Fig. 2.15 shows the data for the number of frozen surface layers versus temperature on each vapor interface for four different $L \sim 64$-layer $\overline{14}$S5 films and fits of the data

Figure 2.13: 4O.7 Surface Freezing. Plots of the number of frozen surface layers on each surface versus temperature for five different $L \sim 64$-layer 4O.7 films. The top panel displays the fit to the van der Waals force model, $l = l_o t^{-\nu}$, to the data with the best-fit exponent $\nu = 0.56$. The bottom panel displays results from the fit to the exponential force model, $l = l'_o + \xi \log(1/|t|)$. Each data set was fit separately to determine the model parameters and the solid line displays the best-fit parameters to the respective models from the combined data set. The van der Waals power-law model shows larger deviations from the data than the exponential force model, but these deviations are not large enough to exclude this model on goodness-of-fit alone. However because the exponent, ν, is inconsistent with the expected van der Waals exponent of, $\nu = 1/3$, the simplest form of the van der Waals force model is not consistent with the data within the experimental errors indicated by the spread in the data from the different data sets. The exponential force model does give an acceptable fit and physically reasonable characteristic length, $\xi = 0.8$ layers. The dominant forces in 4O.7 are therefore short-range exponential forces.

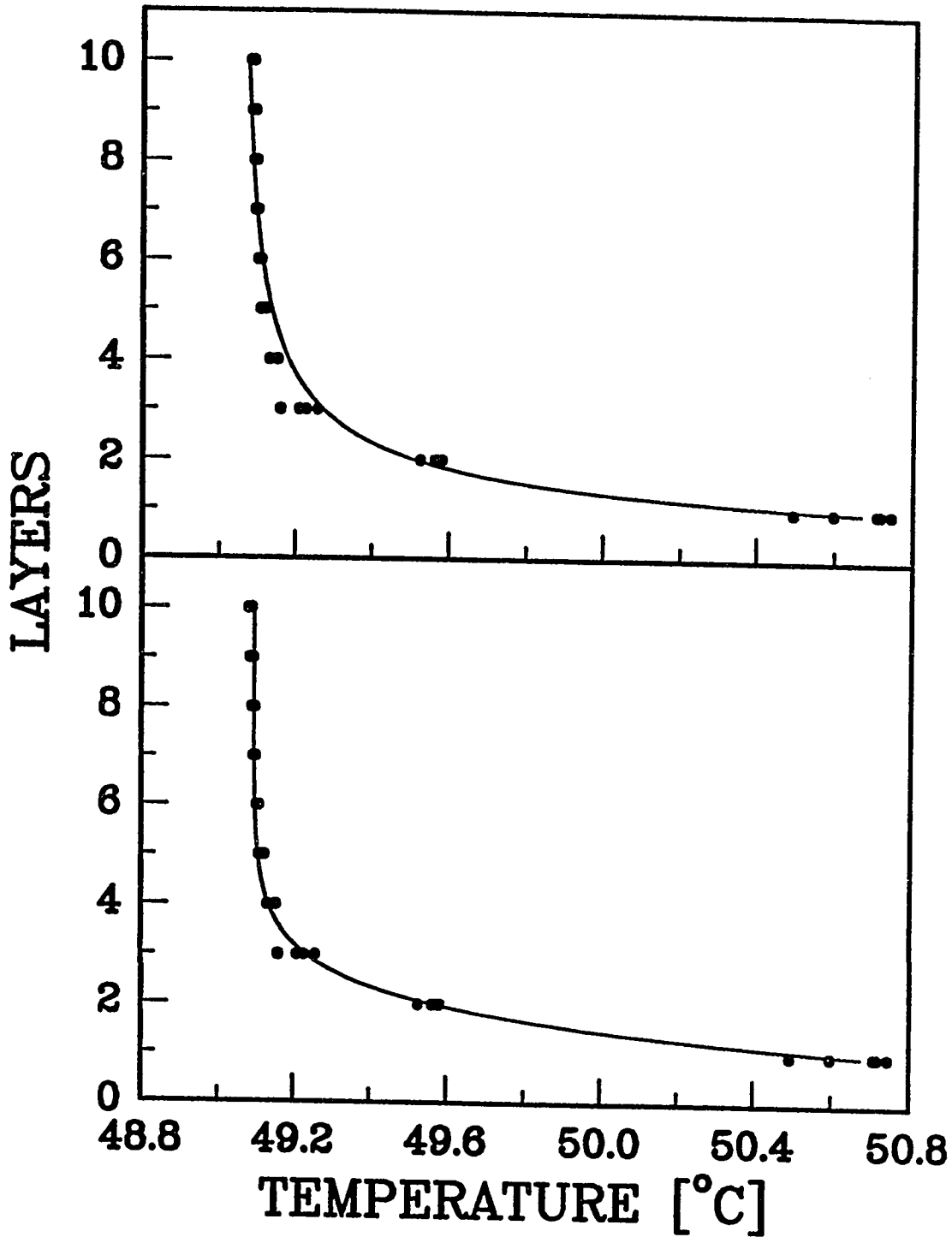
LAYERS
10
8
6
4
2
0
10
8
6
4
2
0
48.8
49.2
49.6
50.0
50.4
50.8
TEMPERATURE [°C]

Figure 2.14: 7O.7 Surface Freezing. Plots of the number of frozen surface layers on each surface versus temperature for three different 64-layer 7O.7 films. The upper panel displays the fit to the long-range van der Waals force model, $l = l_o t^{-\nu}$, with the best-fit exponent $\nu = 0.16$. The lower panel displays the fit to the short-range exponential force model, $l = l'_o + \xi \log(1/|t|)$ with $\xi = 0.2$ layers. Each data set was fit separately to determine the model parameters and the solid line in each panel displays the best-fit parameters to the respective model from the combined data set. Both the van der Waals and exponential force models give acceptable fits to the data. However, the best-fit exponent ν is not consistent with the predicted van der Waals exponent of $\nu = 1/3$. Since the exponential force model gives a good fit with a physically reasonable ξ the dominant interactions in 7O.7 are due to short-range exponential forces.

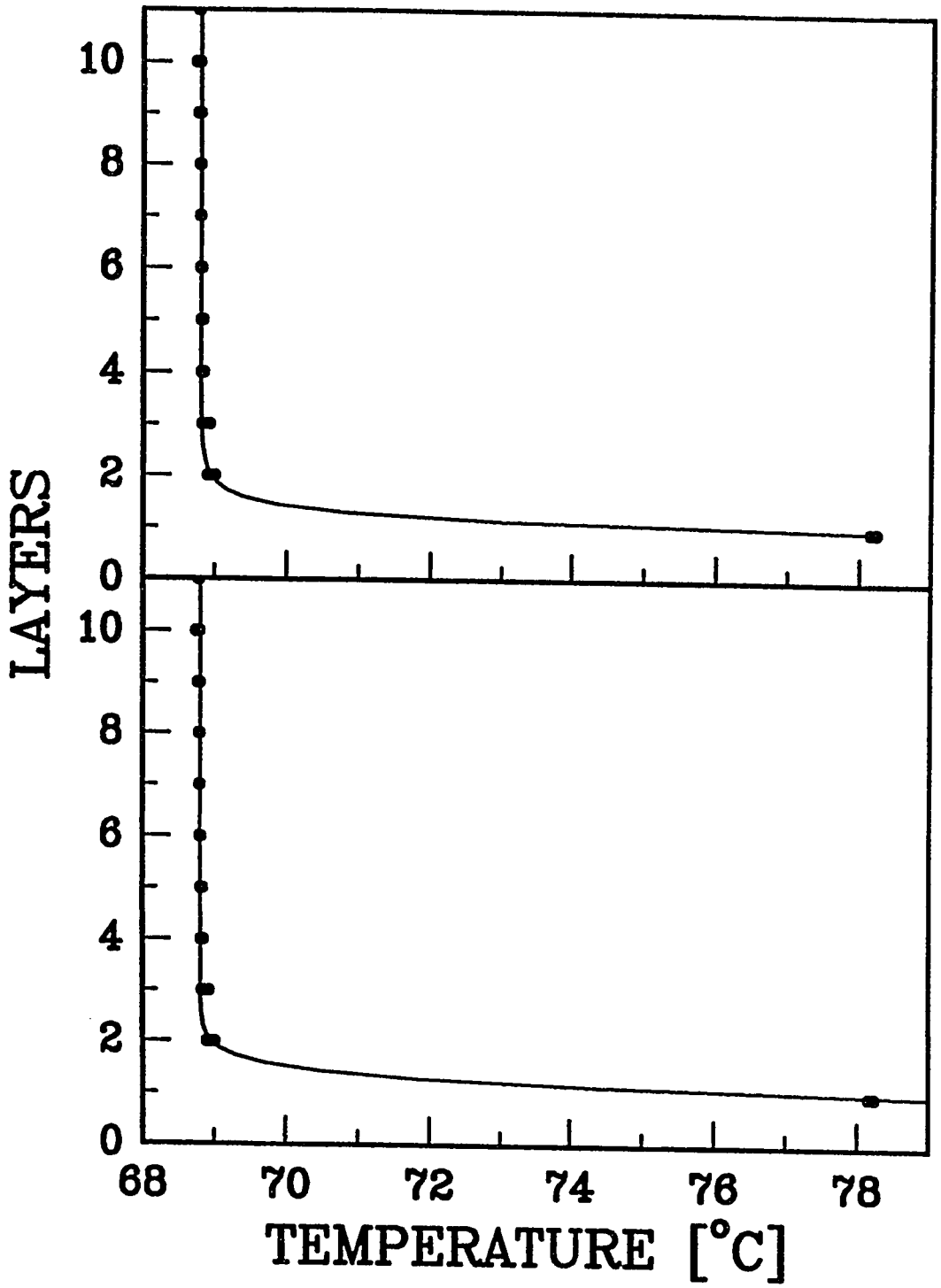
LAYERS
10
8
6
4
2
0
10
8
6
4
2
0
68
70
72
74
76
78
TEMPERATURE [°C]

Figure 2.15: $\overline{14}$S5 Surface Freezing. Plots of the number of frozen surface layers on each surface for four different $L \sim 64$-layer $\overline{14}$S5 films. The upper panel displays the fit to the long-range van der Waals force model, $l = l_o t^{-\nu}$. The lower panel displays the fit to the short-range exponential force model, $l = l'_o + \xi \log(1/|t|)$. Each data set was fit separately to determine the model parameters and the solid line in each panel displays the best-fit parameters to the respective model from the combined data set. Both the van der Waals and exponential force models give good fits to the data with physically reasonable best-fit parameters: $\nu = 0.36$, and $\xi = 0.53$ layers. The $\overline{14}$S5 data is therefore consistent with either model for the dominant force.

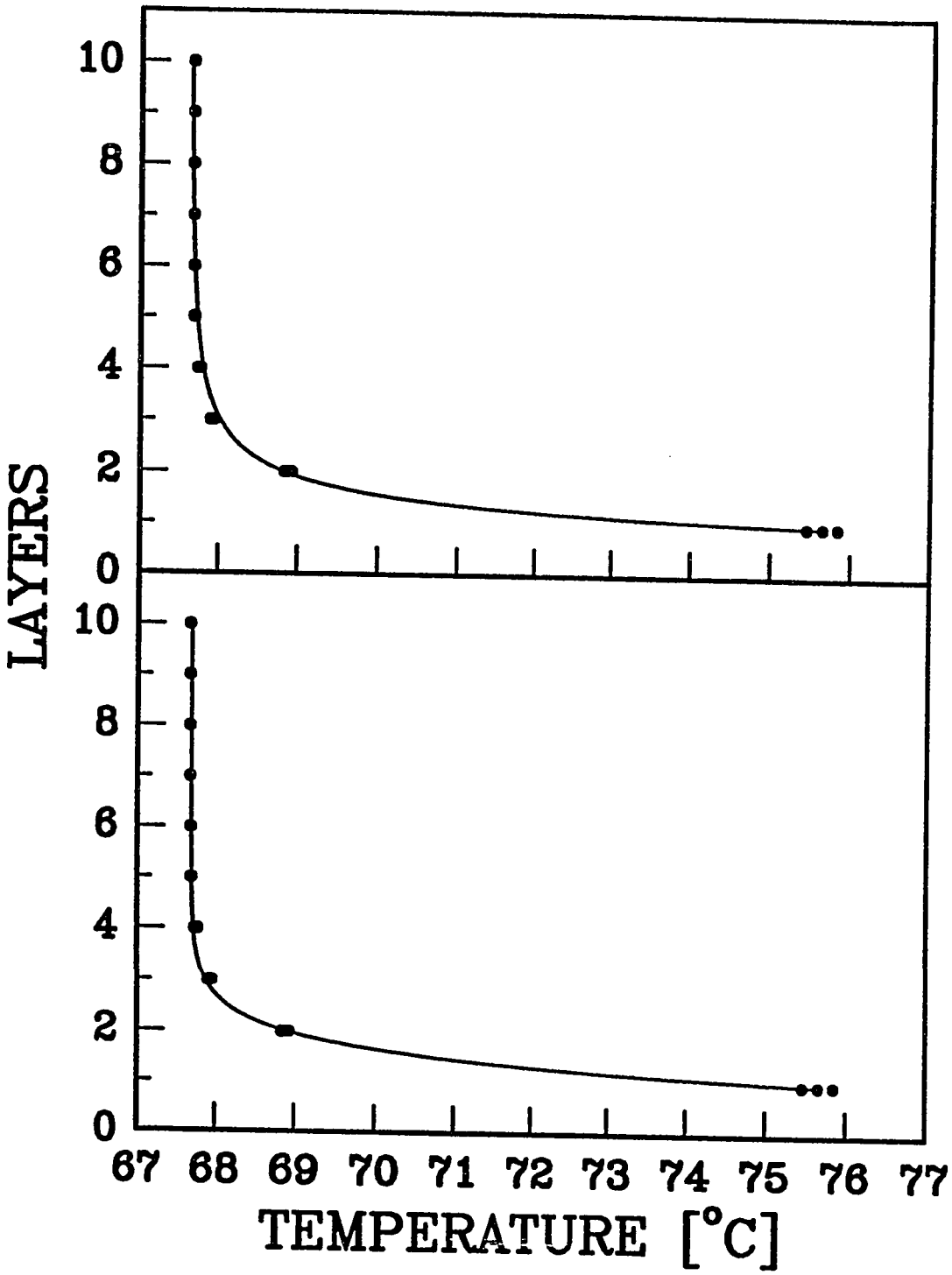
LAYERS
10
8
6
4
2
0
10
8
6
4
2
0
67 68 69 70 71 72 73 74 75 76 77
TEMPERATURE [°C]

to both the long-range van der Waals and short-range exponential force models. The parameters from the van der Waals force model are $\alpha = 8.03 \pm 0.16$ and $\nu = 1/n = 0.36 \pm 0.03$, while the parameters from the exponential model are $\beta = 53 \pm 3$ and $\xi = 0.53 \pm 0.01$. As can be seen, both models fit the data equally well. Because the exponent for the power-law model is consistent with the predicted van der Waals exponent, this model is physically acceptable. However, the $\overline{14}$S5 data also agrees with the values of ξ which are physically acceptable for a short-range exponential force model system. So from this data we cannot conclude which model is correct. In fact, a combination of both models is also allowed. After ten layers on each vapor interface surface freeze, the optical contrast becomes so poor in $\overline{14}$S5 films that it is difficult to see the subsequent SF transitions. Although, many more transitions are faintly evident, the optical contrast does not allow extended measurements of the SF transition temperatures or of the total number of transitions in these films.

Previous x-ray [44] and shear mechanical measurements [43] gave early indications of surface ordering in thin $\overline{14}$S5 films but the identification [44] of the surface phase as an untilted crystalline-B phase below 72° could not be confirmed optically in our experiments since the crystalline-B is not birefringent. The surface freezing transition in $L \sim 64$-layer films is from an untilted to a tilted surface phase. The existence of this tilted phase has not been reported previously but the specific phase assignment of the untilted surface phase is not important to the determination of the dominant forces in this system. $\overline{14}$S5 is a thermally stable material with a wide bulk smectic-A range 86.6° to 66.5° C. The thickness dependent phase diagram has not been studied. For two-layer films, the 2D crystalline-B phase remains when heated to 77.7° C, then melts to smectic-A by a first-order hysteretic phase transition (10° above bulk T_o). For three and five-layer films, transitions are seen from crystalline-B to a 2D hexatic at 72°, and a strong first-order transition from 2D hexatic to smectic-A at 75° C. For the smectic-A phase at 75° C, resolution limited x-ray peaks are observed corresponding to uncorrelated monolayer crystalline surface layers and interlayer order was not observed until T = 68° C. An identical phase sequence was proposed for 12-layer films but mechanical oscillator measurements were impossible for this thickness. X-ray scattering data for a 200-layer film exhibits peaks [44] perhaps indicating the presence of the tilted surface frozen phase seen in the surface freezing of $L \sim 64$-layer films.

2.8.5 Summary of Surface Freezing Results and Fits to Other Models

To summarize, four different LC systems, 9O.4, 4O.7, 7O.7, $\overline{14}$S5, have been discovered which exhibit layer-by-layer surface freezing. From measurements of the first ten surface freezing transitions in $L \sim 64$-layer FSLC films of these four LC materials, the dominant forces acting in each system has been determined. Data from these four systems has been fit to simple models for surface freezing dominated by the two simplest forces expected to be present in LC's: long-range van der Waals forces and short-range exponential forces. The observed power-law growth, $l = l_o t^{-\nu}$, of the thickness, l, of the of the frozen surface region, with $\nu \approx 1/3$, in the first system studied, 9O.4, indicated that the dominant interactions in that system are due to long-range van der Waals forces [29]. After finding this SF system, a search was made for SF transitions in other LC materials. This search resulted in the discovery of the three other LC systems which also exhibit layer-by-layer SF transitions described in this thesis. Both 4O.7 and 7O.7 were found to exhibit the logarithmic behavior, $l = l'_o + \xi \ln(1/|t|)$, with physically reasonable characteristic range, ξ, consistent with systems dominated by short-range exponential forces; $\overline{14}$S5 was found to be consistent with either van der Waals or exponential force models with physically reasonable values of both ν and ξ. All four systems exhibit layer-by-layer SF transitions. These results show that LC systems have SF transitions with both of the characteristic surface freezing universality classes expected for the forces in these systems: layer-by-layer surface freezing dominated by van der Waals and by exponential forces. Table 2.2 displays the best-fit parameters for each of these two force models for these four LC systems.

For all four LC systems, after about ten layers, there is a systematic and progressive deviation of the data from the divergence expected for either long-range van der Waals or short-range exponential forces. As the SF transitions continue into the interior of the film, the experimentally measured thickness of the frozen layer on the each surface grows slower with decreasing temperature than these simple models predict. This deviation, first seen in 9O.4, has been studied versus the film thickness for 4O.7 and 7O.7. For $l >> 10$, the surface freezing transitions clearly depend on the thickness of the film: the transitions in thicker films diverge more rapidly with decreasing temperature than do the transitions in thinner films. A phenomenological parameterization of these finite-size effects is presented in Section 2.9 where it is also shown that the finite-size effects for all thickness films can be described with a model-

Table 2.2: Best-Fit Power-law and Logarithmic Model SF Parameters. Results from fits to both the power-law, $l = l_o t^{-}\nu$ ($t = \alpha l^{-n}$, $\nu = 1/n$), and logarithmic, $l = l'_o + \xi \ln(1/|t|)$ ($t = \beta e^{-l/\xi}$), SF models for all four Liquid Crystal materials. These are the best-fit parameters from fits made to the first ten surface freezing transitions in $L \sim 64$-layer films.

LC	Power-law			Logarithmic	
	α	n	ν	β	ξ
9O.4	6.78 ± 0.05	2.68 ± 0.02	0.373 ± 0.015	43.3 ± 0.5	0.53 ± 0.01
4O.7	1.62 ± 0.10	1.81 ± 0.14	0.56 ± 0.04	5.4 ± 0.8	0.82 ± 0.06
7O.7	9.39 ± 0.05	6.0 ± 0.7	0.17 ± 0.02	$6.8 \pm 2.9 \times 10^2$	0.24 ± 0.02
$\overline{14}$S5	8.03 ± 0.16	2.76 ± 0.07	0.36 ± 0.03	53 ± 3	0.53 ± 0.01

independent effective interfacial potential. The same parameterization also fits the data from the 64-layer 9O.4 films quite well. These film thickness effects demonstrate the existence of a new contribution to the effective interfacial potential in LC films. Before discussing these finite-size results, we discuss fits to other crossover models for the intermediate thickness films.

For the two LC systems dominated by exponential forces, 4O.7 and 7O.7, a crossover [36] to van der Waals forces is expected at large distances since the exponential forces decay more rapidly than the power-law van der Waals forces. The range and precise functional form of the crossover depends on the detailed forms of both forces. The simplest model for this crossover is given by the sum, $t = \alpha l^{-3} + \beta \exp(-l/\xi)$ and has three free parameters. The resulting χ^2 values for fits to this model for the first ten SF transitions in these two systems is not decreased from the χ^2 values found for the original exponential force model and, in addition, the parameter β' requires the limit: $\beta < 0$. The conclusion from these fits is that there is no evidence for power-law terms in these two systems. Since the dominant LC interactions have both power-law and exponential forms, the 9O.4 data was also fit with the same crossover form, $t = \alpha l^{-3} + \beta \exp(-l/\xi)$. Again these fits showed that χ^2 was not decreased and that the parameter β requires the limit: $\beta < 0$. The conclusion from these fits is that the contribution of the exponential terms is negligibly small in 9O.4.

Ajdari, Peliti and Prost [97] and Li and Kardar [98] have recently shown that the orientational fluctuations in the smectic phase should give rise to a fluctuation-induced long-range force which can be comparable in size to the usual van der Waals force. This new force, caused by thermal fluctuation-induced dipole-dipole interactions, has the form, $V(l) \propto l^{-1}$. If this force were the only force acting then fits made to the variable exponent power-law model, $l = l_o t^{-\nu}$, would check for its existence and yield an exponent $\nu = 1/2$. Fits to $l = l_o t^{-\nu}$ indicate that the data for the first ten SF transitions in 64-layer 4O.7 films is consistent with $\nu = 1/2$ at the two-sigma level! The power-law exponents from 9O.4 and $\overline{14}$S5 also may have a small contribution due to this force since the best-fit exponents for both systems have $\nu > 1/3$.

For larger intermolecular separations, the nonretarded van der Waals interactions become retarded and, to lowest order, there is a crossover to $V(r) \propto r^{-7}$. Fits were made to test qualitatively for this crossover to the retarded van der Waals form, $t = \alpha' l^{-4}$, which is expected for thick films dominated by retarded van der Waals

forces. The functional form of this crossover must vary with distance and be $t = \alpha l^{-3}$ at small l, and $t = \alpha' l^{-4}$ at large l. The detailed form of this crossover, where $\alpha = \alpha(l)$ and $\alpha' = \alpha'(l)$, is not known so fits were made to a simpler model, $t = \alpha l^{-3} + \alpha' l^{-4}$ with α and α' free parameters independent of l. This crossover form could not account for the slowing down seen after the first ten SF transitions in 9O.4. The conclusion from these fits is that no evidence for retardation was found for the first ten transitions (below 300Å) in either 9O.4 or $\overline{14}$S5 films or past ten layers (above 300 Å) for 9O.4.

A recent model by Holyst [19] for surface freezing proposes that surface freezing is produced by the surface tension quenching of the layer fluctuations. The calculated behavior for this model has a "surface freezing like" behavior in thin films, but does not agree quantitatively with the experimental results. This theory is described and is compared with the experimental data for 7O.7 in Chapter 4.

2.9 Finite-Size Effect Results

2.9.1 Finite-Size Effects in 9O.4

The deviation from the predicted growth after about the first ten SF transitions was first observed in the original SF study of 64-layer thick 9O.4 films [29]. Fig. 2.16 shows that after about the first ten layers freeze at each vapor interface, the data deviates from the power-law form. In this figure, the dashed line indicates the continuation of the best-fit power-law form fit to the first ten surface freezing transitions. The data for all 32 layer surface freezing transitions can be fit by a phenomenological model, $t = \alpha l^{-n} + \beta' l^3$, which is the solid line shown in Fig. 2.16. The best-fit parameters are $\alpha = 6.79 \pm 0.46$, $n = 2.68 \pm 0.17$, and $\beta' = 9.0 \pm 3.5 \times 10^{-6}$. The critical exponent determined from this phenomenological model, $\nu = 1/n = 0.373 \pm 0.24$, is in good agreement with the predicted van der Waals exponent at the two-standard-deviation level. Kroll and Gommper [47] calculated that the slowdown for the SID transitions in a system dominated by short-range forces with a two-phase coexistence region is $t = \beta e^{-l/c} - \beta' l$. The analogous model for SIO would correspond to $t = \alpha l^{-n} - \beta' l$ for a system dominated by long-range van der Waals forces. A linear shift at large l is also consistent with the 9O.4 data, but then a crossover would be required from a constant shift at small l to a linear shift at large l. The total shift produced in 9O.4 by the cubic term, l^3, for thirty frozen surface layers is about 0.2° C. As will be discussed

below, all the SF transitions in 9O.4 are described very well by the finite-size model in Eq. 2.13. In addition, this finite-size model also fits very well all of the thickness dependence of the 4O.7 and 7O.7 data for films ranging from 17 to about a thousand layers thick.

2.9.2 Finite-Size Effects in 4O.7 and 7O.7

As first seen in 9O.4, after about ten transitions the surface freezing transitions in 4O.7 and 7O.7 films also fall off from the original steep logarithmic divergence. The SF transitions in many different thickness 4O.7 and 7O.7 films were measured for four reasons: to study the deviations from the simple force models, to understand the reason for the slowdown of the divergence, to look for possible universal behavior among different LC materials, and to understand the influence of the proximity of two internal interfaces near the center of the film. It was found that for $l >> 10$, the surface freezing transitions clearly depend on the thickness of the film with the transitions in thinner films diverging more rapidly with l from the original logarithmic divergence than the transitions in thicker films; the growth of the SF tail is steeper for thick films than it is for thin films. Figure 2.17 shows data from nine representative 4O.7 films with thicknesses ranging from 17 to $\sim$ 1000 layers thick. The logarithmic divergence which fits the first ten transitions of films thicker than about 30 layers is plotted with a dashed line. After about ten layers, all these films deviate from the logarithmic divergence – after the first ten transitions, the SF transitions in films with increasing thickness, L, exhibit a systematically increasing slope $\Delta l/\Delta T$.

The data from 9O.4, 4O.7, and 7O.7 does not fit the simple van der Waals or exponential force models after the first ten SF transitions and these deviations are film thickness dependent. Consequently a crossover to a new thickness-dependent term in the effective interfacial potential is required. Fig. 2.18 to 2.20 show nine representative 4O.7 data sets with film thicknesses of 17, 27, 41, 64, 141, 207, 337, 477, and 983. The solid lines, which pass through each data set are the best-fit finite size models given by Eq. 2.12, $t = \beta \exp(-l/\xi) - \beta' L/(L - \varepsilon l)$. These same solid lines are plotted in Fig. 2.17 but are difficult to see because of the agreement. This finite-size model fits this data very well with a single set of parameters for all thickness 4O.7 films. The best-fit parameters for the fits shown are $\beta = 5 \pm 1, \xi = 0.84 \pm 0.07$, $\beta' = 0.3 \pm 0.2$, and $\varepsilon = 1.1 \pm 0.4$. To obtain these parameters the surface freezing data

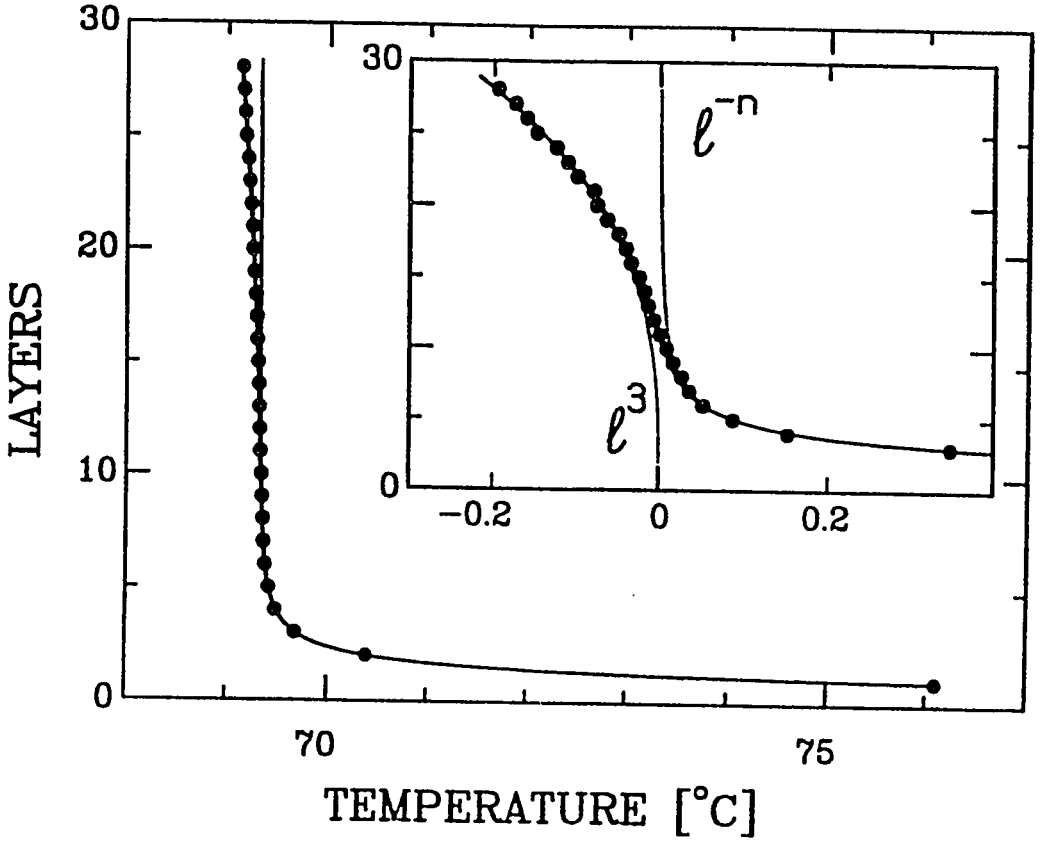

Figure 2.16: 9O.4 Crossover After Ten Transitions. Plot of the number of frozen surface layers (on each surface) versus the reduced transition temperature in the crossover region for 9O.4. The dashed line indicates the power-law form $l = l_o t^{-\nu}$, which fits the transitions near the surface, but progressively deviates from the data as the freezing continues inward. The solid line indicates the phenomenological crossover form $t = \alpha l^{-n} + \beta l^3$, which fits all the freezing transitions. Inset: A $T - T_o$ plot of the contributions of the two terms close to T_o; the dashed lines indicate the power-law l^{-n} and cubic l^3 contributions. The solid line indicates the combined crossover form.

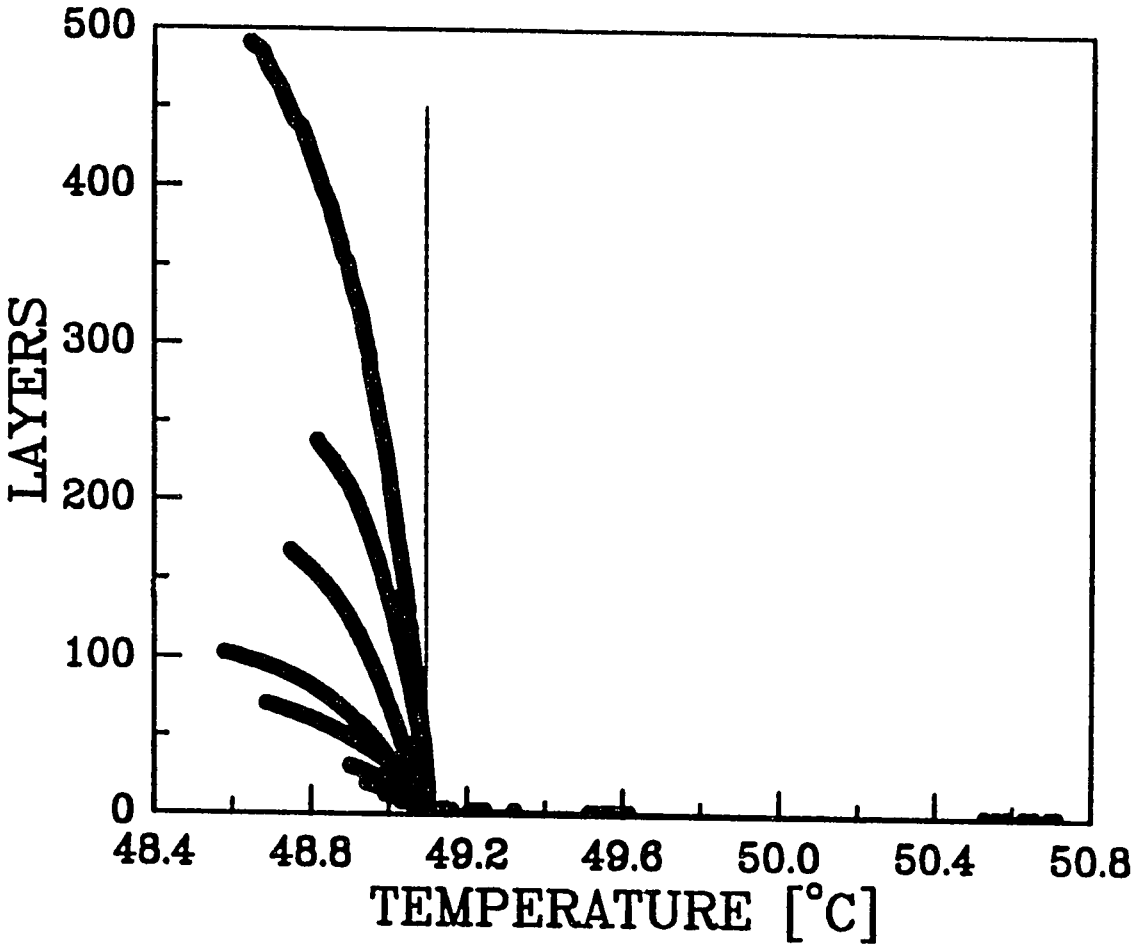

Figure 2.17: Overplot of 4O.7 Surface Freezing Data. Representative surface freezing data from 9 different 4O.7 films with thicknesses $L = 17, 27, 41, 64, 141, 207, 337, 477,$ and 983 layers. The solid lines through each data set is the best-fit finite-size model for exponential short-range forces, $t = \beta \exp(-l/\xi) - \beta' L/(L - \varepsilon l)$. Note the growth of the tail is faster for thick films than for thin films. The dashed line indicates the continuation of the logarithmic form which fits the first ten SF transitions in thicker films.

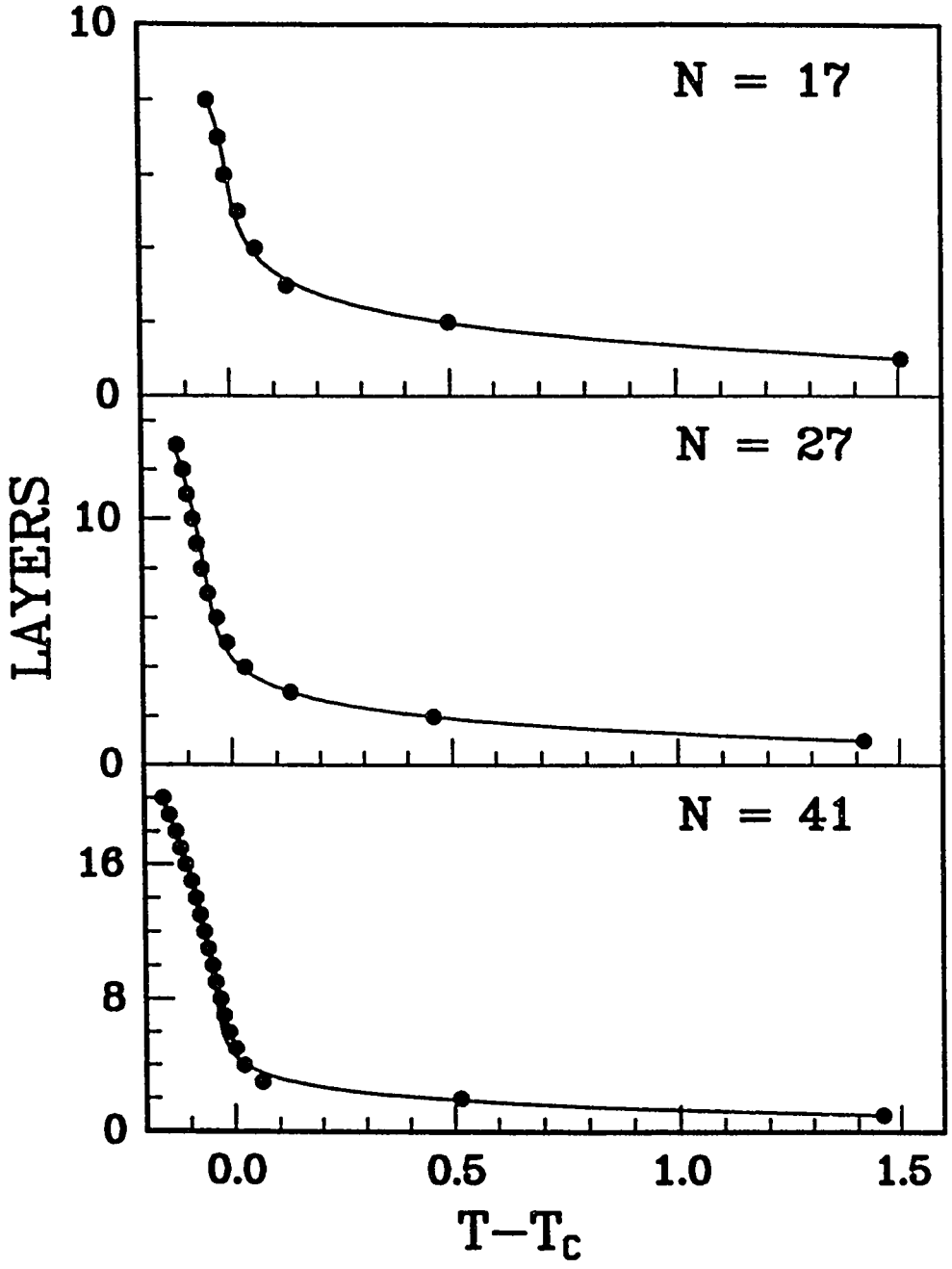

Figure 2.18: 4O.7 Finite-Size Effects: Thin Films. The surface freezing data from 4O.7 films with thicknesses $L = 17, 27$, and 41 layers. The solid line is the best-fit finite-size model with exponential short-range forces, $t = \beta \exp(-l/\xi) - \beta' L/(L - \varepsilon l)$.

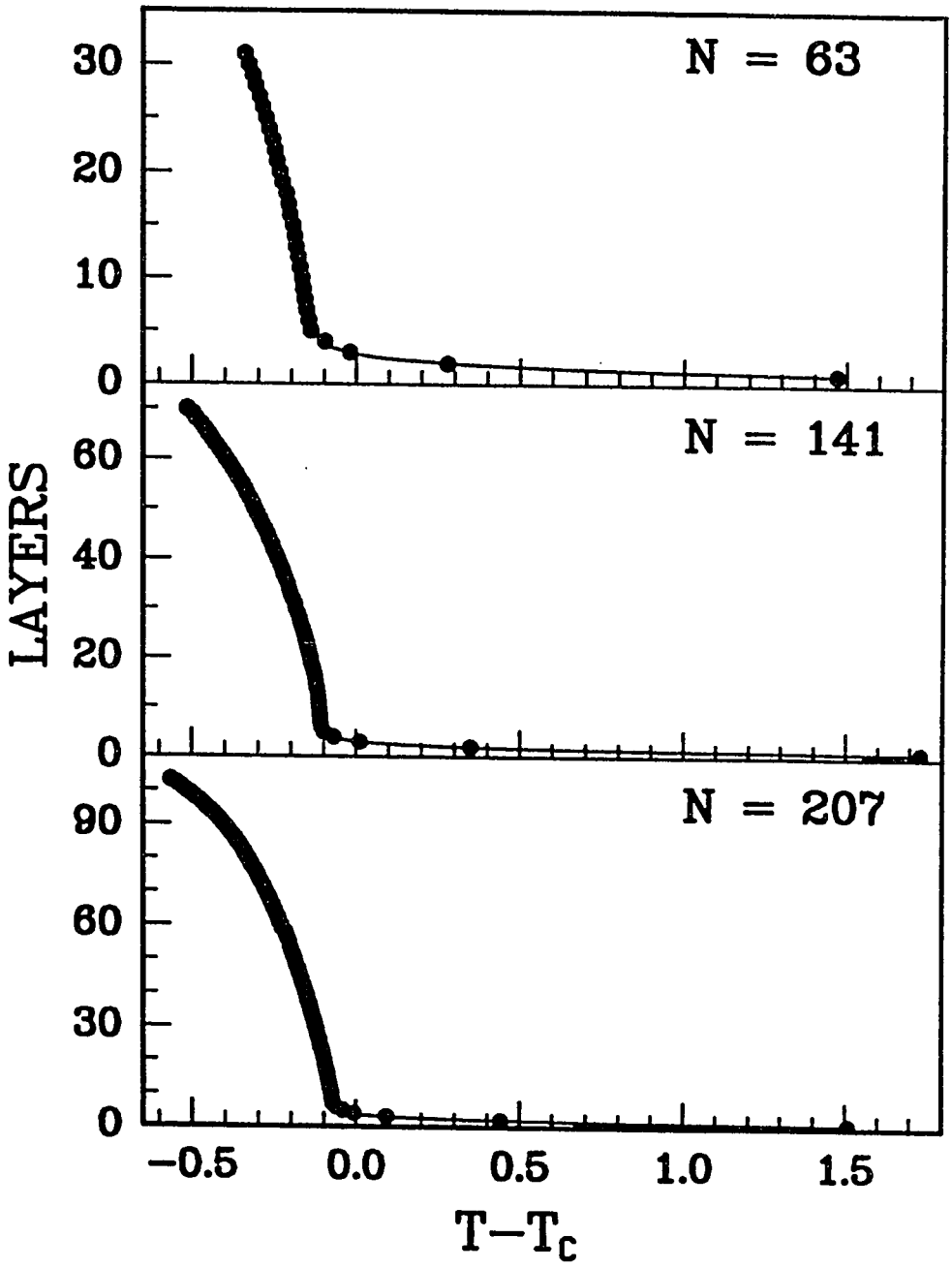

Figure 2.19: 4O.7 Finite-Size Effects: Intermediate Thickness Films. The surface freezing data from 4O.7 films with thicknesses $L = 64, 141$, and 207 layers. The solid line is the best-fit finite-size model with exponential short-range forces, $t = \beta \exp(-l/\xi) - \beta' L/(L - \varepsilon l)$.

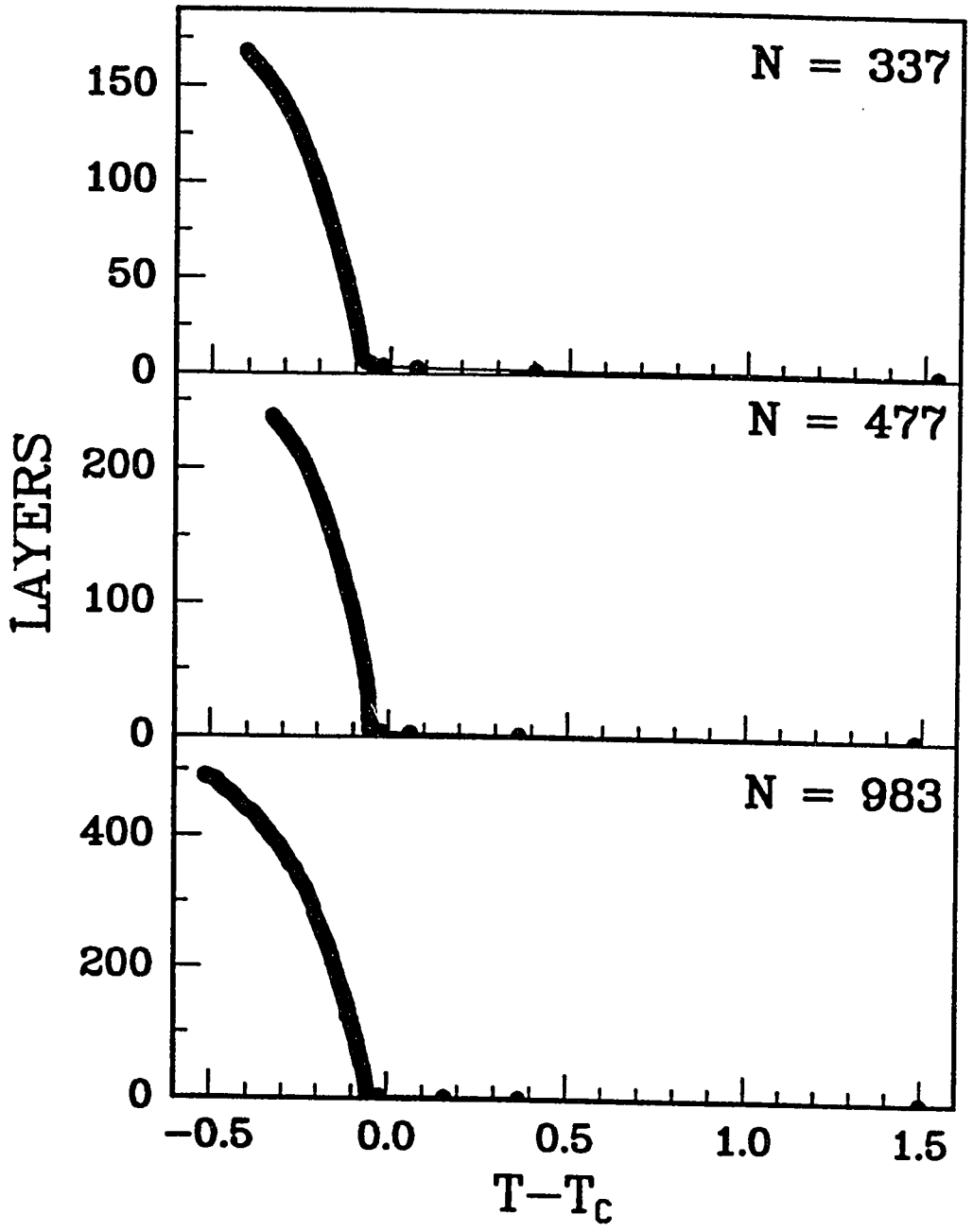

Figure 2.20: 4O.7 Finite-Size Effects: Thick Films. The surface freezing data from 4O.7 films with thicknesses $L = 337, 477$, and 983 layers. The solid line is the best-fit finite-size model with exponential short-range forces, $t = \beta \exp(-l/\xi) - \beta' L/(L - \varepsilon l)$.

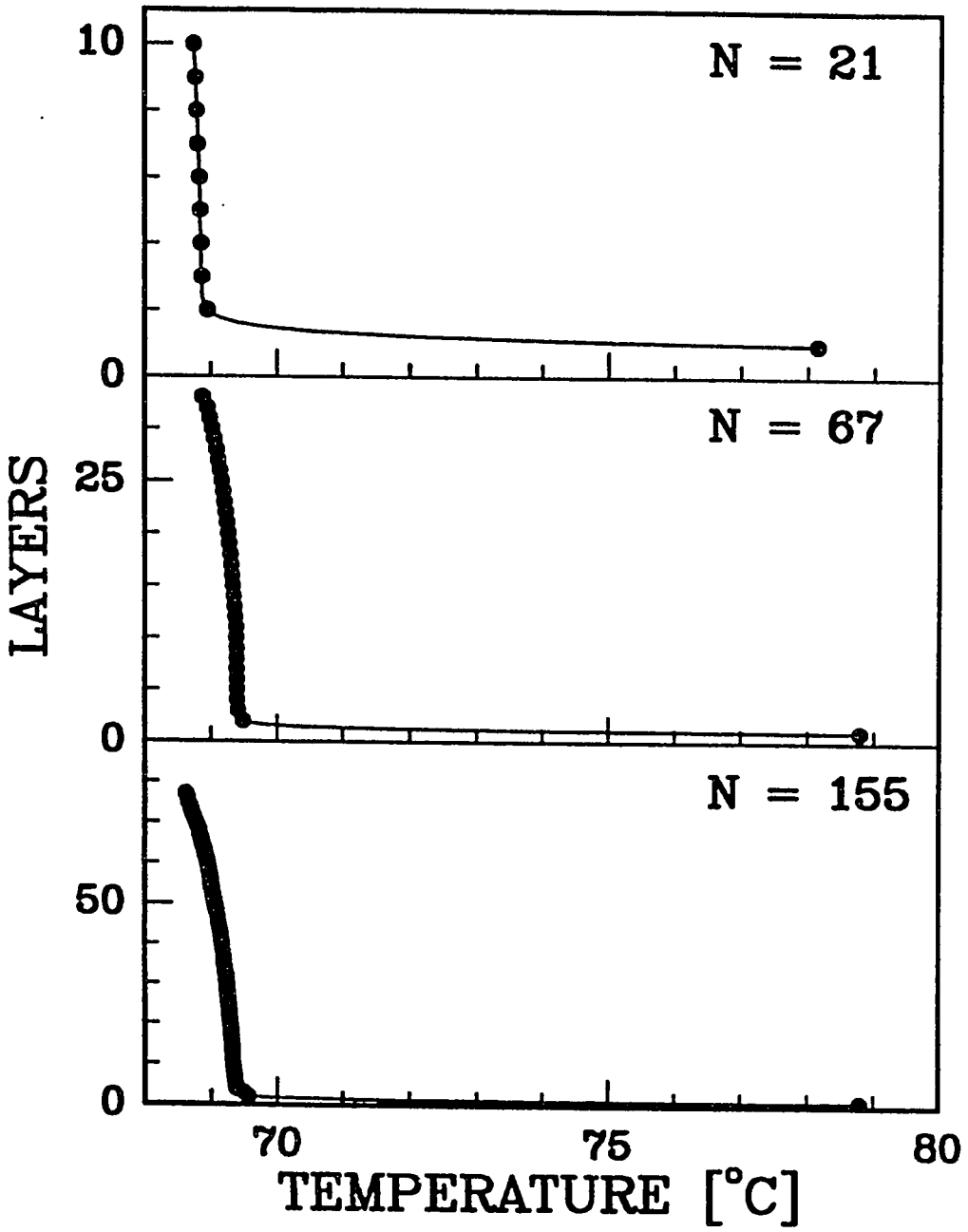

Figure 2.21: 7O.7 Finite-Size Effects. The surface freezing data from 7O.7 films with thicknesses $L = 21, 64$, and 155 layers. The solid line is the best-fit finite-size model with exponential short-range forces, $t = \beta \exp(-l/\xi) - \beta' L/(L - \varepsilon l)$.

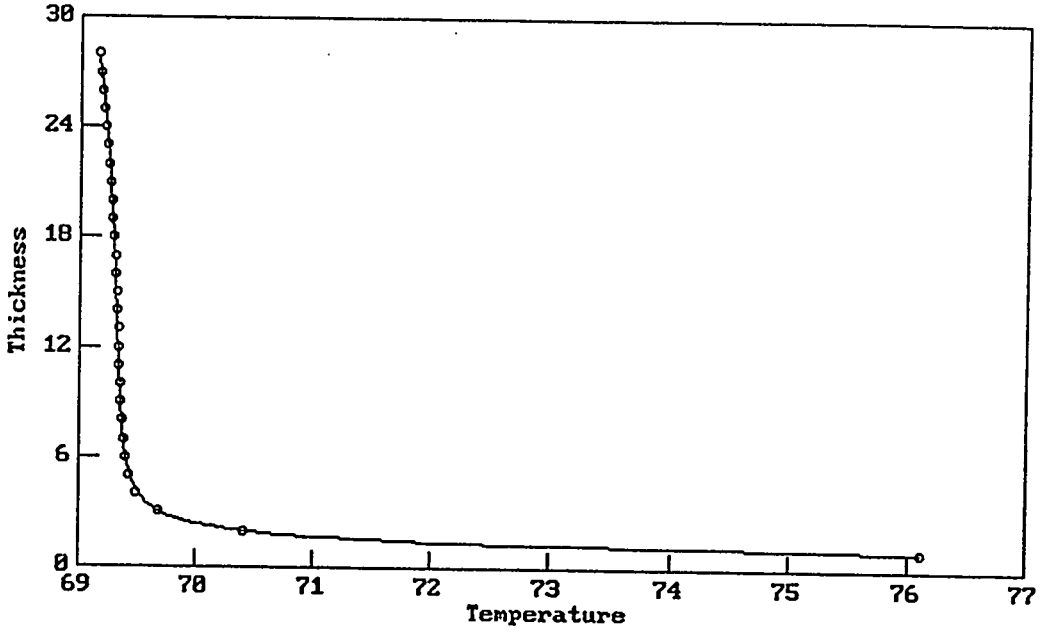

Figure 2.22: 9O.4 Finite-Size Effects. The surface freezing data from a 64-layer 9O.4 film. The solid line is the best-fit finite-size model with van der Waals forces, $t = \alpha l^{-n} - \beta' L/(L - \varepsilon l)$.

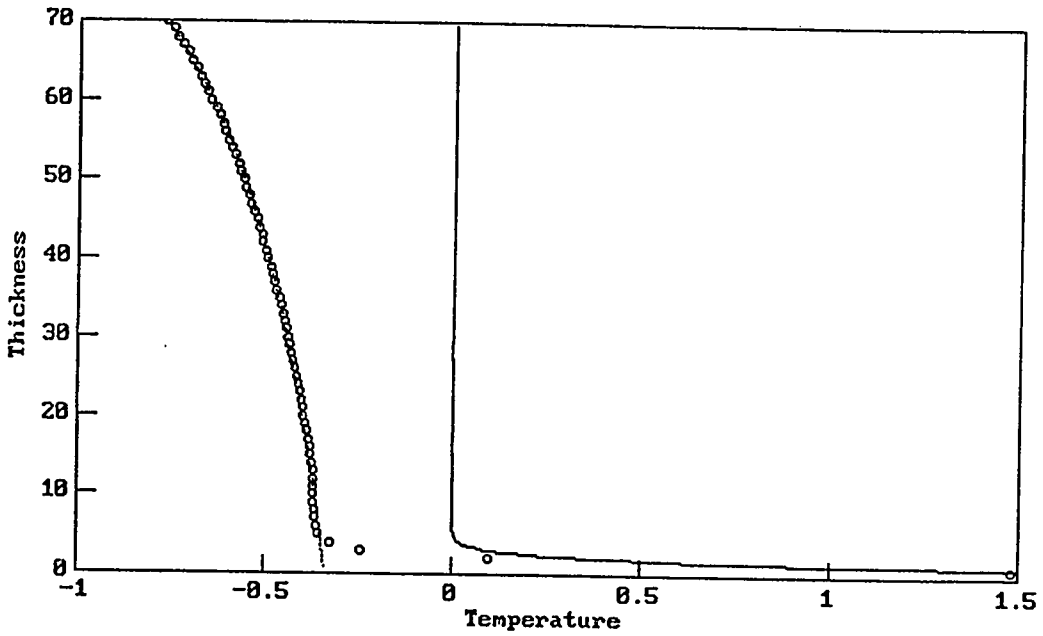

Figure 2.23: Finite-Size Model Pieces. The contribution of the two terms in Eq. 2.12, $t = \beta \exp(-l/\xi) - \beta' L/(L - \varepsilon l)$, describing the finite-size model fit to the 141-layer 4O.7 film. The slowdown after the first ten transitions is fully accounted for by the thickness dependence of the second term, $\beta' L/(L - \varepsilon l)$. The contribution of the first term, $\beta \exp(-l/\xi)$, is negligible after the first ten surface freezing transitions.

from each film shown was fitted separately to the finite-size model and the average best-fit parameters were then calculated from the nine independent fits. Figure 2.21 shows the data and the fits for the three representative 7O.7 films with thicknesses of 21, 64, and 155 layers. The solid line indicates the best-fit finite-size model given by Eq. 2.12, which again fits the data very well with a single set of parameters for all thickness 7O.7 films: $\beta = 10 \pm 6 \times 10^2, \xi = 0.22 \pm 0.03$, $\beta' = 0.3 \pm 0.1$, and $\varepsilon = 1.2 \pm 0.3$. This finite-size model fits this data very well with a single set of parameters for all thickness 7O.7 films. For both systems, equally acceptable fits were also obtained using a different phenomenological parameterization with two exponential length scales, $t = \beta \exp(-l/\xi) + B \exp(-4l/L)$. The best fit parameters from this parameterization were $\beta = 5 \pm 1, \xi = 0.85 \pm 0.07$, and $B = -0.04 \pm 0.02$ for 4O.7, and were $\beta = 10 \pm 5 \times 10^2, \xi = 0.22 \pm 0.03$, and $B = -0.08 \pm 0.05$ for 7O.7. This "two exponential" model is equivalent to Eq. 2.9 with the ξ in the third term different from the ξ in the first two terms. Fig. 2.23 shows the contribution from both terms in Eq. 2.12 for the 141-layer 4O.7 film. The first term is negligible, less than 5×10^{-5}, after ten layers for all thickness films and all materials. The results are similar for the two terms in the two-exponential model. Fig. 2.22 exhibits the data from a 64-layer 9O.4 film and the solid line, which is the best-fit finite size model with long-range van der Waals forces, given by Eq. 2.13. This model fits the data very well with best-fit parameters: $\alpha = 6.7, n = 2.71$, $\beta' = 0.096$, and $\varepsilon = 1.6$. Although questions remain as to whether this finite-size model has a physical justification, this model provides an excellent parameterization of the surface freezing and can be used to make a model-independent determination of the complete effective interfacial potential for these systems as will be described in Sec. 2.10.

2.9.3 Summary of Surface Freezing Finite-Size Effects

To summarize, the finite-size effects in 9O.4, 4O.7 and 7O.7 can be described quite well by a simple model which assumes that the temperature shift of the transitions near the center of the film varies as $\Delta T = \beta' L/(L - \varepsilon l)$ for all three materials. The parameter ε is found to be less than that expected for standard finite-size effects where $\Delta T \sim 1/(L - 2l)$ with $\varepsilon = 2$, but this finite-size model is still quite similar to the transition temperature shifts found in other systems due to confinement. The fact that $\varepsilon < 2$ might be partially accounted for by the film thickness changes caused by the

molecular tilt. In FSLC films, the surface tension and the solid surface frozen layers on both vapor surfaces of the film may play the analogous roles in reducing the transition temperature as the curvature of the interface plays in capillary condensation. The finite-size data is also consistent with a model with two exponential forces, the second exponential force having a length-scale $\xi' = L/4$.

2.10 Model-Independent Effective Interfacial Potential

Since more than one model fits the finite-size data, an important question is: Which model is physically correct? Without answering this question, the excellent parameterization of the data provided by both of these models can still be used to make a model independent determination of the complete effective interfacial potential and to demonstrate the existence of a new contribution to the effective interfacial potential in LC films. As described in Sec. 2.3, the complete effective interfacial potential determines the thickness of the surface frozen layer, l, as the temperature approaches T_o. Fig. 2.2 displayed the qualitative features of the simple effective interfacial potential which describes the first ten transitions in $L \approx 64$-layer films. The complete effective interfacial potential, $V_C(l)$, given by Eq. 2.14 for systems with short-range exponential forces like 4O.7 and 7O.7, must include a new film thickness-dependent finite-size term, $V_N(l, L) = (\beta' L/\varepsilon)\ln(L - \varepsilon l)$, which is responsible for the finite-size effects. The complete effective interfacial potential,

$$V_C(l) = \begin{pmatrix} \text{Phase} \\ \text{Conversion} \\ \text{Cost} \end{pmatrix} + \begin{pmatrix} \text{Interface-} \\ \text{Interface} \\ \text{Interaction} \end{pmatrix} + \begin{pmatrix} \text{New} \\ \text{Finite-Size} \\ \text{Term} \end{pmatrix}$$

$$= \quad Ctl \quad + \quad \Delta\gamma(1 - \lambda e^{-\frac{l}{\xi}}) \quad - \quad \tfrac{\beta' L}{\varepsilon}\ln(L - \varepsilon l) \qquad (2.14)$$

contains three terms corresponding to the phase conversion cost, the interface-interface interactions, and the new finite-size term, respectively. This potential arises from the parameterization provided by Eqs. 2.12 and 2.13. The resulting best-fit parameters can be used to construct a model-independent determination of the complete effective interfacial potential for all thickness films. Fig. 2.24a, b, and c, show the complete effective interfacial potential constructed from the fits for a 100-layer 4O.7 film using the best-fit parameters. The complete effective interfacial potential is plotted for

Figure 2.24: Complete Effective Interfacial Potential. The complete effective interfacial potential, $V_C = Ctl + \Delta\gamma(1 - \lambda \exp(-l/\xi)) - (\beta' L/\varepsilon) L \ln(L - \varepsilon l)$, which describes the finite-size effects in 100-layer thick 4O.7 films. This complete effective interfacial potential is the sum of the phase conversion cost, $V_{Conversion} = Ctl$, the interface-interface interaction, $V_{Interface} = \Delta\gamma(1 - \lambda \exp(-l/\xi))$, and the new finite-size energy, $V_N(l, L) = (\beta' L/\varepsilon) L \ln(L - \varepsilon l)$. In all four LC systems studied, the surface freezing transitions appear layer-by-layer and therefore the complete effective interfacial potential is corrugated with the spatial periodicity of the LC layer spacing. Only the envelope of $V_C(l, 100)$ is shown; the periodic structure has been omitted for clarity.

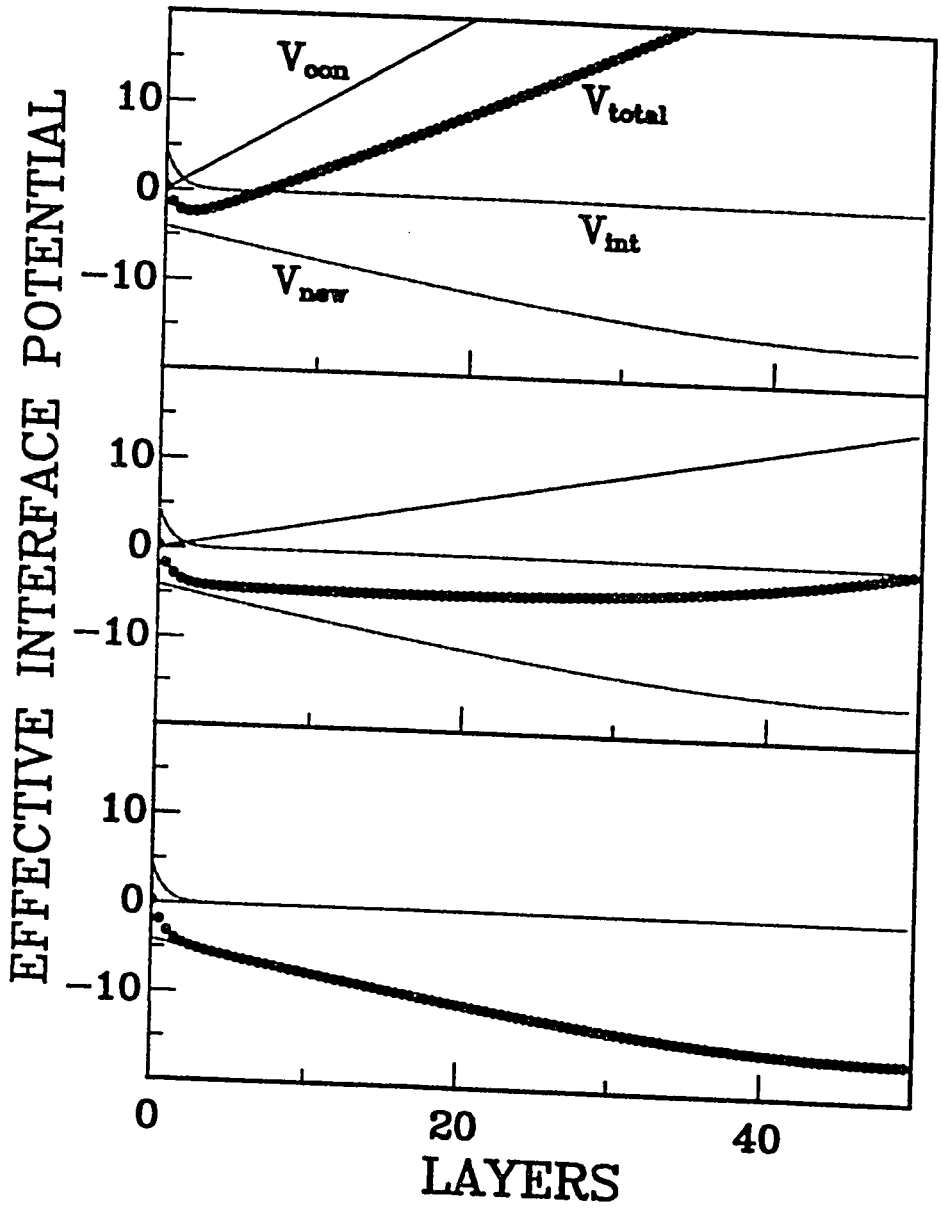
EFFECTIVE INTERFACE POTENTIAL
LAYERS
V_{con}
V_{total}
V_{int}
V_{new}
10
0
−10
20
40

$t = 1.0$, 0.3, and 0, along with the three terms in Eq. 2.14. The minimum of the complete interfacial potential determines the position of the interface which is located in Fig. 2.24 at $l = 2, 15$, and 50 (the center of the film), respectively. Minimization of this complete effective interfacial potential results in Eq. 2.12. Fig. 2.24 shows that at a reduced temperature of $t \sim 1$, the potential is narrow and well defined and as $t \rightarrow 0$ the potential flattens into a broad minimum. The "repulsion" which slows down transitions near the center of the film is due to the new finite-size term which, in the simplest case assumed here, is independent of temperature. Fig. 2.25 shows the thickness dependence of the complete effective interfacial potential calculated for $L = 60, 120, 180, 240$, and 300 layer films. The shape of V_N for the first few transitions in thicker films is linear which results in a simple renormalization of the "bulk" transition temperature, T_o, and in this region only the first two terms in Eq. 2.14, corresponding to just the simple effective interfacial potential, are required to describe the first ten transitions in intermediate thickness films. The value of T_o cannot be determined independently because the frozen surface phase does not appear in the bulk phase diagram. Transitions near the center of very thick films also exhibit a similar slowdown produced by the curvature of the complete effective interfacial potential at large l.

2.11 Surface Freezing Interfacial Velocities

The speeds of the surface freezing interfaces or 'waves' during SF have been measured for films of 9O.4, 4O.7, 7O.7, and $\overline{14}$S5. Measurements were made by marking the position of the interface for each video frame time step of 1/30 sec. All waves measured had center nucleation points to simplify the possible complications due to the radial temperature gradients of the films. Fig. 2.26 shows measurements of the interface diameter versus time for waves two, three, and four (70.3°, 69.6° and 69.4°) from a 64-layer 9O.4 film during a constant temperature ramp of 0.5 mK/sec. A constant radial interface speed is seen for measurements from the center out to 2.5 mm for 5 mm diameter films. No discernable increase in the interface speed is seen at the initial appearance of the transition. A 'jump' in the interface speed might be expected if a large nucleation barrier is present since the films must be supercooled before making the transition. Any possible 'jump' during nucleation is less than 0.1 mm and corresponds to less than 1 mK of under-cooling. All waves exhibit the same constant

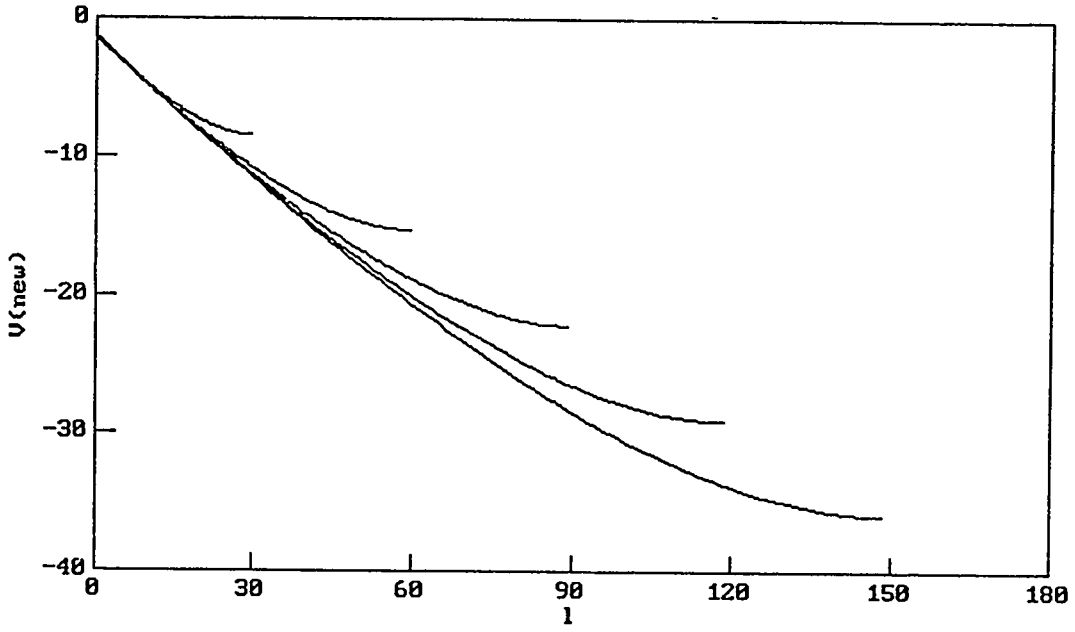

Figure 2.25: Thickness Dependence of the Complete Effective Interfacial Potential. The film thickness dependence of V_N from the complete effective interfacial potential for a 4O.7 film with thicknesses $L = 60, 120, 180, 240$, and 300 layers. For the first ten transitions in thicker films, V_N is linear and simply shifts T_o which is a fitting parameter in the model. T_o cannot be determined independently since the frozen surface phase does not appear in the bulk phase diagram.

speed of 2.9 mm/sec at this cooling rate from 0 to 2.5 mm diameter. Additional experiments are needed with different ramp rates to confirm that the waves are not following the ramped temperature profile of the film. Work is planned to measure the wave velocity versus ramp rate to confirm that these surface freezing transitions are first-order using the linear-interface-velocity criterion [99]. The other materials also do not exhibit an initial 'jump' and have similar constant wave speeds indicating that the interface is perhaps just following the temperature profile of the film.

2.12 Surface Freezing Summary and Conclusions

Surfaces, in systems with a large surface to volume ratio and accordant interfacial energies, can have important influences on the character of the system's phase transitions and can convert a first-order 3D phase transition without any universal critical exponents into a surface-induced first-order phase transition like surface freezing. Even in bulk systems, the presence of the ubiquitous surface cannot be neglected since it may be the nucleation point of phase transitions. The fact that liquids may be easily under-cooled but crystals cannot be overheated indicates that melting is initiated at the crystal surface, whereas freezing in most materials requires overcoming a the kinetic barrier of nucleation. In this chapter, surface freezing has been described in terms of the interfacial wetting of the surface of a 'liquid' FSLC film by the frozen 'solid' LC phase. An additional feature of FSLC films, which will be discussed further in Chapter 4, is that the surface also provides the natural nucleation point for freezing due surface tension-quenched fluctuations [22]. Freezing may begin at the point in the system where the fluctuations are the smallest, which, for FSLC films, is at the surface.

At a liquid-vapor interface, thermally-induced fluctuations or long wavelength capillary waves disorder the surface and the liquid-vapor interface is not smooth. If the interfacial fluctuations are not sufficient in amplitude to disorder the natural periodic layering of the sample on the scale of a few layers, the growth of the wetting layer will be layer-by-layer. The fact that the SF transitions in these FSLC films are layer-by-layer indicates that, as shown in Chapter 3, the 4 Å mean-squared displacement of the layers is not sufficient to destroy the smectic ordering which has a 30 Å layer spacing. For surface melting or freezing at the free vapor interfaces of a thick sample, small amounts of roughness at the interface might grow as the disordered

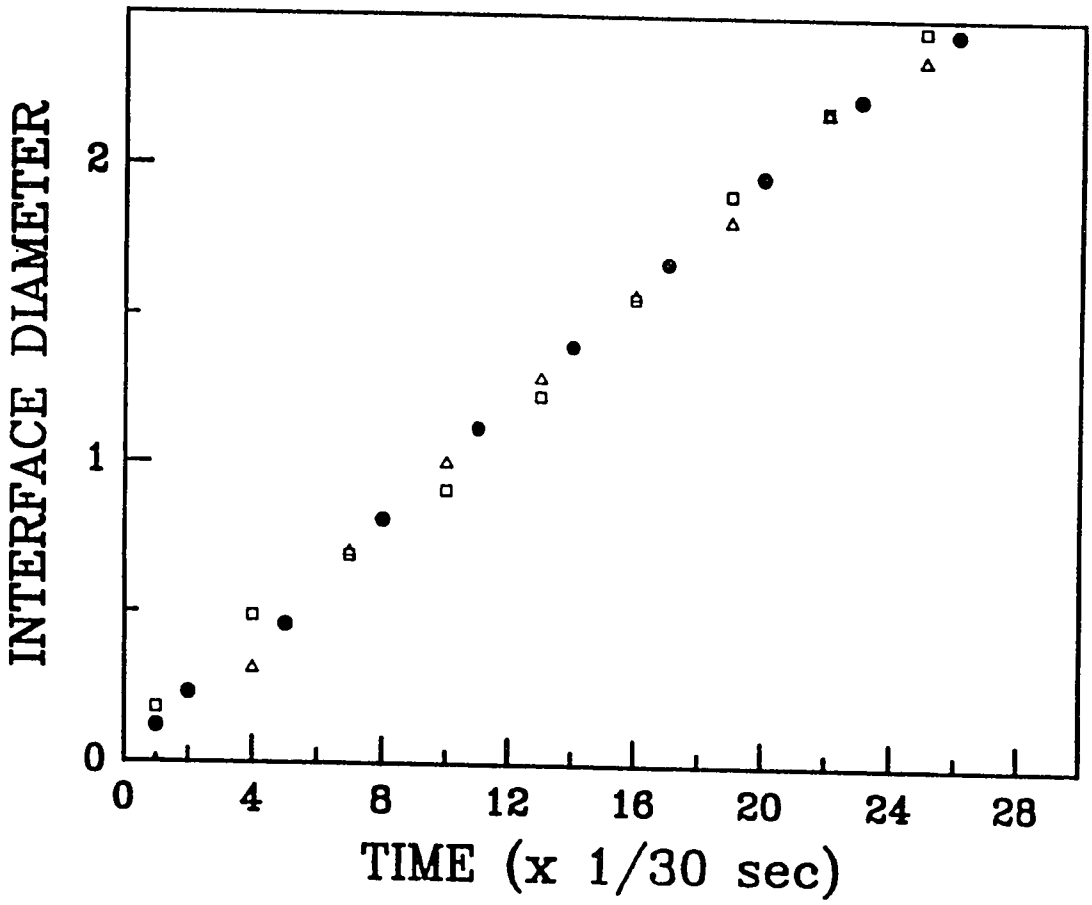

Figure 2.26: Wave Speeds of Surface Freezing Interfaces. The wave diameters versus time for the 90.4 surface freezing transitions beginning at 70.3, 69.6, and 69.4° C are plotted here. All waves appear to have about the same constant speed suggesting that the interfaces are simply following the radial temperature profile of the film.

layer becomes thicker, and if so, can eventually wash out the layer-by-layer growth [100] as the natural periodicity in the effective interfacial potential becomes washed out. This crossover to continuous growth has not been observed in LC films up to about a thousand layers thick. For thin films, the magnitude of the interfacial roughness is limited by the thickness of the film and as long as the film is thin enough, the interface will be effectively smooth. It is interesting to note that all surface melting transitions seen so far are continuous which indicates rough interfaces or significant system heterogeneity, whereas all surface freezing transitions are layer-by-layer indicating smooth interfaces.

The focus in this chapter has been the two simplest forces which are known to exist in liquid crystal systems, attractive van der Waals forces and steric short-range exponential forces. However, it is really not clear why some materials exhibit dominant exponential forces whereas others exhibit dominant van der Waals forces.

In conclusion, near the surface of intermediate thickness films, the layer-by-layer surface freezing transitions of 9O.4 have the power-law form expected for surface freezing governed by van der Waals interactions, while 4O.7 and 7O.7 exhibit the exponential form expected for surface freezing governed by exponential interactions. This is the first demonstration of layer-by-layer surface freezing governed by exponential interactions. After about the first ten SF transitions, the layer-by-layer surface freezing transitions exhibit a slowdown, dependent upon the film thickness. This slowdown is described nicely by a finite-size model which is similar to models used to describe transition temperature shifts due to confinement. The data is also fit by a model with two exponential forces. Which of these models is correct remains an open question, but a model-independent construction of the complete effective interfacial potential has been made using these two models to parameterize the surface freezing behavior in these LC systems. From this complete effective interfacial potential, the shape of the repulsive potential responsible for the finite-size slowdown has been deduced.

Chapter 3

DIRECT INVERSION OF THIN FILM X-RAY DIFFRACTION: SOLUTION OF THE PHASE PROBLEM IN ONE-DIMENSION

If we know the nature of the periodic variation of the medium we can analyse it by Fourier's method into a series of harmonic terms. The medium may be looked on as compounded of a series of harmonic media, each of which will give the medium the power of reflecting at one angle. The series of spectra which we obtain for any given set of crystal planes may be considered as indicating the existence of separate harmonic terms. We may even conceive the possibility of discovering from their relative intensities the actual distribution of the scattering centres, electrons and nucleus, in the atom.

- W. H. Bragg (1915)

3.1 Introduction and Summary of Results

This chapter describes a new method developed to directly invert interlayer x-ray diffraction data from thin centrosymmetric films resulting in a model-independent

determination of the electron and center-of-mass densities. An experimental demonstration of this method is presented for freely-suspended liquid crystal (FSLC) films of 7O.7 with thicknesses from three to fifteen layers in both the smectic-G phase and the smectic-I/C phase. The direct inversion analysis involves first removing the instrumental broadening from the measured diffraction intensity by deconvolution, and then obtaining the interlayer electron density by explicitly solving the one-dimensional crystallographic phase problem. The phase problem can be solved for thin FSLC films since the phase assignments can be made by inspection using three facts: 1) The electron density is real, positive, and centrosymmetric and therefore the scattering amplitude is real and even. 2) The measured thin film diffraction pattern reveals the zero-crossings or phase changing points of the scattering amplitude. 3) The phase of the primary and subsidiary maxima in the scattering pattern switch between 0 or π in a well-defined way since the zeros are due to the product of the molecular form factor and the thin film 'N-slit' interference zeros. Since the molecular tilt angle is known from the position of the molecular form-factor zeros in the measured scattering intensity, the center-of-mass density can be derived from the electron density by a second deconvolution, removing the broadening due to the 7O.7 molecular density. The direct inversion densities are thereby obtained without refinement and without significant unphysical electron density outside the LC film region.

The LC film densities obtained using the direct inversion method are compared with those obtained by forward modeling: a model interlayer density is fit to the measured scattering intensity [22, 26]. In the forward model, the model density assumes the LC molecules are aligned in layers, each positioned with their long axis tilted at an angle with respect to the layer normal direction. The molecular center-of-mass distribution in each layer is parameterized by a Gaussian distribution which indicates the amplitude of the thermally excited, long wavelength hydrodynamic fluctuations of the layers. This model for the interlayer density was Fourier transformed, convolved with the instrumental resolution and then fit to the measured scattering intensity by varying the various parameters for the molecular tilt angles and layer fluctuation amplitudes. The forward model results indicate that the crystalline smectic-G films have a uniform tilt, large fluctuation amplitudes, and very small interlayer fluctuation profiles. In contrast, the fluid smectic-I/C films exhibit both layer fluctuation and molecular tilt angle profiles which have systematic variations with film thickness. For

both phases, the Gaussian fluctuation width, σ_i, is smallest at the surfaces of the film and reaches a maximum at the film center. For the smectic-I/C films, the tilt angle is maximum on each surface and minimum at the center of the film.

Detailed comparisons are made in Sec. 3.11 between the densities obtained from the forward model and those obtained using the direct inversion analysis. To summarize the main results, the electron and center-of-mass densities from both the direct inversion and forward model analysis have many similar features: The center-of-mass densities for each layer of thick smectic-G films have uniform height and width throughout the film. In contrast, the center-of-mass densities for the smectic-I/C films show enhanced surface density and/or quenched fluctuations of the surface layers attributable perhaps to the influence of the monolayer hexatic smectic-I layers on each surface and/or surface tension quenched fluctuations. The electron density modulation produced by the individual smectic layers is not simply the pure sinusoidal density wave usually proposed for bulk smectic-A samples. There are also some differences between the forward model and direct inversion results: The direct inversion center-of-mass densities are not as flat in the smectic-G phase and, in general, the width, σ_i, of the interlayer fluctuations are wider than those resulting from the forward model analysis.

3.2 Motivation

There are three main motivations and justifications for this study: 1) The crystallographic phase problem is of long standing interest. The direct inversion method described here provides an unusual experimental demonstration of the solution of this problem for thin centrosymmetric films. 2) There is intrinsic interest in understanding the structure of films in the intermediate crossover range between two and three dimensions. The direct inversion method provides a model-independent determination of the structure of such films and is an independent test of the structure derived from forward modeling. 3) The direct inversion method provides a way of seeing where the important information which determines the interlayer structure is hidden in the associated x-ray diffraction pattern.

The direct inversion method is used to extract the film structure and study the evolution of this structure during the crossover from two to three-dimensions [2]. Aside from intrinsic interest in the structure of FSLC films, these films are good sys-

tems to study dimensional crossover since they are substrate free and their thickness can be easily varied from two to thousands of molecular layers. Previous structural studies of FSLC films have focused on the *intralayer* order of the films, but the evolution of the *interlayer* order has just now begun to be studied in detail [22, 23]. The direct inversion and forward modeling techniques have been used to answer the following questions about FSLC films: What is the interlayer structure of these LC films? How important are the inherent smectic fluctuations to the interlayer structure of these films? How does the structure of the film change with film thickness? How does the surface tension, the presence of frozen surface layers, and the finite-size of the film influence the structure? What is the interplay between the Landau-Peierls instability and the surface tension in FSLC films?

3.3 X-ray Diffraction Pattern from Thin Smectic Films

LC phases have symmetries and order intermediate between isotropic liquids and fully ordered crystals [3]. Because of this "intermediate dimensionality", the effects of thermal fluctuations on the smectic-A phase, in particular, is very unusual. For a 3-dimensional (3D) crystal, the kinematic x-ray scattering intensity consists of a lattice of delta function Bragg peaks, at reciprocal lattice vectors corresponding to the long-range order of the 3D crystal. These Bragg peaks are connected by crystal truncation rods (CTR's) which reflect the Fourier transform of the surface termination shape-function. The smectic-A phase, which has divergent fluctuations on all length scales, exhibits a scattering pattern characterized by algebraic singularities instead of Bragg peaks. The smectic-A phase is at lower marginal dimensionality and has quasi-long-range layer order. Thermal fluctuations in bulk smectic-A material cause a slow algebraic decay of the interlayer density-density correlation function. In the thermodynamic limit, these divergent thermal fluctuations are predicted to destroy the long-range layer order in this periodic one-dimensional system [101, 102], but the logarithmic growth of the thermal fluctuations with the size of the system is so slow that it has been difficult to observe the destruction of this long-range order directly [103].

Bulk smectic-A's have a highly localized x-ray scattering pattern dominated by singular algebraic peaks with wave vectors, $q_n = 2\pi n/d$, set by the layer spacing, d, of the LC molecules. These materials are so highly disordered that the interlayer

diffraction pattern exhibits at most only a few harmonics and for many materials the second harmonic is very weak or unobservable: $I(002) < 2\times10^{-7} I(001)$ [104, 105, 106]. Therefore, for these LC's the electron density, $\rho(z)$, has only a few significant Fourier components, $\rho(z) = \rho_o + \rho_1 \sin(q_o z) + \rho_2 \sin(2q_o z)$ with $\rho_2 < 10^{-3}\rho_1$, and the sine wave density modulation is very pure. This has led to suggestions that the smectic phase contains only 'statistical layers' [107]. However, the measured FSLC film densities described in this chapter show that distinct smectic layers exist in these films. The nearly sinusoidal density is not due to statistical layering, but is a result of long-wavelength hydrodynamic fluctuations which disorder the layers and decrease the scattering intensity with increasing momentum transfer, q.

The diffraction pattern of thin FSLC films is rich with information spread out in reciprocal space due both to the finite-size broadened diffraction peaks and to the 'N-slit' subsidiary maxima. The scattering from finite thickness smectic-A LC films is quite different from bulk smectic-A since the layer fluctuations are limited by the size of the sample and the algebraic singularities are cut-off [108]. Film scattering also exhibits the characteristic 'N-slit' interference due to the N LC layers in the film that continuously distribute the scattering in reciprocal space. This interference modulates the crystal truncation rod (CTR) near $q = 0$ and is closely related to the characteristic 'N-slit' optical interference patterns. In addition, for all systems at finite temperature, there are Debye-Waller factors due to the thermal fluctuations of the individual molecules in the system, that systematically decrease the height of the diffraction peaks with increasing q. Enhanced surface order is clearly displayed in the interlayer structure of FSLC films. This enhanced order is probably due to surface tension quenched fluctuations and to the presence of surface frozen phases. The effects of surface tension, finite-size, and surface-frozen monolayers on the structure of these films is the subject of this study, and has only recently begun to be appreciated [22, 26].

The origin of the important features of the thin film diffraction pattern, which is intermediate between two- and three-dimensional crystallography can be seen by considering the evolution of the diffraction pattern during buildup of a thin film from a monolayer sheet. For a single layer of atoms, localized in the $\hat{z}$ direction, the scattering intensity is sharp in the two in-plane directions and has diffuse streaks of scattering, or Bragg rods, perpendicular to the surface. The Bragg rods from a 2D monolayer

of atoms and the crystal truncation rods of an ideally bulk terminated surface have very similar appearances; both have a scattering intensity corresponding to about one monolayer of scatterers and both are rods perpendicular to the surface. However, their functional forms are quite different since the CTR is the Fourier transform of the surface termination while the 2D Bragg rod is the Fourier transform of the atomic form factor. As the 2D layer becomes thicker, the rods become modulated and the peaks of the modulations become more intense as an 'N-slit' interference pattern develops. As will be seen, the scattering intensity of the mid-zone subsidiary maxima remain about the same and the subsidiary maxima eventually develop into the CTR. This development is illustrated for film thicknesses $N = 3$ to $N = 8$ in Fig. 3.1 which plots the 'N-slit' intensity function $\mathrm{I} = \sin^2(Nx)/\sin(x)$. As can be seen, there are $N - 2$ subsidiary maxima between each primary maxima. With increasing thickness, the primary maxima of the 'N-slit' interference pattern narrow and eventually evolve into the Bragg peaks. As described below, the phase of these 'N-slit' interference patterns jumps by π at each of the zeros of this pattern. This important fact will be used to 'phase' the scattering amplitude derived from the measured LC film scattering intensity.

The measured scattering pattern for a five-layer smectic-G film, which is quite different from bulk 3D crystal and bulk smectic-A scattering with the momentum transfer, q_z, along the direction perpendicular to the smectic layers, is illustrated in Fig. 3.2. The measured scattering along the specular rod (perpendicular to the surface of the film) is similar to the optical 'N-slit' interference patterns shown in Fig.3.1. Note that the primary maxima are twice as wide as the subsidiary peaks and, for the five-layer film shown in Fig. 3.2, the primary maximum at $q_z = 0.22$ is split by the first zero of the molecular form factor. The origin of the different features in this diffraction pattern is described in detail later in Sec. 3.5.

3.4 The Phase Problem in X-ray Diffraction

The magnitudes of the structure factors, $|\mathrm{F}_{hkl}|$, can be derived from the measured x-ray diffraction intensities, but the phase angles, φ_{hkl}, cannot be directly determined. The electron density can be easily calculated from the complex structure factors, $\mathrm{F}_{hkl} = |\mathrm{F}_{hkl}|e^{i\varphi_{hkl}}$, once both the magnitude, $|\mathrm{F}_{hkl}|$, and the phase, φ_{hkl}, are known for each reflection hkl. The inability to derive the electron density from the measured x-

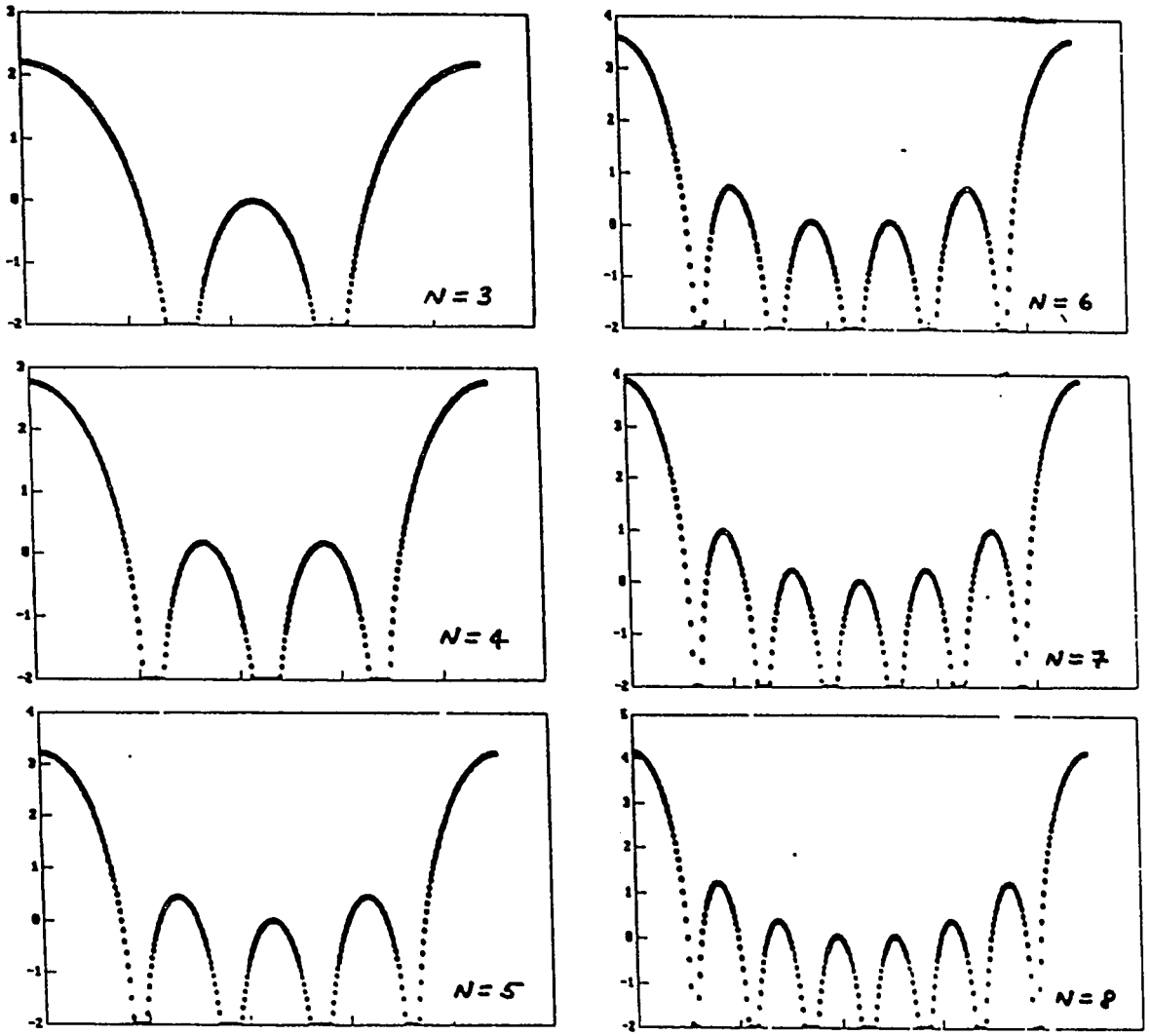

Figure 3.1: 'N-slit' Interference Pattern Development. Plots of 'N-slit' interference patterns for film thicknesses $N = 3$ to $N = 8$. There are $N - 2$ subsidiary maxima between primary maxima and with increasing thickness, the primary maxima of the 'N-slit' interference pattern narrow and eventually evolve into Bragg peaks while the subsidiary maxima evolve into the specular crystal truncation rod.

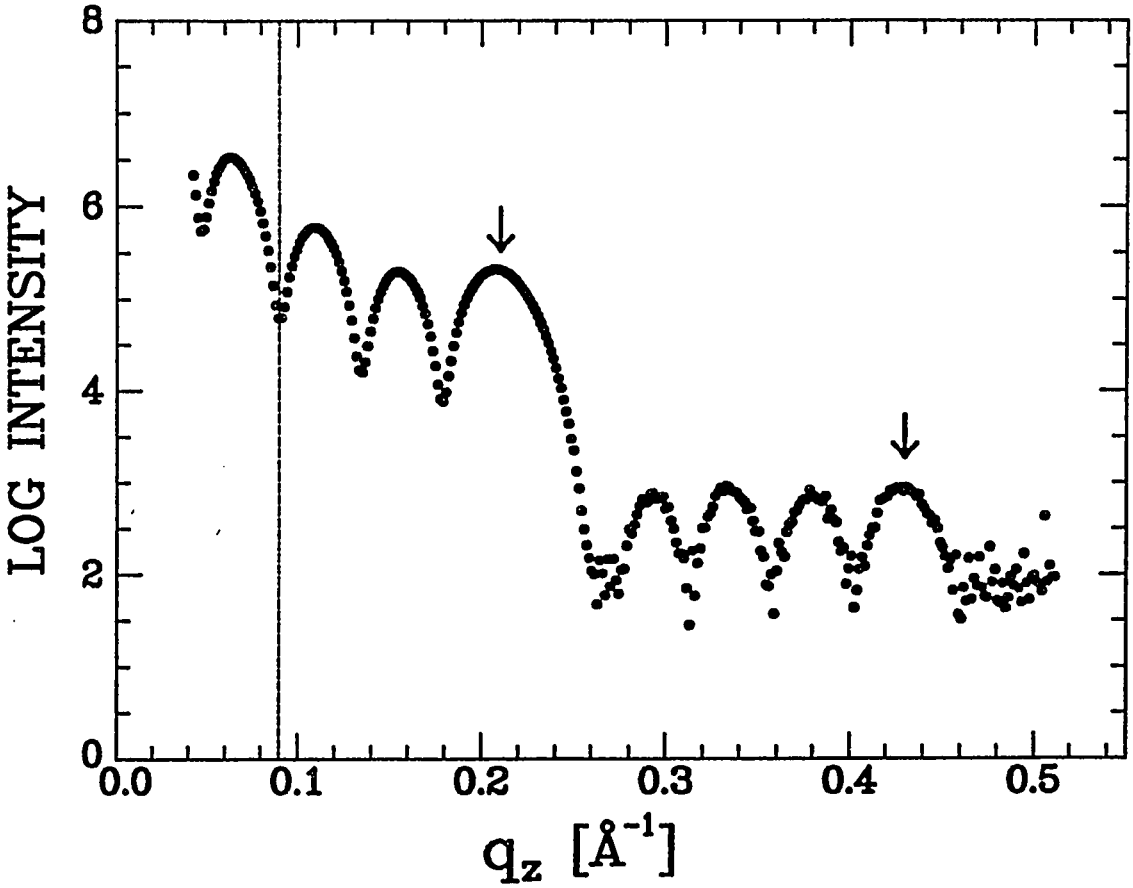

Figure 3.2: Representative LC Film X-ray Scattering Intensity. Measured x-ray diffraction data from a five-layer smectic-G film. Plotted on a logarithmic scale, the two primary maxima, at $q_z = 0.22$ and 0.44, are indicated by the arrows. This mosaic averaged scan displays the characteristic thin film 'N-slit' interference pattern. The vertical dashed line indicates the lower limit in q_z of the measured data used for density determination with the forward model analysis. The scattering intensity was not measured all the way to $q_z = 0$ since at low angles, the x-ray beam overflows the film and is eventually blocked by the film holder.

ray scattering intensity is called the crystallographic phase problem and is the central problem in structure determination using diffraction. In 1915, Bragg [109] pointed out that a crystal is a periodic assemblage of atoms that can be represented by a 3D Fourier series, in which the Fourier coefficients are related to the orders of diffraction. In this direct correspondence, the moduli of the structure factors are proportional to the scattering intensity of the observed x-ray reflections, whereas the phases contain the directional information. The φ_{hkl}'s indicate the relative phase of the scattered waves from any particular set of planes. The scattering intensity from a bulk crystal is restricted to reciprocal lattice points $\mathbf{h} = (hkl)$ which satisfy the Laue conditions. In the kinematic approximation, the structure factor F_{hkl} for a unit cell of volume V, is given by,

$$\mathrm{F}_{hkl} \sim V \int_0^1 \int_0^1 \int_0^1 \rho(x,y,z) e^{2\pi i(hx+ky+lz)} dx dy dz. \tag{3.1}$$

So F_{hkl} can be calculated for any Bragg point $\mathbf{h}$, given the electron density $\rho(x,y,z)$. The traditional experimental problem is the inverse problem: determining the electron density given the measured x-ray scattering intensity. The electron density is given by the Fourier series

$$\rho(x,y,z) \sim \frac{1}{V} \sum_{hkl} F_{hkl} e^{-2\pi i(hx+ky+lz)}. \tag{3.2}$$

Consequently, as noted above, the electron density can be calculated given the complex structure factors, $\mathrm{F}_{hkl} = |\mathrm{F}_{hkl}| e^{i\varphi_{hkl}}$. Since x-ray experiments involving incoherent sources can measure only the scattering intensity, $\mathrm{I}_{hkl} \propto |\mathrm{F}_{hkl}|^2$, the phases, φ_{hkl}, which, in general, can have any value between 0 and 2π, are not directly observable. This crystallographic phase problem remains the central problem in x-ray structural analysis. In the case of centrosymmetric crystals without anomalous scattering contributions, the problem is considerably easier since the phase is limited to either 0 or π and the structure factors are given by $\mathrm{F}_{hkl} = \zeta_{hkl} |\mathrm{F}_{hkl}|$, with $\zeta_{hkl} = \pm 1$. In the next section, the ζ's will be determined explicitly from the known components of the thin film diffraction pattern.

3.5 Solution of the 1D Phase Problem for Thin Films

The direct inversion analysis described in this chapter is a demonstration of direct phase determination for a one-dimensional centrosymmetric thin film. The direct in-

version method is a completely new method for solving the phase problem that does not depend on the scattering intensity relationships between different Bragg peaks used by "direct methods", but instead uses the directly measured zeros of the primary and subsidiary maxima of the structure factor to determine the phase of each 'Bragg peak' (primary maximum) and of each subsidiary maximum. Many crystal structures have been solved over the years with x-ray diffraction using different techniques to overcome the phase problem. The earliest x-ray crystallographers attempted to solve the phase problem by trial-and-error. Using additional information about the crystal symmetry, some simple structures were deduced [110]. In the 1930's, the Patterson [111] function and isomorphous replacement methods allowed the solution of more complicated structures, once the coordinates of a few heavy atoms were known. Since, in principle, if enough reflections are measured, the problem is overdetermined, modern "direct methods" [112] were developed in an attempt to derive the phases of the structure factors mathematically using only the measured intensities. Early direct methods relied on using the combination of Harker-Kasper [113] inequalities and the non-negativity of the density to obtain determinant inequalities and probabilistic relationships between the structure factors. For centrosymmetric crystals, sign relationships exist between the normalized structure factors. With modern computers it has been possible to use numerical refinement and maximum-entropy methods. Analysis of macromolecular structures has succeeded because a large number of reflections can be collected, and because direct methods can be combined with the techniques of isomorphous replacement and anomalous scattering. In 1964, the first direct method solution of a non-centrosymmetric structure was made using a symbolic addition procedure [114]. In 1985 H. Hauptman and J. Karle received the Nobel prize in chemistry in recognition of the importance of these techniques and their contributions to them [115].

The interlayer electron density, $\rho(z)$, is the 1D projection of the 3D electron density, $\rho(\vec{r})$, onto the axis normal to the film, i.e., the projection of $\rho(\vec{r})$, onto $\hat{z}$, the direction normal to the smectic layers, produces $\rho(z)$. By the central-slice theorem [116], the 1D Fourier transform of $\rho(z)$ corresponds to the 3D Fourier transform of $\rho(\vec{r})$ evaluated along q_z, with the scattering amplitude $\mathrm{S}(q_z) \equiv \mathrm{S}(0,0,q_z)$ given by

$$\mathrm{S}(q_z) \sim \int \rho(z) e^{-iq_z z} dz. \tag{3.3}$$

At the x-ray wavelength used in these experiments, $\lambda = 1.54$ Å, the LC molecules in the film do not have large anomalous scattering contributions and the one-dimensional electron density $\rho(z)$ is therefore essentially real and non-negative. The density is also centrosymmetric since the two surfaces of the film are equivalent and the LC molecules in each layer are expected to have equal probability of orientation along and opposite the director. Therefore $S(q_z) = S(-q_z)$.

The 1D phase problem can be solved explicitly for thin centrosymmetric films because all the zeros in the measured scattering intensity are visible and the origin of all these zeros, which are the phase switching points, are known. A thin smectic LC film exhibits the characteristic 'N-slit' interference pattern with primary maxima instead of Bragg peaks at the locations corresponding to the smectic layer periodicity [117]. The underlying periodicity of an N-layer smectic film is described by the center-of-mass density, $CM(z)$, which is the convolution of the layer disorder, $G_i(z)$, with the 'N-slit' interference pattern. The layer disorder for the i^{th} layer, $G_i(z)$, with width, σ_i, represents the hydrodynamic and Debye-Waller fluctuations, and the static disorder of the center-of-mass positions of each layer. The electron density, $\rho(z)$, is the convolution of the center-of-mass density with the symmetrized molecular density, $MD(z, \phi)$, where each LC molecule is tilted at angle ϕ. The LC molecules in all the phases studied here are tilted with respect to the layer normal. The electron density is therefore given by,

$$\rho(z) = \int CM(z')MD(z - z')dz' \equiv CM(z) \otimes MD(z, \phi), \tag{3.4}$$

with

$$CM(z) = \sum_{n=1}^{N} [\delta(z - nd) \otimes G_i(z)]. \tag{3.5}$$

Because the film is centrosymmetric, $CM(z)$ must also be centrosymmetric. The shape of $CM(z)$ and the shape and width, σ_i, of each surface layer probability distribution, $G_i(z)$, describe the structure and fluctuations of the film. Comparisons of the various G_i throughout the film reveal the detailed behavior of the structure. In the forward model, all the $G_i(z)$ were taken to be Gaussian and therefore symmetric with equal areal density. The direct inversion method will check this assumption since this symmetry and areal density assumption are not built in. The combination of Eq. 3.3

and Eq. 3.4 gives the scattering intensity for a smectic film,

$$|\mathrm{S}(q_z)|^2 \propto \frac{\sin^2(\frac{1}{2}Nq_zd)}{\sin^2(\frac{1}{2}q_zd)}) \cdot \mathrm{MFF}^2(q_z) \cdot \tilde{\mathrm{G}}_i^2(q_z). \tag{3.6}$$

where the molecular form factor $\mathrm{MFF}(q_z)$, is the Fourier transform of MD(z,ϕ) denoted $\mathrm{MFF}(q_z) = \widetilde{\mathrm{MD}}(z,\phi)$. This scattering amplitude, $\mathrm{S}(q_z)$, is clearly the combination of the 'N-slit' interference pattern, the molecular form factor $\mathrm{MFF}(q_z)$, and the fluctuation/disorder factor for each layer $\tilde{\mathrm{G}}_i(q_z)$. Understanding that the scattering intensity is real and consists of these three components allows the explicit assignment of the phases to $|\mathrm{S}(q_z)|$. Inverting this (via Eqn. 3.2) produces model-independent densities that do not assume any particular functional form for the G_i's. If variations in the smectic layer spacing produced by, e.g., variations in the tilt angles, are allowed, $\delta(z - nd)$ is replaced with $\delta(z - z_i)$ and $\mathrm{MD}(z,\phi)$ with $\mathrm{MD}_i(z,\phi_i)$ where $z_i = \sum_{i=1}^{j} d\cos(\phi_i)$. In this case,

$$\rho(z) = \sum_{i=1}^{N} \mathrm{CM}_i(z) \otimes \mathrm{MD}_i(z,\phi_i). \tag{3.7}$$

This degree of freedom was needed in the forward model density to fit the measured smectic-I/C scattering intensity. The direct inversion molecular density deconvolution procedure does not allow $\mathrm{MD}_i(z,\phi_i)$'s with a different molecular tilts, ϕ_i, for each layer, i, in the film as were used in the forward model for the smectic-I/C data. However, as will be seen, the average molecular tilt angle, ϕ is well determined, and the qualitative shape of the final CM(z) is quite insensitive to small variations in the average molecular tilt. This was checked by comparing the resulting center-of-mass densities derived by deconvolution using $\mathrm{MD}(z,\phi)$'s with different values of the average molecular tilt angle, ϕ.

To show explicitly the pattern of phase jumps at the zeros of the 'N-slit' interference pattern which is an important component of the thin film scattering amplitude, we consider a system of stacked 2D layers of coherently scattering 'point atoms' without the complication of form-factors and Debye-Waller fluctuations. For a parallelepiped crystal with N_1, N_2, and N_3 unit cells, each with lattice constant a_1, a_2, and a_3, the scattering intensity is proportional to,

$$|\mathrm{S(q)}|^2 = |\sum_{n_1=1}^{\mathrm{N}_1} e^{in_1q_1a_1} \sum_{n_2=1}^{\mathrm{N}_2} e^{in_2q_2a_2} \sum_{n_3=1}^{\mathrm{N}_3} e^{in_3q_3a_3}|^2. \tag{3.8}$$

When N_1, N_2, and N_3 are large, S(q) is sharply peaked at the Bragg points which satisfy the three Laue conditions: $q_1a_1 = 2\pi h$, $q_2a_2 = 2\pi k$, and $q_3a_3 = 2\pi l$ (h,k,l: integer). This defines the reciprocal lattice with peaks having scattering intensity $(N_1N_2N_3)^2$. Doing the sums in the above expression yields,

$$|S(q)|^2 = \frac{\sin^2(\frac{1}{2}N_1q_1a_1)}{\sin^2(\frac{1}{2}q_1a_1)}\frac{\sin^2(\frac{1}{2}N_2q_2a_2)}{\sin^2(\frac{1}{2}q_2a_2)}\frac{\sin^2(\frac{1}{2}N_3q_3a_3)}{\sin^2(\frac{1}{2}q_3a_3)}. \tag{3.9}$$

If the Laue condition is relaxed for $q_3 \equiv q_z$ then for N_3 large,

$$|S(q_z)|^2 = (N_1N_2)^2\frac{\sin^2(\frac{1}{2}N_3q_za_3)}{\sin^2(\frac{1}{2}q_za_3)} \tag{3.10}$$

and the scattering amplitude, $S(q_z) \propto \frac{\sin(\frac{1}{2}N_3q_za_3)}{\sin(\frac{1}{2}q_3a_3)}$, changes sign at each zero crossing. Since this is a real function, the phase of the 'N-slit' interference pattern jumps by π at each of the zeros of the scattering amplitude.

Crystal truncation rods and the 1D 'N-slit' interference patterns seen experimentally from thin films are intimately related. The functional form of the CTR is important because any roughness of the LC film-vapor interface can be detected by comparing the measured scattering intensity with the functional form from an ideally terminated surface. Eq. 3.10 illustrates the origin of these diffuse streaks of scattering intensity, normal to the crystal surface, which make up the CTR [118] since,

$$\lim_{N_3\to\infty}|S(q_z)|^2 \propto (N_1N_2)^2\frac{1}{\sin^2(\frac{1}{2}q_za_3)}. \tag{3.11}$$

The characteristic fall off of the CTR is determined by the abruptness of the crystal termination. In a system of stacked 2D layers, the finite series of delta-functions representing the layer positions can be thought of as the product of an infinite series of delta-functions with the crystal termination function, $s(z)$. In reciprocal space, this results in the convolution of the crystalline Bragg peaks with the Fourier transform of $s(z)$ and determines the fall-off around each Bragg peak and near $q_z = 0$. For an ideally terminated crystal, $s(z)$ is a step function which results in $\frac{1}{q_z^2}$ tails for each Bragg peak due to the missing upper half plane. Near $q_z = 0$ the scattering for a perfectly terminated surface falls off as $\frac{1}{q_z^4}$ due to the additional scattering volume correction and Lorentz factor. If the surface is terminated more gradually, the CTR falls off more quickly with q_z. The measured scattering out to the first harmonic is shown

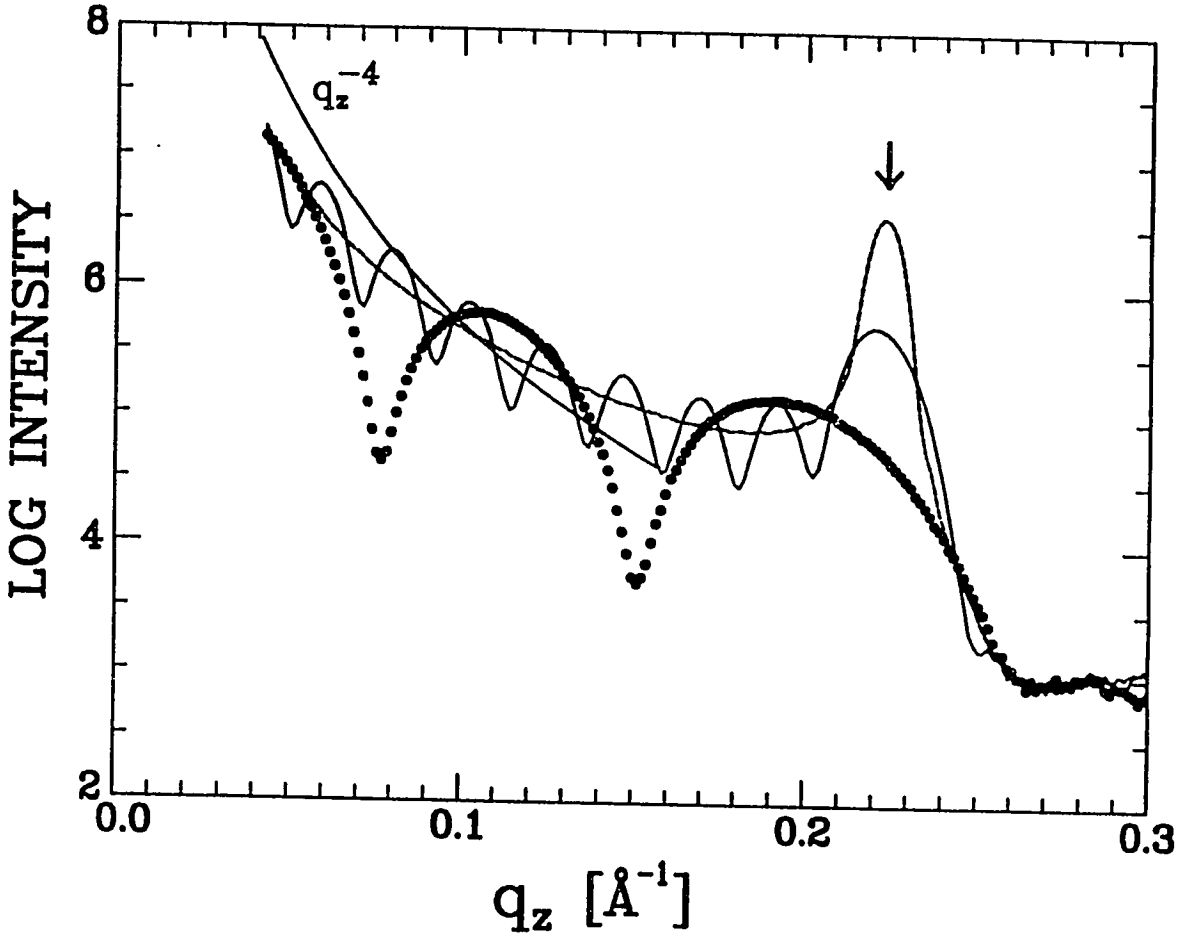

Figure 3.3: Crystal Truncation Rod Development. Crystal truncation rod development throughout the first harmonic region illustrated by the measured scattering intensity from $N = 3$ (dots), 10 (solid line) and 35-layer (dashed line) smectic-G films. The first harmonic indicated by the arrow appears shifted to lower q_z for the three-layer film due to the molecular form factor zero. For films thicker than about 21 layers, the finite resolution of the spectrometer does not allow the subsidiary maxima to be resolved.

for three different thickness films in Fig. 3.3. Here, the crossover between the 'N-slit' interference pattern and Bragg peaks is illustrated along with the development of the CTR. The solid line indicates the $\frac{1}{q_z^4}$ factor from the sharply terminated interface convolved with the instrument resolution. The $\frac{1}{q_z^4}$ factor falls somewhat slower than the data indicating perhaps a small amount of surface roughness. More careful analysis is needed to quantify this result. The evolution of the CTR with increasing film thickness exhibits the increased spatial frequency of phase jumps as the films become thicker. From this figure, one can see that if the number of subsidiary maxima and the phase jump at each zero crossing point are known, the phase of the Bragg peaks, for even a thick sample, can be determined.

The constituent features of the measured scattering intensity, $M(q_z)$, shown in Fig. 3.4a can be recognized by comparing $M(q_z)$ with the component parts of Eq. 3.6 illustrated in Fig. 3.4b. The components of the best-fit forward model scattering intensity are illustrated by solid lines indicating the 'N-slit' interference factor, the $MFF^2(q_z)$ factor, and the $\tilde{G}^2$ factor. This best-fit forward model scattering intensity which passes through the five-layer smectic-G data will be discussed in detail later (see Fig. 3.6). Fig. 3.4 compares the measured scattered intensity with the best-fit forward model scattering intensity from Eq. 3.6. The overall scattering intensity falls off with increasing q_z due to the hydrodynamic fluctuations, Debye-Waller fluctuations, and disorder factor $\tilde{G}(z)$. Only a few diffraction orders are intense enough to be measured in these LC films and all the zeros in the components which make up the diffraction pattern are easily identified in the measured scattering intensity and therefore the points where the scattering amplitude changes sign are obvious. Notice that $\tilde{G}^2$ does not introduce any zeros in the scattering intensity. As can be seen in Fig. 3.4, the zeros in the scattering intensity correspond to the zeros of the $MFF(q_z)$ and of the 'N-slit' interference factor. The $MFF(q_z)$ for this thickness film produces a zero just after the first primary maximum. Since the scattering amplitude is real and even, $S(q_z) = \zeta(q_z)|S(q_z)|$, where the phase factors, $\zeta(q_z) = \pm 1$ are simply the product of those from the 'N-slit' interference pattern and the molecular form factor. The phase factors can be determined by inspection since $\zeta(q_z)$ only changes sign at the zero crossings of the scattering amplitude starting with the forward direction where $\zeta(q_z = 0) = 1$. For all the intensities reported in this thesis, the 'N-slit' interference pattern zeros and the molecular form factor zeros did not exactly coincide, allowing

Figure 3.4: Measured X-ray Scattering Intensity and the 'N-slit' Interference Pattern. The origin of the diffraction pattern zero's are seen comparing the measured scattering intensity with its component features. (a) Shows a logarithmic plot of the measured scattering intensity from a five-layer smectic-G film. (b) is an over-plot of the pieces which comprise the overall thin film scattering pattern. This plot consists of the '5-slit' pattern with $d = 31.0$ Å and $\phi = 21°$ (solid-line), the molecular form factor squared $|MFF(q_z)|^2$, with $\phi = 21°$ (dashed line), and Debye-Waller-like disorder factor with $\sigma = 3.0$ Å(dotted line). The zero's in the scattering pattern are due to the product of the 'N-slit' interference pattern zeros with those from the molecular form factor. The Debye-Waller factor induces only an overall decrease in scattering intensity over this region of reciprocal space.

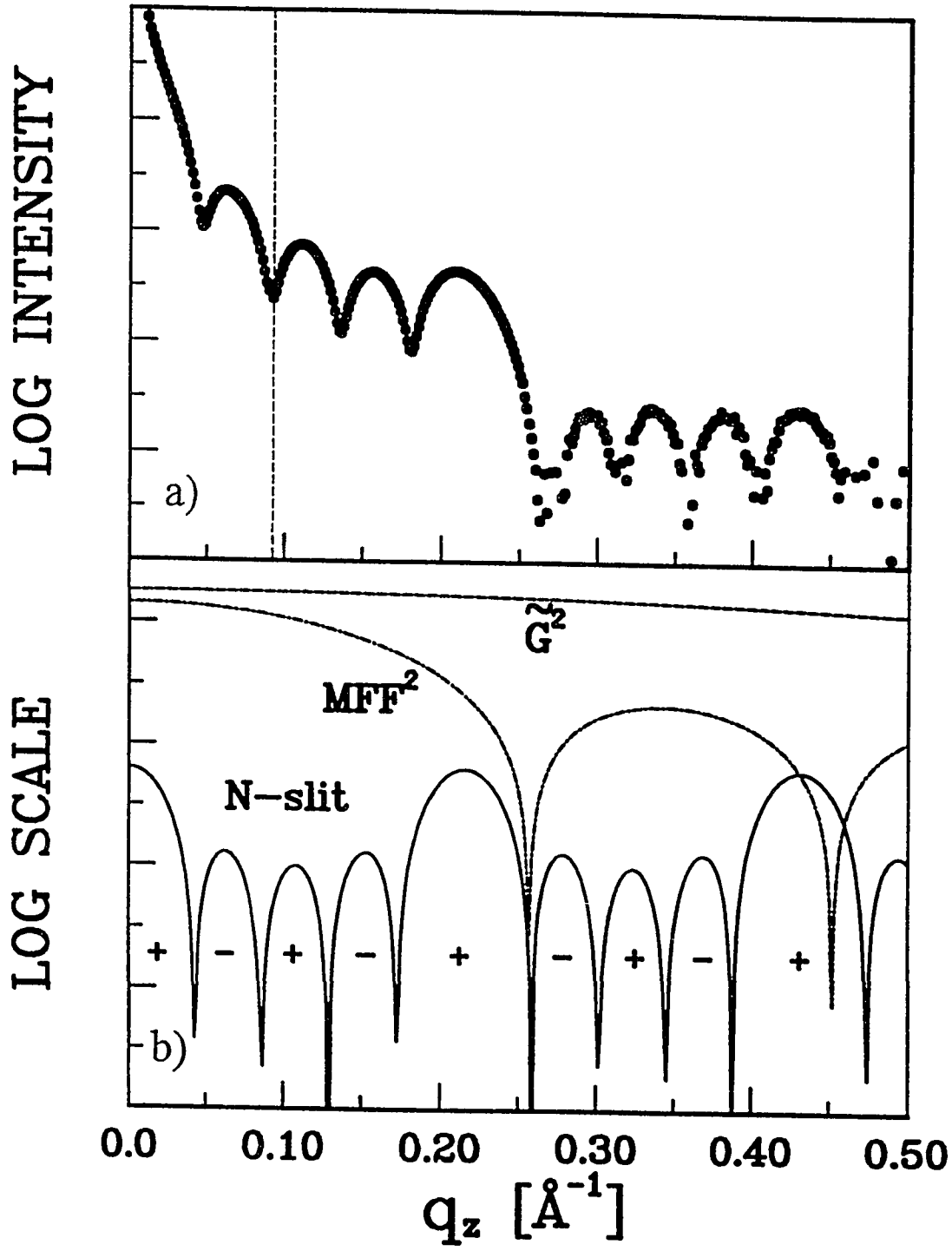
LOG INTENSITY
a)
LOG SCALE
G^2
MFF^2
N–slit
+ − + − + − + − +
b)
0.0
0.10
0.20
0.30
0.40
0.50
q_z [Å^{-1}]

the scattering intensity to be hand-phased by inspection. In this case, the $\zeta(q_z)$'s alternate in sign as indicated in Fig. 3.4b. If the molecular form factor and the 'N-slit' interference pattern zeros were to coincide then the phase would jump by 2π at this point and $\zeta(q_z)$ would remain the same sign over the next subsidiary maxima region then continue again to alternate in sign.

3.6 Forward Model Analysis

The measured scattering intensity used here to demonstrate the direct inversion procedure has been analyzed previously using forward modeling techniques [22, 26]. Fig. 3.5 shows a schematic illustration of the forward model used to determine the structure of the film. In this figure, the 7O.7 LC molecules, aligned in layers i, are represented by rectangles positioned with their long axes tilted at an angle ϕ_i with respect to the layer normal direction $\hat{z}$. Both the thermally excited, long wavelength hydrodynamic fluctuations of the layers and the static equilibrium layer positions perpendicular to $\hat{z}$ are shown. The molecular center-of-mass distribution in each layer is parameterized by a Gaussian distribution $G_i(z)$ with width, σ_i. This forward model for the interlayer density, described by Eq. 3.4 for the smectic-G films and Eq. 3.7 for the smectic-I/C films, was fit to the measured scattering intensity to obtain the best-fit CM(z) for both the crystalline smectic-G and the fluid smectic-I/C films. Results from this model indicate that crystalline smectic-G films have a uniform tilt, large fluctuation amplitudes, and very small interlayer fluctuation profiles. The fluid smectic-I/C films exhibit both layer fluctuation and molecular tilt angle profiles which have systematic variations with film thickness. For both phases and for all films, the Gaussian fluctuation width, σ_i, is smallest at the surfaces of the film and reaches a maximum at the film center. For the smectic-I/C films, the tilt angle is maximum at each surface and minimum at the center of the film. The finite size, surface tension, and presence of frozen surface layers all contribute to the quenching of the smectic-layer hydrodynamic fluctuations. For the smectic-I/C films, both the quenched surface-layer fluctuations and the surface-frozen smectic-I monolayers may induce a tilt profile into the interior layers of the film. The resulting thickness dependent layer fluctuations, G_i, and molecular tilt angles, ϕ_i, for layers $i = 1, 2, ..., N$, are described by a single set of parameters dependent only on the film thickness, surface tension, and surface and interior elastic constants. The molecular tilt profile agrees with a simple

elastic theory and the layer fluctuation profile agrees with a calculation of the hydrodynamic layer fluctuations [119, 26]. In Sec. 3.9, detailed comparisons are made between the densities obtained from the forward model and those obtained using the direct inversion analysis. These comparisons are important to determine where in the diffraction pattern the information, which determines the interlayer structure, is contained.

3.7 Experimental Method

The X-ray scattering measurements were made using a 0.3 mm x 0.03 mm beam of copper K_α radiation from a Rigaku rotating anode x-ray generator operated at 4.2 kW and a triple axis spectrometer with graphite monochromator and analyzer crystals. The monochromator and analyzer slits were set narrower than the graphite acceptance to increase the instrumental resolution and to prevent the incident beam from illuminating the film holder. Large FSLC films (8cm x 1.25 cm) of 4-(n-heptyl)benzylidene-4-(n-heptyl)aniline (7O.7), were used in the experiment. The liquid crystal 7O.7 was chosen since its phase diagram versus film thickness has been well characterized [6, 8, 9, 93]. The x-ray intensities were measured at two temperatures, 40°C and 72.5°C, for film thicknesses: $N = 3, 4, 5, 6, 7, 8, 10, 15$, and 35 layers. At these two temperatures, the LC phase is independent of the film thickness. At 40°C, the films are in a crystalline smectic-G phase. At 72.5°C, the films are in a stratified phase denoted smectic-I/C – a phase with two surface monolayers of hexatic smectic-I on a tilted liquid smectic-C interior.

The Fourier transform is intimately related to the physical imaging process and how information is extracted from x-ray diffraction patterns [120]. Imaging theory describes image formation in terms of two sequential diffractions which correspond mathematically to sequential Fourier transforms [121]: the first transform produces the initial diffraction pattern due to the diffraction of the incident beam by the object, while the second transform results from the recombination of the scattered wave into the interference pattern responsible for the image. For x-ray scattering, it is necessary to compute the electron density from the measured initial scattering intensity using a Fourier transform since the index of refraction at these wavelengths is nearly equal to 1 for all materials and the diffracted beam cannot be easily focused physically. All Fourier transforms were done using a fast Fourier transform algorithm (FFT) routine

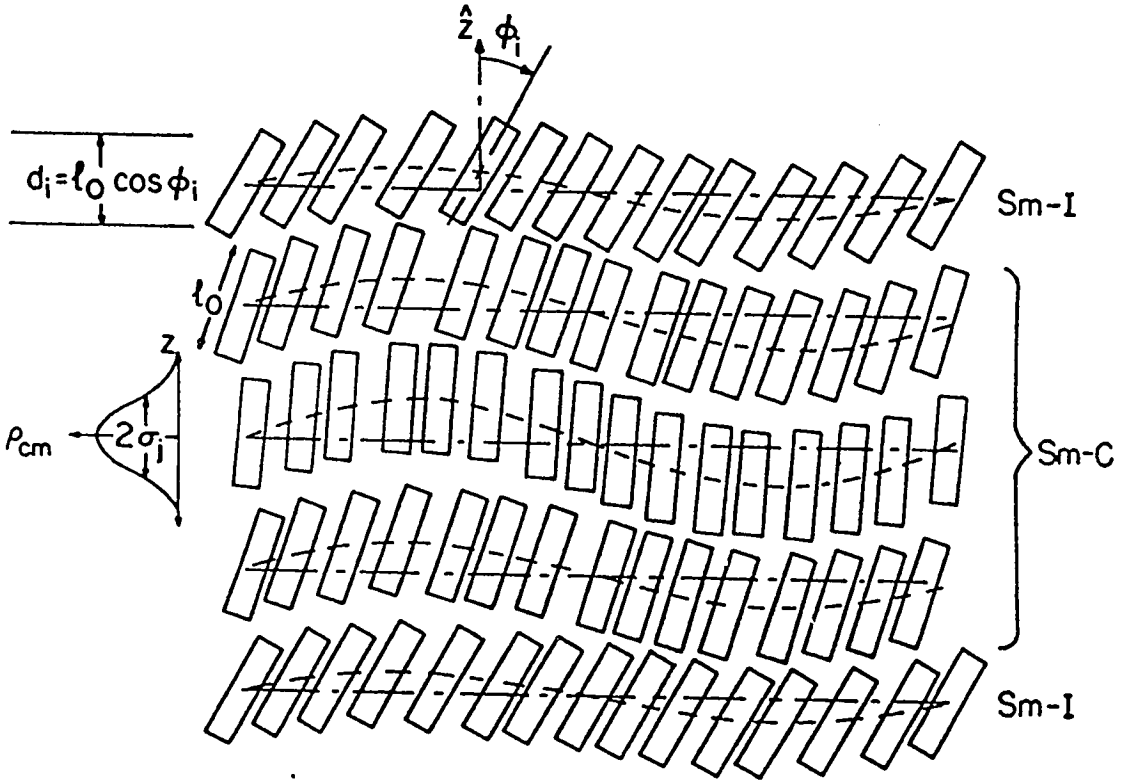

Figure 3.5: Forward Model Illustration. Schematic illustration of the forward model parameters for a five-layer smectic-I/C film. The two surface layers are smectic-I and the interior layers are smectic-C. The mean fluctuation amplitudes, G_i, and tilt angles, ϕ_i, are indicated as well. The static equilibrium layer positions are indicated by the parallel lines perpendicular to the $\hat{z}$ direction. The thermally excited, long wavelength hydrodynamic fluctuations of the layers are illustrated also by dashed lines indicating the instantaneous molecular center-of-mass positions.

[122]. The data arrays had 4096 points with at least 1500 zeros on both ends of the data to avoid aliasing.

3.8 Direct Inversion Analysis Steps

The results for all film thicknesses and temperatures were obtained using the same steps and the complete results are shown in Sec. 3.9. The direct inversion method used to extract the electron density, $\rho(z)$, and the center-of-mass density, CM(z), from the measured intensities, $I(q_z)$, is illustrated in this section for a single data set, the five-layer smectic-G data. The direct inversion analysis consists of the following six steps: 1) Adding a $q_z = 0$ patch to the experimental data in the unmeasured region near $q_z = 0$ to produce the extended measured scattering intensity, M(q_z), which begins at $q_z = 0$. 2) Removing the instrumental broadening from $M(q_z)$ to produce the intrinsic scattering intensity, I(q_z). 3) Making scattering corrections and taking the square-root of I(q_z) to give the magnitude of the scattering amplitude, |S(q_z)|. 4) Hand phasing |S(q_z)| to give the scattering amplitude, $S(q_z)$. 5) Back-transforming S(q_z) to give the electron density, $\rho(z)$. 6) Removing the molecular form factor from $\rho(z)$ to give the center-of-mass density, CM(z).

3.8.1 Adding $q_z = 0$ Patch to the Experimental Scattering Intensity

The scattering intensity from the film was measured in the region from $q_z = 0.04$ to 0.48Å^{-1}. The measurements stopped after the second harmonic where the scattering signal becomes too small to measure with a rotating anode x-ray source. The scattering intensity below $q_z = 0.09$ Å^{-1} was not measured reliably due to the occlusion by the LC film holder of the incident x-ray beam, which spreads out on the film at low angles. The FFT routines used in the direct inversion analysis require continuous information all the way to $q_z = 0$. Since experimental data was not measured in this low q_z region, a forward model scattering intensity was substituted place of the missing experimental scattering intensity. The model used to represent the scattering intensity in this region was based on a forward model scattering intensity which produced a good fit to the data in the measured region. This model was placed throughout the region from $q_z = 0$ to $\sim 0.09\text{Å}^{-1}$ to make a smooth transition to the measured data from $q_z \sim 0.09$ to 0.48Å^{-1} – the $q_z = 0$ patch joins the measured scat-

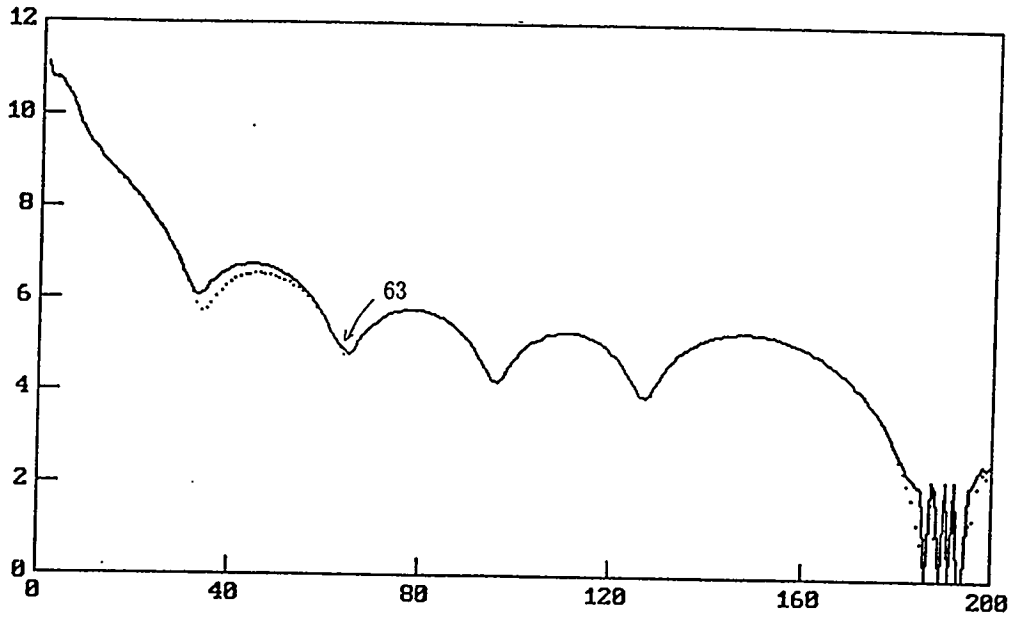

Figure 3.6: Forward Model Used for the $q_z = 0$ Patch. Plot of the forward model scattering intensity (solid line) used for the patch in the region $q_z < 0.09\text{Å}^{-1}$ for the five-layer smectic-G film. This was the basis of the model used for all forward model densities presented in Sec. 3.11. The measured scattering intensity (dotted line) is significantly less than the forward model calculation before point 63 due to the shadowing of the beam by the LC film holder.

tering intensity at the nearest zero to this point in the scattering intensity. Fig. 3.6 shows this forward model scattering intensity and the measured scattering intensity up to the first harmonic. The arrow indicates the point at which the model scattering intensity joins the measured scattering intensity. This model, and its analogues for the other thicknesses films, fit the measured scattering intensity quite well, and were used to obtain the direct inversion densities shown in Sec. 3.11. The q_z region over which the forward model scattering intensity was substituted must be large enough so that the resulting density is not affected by the shadowing of the incident beam by the LC film holder. The measured scattering intensity in the region $q_z < 0.09$ is much less than the forward model scattering intensity because the film is shadowed by the film aperture. As will be discussed in Sec. 3.10, the inclusion of this deficit into $M(q_z)$ results in significant changes in the shape of the derived $\rho(z)$. The $q_z = 0$ patch extends to $q_z \sim 0.09$ since after this point, additional length of the $q_z = 0$ patch had no distinguishable difference in the resulting density. For all thickness films the forward model scattering intensity, which was used from $q_z = 0$ to ~ 0.09 Å^{-1}, was calculated with the $\frac{1}{q^2}$ volume correction adjustment and without a critical angle adjustment. The importance of the shape of this $q_z = 0$ patch intensity to the resulting electron density is discussed further in Sec. 3.10.

The $q_z = 0$ position of the spectrometer was not absolutely determined during the experiment and this posed a small complication in both the forward model and direct inversion analysis of the measured data. The forward model analysis accounted for this variation by including a q_z translation variable as a fitting parameter in the model for the scattering intensity. This parameter was generally found to be within two measurement steps, 0.04°, in 2θ from the nominal spectrometer zero. The measured scattering intensity was shifted in q_z with respect to the forward model scattering intensity, used as the $q_z = 0$ patch so that the $q_z = 0$ patch intensity lined up with and connected smoothly with the data in the connecting region ($q_z \sim 0.09$ Å^{-1}). In the direct inversion analysis, the criterion for determining the correct position of the data with respect to the $q_z = 0$ patch was that the $q_z = 0$ patch intensity fitted smoothly onto the data near $q_z = 0.09$, matched the measured scattering intensity throughout the whole q_z region, and that the resulting $\rho(z)$ had no anomalies (odd shape or unphysical electron density outside the film) due to this translation position. The effect of translation on the resulting density is discussed further in Sec. 3.10.

3.8.2 Resolution Function Deconvolution

To determine the shape of the intrinsic film scattering intensity, it is necessary to remove the broadening due to the spectrometer resolution from the measured scattering intensity. The measured scattering intensity, $M(q_z)$ is the convolution of the intrinsic scattering intensity, $I(q_z) \propto |S(q_z)|^2$, with the resolution function, $R(q_z)$,

$$M(q_z) = I(q_z) \otimes R(q_z). \tag{3.12}$$

The sharp diffraction features in $I(q_z)$ are blurred in $M(q_z)$ by the convolution. Features much broader than the resolution function width have smaller shape distortions, but do have modified intensities.

The measured instrumental resolution function, determined by averaging five mosaic-averaged scans of the first primary maximum of a 600-layer film, is shown in Fig. 3.7. For the direct inversion density determinations reported here, this slightly asymmetric resolution had to be deconvolved from the measured intensities. The longitudinal resolution was $\Delta q_z = 9.3 \times 10^{-3}$ Å^{-1} full width at half maximum (FWHM) and was comparable to the corresponding finite size FWHM of a 21-layer film. The resolution perpendicular to the scattering plane was $\Delta q_{xy} = 1.6 \times 10^{-2}$ Å^{-1} FWHM and was controlled by out-of-plane slits. The combination of the film mosaic spread and the instrumental transverse resolution was $\Delta\theta = 0.4°$ FWHM. The main contributions to the resolution function of a double crystal spectrometer are: 1) The width, angular divergence and energy spread of the x-ray beam. 2) The angular and energy acceptance of the monochromator and analyzer crystals. 3) The angular acceptance of the various slits along the incident and scattered beam flight path. All the x-ray scattering intensities were measured from $q_z = 0.04$ to 0.48 Å^{-1}. The momentum transfer, q_z, was nominally perpendicular to the smectic layers. All the scans were mosaic averaged to obtain reliable intensities. The x-ray beam begins to illuminate the film holder below $q_z \sim 0.09$ Å^{-1} and therefore data below this point was not used in either the forward model or the direct inversion analysis.

The intrinsic scattering intensity, $I(q_z)$, can be reconstructed exactly by deconvolution if the resolution function and the noise are known. If the measurements are noise-free, the deconvolution can be performed by simply dividing the Fourier transformed data by the Fourier transformed resolution function and back transforming. However, to extract the best estimate of the intrinsic scattering intensity, $I(q_z)$, in the

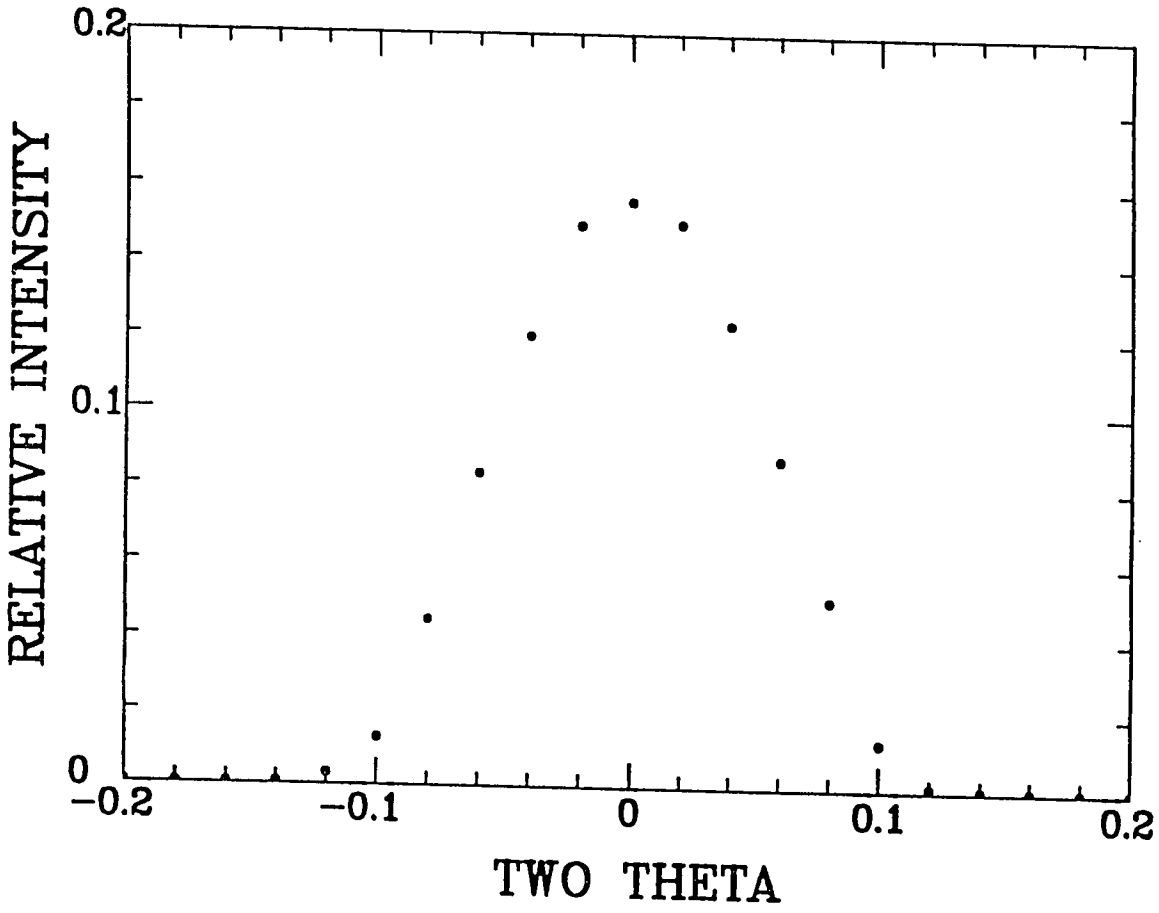

Figure 3.7: Measured Instrumental Resolution Function. The measured instrumental resolution which was deconvolved from the scattering intensity to obtain the scattering amplitude. The FWHM of the resolution function was about 0.13° in 2θ.

presence of noise, N, when only the power spectral density of the noise $\tilde{N}$ is known, a linear operator, called the Wiener-Hopf filter, $\tilde{L}$, can be constructed which produces the least-mean-square error estimate of the intrinsic scattering intensity from the measured scattering intensity [123]. Since the measured scattering intensity, M, is given by $M = I \otimes R + N$, its Fourier transform is given by, $\widetilde{M} = \tilde{I}\tilde{R} + \tilde{N}$. The error, E, we want to minimize is given by $\tilde{E} = \tilde{I} - \tilde{L}\widetilde{M}$. The Wiener-Hopf operator is related to the Fourier transform of the instrument resolution $\tilde{R}$, the noise $\tilde{N}$, and the intrinsic scattering intensity $\tilde{I}$ by [124],

$$\tilde{L} = \frac{1}{\tilde{R}} \frac{|\tilde{R}|^2}{|\tilde{R}|^2 + \frac{|\tilde{N}|^2}{|\tilde{I}|^2}}. \tag{3.13}$$

The direct inversion analysis was done by letting the Wiener-Hopf filter parameter, $\eta_R = \frac{|\tilde{N}|^2}{|\tilde{I}|^2}$ be a constant independent of both $M(q_z)$ and q_z. This was done for simplicity and because it has been shown to work quite well empirically. This is a reasonable assumption if the power spectral density of the noise is proportional to that of the intrinsic scattering intensity.

Once the $q_z = 0$ patch was included, the second step is to subtract off the inelastic or diffuse scattering background from the measured scattering intensity then remove the instrument broadening by deconvolution. The resulting deconvolved scattering intensity, $I'(q_z)$, is the best estimate of the intrinsic scattering intensity, $I(q_z)$ and this distinction, denoted by the prime, will be dropped from here on. $I(q_z)$ is illustrated in Fig. 3.8.

To determine the value of η_R in the deconvolution process, the deconvolved scattering intensity was reconvolved with the resolution function and compared with the measured scattering intensity. The value of η_R was chosen to give the best correspondence between the reconvolved scattering amplitude and the measured scattering intensity. The value of the Wiener-Hopf filter parameter determines the depth of the zero's between the subsidiary minima; this is illustrated in Fig. 3.9 where the results for $\eta_R = 4 \times 10^{-4}$, 4×10^{-5}, and 4×10^{-6} are compared with the measured scattering intensity. The comparison of the reconvolved scattering amplitude with the measured scattering intensity show that $\eta_R = 4 \times 10^{-5}$ gives the best match to the measured scattering intensity without loosing information near $q_z = 0$ and introducing 'frequency noise'.

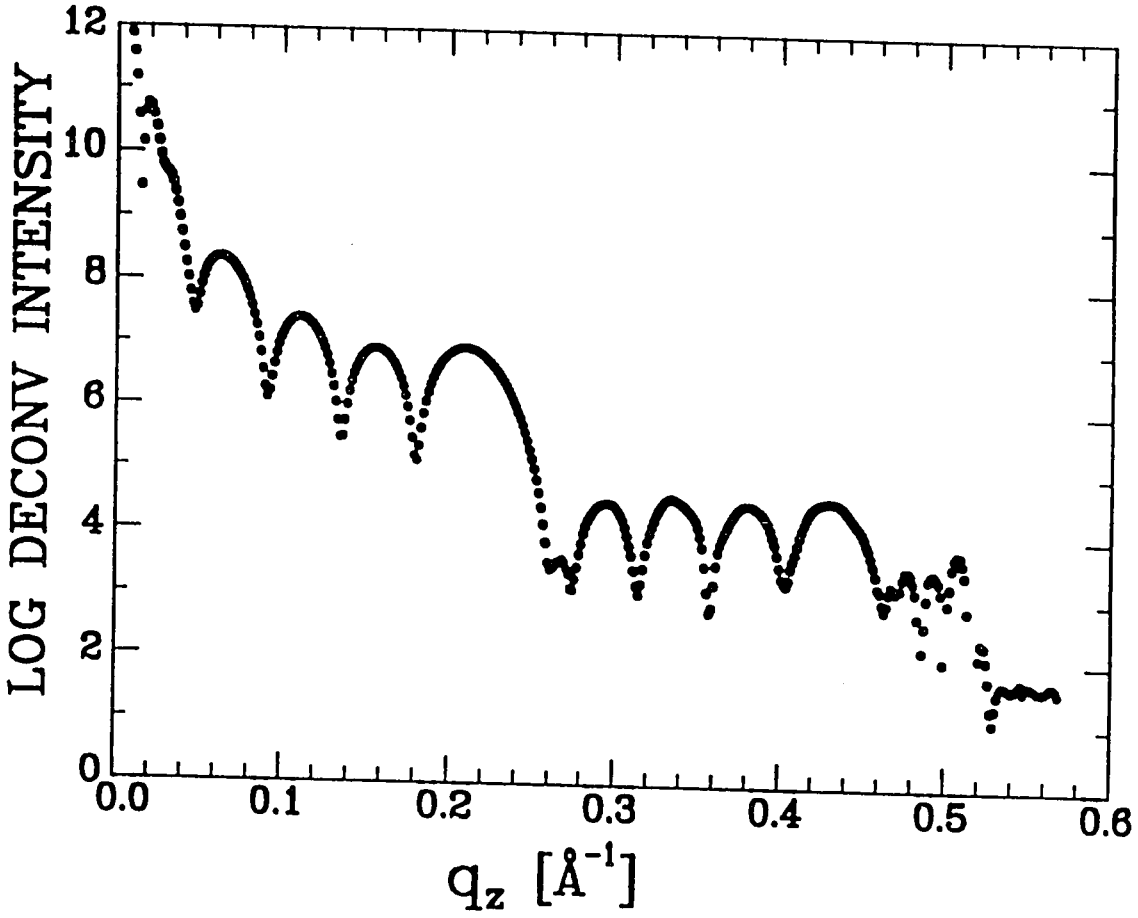

Figure 3.8: The Deconvolved Scattering Intensity. The deconvolved scattering intensity, $I'(q_z)$, obtained from the measured scattering intensity, for the five-layer smectic-G film data, by removing the instrumental resolution broadening using Wiener-Hopf deconvolution. $I'(q_z)$ is the best estimate of the intrinsic intensity, $I(q_z)$. The 'noise' that appears near $q_z = 0$ is an artifact of the deconvolution and is removed from $|S(q_z)|$ by the substitution of the model scattering amplitude corresponding to the model scattering intensity used as the $q_z = 0$ patch.

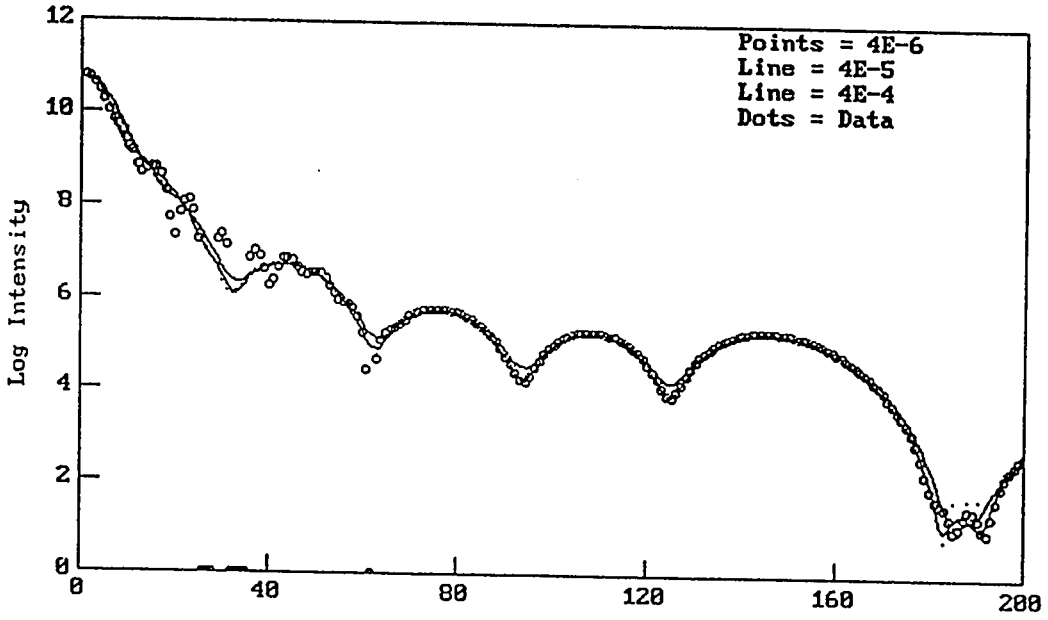

Figure 3.9: η_R Determination. The value of the Wiener-Hopf filter parameter, η_R, determines the depth of the zero's between the subsidiary maxima in the deconvolved intensities, $I'(q_z)$. The reconvolved data is compared with the measured scattering intensity (Small Points) for $\eta_R = 4 \times 10^{-4}$ (Upper Line), $\eta_R = 4 \times 10^{-5}$ (Lower Line), and $\eta_R = 4 \times 10^{-6}$ (Large Points). Unacceptably small values of η_R introduce extraneous 'frequency noise' into the reconvolved scattering intensity near $q_z = 0$ and at the zeros in $I'(q_z)$. $\eta_R = 4 \times 10^{-5}$ results in the best match to the measured scattering intensity for all thickness films and is the value used for the results shown in Sec. 3.11.

3.8.3 Scattering Corrections and Square-Root

The third step is to remove the non-instrumental resolution and scattering corrections and to convert the deconvolved scattering intensity to an unsigned scattering amplitude. The intrinsic scattering intensity, $I(q_z)$, is proportional to the square of the scattering amplitude, $S(q_z)$, and involves some correction terms [126],

$$\mathrm{I}(q_z) \propto \frac{1+\cos^2(2\theta)}{2\sin(2\theta)} \frac{1}{q_z} |\mathrm{S}(q_z)|^2 \tag{3.14}$$

where $(1+\cos^2(2\theta))/2\sin(2\theta)$ is the combined polarization and Lorentz correction factor, and $1/q_z$ is the scattering volume correction factor. These correction factors, proportional to $\frac{1}{q_z^2}$, were removed from $\mathrm{I}(q_z)$ and the square-root was taken to produce the magnitude of the scattering amplitude $|\mathrm{S}(q_z)|$. Finally, after removal of the correction factors, since a forward model scattering intensity was substituted for the experimentally inaccessible region near $q_z = 0$, the scattering amplitude of the $q_z = 0$ patch was substituted into this patched region. This removed the 'frequency noise' introduced into $\mathrm{I}(q_z)$ near $q_z = 0$ by the deconvolution process.

3.8.4 Hand Phasing

In the fourth step, the scattering amplitude phases were determined. The hand phasing of the scattering amplitude is illustrated in Fig. 3.10 using the fact that $|\mathrm{S}(q_z)|$ displays all of the zeros of the scattering amplitude. Since the phases of the scattering amplitude are 0 and π, and since the phases switch only at the zeros of the scattering intensity, the sign of each primary and secondary maximum in the scattering amplitude can be assigned by inspection using the fact that the phase changes result from the product of the 'N-slit' interference pattern and the $\mathrm{MFF}(q_z)$ zeros. The scattering amplitude has an apparent flip in phase after the first harmonic due to the zero in $\mathrm{MFF}(q_z)$ which is also plotted in Fig. 3.10. Therefore, the scattering amplitude phases simply alternate: $+, -, +, -, \ldots$. The resulting scattering amplitude is illustrated in Fig. 3.11.

3.8.5 Fourier Transforming to Obtain $\rho(z)$

The fifth step is to Fourier transform $\mathrm{S}(q_z)$ to obtain the direct inversion electron density, $\rho(z)$ which is shown in Fig. 3.12. Fig. 3.12 illustrates that the resulting direct

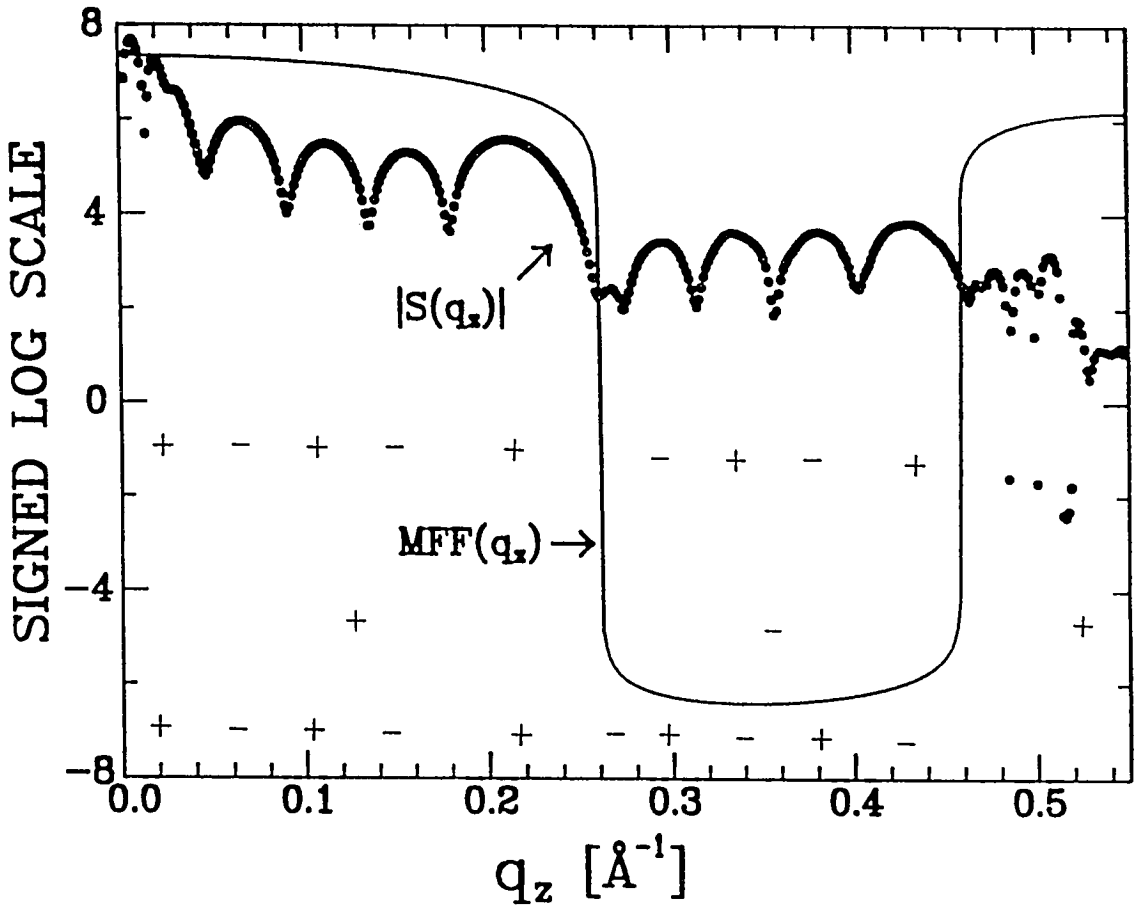

Figure 3.10: Scattering Amplitude Phase Assignment. The phase assignment of the scattering amplitude can be made by inspection since the zeros in the diffraction pattern result from the product of the molecular form factor, MFF(q_z) and the 'N-slit' interference pattern. This plot shows the signed-logarithm of these quantities: $\log_{10}(S)$ if $S > 1$ and $-\log_{10}(S)$ if $S < -1$. The phases of each term and their product are shown. The magnitude of the scattering amplitude, $|S(q_z)|$, is over-plotted with the molecular form factor MFF(q_z) for the five-layer smectic-G film. MFF(q_z) is the Fourier transform of the molecular density.

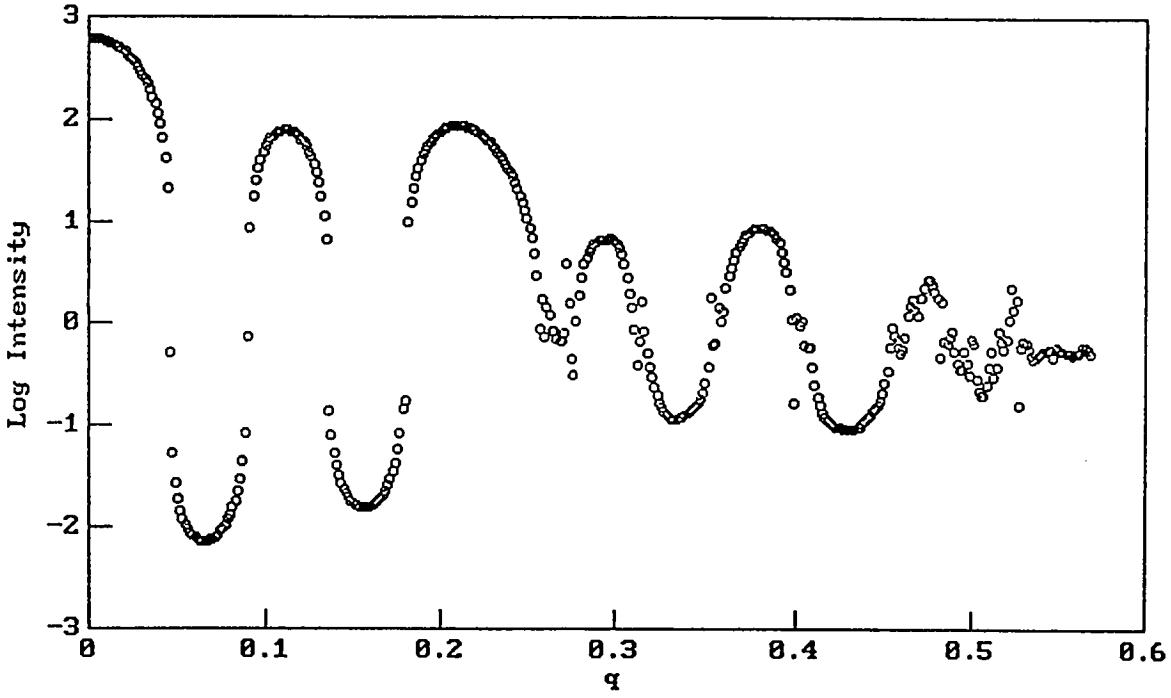

Figure 3.11: Scattering Amplitude. A signed-logarithmic plot of the scattering amplitude for the five-layer smectic-G film. This plot shows the signed-logarithm: $\log_{10}(S(q_z))$ if $S(q_z) > 1$ and $-\log_{10}(S(q_z))$ if $S(q_z) < -1$. Since the zeros of the molecular form factor and the 'N-slit' interference pattern do not coincide, the phases of the resulting scattering amplitude oscillations simply alternate: $+, -, +, -, \ldots$

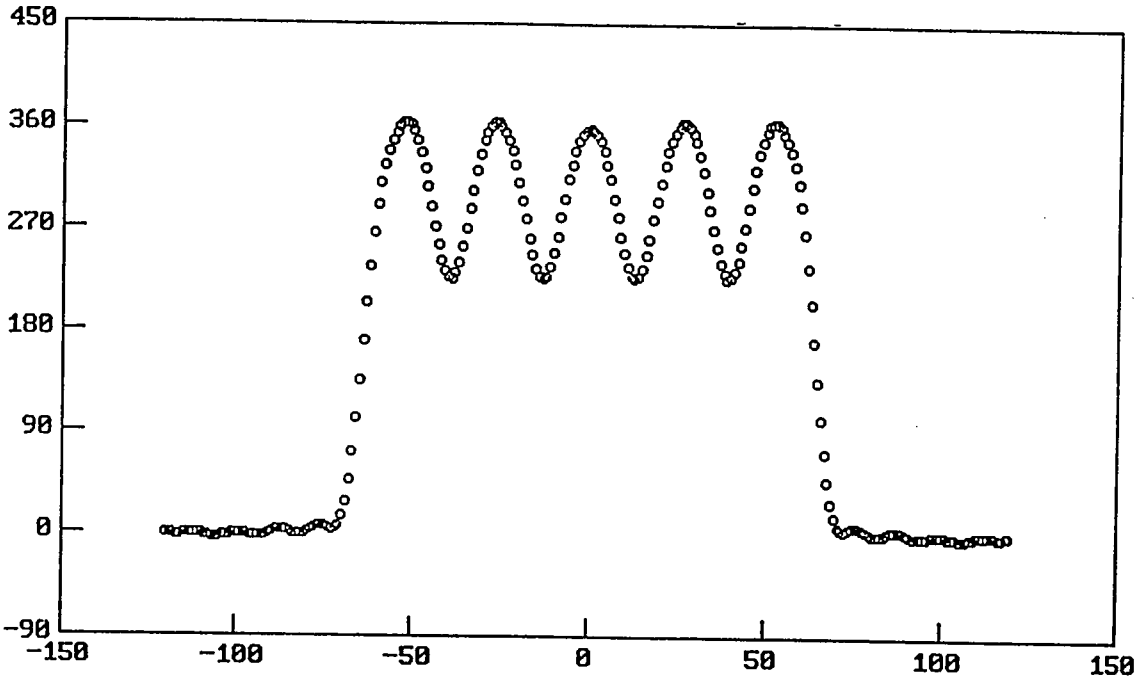

Figure 3.12: Interlayer Electron Density. The electron density, $\rho(z)$, for the five-layer smectic-G film. The modulations in the density are nearly flat (independent of z) with the amplitude of the smectic modulation about 40% of the peak density. Note that even without refinement, the electron density exhibits only a very small amount of unphysical electron density outside the film surfaces. Section 3.11 contains the direct inversion and forward densities for all the other thickness and phase films.

inversion densities exhibit only small amounts of unphysical electron density outside the film. This is true for both the smectic-G and the smectic-I/C films. All direct inversion densities were obtained without refinement. To test whether this small amount of unphysical density is due to an error in the assignment of phases or some other aspect of the direct inversion process, the residual density outside the film region was back-transformed to locate its origin in reciprocal space. Fig. 3.13 displays the full back-transformed density (Top Panel), back-transformed central film portion (Center Panel), and back-transformed density outside the surfaces of the film (Bottom Panel) for the five-layer smectic-G film. (Similar analysis has been done with similar results for the other thickness films.) The central film density was constructed by zeroing all density outside the central portion of the density and vice versa for the density outside the film. These plots indicate that any residual unphysical density outside the film has a uniform spectral weight with some enhanced modulation at the spatial frequency of the layer spacing, but that the overall scattering intensity is at least two orders of magnitude less than that due to the film. No single feature in the measured scattering intensity is responsible for this 'noise' and the back-transformed 'film' density is nearly identical with the measured scattering intensity. The fact that thicker films do exhibit more unphysical density outside the film surface is perhaps due to the relatively large experimental data point spacing, $\Delta(2\theta) = 0.02°$, which becomes more important for thicker films since there are then relatively fewer scattering intensity samples over the increasingly closely spaced subsidiary maxima.

To check that the phase assignments and the deconvolution routines are correct, the Fourier transform of $\rho(z)$ was calculated, squared, multiplied by scattering corrections, reconvolved with the instrument resolution, and compared with the measured scattering intensity. The agreement is quite good and is shown in the top panel of Fig. 3.13.

3.8.6 Molecular Density Deconvolution to Obtain CM(z)

Since the average molecular density of the 7O.7 molecule can be calculated [125], the center-of-mass density, CM(z), can be extracted from the electron density, $\rho(z)$, by deconvolution, removing the broadening due to the average molecular density, MD(z), using a second Wiener-filter parameter η_{MD}. In this procedure, it is implicitly assumed that the molecules in each layer all have the same tilt angle so that the electron

Figure 3.13: Smectic-G Density Back-Transformed. Comparison of the measured scattering intensity with the back-transformed density. The back-transformed full density (Top Panel), the film portion (Middle Panel), and the unphysical outside-film portion (Bottom Panel) are displayed along with the original scattering intensity (small dots). The unphysical outside-film portion has the central film portion set to zero. Note: the power spectral density of the unphysical outside-film density both is $\sim 10^{-3}$ $M(q_z)$ and is nearly uniform in q_z indicating that it is negligibly small and is not due to a specific feature in $M(q_z)$. The back-transformed electron density, plotted in the top panel, matches $M(q_z)$ demonstrating that the Wiener filter parameter, $\eta_R = 4 \times 10^{-5}$, the phase assignments, and the deconvolution procedure are correct.

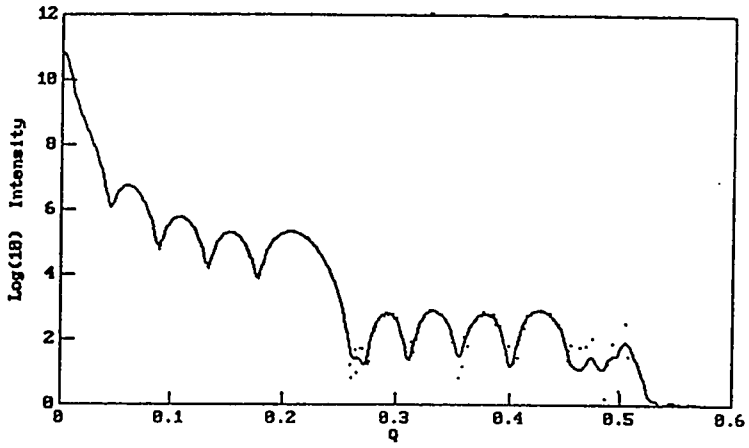
Log(10) Intensity
12
10
8
6
4
2
0
0
0.1
0.2
0.3
0.4
0.5
0.6
Q

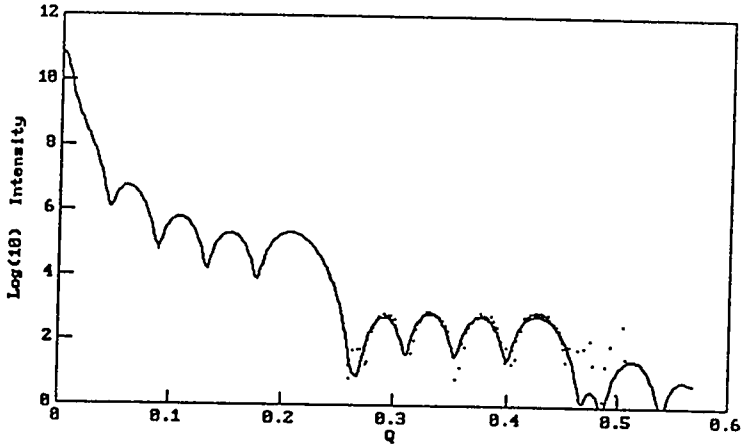
Log(10) Intensity
12
10
8
6
4
2
0
0
0.1
0.2
0.3
0.4
0.5
0.6
Q

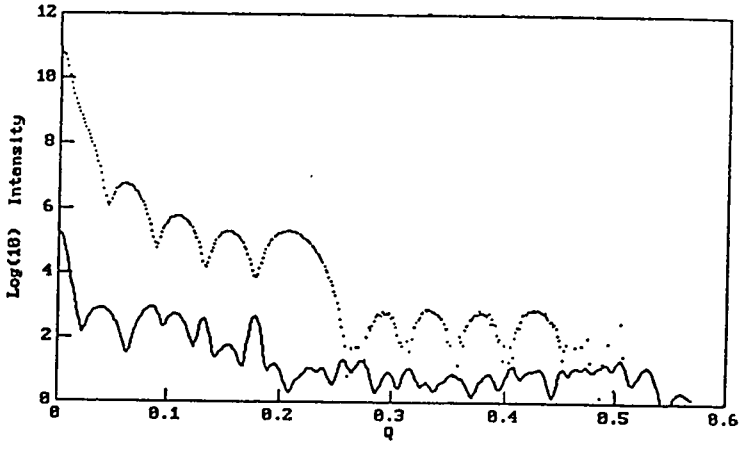
Log(10) Intensity
12
10
8
6
4
2
0
0
0.1
0.2
0.3
0.4
0.5
0.6
Q

density, $\rho(z)$, is the convolution of the center-of-mass density CM(z), with a single average molecular density, MD(z),

$$\rho(z) = \mathrm{CM}(z) \otimes \mathrm{MD}(z). \tag{3.15}$$

The molecular density of the 7O.7 molecule was calculated from the known atomic structure of the molecule using bond angles and lengths obtained from crystallographic measurements of a related molecule [125]. The atomic positions were projected onto the long axis of the molecule and the average molecular tilt angle ϕ was determined to be 21° for both phases as will be discussed below. The unsymmetrized and symmetrized 7O.7 molecular density is illustrated in Fig. 3.14. The symmetrized form was used here since the LC molecules in each layer are expected to have random orientations with respect to the director.

The value of the molecular tilt angle determines the position of the molecular form factor zero and therefore the position of the zero in the measured scattering intensity after the first and second harmonics. Fig. 3.15 shows a comparison of the intrinsic scattering intensity with models of the molecular form factor calculated for a molecular tilt of 15°, 21°, and 25°. A molecular tilt angle of 21° results in a molecular form factor which best matches the molecular form factor zeros in the intrinsic scattering intensity. This value is slightly smaller than the reported bulk smectic-G value of 24.5° [127]. Similar plots for other thickness smectic-G and smectic-I/C films indicates that the MFF(q_z) generated with a 21° tilt angle corresponds with the molecular form factor zeros seen in the intrinsic scattering intensity and therefore this $MFF(q_z)$ was used for all the CM(z) deconvolutions. This MFF(q_z) is somewhat different than that used to generate the forward model CM(z): For the smectic-G films, the forward model tilt angle was found to vary from 26.5° for the three-layer film to 24.5° for the 35-layer film. For all thickness smectic-I/C data the forward model surface smectic-I and interior smectic-C asymptotic tilt angles were taken to be 25° and 12.5°, respectively.

As above, to extract the best least-mean-square error estimate of the center-of-mass density, CM(z), in the presence of noise, N, where only the power spectral density of the noise, $\tilde{\mathrm{N}}$, was known, a second Wiener-Hopf filter, $\widetilde{\mathrm{L}'}$ was used. In analogy with the resolution function deconvolution procedure described in Sec. 3.8.2, the electron density, ρ, is given by $\rho = \mathrm{CM} \otimes \mathrm{MD} + \mathrm{N}$ and the error, E′, we want to

minimize is now given by $\widetilde{E'} = \widetilde{CM} - \widetilde{L'}\widetilde{\rho}$. The Wiener-Hopf operator, L', is therefore

$$\widetilde{L'} = \frac{1}{MFF}\frac{|MFF|^2}{|MFF|^2 + \frac{|\widetilde{N}|^2}{|\widetilde{CM}|^2}}. \tag{3.16}$$

Where $\widetilde{MD} = MFF$, the average molecular form factor. This deconvolution was also done by letting the Wiener-Hopf filter parameter, $\eta_{MD} = \frac{|\widetilde{N}|^2}{|\widetilde{CM}|^2}$ be a constant independent of both $\rho(z)$ and z.

The final step is to remove the molecular density broadening. Fig. 3.16 displays the center-of-mass density, CM(z), for the five-layer smectic-G film produced by deconvolving the molecular density, MD(z), from the electron density, $\rho(z)$. The peaks in the center-of-mass density correspond to the center-of-mass distribution of the molecules in each layer. The individual smectic layer positions are broadened due to intrinsic disorder and Debye-Waller fluctuations.

To determine the 'best' value of η_{MD} for this deconvolution process, the deconvolved center-of-mass density was reconvolved with the average molecular density and compared with the electron density. The value of η_{MD} was chosen to give the best correspondence between the reconvolved center-of-mass density and the electron density. The value of this Wiener-Hopf filter parameter determines the depth of smectic modulation in the reconvolved CM(z) and the noise in the region between the peaks in CM(z). This is illustrated in Fig. 3.17 where the reconvolved CM(z) is compared with $\rho(z)$ for $\eta_{MD} = 1$, 40, and 100. The resulting CM(z)'s for different values of η_{MD} are shown in Fig. 3.18. As can be seen, $\eta_{MD} = 40$ gives the best correspondence between the back-transformed CM(z) and the $\rho(z)$ without introducing excess 'noise' into CM(z). Corresponding plots for the smectic-I/C films indicate that $\eta_{MD} = 40$ is correct for both the smectic-G and smectic-I/C data.

The CM(z) obtained using the direct inversion technique does exhibit a small amount of electron density in the unphysical region outside the film. The CM(z) obtained by 'zeroing' the region outside the density and deconvolving just the physical film portion is nearly identical with the center-of-mass in Fig. 3.16 and the back-transformed CM(z) after 'zeroing' the unphysical portion of the CM(z) appears very similar to the full $\rho(z)$ after a 1.5% re-scaling. This indicates that the origin of the unphysical center-of-mass density outside the film is not due to features in the electron density but is inherent to the deconvolution procedure. This unphysical density has

Figure 3.14: Molecular Density. The unsymmetrized and symmetrized 7O.7 molecular density, MD(z), deconvolved from the electron density, $\rho(z)$ to obtain the center-of-mass density, CM(z). The symmetrized form was used since the LC molecules are expected to have equal probability of alignment with respect to the director. The MD(z) was calculated for a molecular tilt angle of 21°. The molecular form factor is the Fourier transform of the symmetrized molecular density.

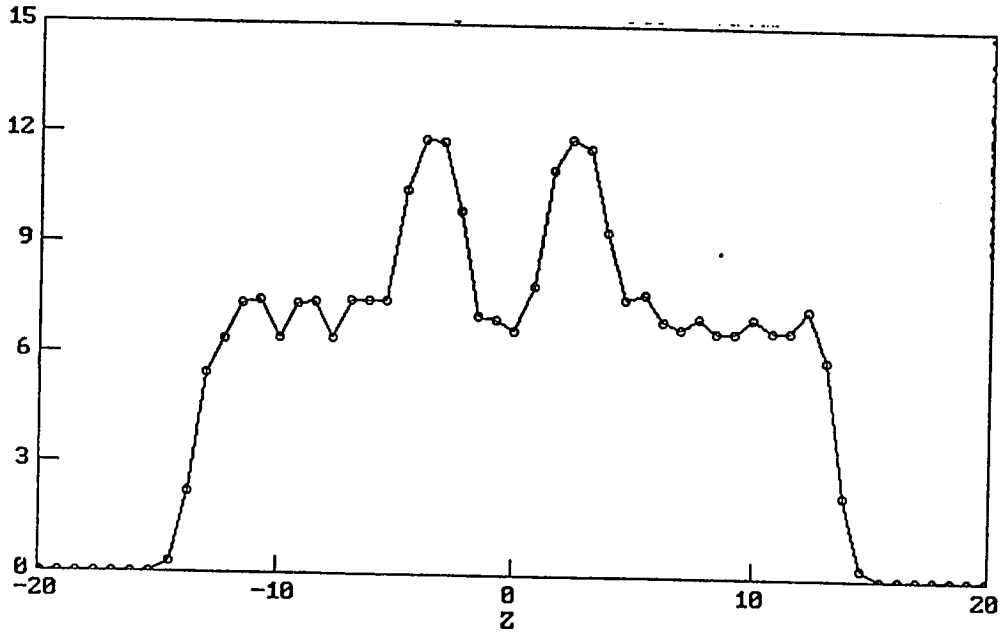
15
12
9
6
3
0
-20
-10
0
10
20
Z

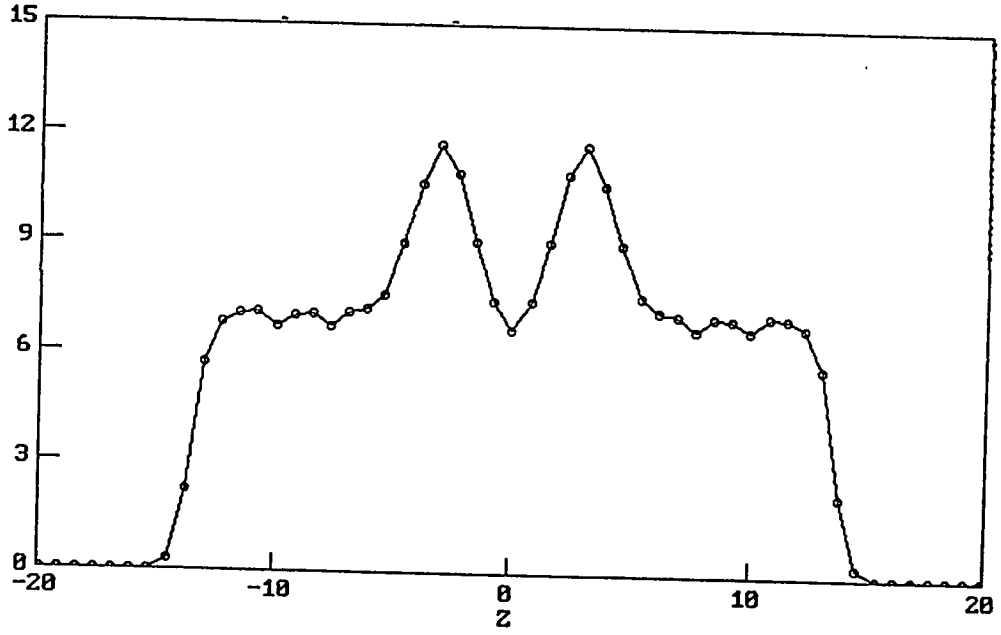
15
12
9
6
3
0
-20
-10
0
10
20
Z

Figure 3.15: Molecular Tilt Angle Determination. Signed-log plot of the deconvolved scattering intensity for the five-layer smectic-G film and MFF(q_z, ϕ) calculated with average molecular tilt angles $\phi = 15°$ (Top Panel), 21° (Middle Panel), and 25° (Bottom Panel). $\phi = 21°$ results in a MFF(q_z, ϕ) which best matches the data at the molecular form factor zeros after the first and second harmonics.

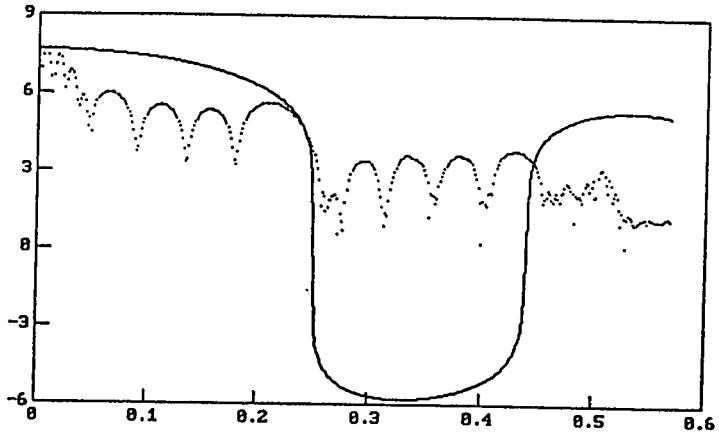
9
6
3
0
-3
-6
0
0.1
0.2
0.3
0.4
0.5
0.6

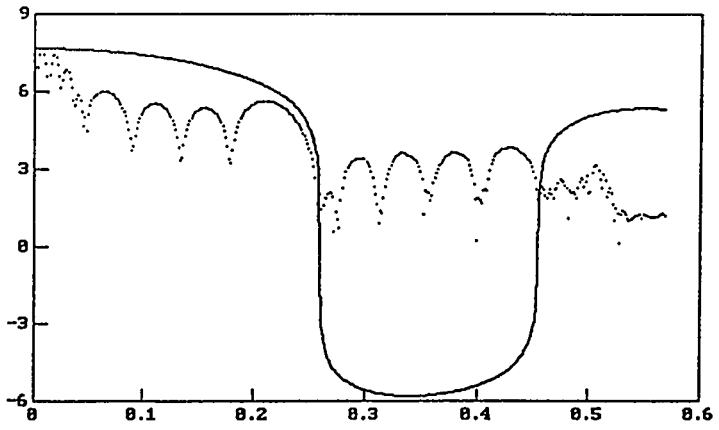
9
6
3
0
-3
-6
0
0.1
0.2
0.3
0.4
0.5
0.6

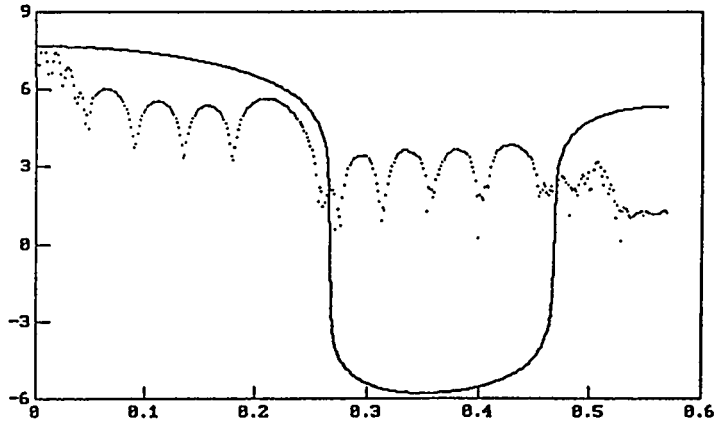
9
6
3
0
-3
-6
0
0.1
0.2
0.3
0.4
0.5
0.6

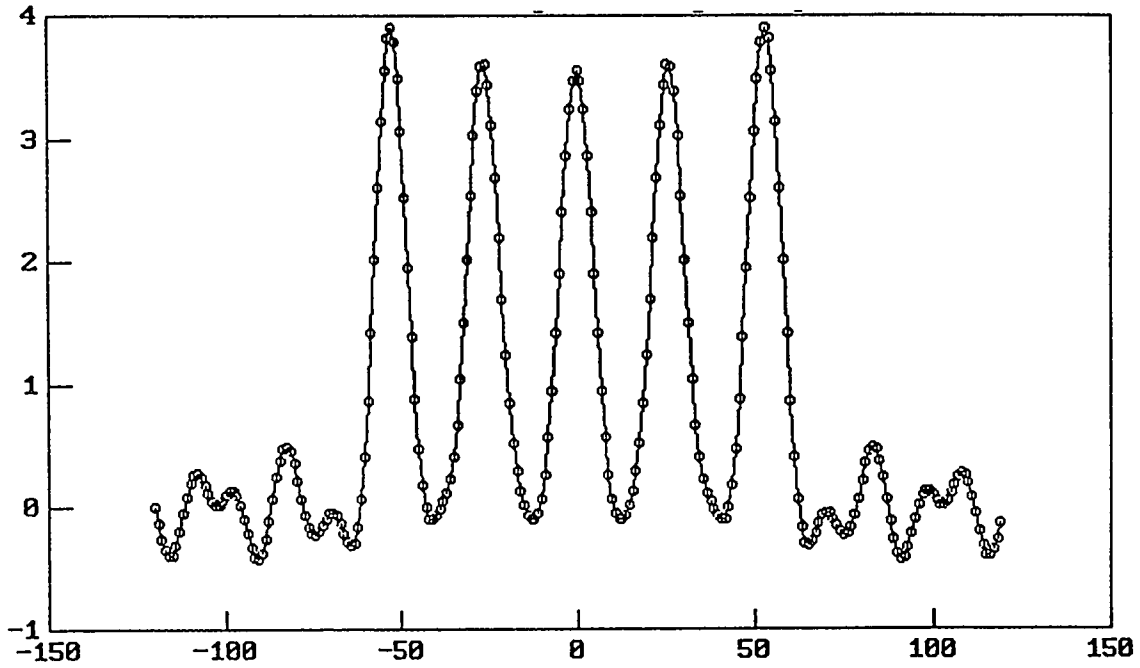

Figure 3.16: Center-of-Mass Density. The center-of-mass density for a five-layer smectic-G film. The center-of-mass positions for each layer are broadened due to the intrinsic disorder and the Debye-Waller fluctuations in the film. The center-of-mass density does exhibit a small amount of electron density in the unphysical region outside the film. Analysis of the power spectral density of this noise indicates that the origin is not due to features in the initial electron density but is inherent in the deconvolution procedure.

been subtracted from the direct inversion CM(z) shown in the center-of-mass density plots comparing the direct inversion and forward model results.

In the most general model for the film, the molecular tilt angle, ϕ_i, and disorder, G_i will be different for each layer, i, in the film. In the limit that the variation in tilt angles is small, $\phi \approx \phi_i$, the average molecular form factor, $\mathrm{MFF}(q_z, \phi)$, can be deconvolved from the density to produce the center-of-mass density, CM(z). Fig. 3.19 shows a comparison of the resulting CM(z) from the five-layer smectic-G film for molecular tilt of 15°, 21°, and 25°. As can be seen, the qualitative shape of CM(z) is only moderately sensitive to large variations of the average molecular tilt angle, ϕ. The value of the average molecular tilt was quite well determined to be $\phi = 21 \pm 1°$, as shown in Fig. 3.15. Whether all layers in the film have the same value for the molecular tilt angle cannot be tested with the direct inversion method – the direct inversion deconvolution procedure does not allow $\mathrm{MD}_i(z, \phi_i)$ with a different molecular tilt, ϕ_i, for each layer, i, as was used in the forward model for the smectic-I/C data. But only small changes are evident in the resulting CM(z) for changes in ϕ of order $\pm 1°$ indicating that to the accuracy of these results, CM(z) is well defined. The CM(z)'s for the smectic-I/C films also exhibit only a small variation with tilt angle so all direct inversion CM(z)'s have been obtained assuming $\phi = 21°$.

3.9 Electron Densities and Center-of-Mass Densities: Comparison of Direct Inversion and Forward Model Results

Fig. 3.20 shows the resulting five-layer smectic-G electron density obtained using forward modeling [26] and the direct inversion techniques. The overall amplitude of the densities have been scaled as they are set by the magnitude of the unmeasured $q_z = 0$ scattering intensity. Both models for the density have peak densities which are nearly flat (independent of z) with the amplitude of the smectic modulation being about 40% of the peak density. The nearly flat densities resulting from the forward model analysis have been attributed to nearly flat interlayer molecular tilt and fluctuation profiles of the film. Section 3.11 contains the figures showing comparisons between the forward model [26] and direct inversion densities for all the smectic-G films. For all thickness films, the resulting direct inversion densities are in qualitative agreement with results obtained using the forward model.

Fig. 3.21 shows the five-layer smectic-I/C electron density obtained using forward

Figure 3.17: η_{MD} Determination: The Resulting CM(z). The value of the Wiener-Hopf filter parameter, η_{MD}, determines the character of the zeros between the center-of-mass layer positions. Plots of a comparison between the resulting CM(z)'s using $\eta_{MD} = 1$ (top panel), 40 (middle panel), and 100 (bottom panel). The value $\eta_{MD} = 40$ gives the least amount of 'noise' between the layer positions with a good match between the reconvolved CM(z) and the $\rho(z)$.

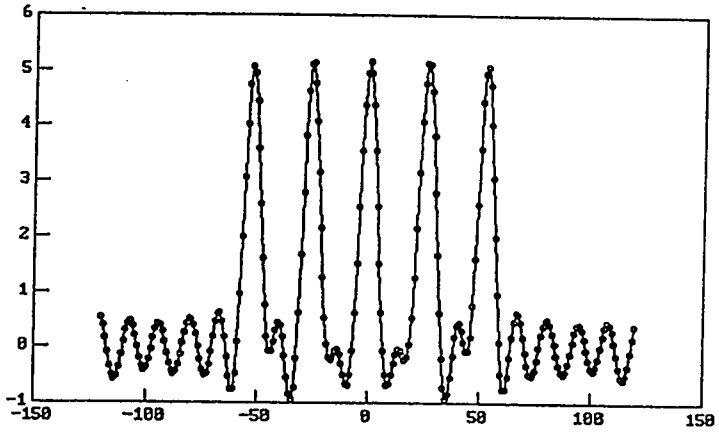
6
5
4
3
2
1
0
-1
-150
-100
-50
0
50
100
150

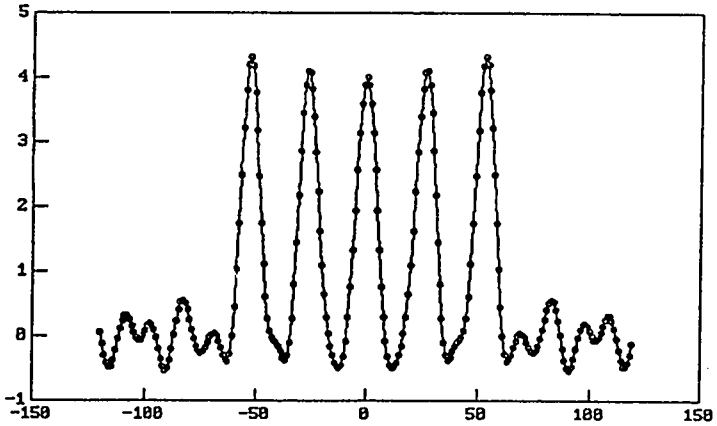
5
4
3
2
1
0
-1
-150
-100
-50
0
50
100
150

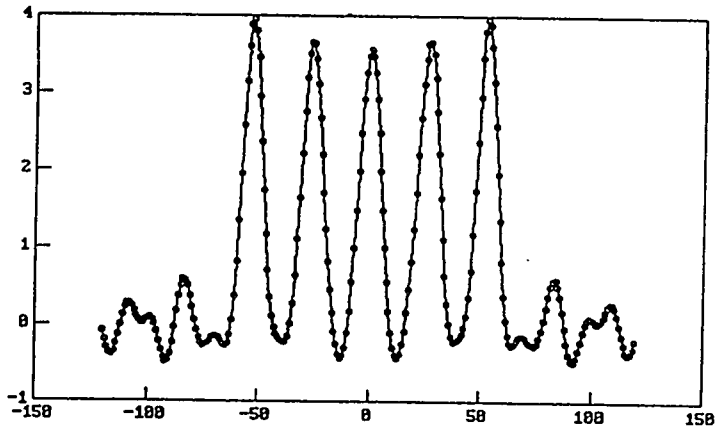
4
3
2
1
0
-1
-150
-100
-50
0
50
100
150

Figure 3.18: η_{MD} Determination: Comparison of the Back-transformed CM(z) with $\rho(z)$. The value of the Wiener-Hopf filter parameter, η_{MD}, determines the height of the center-of-mass peaks and the noise in between these peaks as illustrated in Fig. 3.17. The back-transformed CM(z) (CM$\otimes$MD) is compared with the electron density, $\rho(z)$, for the five-layer smectic-G data with $\eta_{\mathrm{MD}} = 1$ (top panel), 40 (middle panel), and 100 (bottom panel). Unacceptably small values of η_R introduce extraneous 'noise' into CM(z) between the center-of-mass peaks and results in too small a modulation in the back-transformed CM(z). The value $\eta_{\mathrm{MD}} = 40$ gives the least amount of 'noise' between the layer positions while retaining a good match between the back-transformed CM(z) and $\rho(z)$. $\eta_{\mathrm{MD}} = 40$ was the best value for all thickness smectic-G and smectic-I/C films and was used to obtain the results shown in Sec. 3.11.

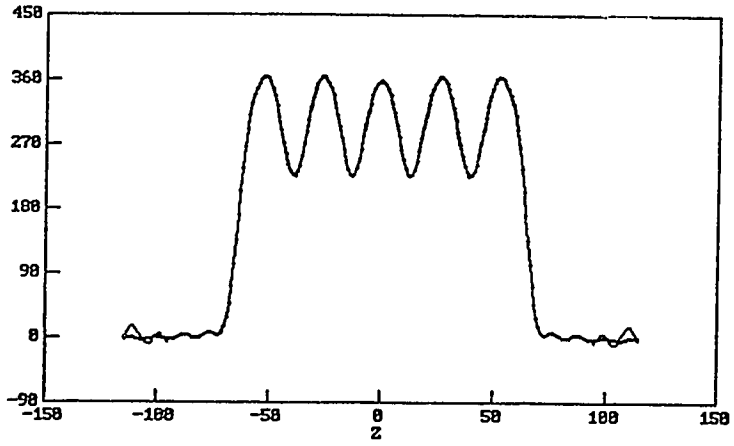
450
360
270
180
90
0
-90
-150
-100
-50
0
50
100
150
Z

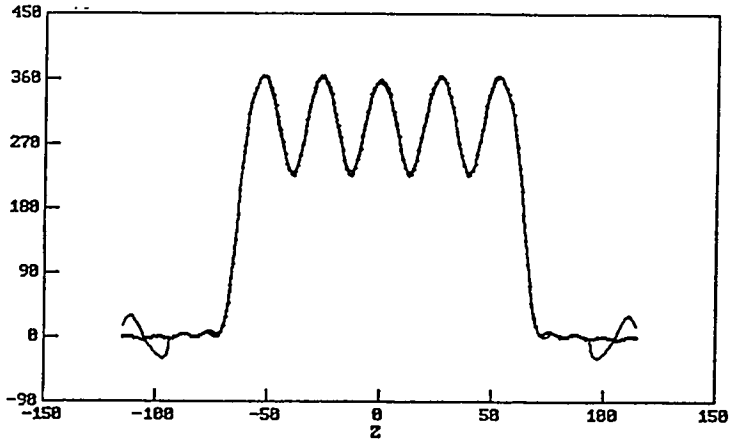
450
360
270
180
90
0
-90
-150
-100
-50
0
50
100
150
Z

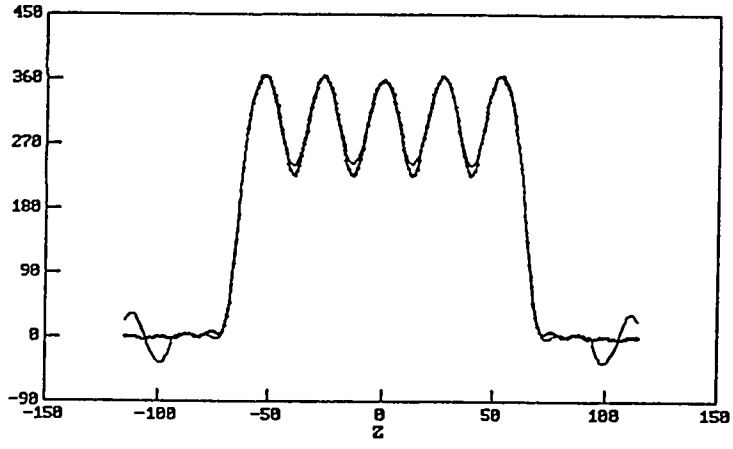
450
360
270
180
90
0
-90
-150
-100
-50
0
50
100
150
Z

Figure 3.19: Center-of-Mass Density versus Molecular Tilt Angle. Comparison of the center-of-mass density for the five-layer smectic-G film using a molecular form factor calculated with average molecular tilt angles of 15° (top panel), 21° (middle panel), and 25° (bottom panel). The value of the average molecular tilt was quite well determined to be $\phi = 21 \pm 1°$, as shown in Fig. 3.15.

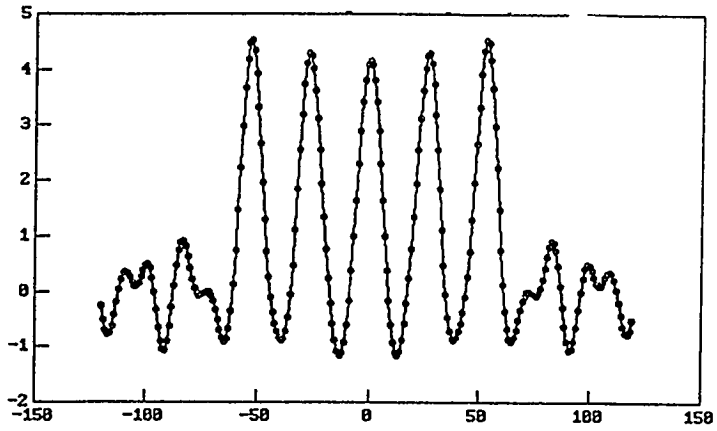
5
4
3
2
1
0
-1
-2
-150
-100
-50
0
50
100
150

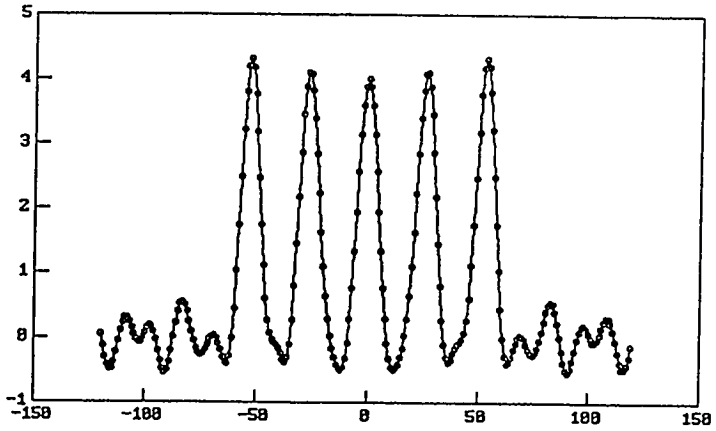
5
4
3
2
1
0
-1
-150
-100
-50
0
50
100
150

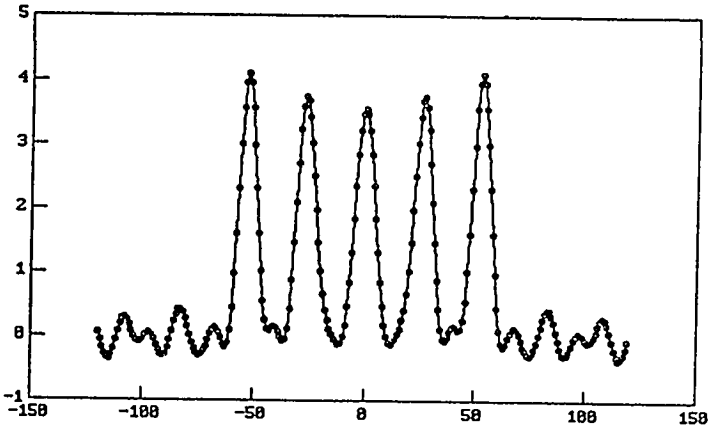
5
4
3
2
1
0
-1
-150
-100
-50
0
50
100
150

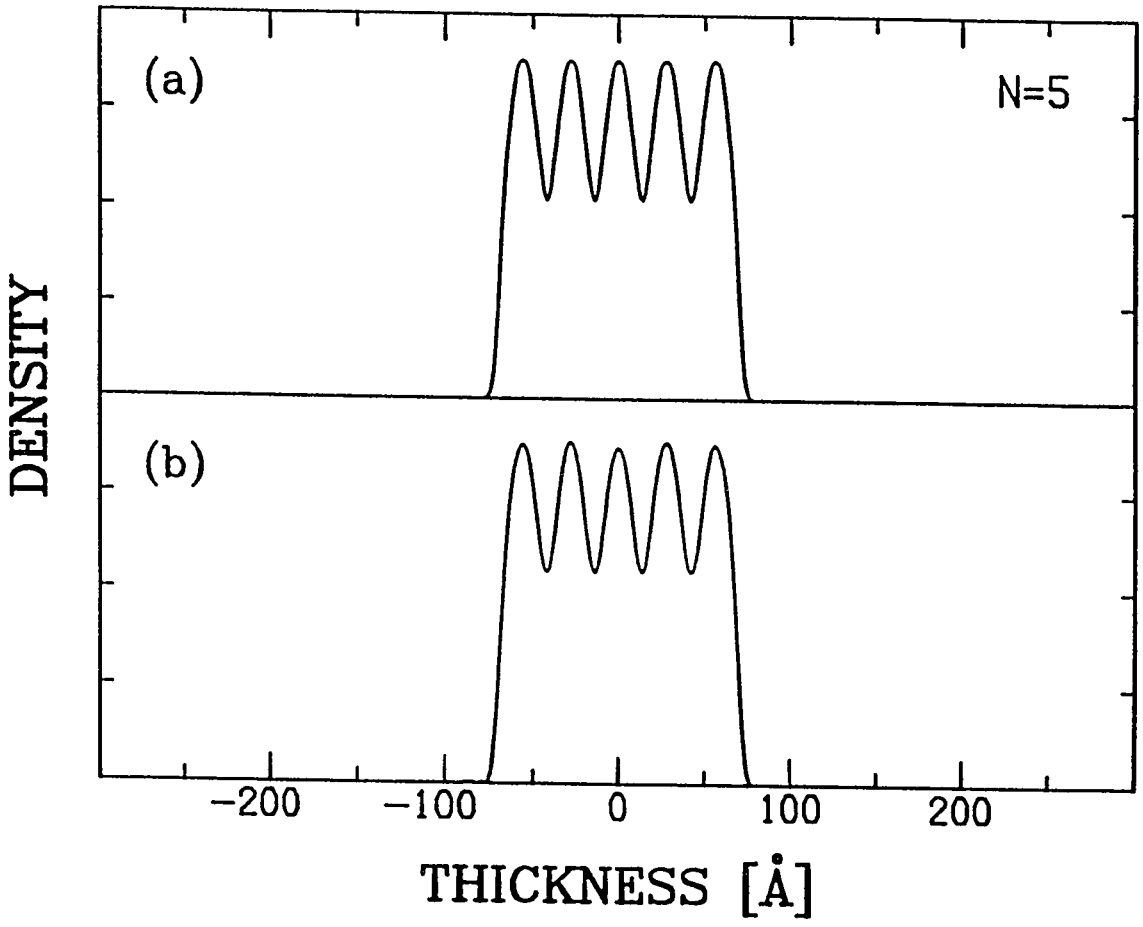

Figure 3.20: Smectic-G Density. Comparison of the interlayer electron density for the five layer-smectic-G films for (a) Forward Model, (b) Direct Inversion. For all thickness films, the densities obtained using the forward model and the direct inversion methods are in qualitative agreement.

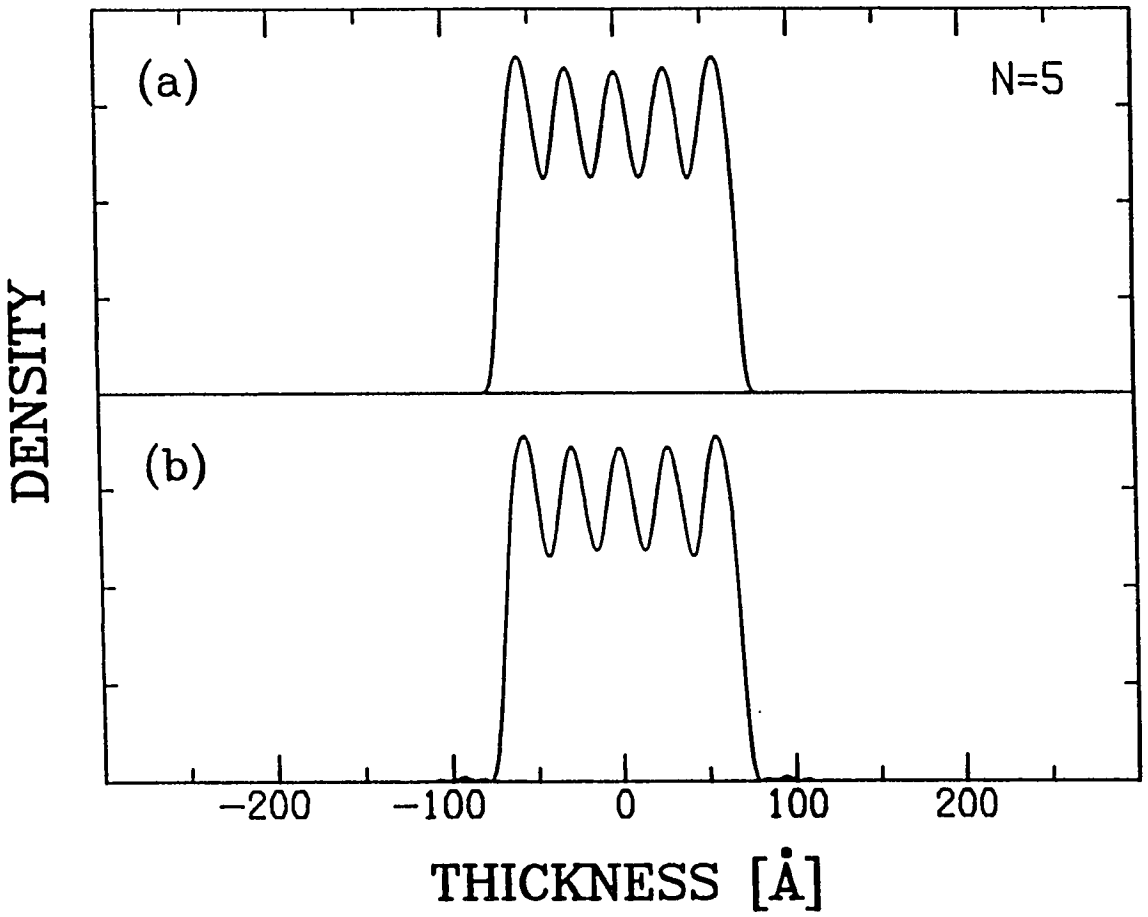

Figure 3.21: Smectic-I/C Density. Comparison of the interlayer electron density for the five-layer smectic-I/C film for (a) Forward Model, (b) Direct Inversion.

modeling [26] and direct inversion techniques. Both densities exhibit qualitatively the same features with enhanced electron density at the surface of the films and an amplitude of the smectic modulation of about 30% of the average density. Section 3.11 contains the figures showing comparisons between the forward model and direct inversion densities for all the smectic-I/C films. In contrast to the smectic-G films, the results for thicker smectic-I/C phase films exhibit decreased electron density near the center of the film compared with the surface layers. For all thickness films, the resulting direct inversion densities are in qualitative agreement with results obtained using the forward model, but thicker films show less surface enhancement in the direct inversion densities than those resulting from forward modeling. The smectic modulation exhibited here is much sharper than the sine wave modulation present in bulk smectics. Both methods of analysis demonstrate the influence of the surface tension and the smectic-I frozen surface monolayers which enhances the density and quenches the fluctuations at the surface of the film. This will be seen more clearly in the plots of CM(z). These results are in contrast with the harmonic modulation model [23] used recently to describe the interlayer density in thin LC films. This model begins with the assumption of a sinusoidal density throughout the film and neglects the importance of the disorder which appears preeminent in these materials.

Fig. 3.22 compares the five-layer smectic-G center-of-mass densities, CM(z), obtained using forward modeling [26] and direct inversion techniques. The direct inversion center-of-mass density shows enhanced surface density with the surface layer probability peaks being about 10% higher and narrower than the interior peaks. This is illustrated clearly in Fig. 3.23 where the surface and center peaks are over-plotted. As can be seen, the center peak is wider and smaller than the surface peak. The peak shapes seem similar and any asymmetry in the surface peak is perhaps within the errors of the direct inversion analysis techniques and not presently attributable to anharmonicity or surface roughening. Section 3.11 contains the figures showing comparisons between the forward model and direct inversion center-of-mass densities for all the smectic-G films. Fig. 3.24 displays a direct comparison of the surface and interior peaks resulting from the direct inversion and forward modeling analysis for the five-layer smectic-G film. This plot illustrates that the smectic-G direct inversion peaks are consistently wider than the forward model peaks (The center peak heights have been scaled to be equal). In the forward model analysis, all peaks shapes are

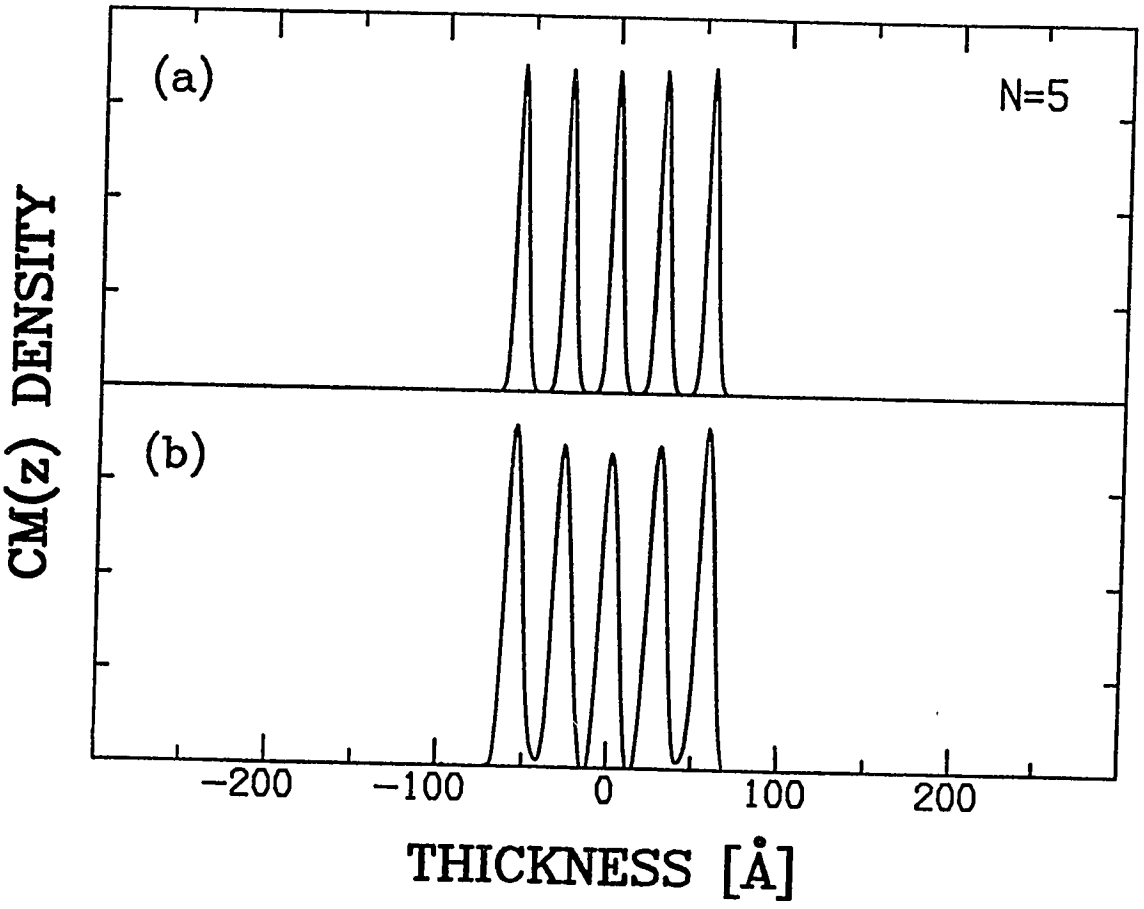

Figure 3.22: Smectic-G Center-of-Mass Density. Comparison of the center-of-mass density for the five-layer smectic-G film for (a) Forward Model, (b) Direct Inversion.

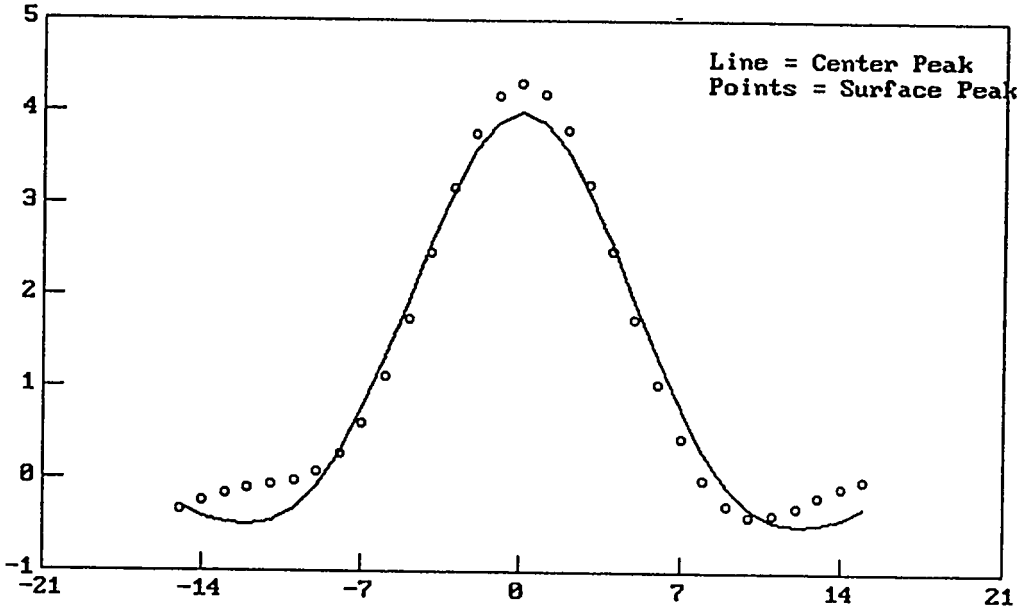

Figure 3.23: Smectic-G Direct Inversion Surface and Interior Center-of-Mass Peak Comparison. Comparison of the interior (Solid Line) and the surface (Points) center-of-mass density peaks for the five-layer smectic-G film derived from the direct inversion analysis. Direct inversion results from thin smectic-G films show quenched fluctuations or enhanced density at the surface of the film.

Fig. 3.25 and Fig. 3.26 illustrate the peak height and FWHM of the direct inversion and forward model center-of-mass peaks measured directly from the CM(z) plots for films up to 10 layers thick. The direct inversion center-of-mass peaks for three to six-layer films show enhanced surface peak heights relative to the interior peaks. This is in contrast to the forward model layer probability peaks which have a similar size and shape throughout the film. The direct inversion and forward model peak heights for thicker films are qualitatively the same, and are uniform throughout the film. The forward model peak widths, σ_i, were uniform for all thickness films. The direct inversion results exhibit narrowing of the peak FWHM for three to six-layer films, while the direct inversion and forward model center-of-mass densities look qualitatively the same for thicker films.

Fig. 3.27 compares the forward modeling [26] and direct inversion center-of-mass densities for the five-layer smectic-I/C film. The direct inversion CM(z) for this thickness film looks quite similar to that shown for the smectic-G film in Fig. 3.22 with an enhanced surface peak about 10% higher and narrower than the interior peaks. This is illustrated clearly in Fig. 3.28 which exhibits an over-plot of the surface and interior peaks. As can be seen, the center peak is somewhat wider and smaller than the surface peak but the peak shapes seem similar with little asymmetry in the surface peak. Fig. 3.29 presents an over-plot of the surface and interior peaks resulting from the direct inversion and forward model analysis. The shape of the center-of-mass positions have been taken to be Gaussian in the forward model analysis. These peaks have a similar shape to the peaks found from the direct inversion analysis. $G_i(z)$ corresponds to the layer disorder and is expected to be Gaussian for harmonic Debye-Waller fluctuations of the center-of-mass position of each layer. The direct inversion peaks look very similar giving no indication of anharmonic fluctuations or roughness of the film-vapor interface. The over-plot of direct inversion results for the surface peaks indicates only slight asymmetry which is interesting but perhaps within the margin of error inherent in the direct inversion analysis. As with the smectic-G films, the center-of-mass peaks resulting from the forward model analysis are consistently narrower than those resulting from the direct inversion analysis. Section 3.11 contains the figures showing comparisons between the forward model and direct inversion center-of-mass densities for all of the smectic-I/C films. Fig. 3.30 and Fig. 3.31 illustrate the peak heights and widths, σ_i, measured directly from the plots of the smectic-I/C

Figure 3.24: Smectic-G Forward Model versus Direct Inversion Center-of-Mass Peak Comparison. Comparison of the surface (Top Panel) and the interior (Bottom Panel) center-of-mass position peaks for the five-layer smectic-G film derived from the direct inversion (Solid Line) and forward model (Points) analysis. The peak-heights of the central interior peaks have been re-scaled to be equal. The direct inversion peaks are constantly wider than those resulting from the forward model.

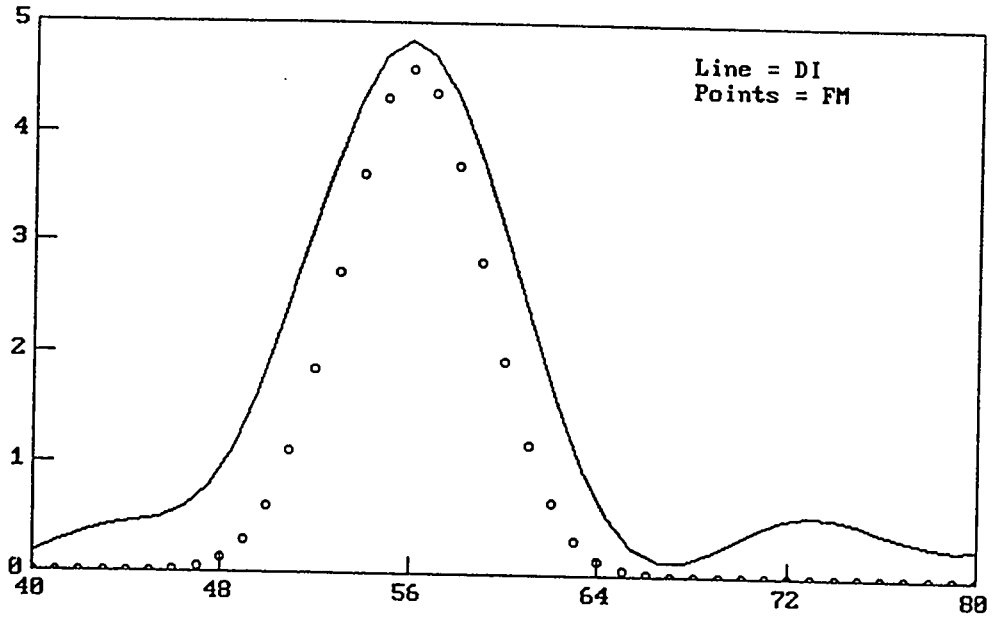
Line = DI
Points = FM
5
4
3
2
1
0
40
48
56
64
72
80

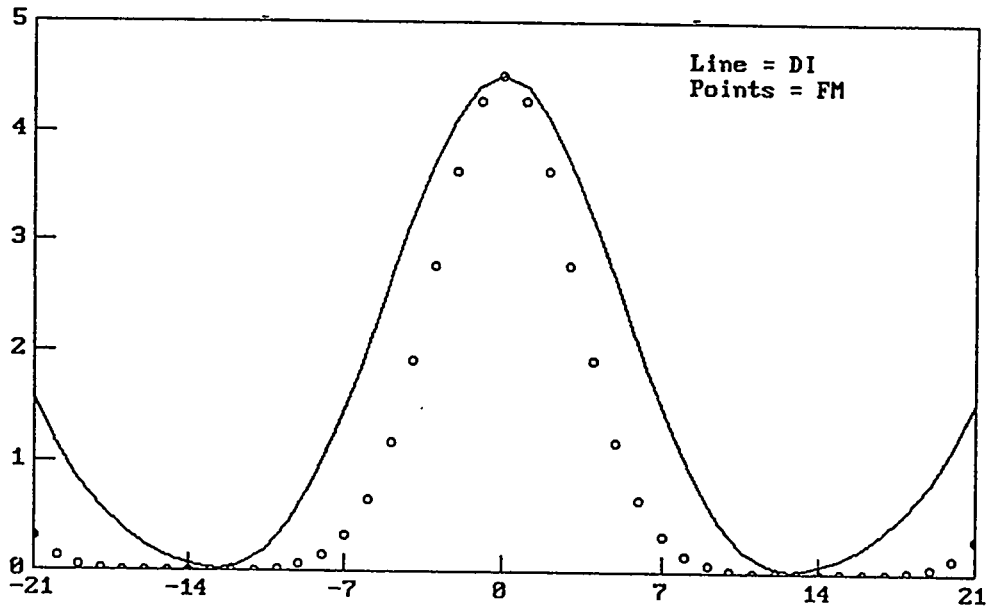
Line = DI
Points = FM
5
4
3
2
1
0
-21
-14
-7
0
7
14
21

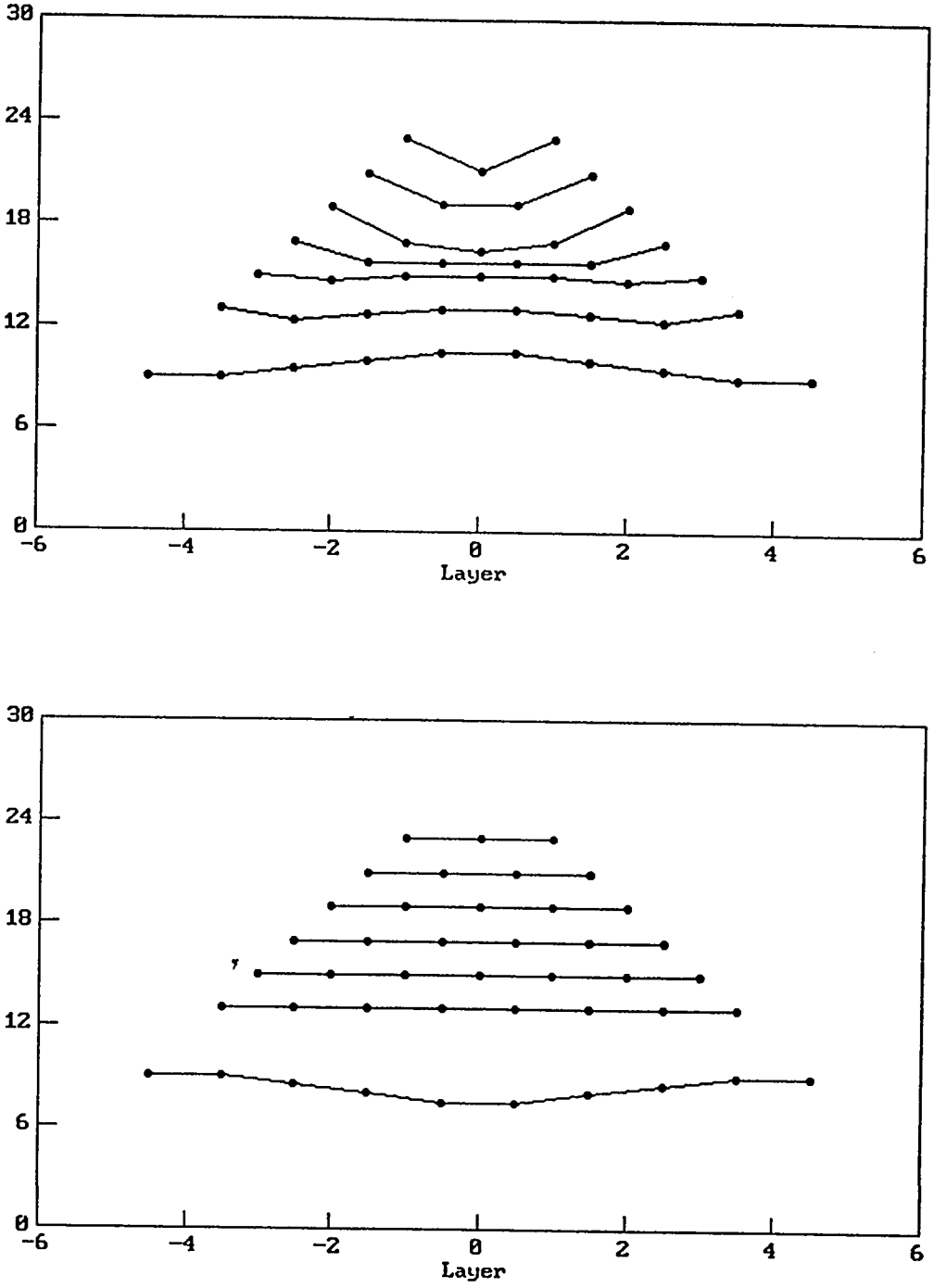

Figure 3.25: Smectic-G Center-of-Mass Peak Height Comparison. Comparison of the direct inversion (Top Panel) and the forward model (Bottom Panel) results for the center-of-mass density peak heights. The peak heights of thicker smectic-G films do not show enhanced surface ordering as do those from the smectic-I/C films. The center-of-mass peak heights have only been measured roughly and have been offset for clarity.

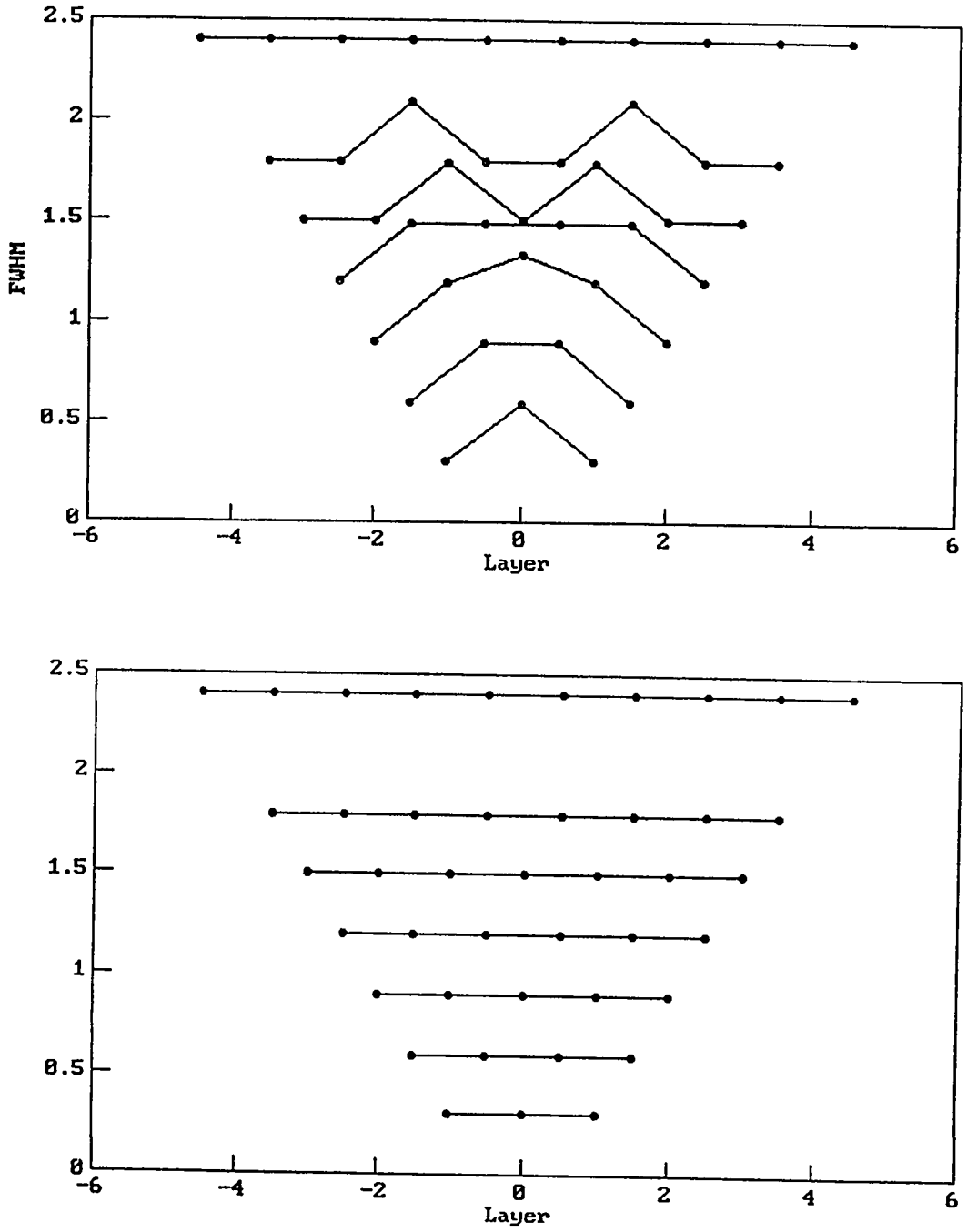

Figure 3.26: Smectic-G Center-of-Mass Peak Width Comparison. Comparison of the direct inversion (Top Panel) and the forward model (Bottom Panel) results for the center-of-mass density peak widths, σ_i. The center-of-mass peaks have only been measured roughly and the measurement quantization is clearly evident in this plot. The peak widths of thicker smectic-G films do not show enhanced surface ordering which is observed for the smectic-I/C films. The results have been offset for clarity.

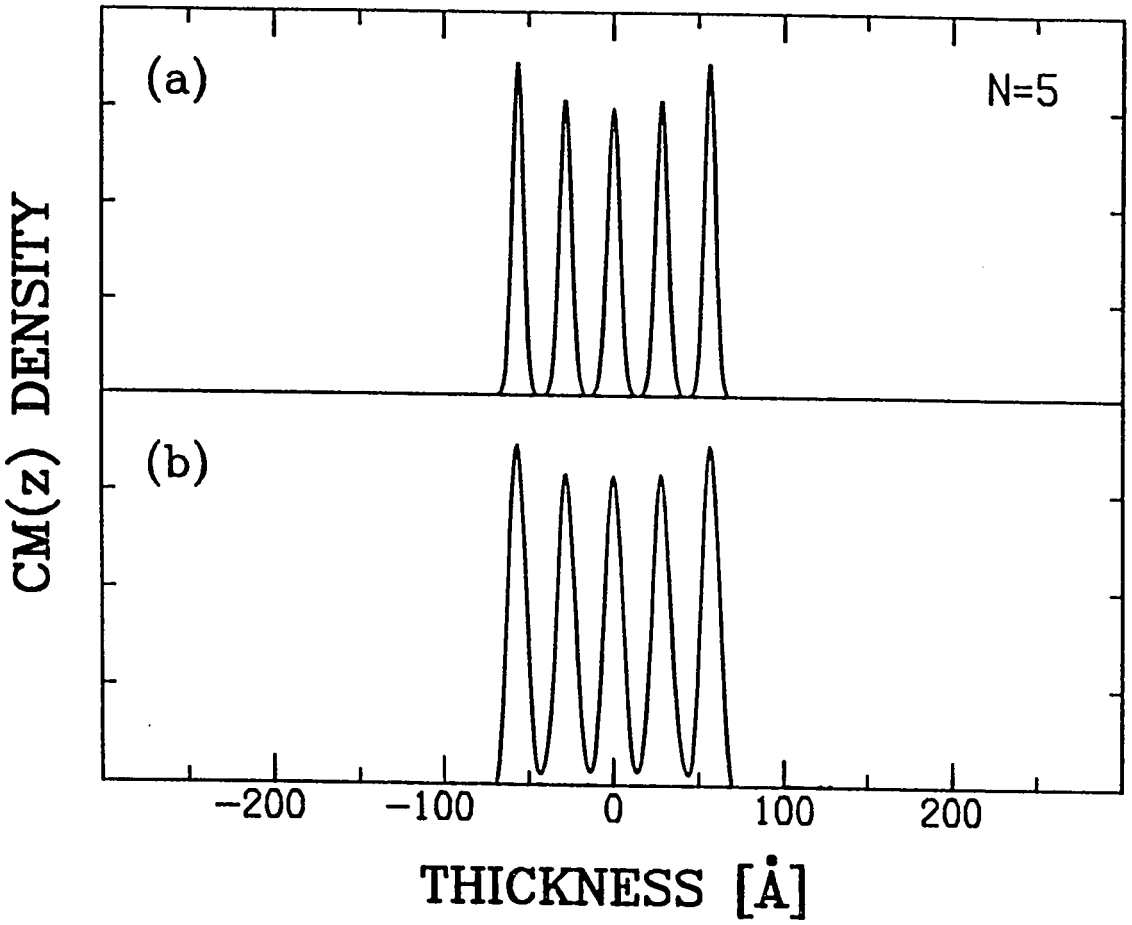

Figure 3.27: Smectic-I/C Center-of-Mass Density. Comparison of the center-of-mass density for the five-layer smectic-I/C film for (a) Forward Model, (b) Direct Inversion. For all thickness smectic-I/C films, forward model and direct inversion center-of-mass densities show enhanced density or quenched fluctuations at the surface of the films.

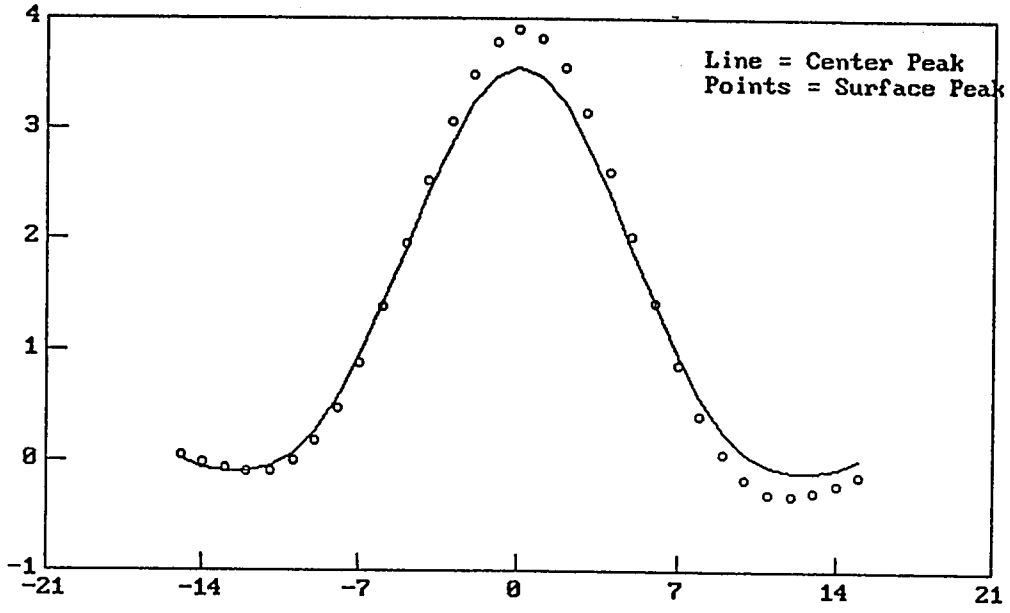

Figure 3.28: Smectic-I/C Direct Inversion Surface and Interior Center-of-mass Peak Comparison. Comparison of the surface (Solid Line) and interior (Dotted Line) center-of-mass position peaks for the five-layer smectic-I/C film derived from the direct inversion analysis. The surface layers show enhanced density and quenched fluctuations due to surface tension and/or the presence of smectic-I frozen surface layers.

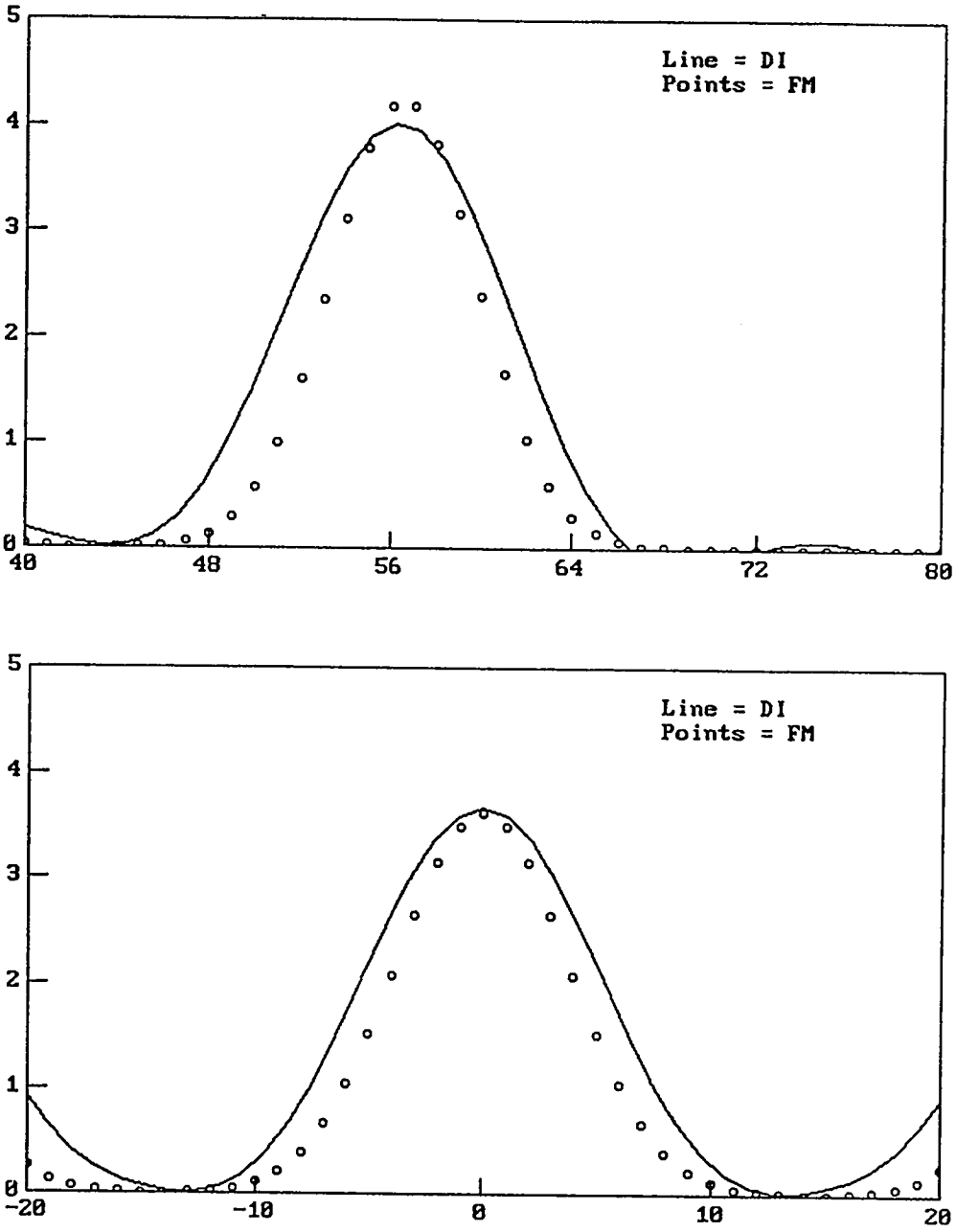

Figure 3.29: Smectic-I/C Forward Model and Direct Inversion Center-of-Mass Peak Comparison. Comparison of the surface (Top Panel) and the interior (Bottom Panel) center-of-mass position peaks for the five-layer smectic-I/C film derived from the direct inversion (Solid Line) and forward model (Points) analysis. The peak-heights of the central interior peaks have been re-scaled to be equal. Results from both analysis methods show enhanced surface density and quenched fluctuations at the surface of the film. The direct inversion peaks are constantly wider than those resulting from the forward model.

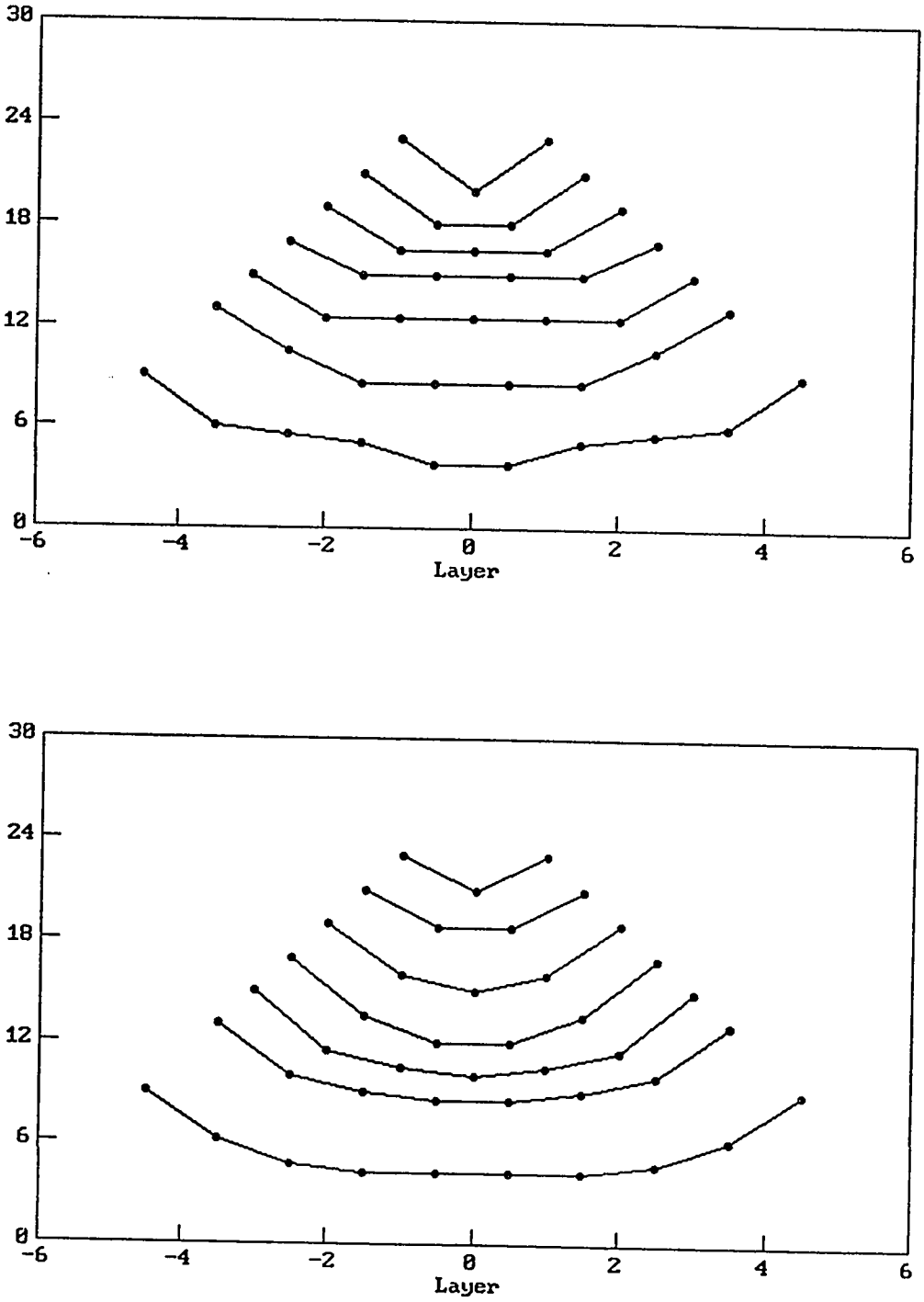

Figure 3.30: Smectic-I/C Center-of-Mass Peak Height Comparison. Comparison of the direct inversion (Top Panel) and the forward model (Bottom Panel) results for the center-of-mass density peak heights. Both results look qualitatively the same and show enhanced ordering at the film surface. The center-of-mass peak heights have only been measured roughly and have been offset for clarity.

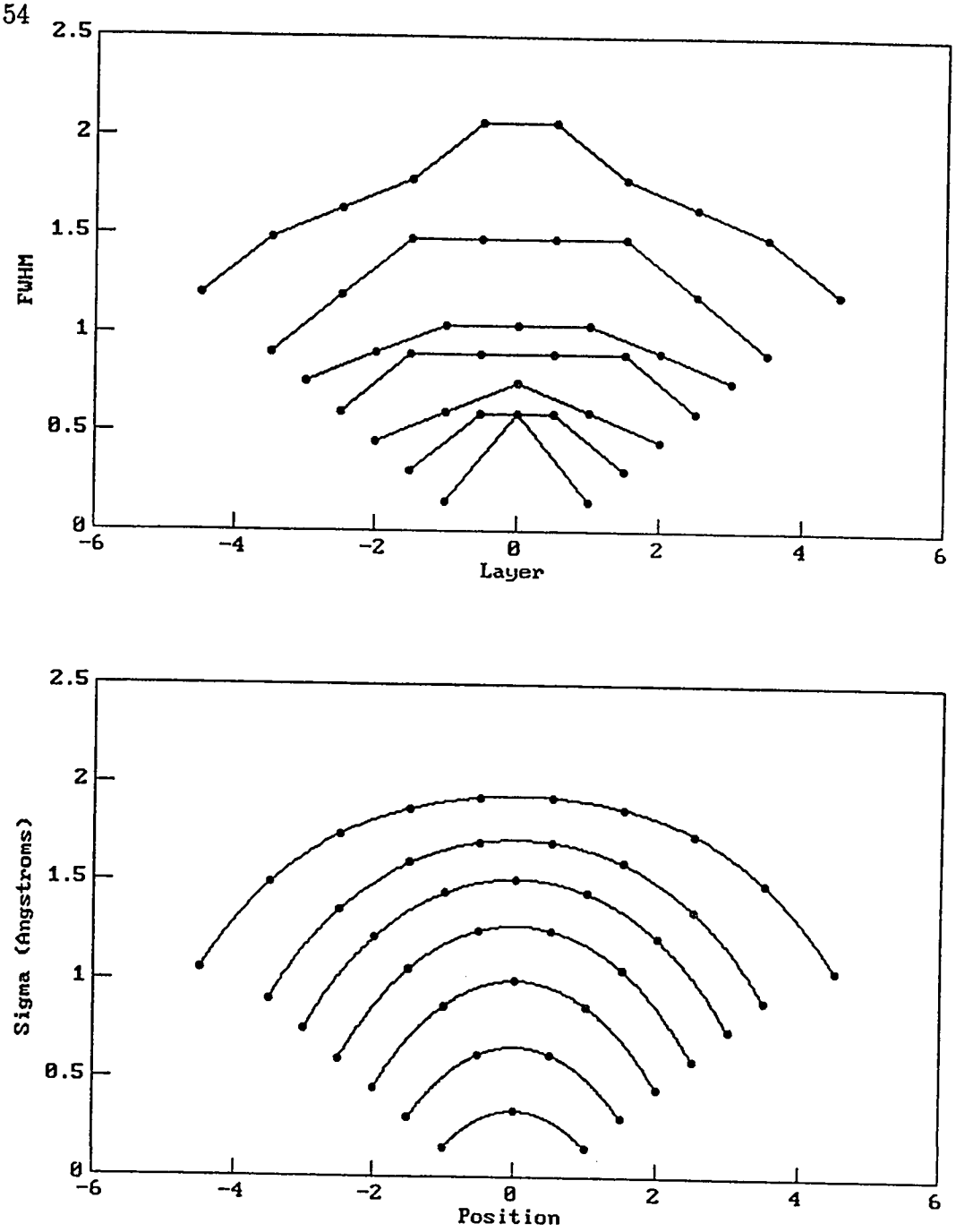

Figure 3.31: Smectic-I/C Center-of-Mass Peak Width Comparison. Comparison of the direct inversion (Top Panel) and the forward model (Bottom Panel) results for the center-of-mass density peak widths, σ_i. The center-of-mass peaks have only been measured roughly and the measurement quantization is clearly evident in this plot. Both results look qualitatively the same and show enhanced ordering at the film surface. The results have been offset for clarity.

CM(z)'s. Unlike the smectic-G films, all thickness smectic-I/C films show enhanced surface density. Furthermore, the results from both the direct inversion and forward model analysis look very much the same for all thickness films. For all films, the surface layer FWHM is narrower and peak height is higher than the interior layers indicating enhanced ordering at the surface of the film. The origin of this enhanced order may be either due to the surface tension which quenches the fluctuations and/or the existence of the more ordered smectic-I layer on the surface. In the direct inversion analysis, many smectic-G films exhibit some increased density at the surface of the film, but the enhancement is generally not as large as that found for the smectic-I/C films.

3.10 Discussion and Conclusions

A new method has been developed to directly invert the scattering intensity to produce the electron density in centrosymmetric films. This method provides a means of obtaining a model-independent determination of the electron and center-of-mass densities of thin centrosymmetric films. These densities are obtained without refinement and without much unphysical electron density outside the film surfaces. Knowing the instrumental resolution function, the method involves deconvolution to remove the instrumental broadening then solving the phase problem using the fact that the films are centrosymmetric and that the scattering intensity is the product of two known quantities: the molecular form factor and the thin film 'N-slit' interference pattern. The CM(z) can also be determined since the form of the molecular form factor is known.

3.10.1 Importance of the $q_z = 0$ Patch in Determining $\rho(z)$

The scattering intensity between $q_z = 0$ and about $q_z = 0.09$ was not measured due to the occlusion of the incident beam by the LC film holder. Consequently, any Fourier components of the density which depend on the detailed shape in this scattering region have not been probed directly by the forward model or by the direct inversion analysis. The densities determined using the forward model analysis simply ignored this region entirely. The lack of any measured information in this region makes suspect any density features which correspond to these reciprocal space length scales

since real measured intensities from this region are needed to correctly determine these details in the density. Since the direct inversion analysis substitutes a forward model scattering intensity into this region, any Fourier components in the density corresponding to this $q_z = 0$ patch are not independent of the forward model. A narrower x-ray beam and a thinner film holder will allow measurement to lower q_z and would improve the accuracy of the derived densities with these spatial frequencies.

An important consideration for both the forward model and direct inversion analysis is the effect of the shape of the scattering intensity below $q_z = 0.09$ Å^{-1} in determining the electron density. The major question is: Of what importance is the scattering in this region in determining the electron density? Large changes in the model scattering intensity near $q_z = 0$ do effect the resulting electron density. To demonstrate the effects on the resulting density of what we consider extreme modifications of the $q_z = 0$ patch on the resulting density, three different model intensities are shown in Fig. 3.32. As can be seen, all three model intensities are identical after the first 20 data points. As shown in the lower panel, these large changes produce drastic modifications of the reconstructed densities. Although such large changes can probably be ruled out, this figure does show that the forward model densities do depend on the scattering intensity in this unmeasured region, $q_z < 0.09$. It is also worth noting that the density changes shown in Fig. 3.32 are due primarily to the effects of the $\frac{1}{q^2}$ volume correction which is removed systematically during the deconvolution process. Modifications of the $q_z = 0$ patch scattering intensity as large as those shown in Fig. 3.32 have not been seen in any forward model which produces acceptable fits to the data. Small shape modifications and rescaling by ± 10 % on either side of the 'match point' near $q_z = 0.09$ of the $q_z = 0$ patch have no noticeable effect on the shape of the density.

The region over which the forward model scattering intensity was substituted must be large enough so the measured scattering intensity is not affected by the beam striking the LC film holder. Fig. 3.33 shows that the data below $q_z = 0.08\text{Å}^{-1}$ contains a significant deficit in scattering intensity due to the shadowing of the beam by the film aperture and displays this effect on the resulting density from inclusion of this deficit. The $q_z = 0$ patch was added out to $q_z \sim 0.09$ where any additional length to the patch made no difference in the resulting density.

To make a smooth transition between the $q_z = 0$ patch and the data in the

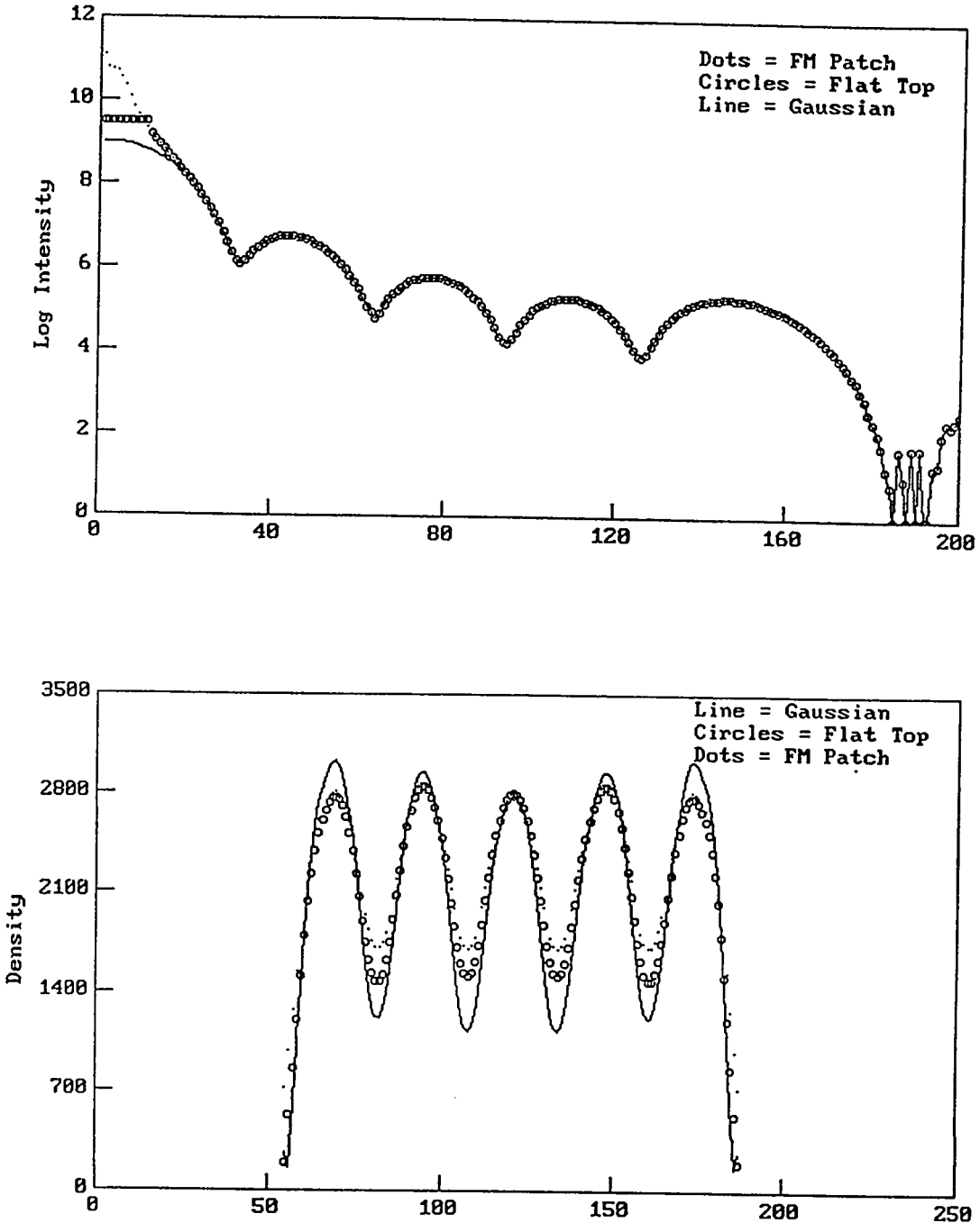

Figure 3.32: Effects on $\rho(z)$ Due to Variations in the $q_z = 0$ Patch. The variation in $\rho(z)$ resulting from different $q_z = 0$ patches for the five-layer smectic-G film. The effects of these modifications are large since the direct inversion procedure makes a $1/q_z^2$ correction near $q_z = 0$ which is not inherent in these models for the $q_z = 0$ patches. The model shown with the dotted line was used for the direct inversion densities presented in Sec. 3.11.

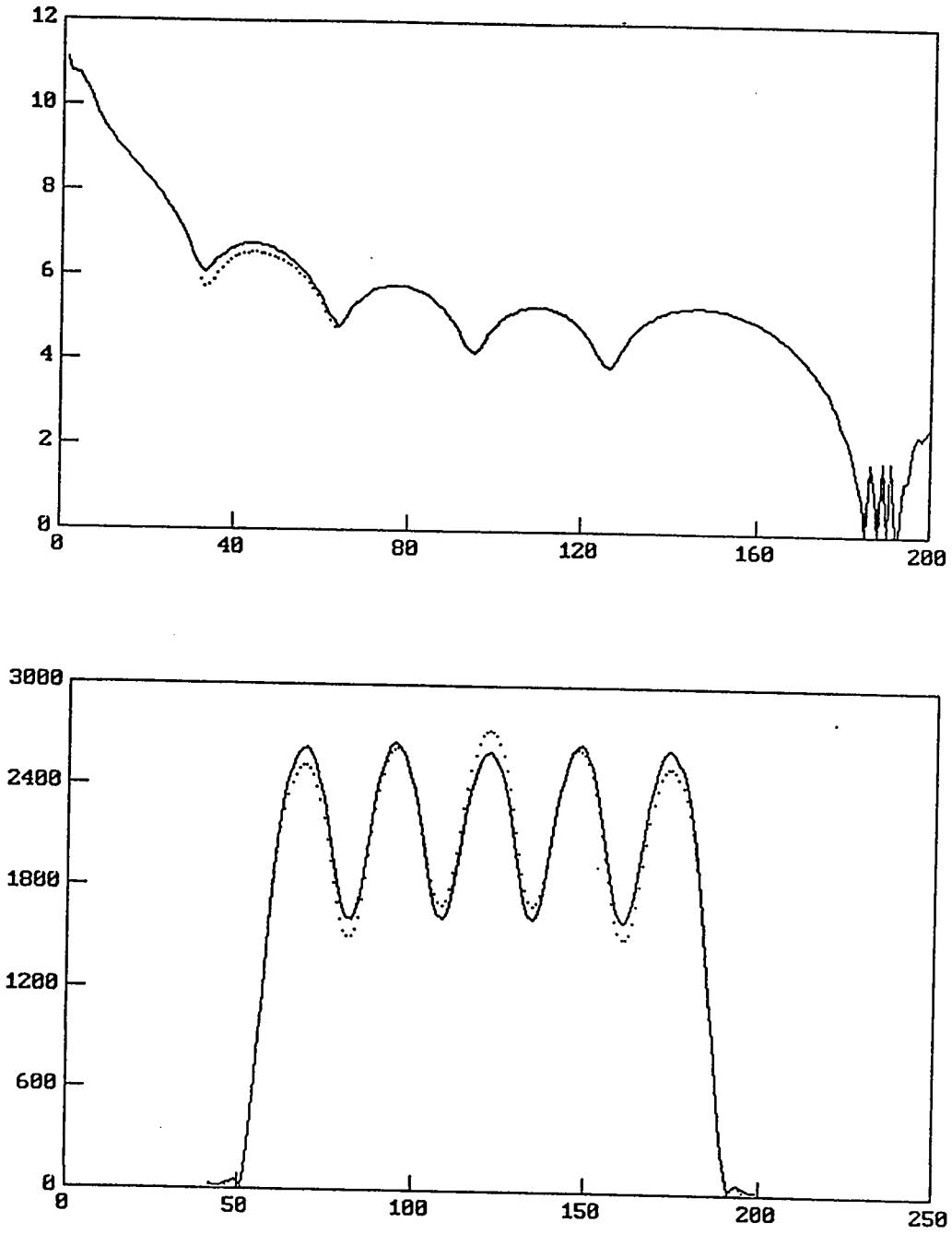

Figure 3.33: Length Determination of $q_z = 0$ Patch. Comparison of $q_z = 0$ patches and the resulting densities for the five-layer smectic-G data. The effect of the $q_z = 0$ patch with the forward model (Solid Line) and with the measured intensity (Dotted Line) substituted into the first subsidiary maxima region of $M(q_z)$. The measured intensity shows a deficit in scattering intensity in this region compared with the forward model calculation due to occlusion of the x-ray beam by the LC film aperture.

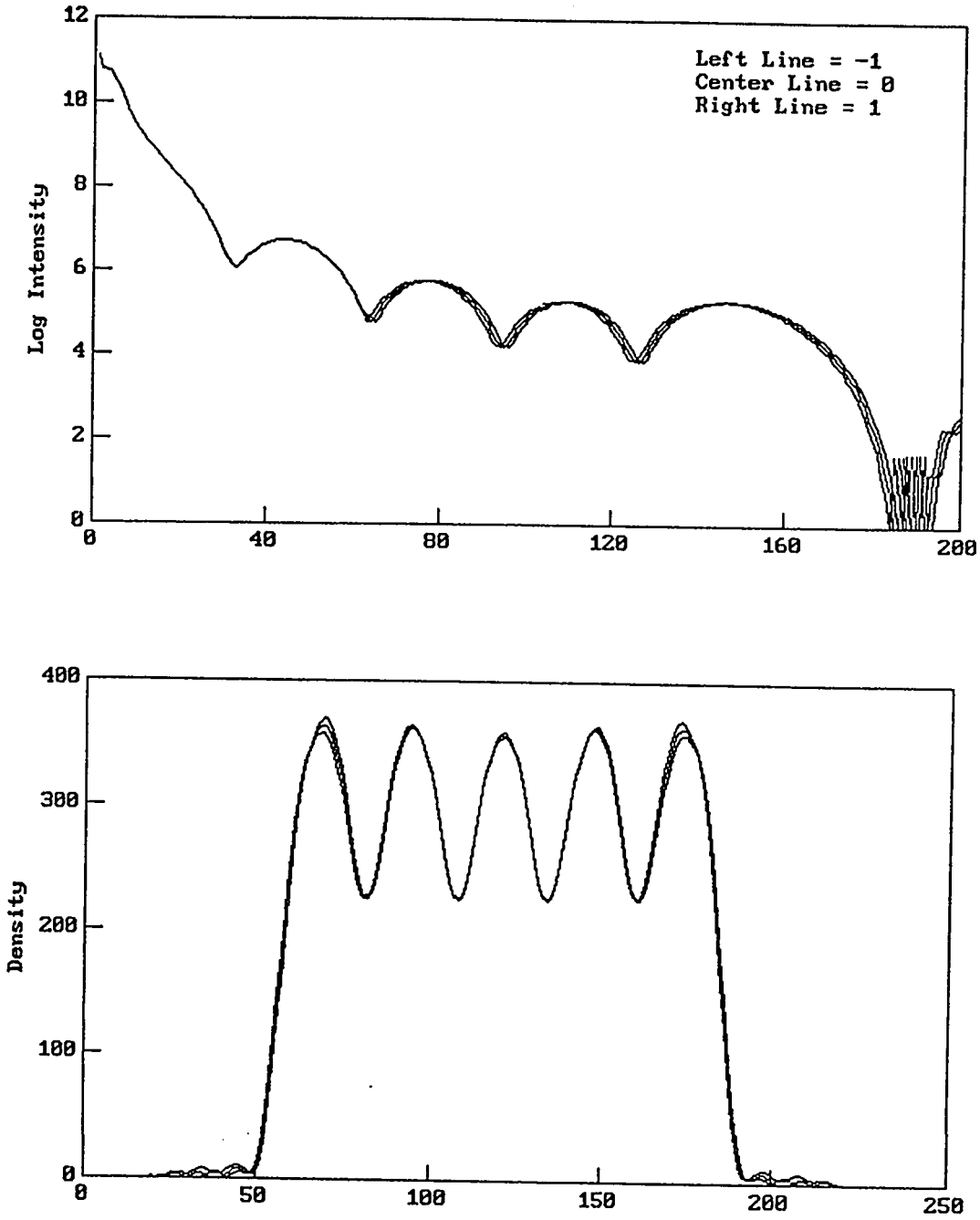

Figure 3.34: Data Translation Effects on $\rho(z)$. The model scattering intensity (Top Panel) and the resulting electron densities (Bottom Panel) for a five-layer smectic-G film resulting from translation of the data by -1, 0, and 1 units. Position 0 (middle line) gave the best match of the $q_z = 0$ patch, which is not translated, to the measured scattering intensity and the resulting density is nearly zero outside the film region. The match of the $q_z = 0$ patch to the measured scattering intensity could be determined within $\pm 1/2$ unit.

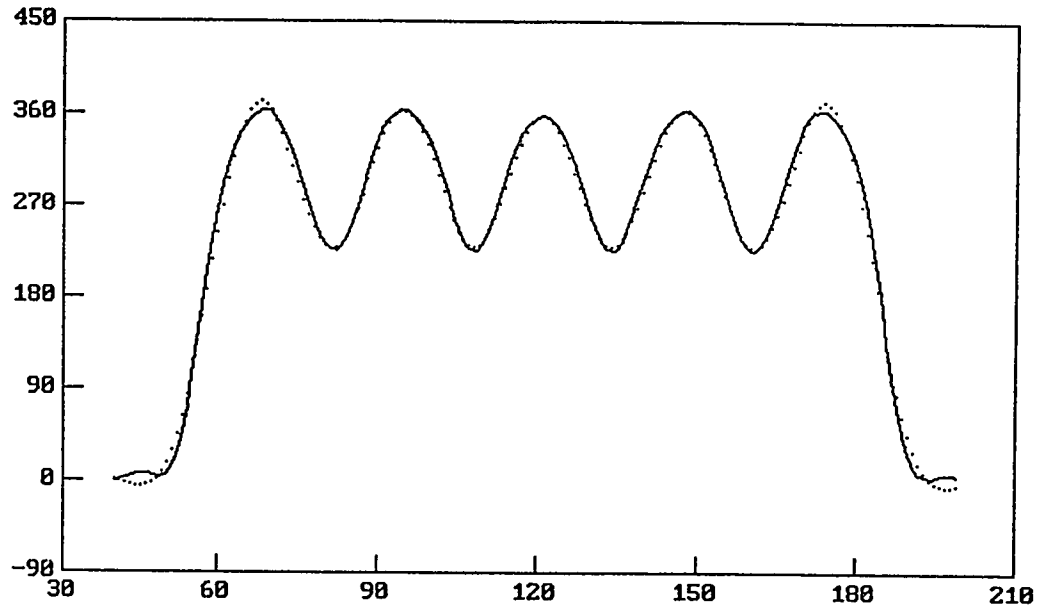

Figure 3.35: Data Truncation Effects on $\rho(z)$. A comparison between the densities derived from the five-layer smectic-G scattering intensity un-terminated (Solid Line) and terminated (Dotted Line) after the first harmonic. The density resulting from truncation after the first harmonic is nearly identical to that obtained using the full experimental data taken to a point past the second harmonic. Small changes are noted only in the shape of the peaks in the density modulation.

connecting region (about $q_z = 0.09$ Å^{-1}), the data was shifted in q_z with respect to the forward model scattering intensity. The criterion for determining the correct position of the data with respect to the $q_z = 0$ patch was that the $q_z = 0$ patch intensity fitted smoothly onto the data near $q_z = 0.09$ and that the resulting density was zero in regions outside the film. To determine the effect of this translation of the data on the shape of the resulting density, the density was calculated over a large range of translation positions. Fig. 3.34 shows the effects of shifting q_z by -1, 0, and 1 (in units of 1.4×10^{-3} Å^{-1}) from the 'best-fit' position between the forward model $q_z = 0$ patch intensity and the measured scattering intensity for the five-layer smectic-G film. As can be seen, the shape of the resulting density is not very sensitive to this shift. The value of the shift parameter was easily determined within $\pm 1/2$ unit and therefore this criterion gave a unique shape for the resulting density.

The scattering intensity from the film was measured from $q_z = 0.05$Å^{-1} to about $q_z = 0.5$Å^{-1}, past the second harmonic region where the scattering signal becomes too small to measure using a 5.6 kW rotating anode x-ray source. It is important to understand how much information is contained in the thin film diffraction pattern, where the information which makes up the important features of the electron density is located in reciprocal space, and whether the unmeasured regions would have any important consequences for determining the shape of the electron density to the accuracy of the resolution of this study. Fig. 3.35 demonstrates that since these systems are so highly disordered, all of the important Fourier components of the density are contained mainly in the interval from $q_z = 0$ to past the first harmonic. In this figure, the model scattering intensity for a five layer smectic-G film has been truncated after the first harmonic and compared to the density derived from the full data set. This plot shows that the resulting density from the truncated scattering intensity is nearly identical with the full density with only small variations produced in the sharpness of the density modulation. A scattering intensity truncated at the minimum just before the second harmonic results in a density indistinguishable from $\rho(z)$. This indicates that to the accuracy of this procedure, most of the important Fourier components of the density are contained in the first harmonic region (as expected!) and that measurements past the second harmonic are not necessary in determining the main features of the electron density.

3.10.2 Conclusions

Detailed comparisons have been made between the densities obtained from the forward model and those obtained using the direct inversion analysis. The resulting electron densities and center-of-mass densities from the direct inversion and forward model analysis have many similar features: The center-of-mass densities for thick smectic-G films are uniform with a similar FWHM of the layer positions throughout the film. The center-of-mass densities for the smectic-I/C films show enhanced surface density attributable to the influence of the monolayer hexatic smectic-I layers on each surface or the induced order due to surface tension. The densities look different than the sinusoidal density-wave found in bulk liquid smectics. There are some differences, however, between the forward model and direct inversion results: The forward model CM(z)'s are flatter in the smectic-G phase than the direct inversion CM(z)'s and, in general, the direct inversion FWHM's of the interlayer positions are wider than those found from the forward model.

Interesting questions still remain in both the forward model and direct inversion analysis. Is the forward model parameterization unique? Is the model correct? Are the model parameters independent? The direct inversion method has more inherent 'noise' in the resulting densities due to the way it extracts the signal in the presence of measurement errors than the forward model method. Both methods lack information about the measured scattering intensity near $q_z = 0$ and Fourier components in the density have not been directly probed experimentally. The application of these two techniques to the same data provides complementary information about the interlayer structure of these FSLC films, but questions remain about the detailed Fourier components of the density with small and large spatial frequencies.

3.11 Direct Inversion and Forward Model Results

The results from the direct inversion and forward analysis determinations of the electron densities and center-of-mass densities are displayed in this section on the following pages:

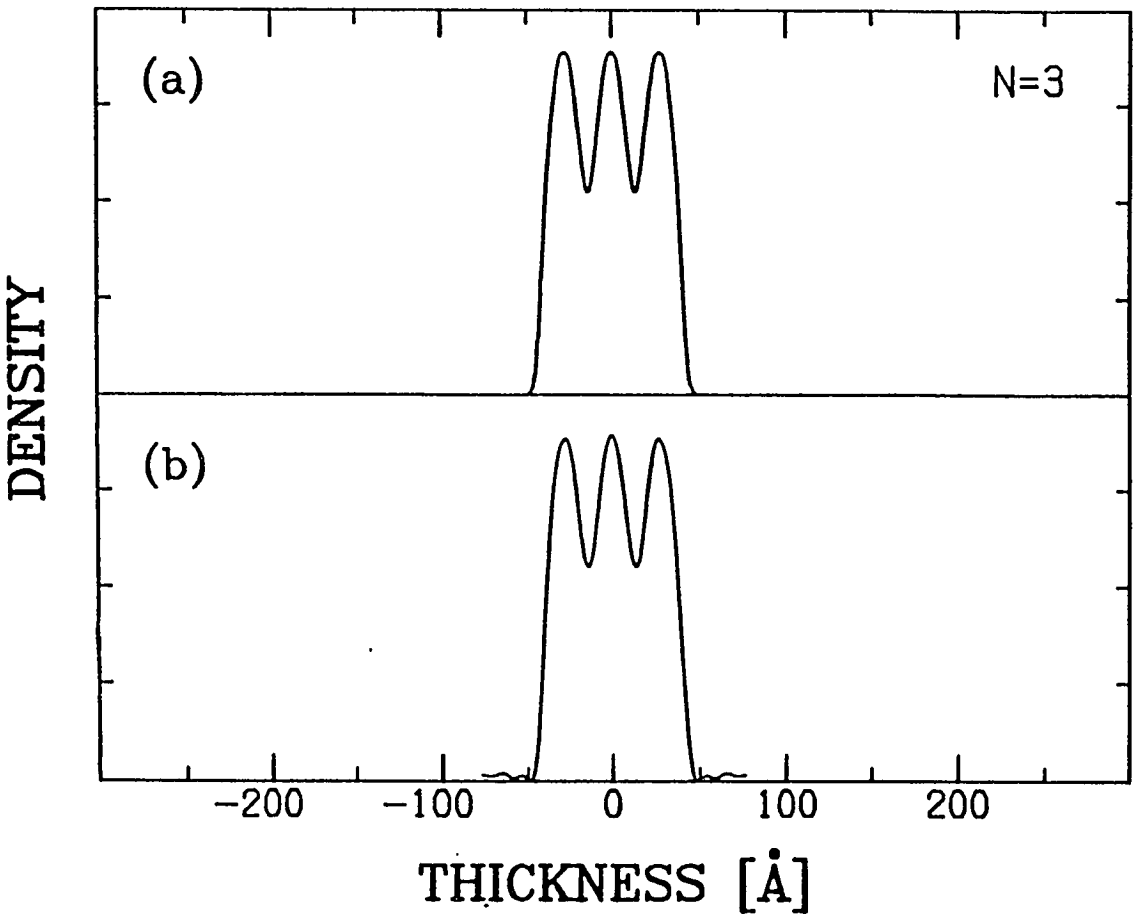

Figure 3.36: 3-Layer Smectic-G Density. Comparison of the electron density, $\rho(z)$, for three-layer smectic-G films for (a) Forward Model, (b) Direct Inversion.

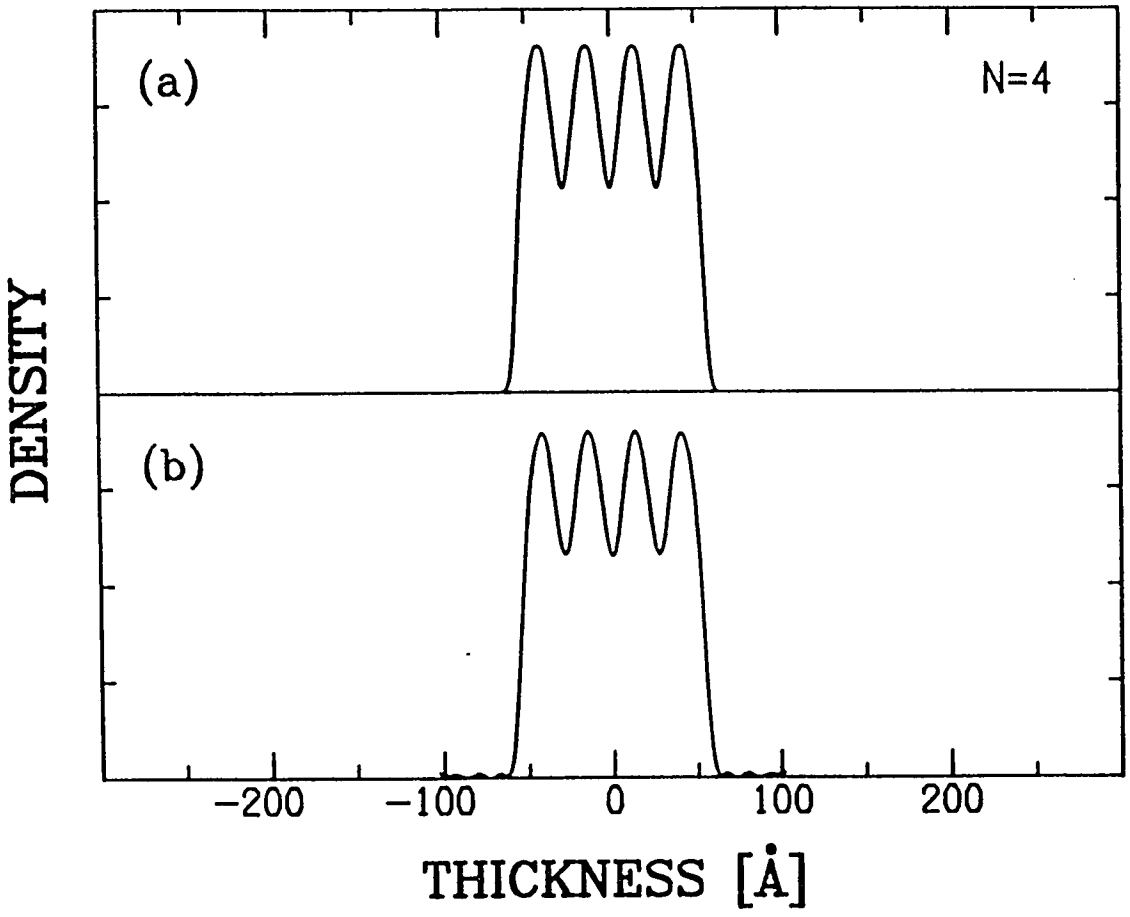

Figure 3.37: 4-Layer Smectic-G Density. Comparison of the electron density, $\rho(z)$, for four-layer smectic-G films for (a) Forward Model, (b) Direct Inversion.

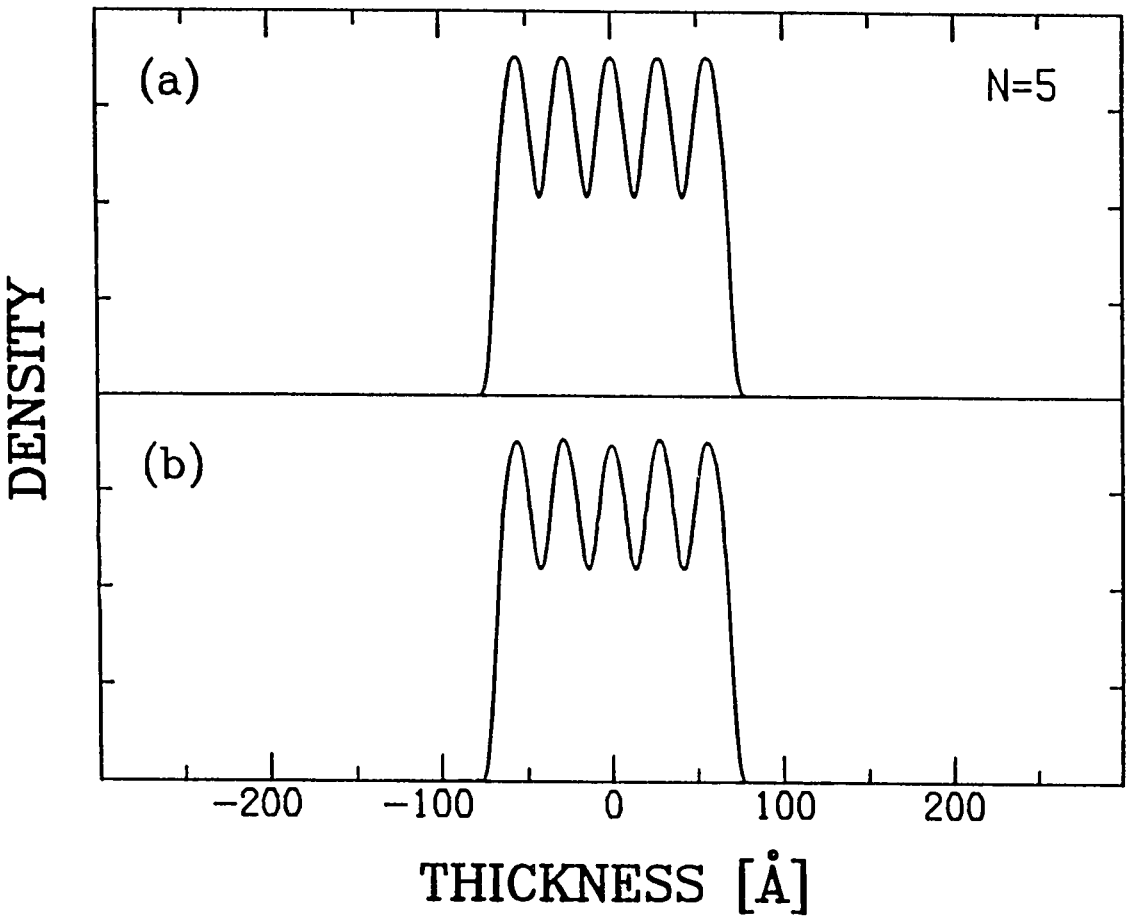

Figure 3.38: 5-Layer Smectic-G Density. Comparison of the electron density, $\rho(z)$, for the five-layer smectic-G films for (a) Forward Model, (b) Direct Inversion.

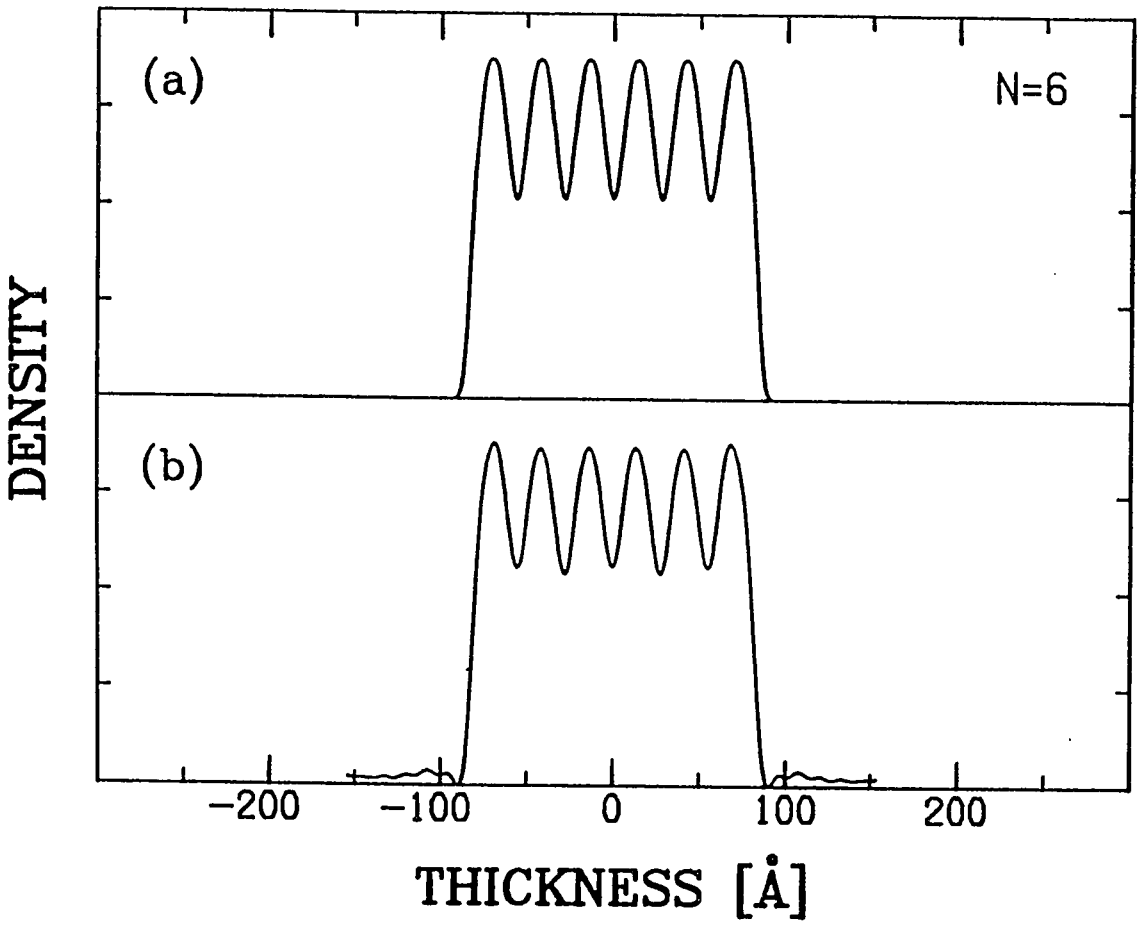

Figure 3.39: 6-Layer Smectic-G Density. Comparison of the electron density, $\rho(z)$, for the six-layer smectic-G films for (a) Forward Model, (b) Direct Inversion.

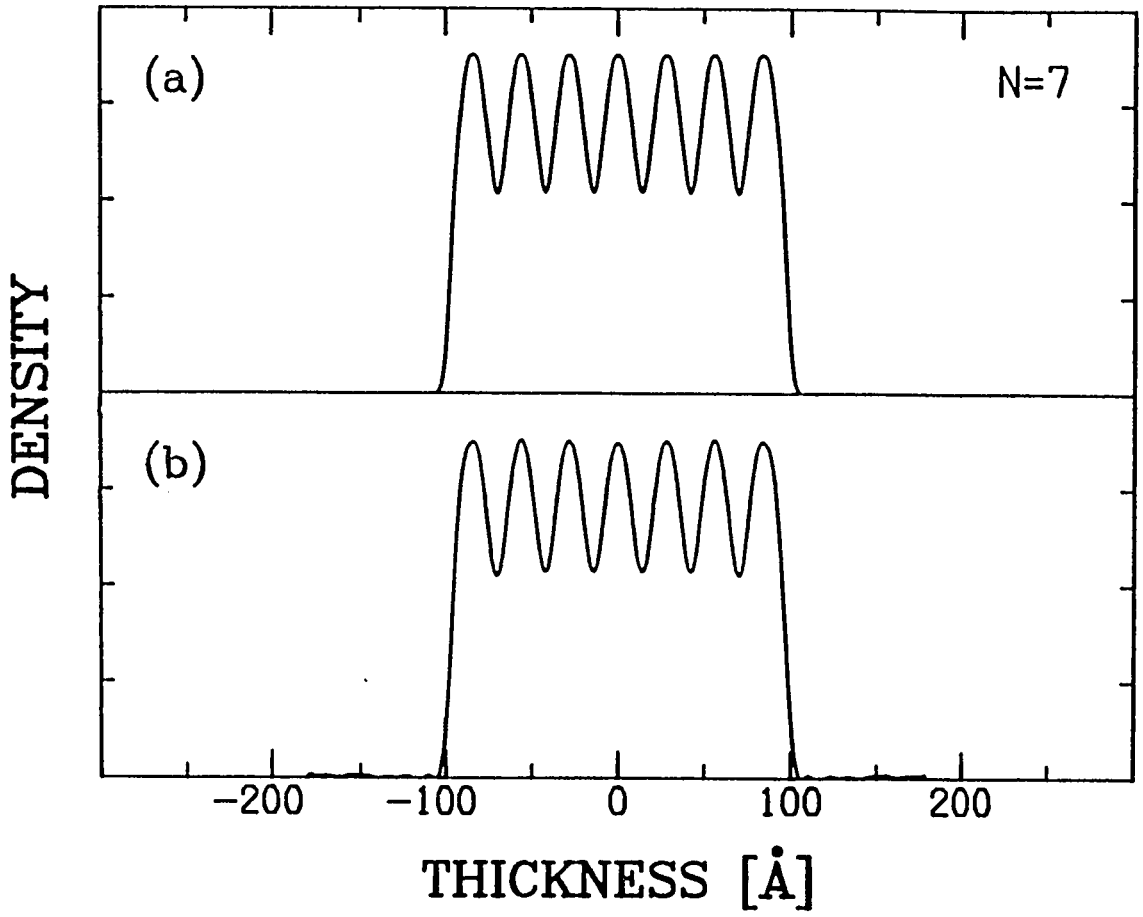

Figure 3.40: 7-Layer Smectic-G Density. Comparison of the electron density, $\rho(z)$, for the seven-layer smectic-G films for (a) Forward Model, (b) Direct Inversion.

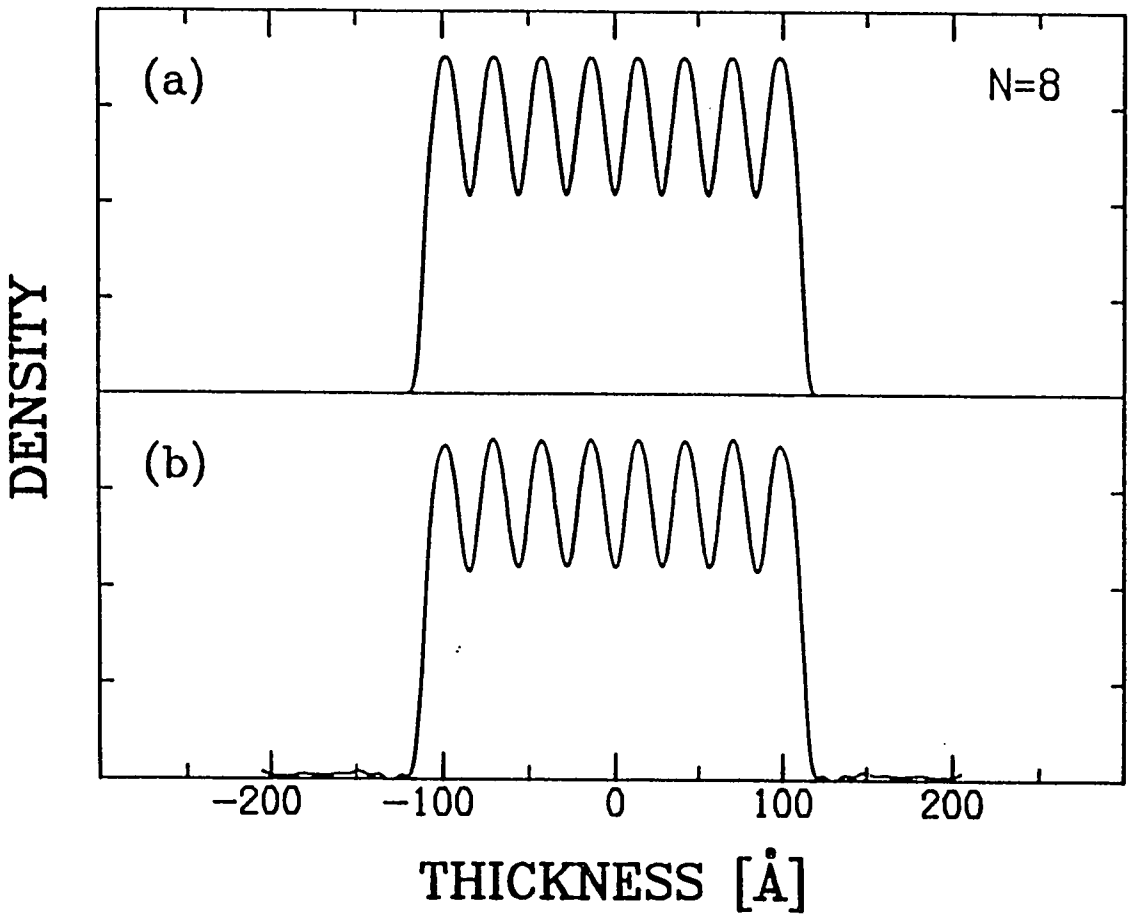

Figure 3.41: 8-Layer Smectic-G Density. Comparison of the electron density, $\rho(z)$, for the eight-layer smectic-G films for (a) Forward Model, (b) Direct Inversion.

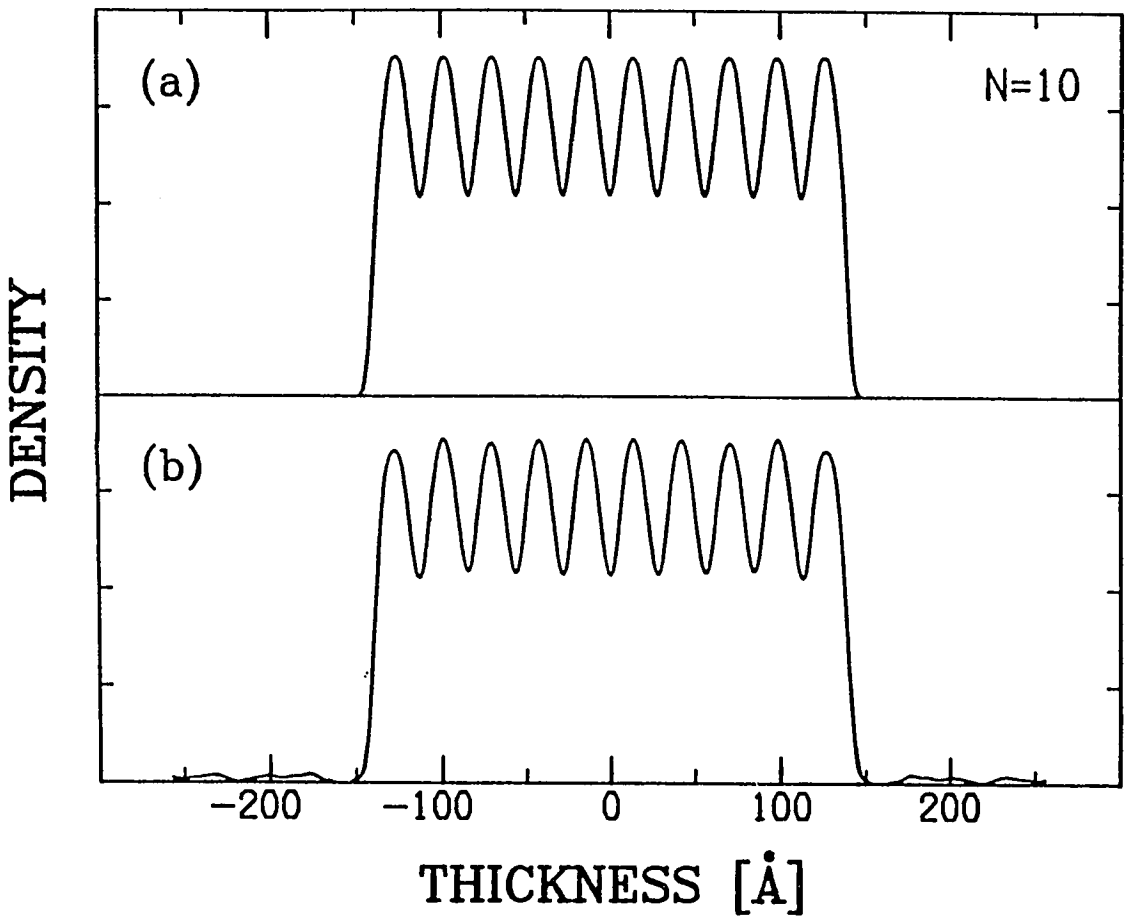

Figure 3.42: 10-Layer Smectic-G Density. Comparison of the electron density, $\rho(z)$, for the ten-layer smectic-G films for (a) Forward Model, (b) Direct Inversion.

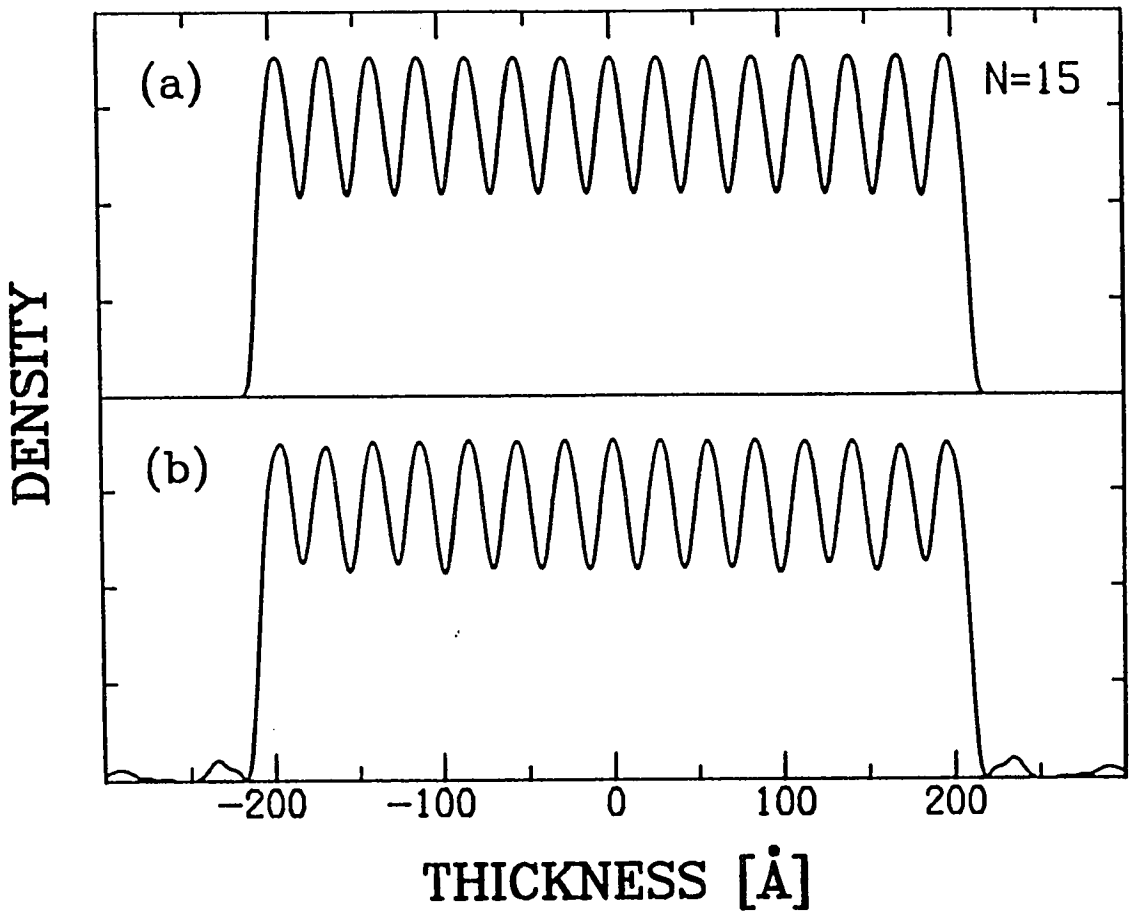

Figure 3.43: 15-Layer Smectic-G Density. Comparison of the electron density, $\rho(z)$, for the 15-layer smectic-G films for (a) Forward Model, (b) Direct Inversion.

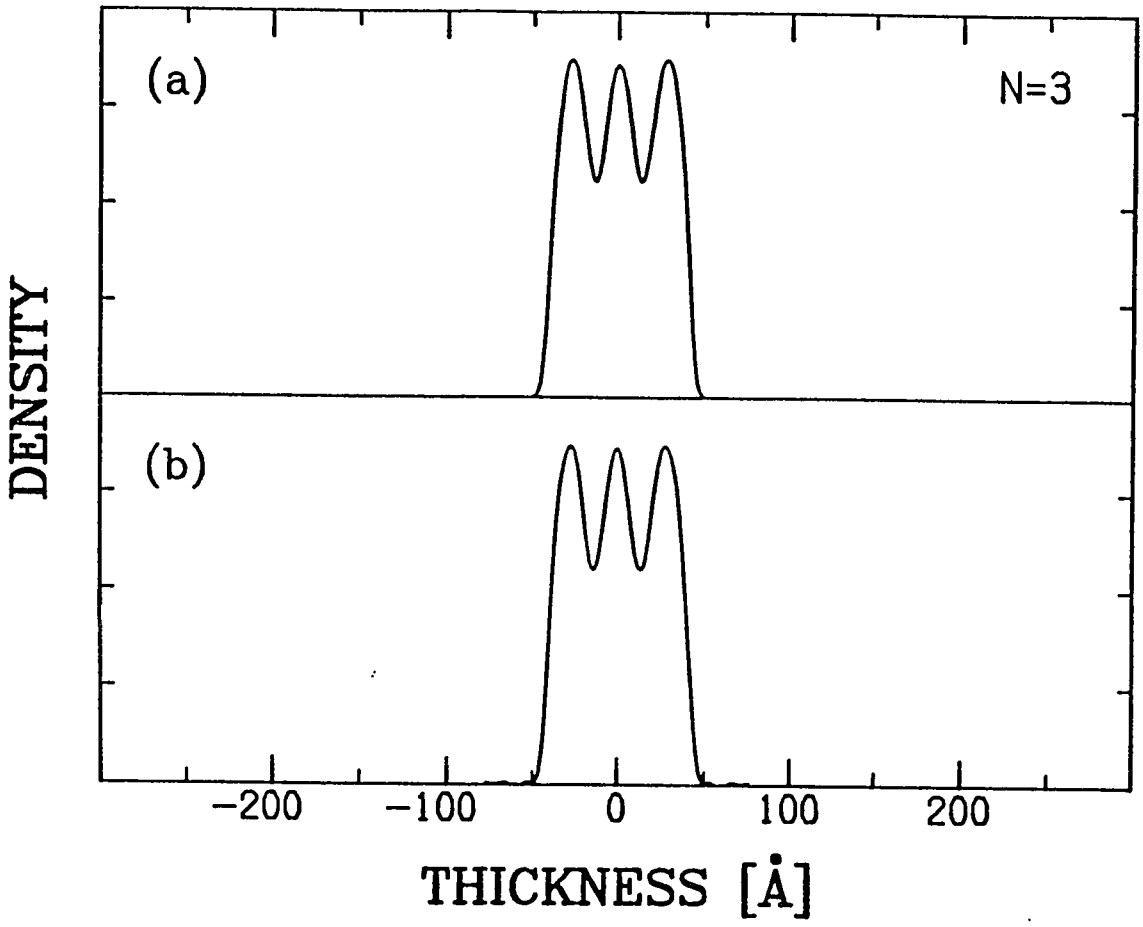

Figure 3.44: 3-Layer Smectic-I/C Density. Comparison of the electron density, $\rho(z)$, for the three-layer smectic-I/C film for (a) Forward Model, (b) Direct Inversion.

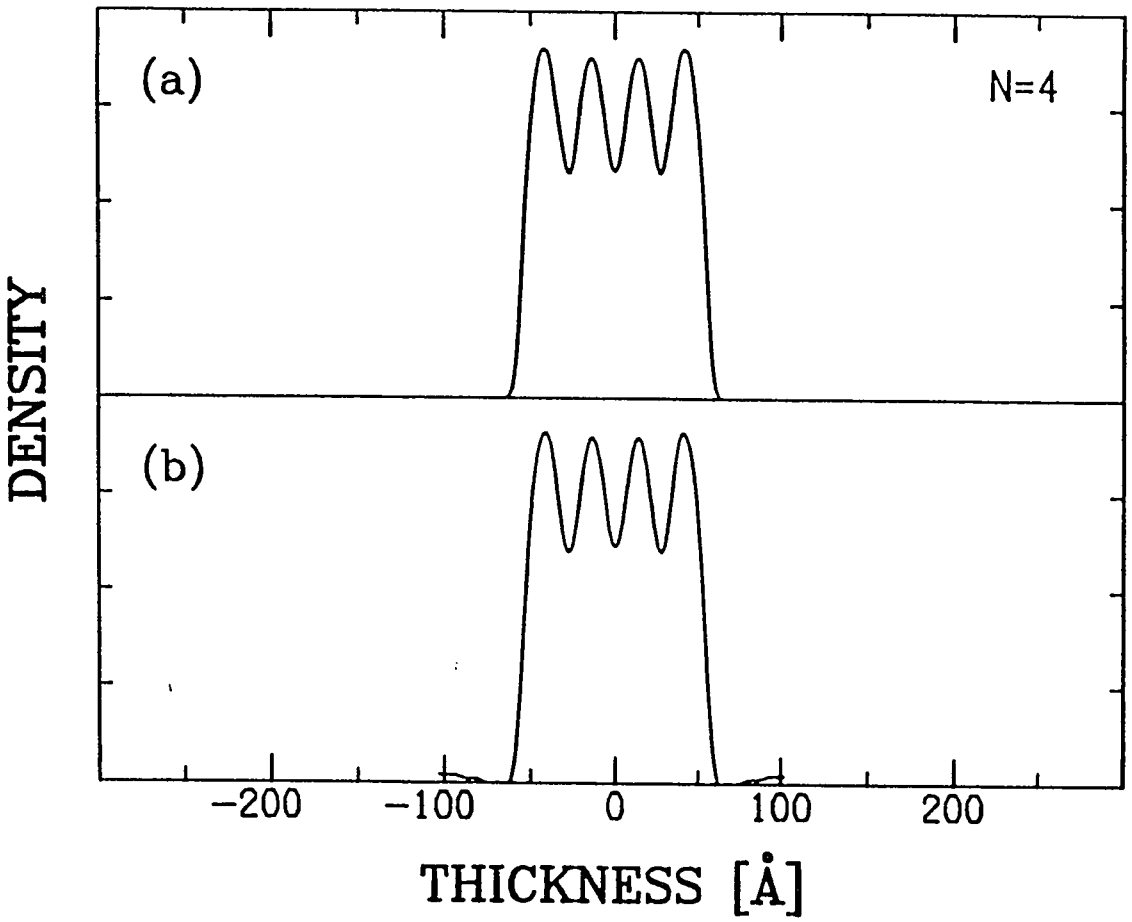

Figure 3.45: 4-Layer Smectic-I/C Density. Comparison of the electron density, $\rho(z)$, for the four-layer smectic-I/C film for (a) Forward Model, (b) Direct Inversion.

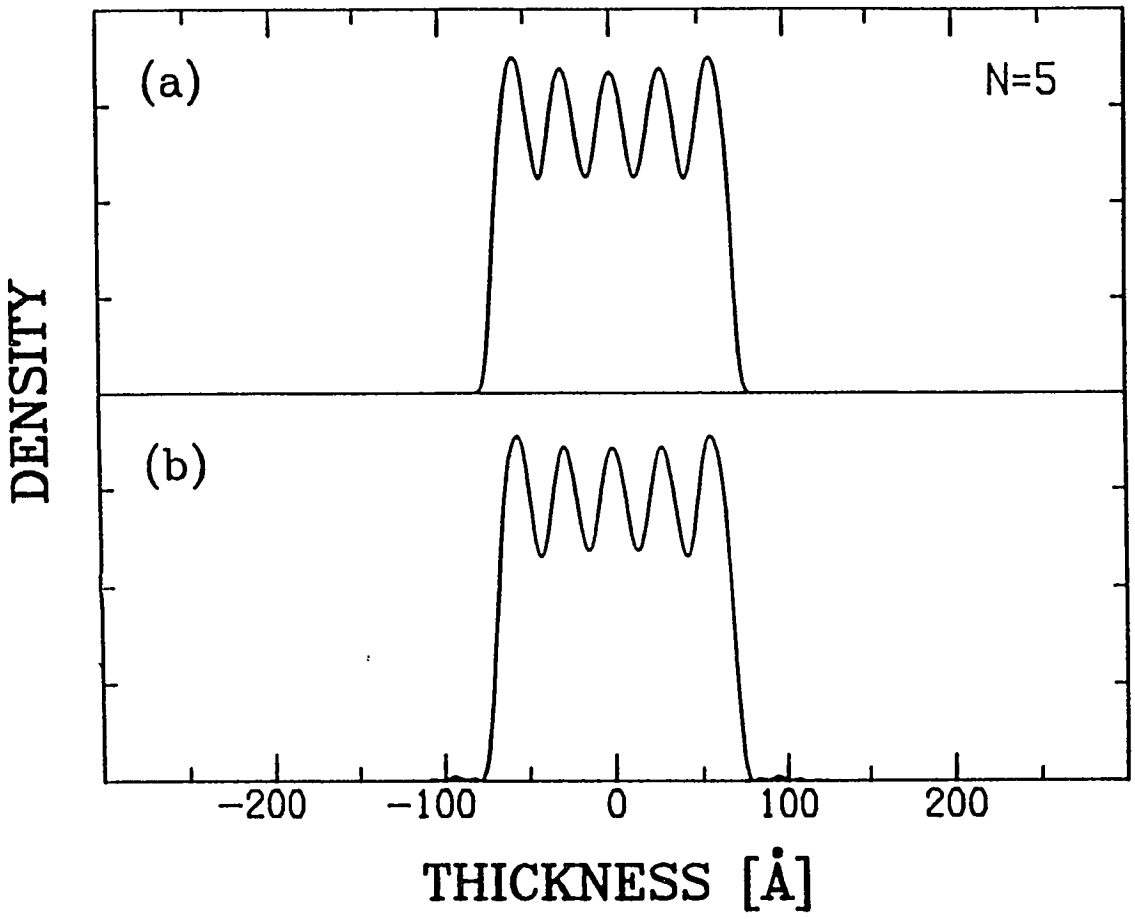

Figure 3.46: 5-Layer Smectic-I/C Density. Comparison of the electron density, $\rho(z)$, for the five-layer smectic-I/C film for (a) Forward Model, (b) Direct Inversion.

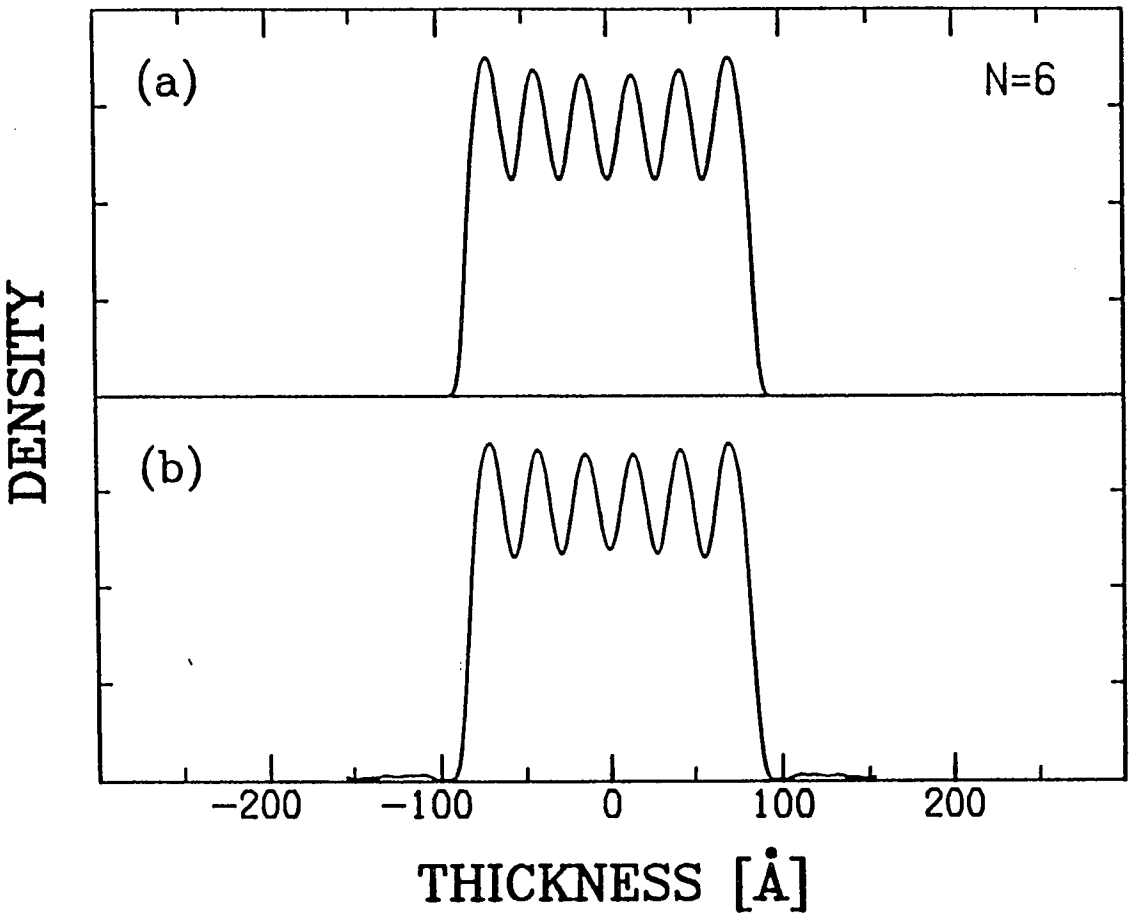

Figure 3.47: 6-Layer Smectic-I/C Density. Comparison of the electron density, $\rho(z)$, for the six-layer smectic-I/C film for (a) Forward Model, (b) Direct Inversion.

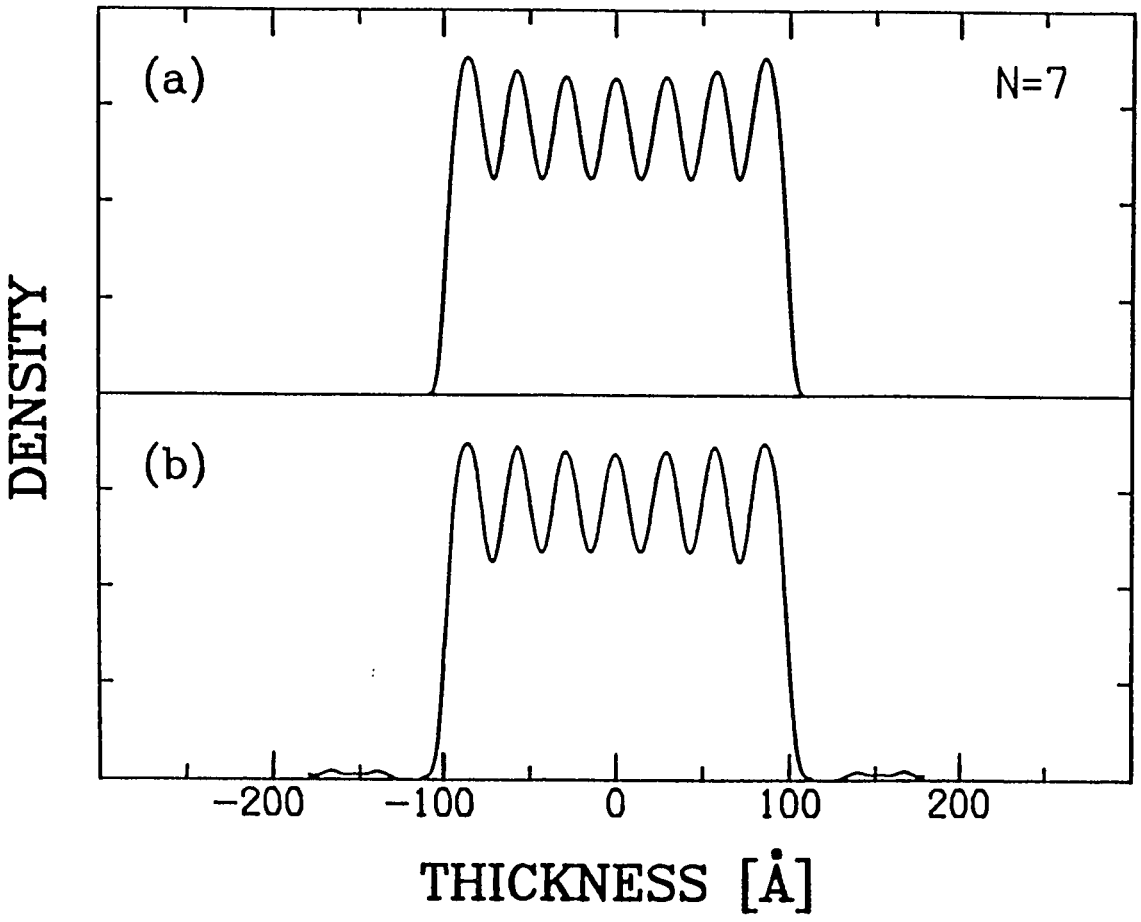

Figure 3.48: 7-Layer Smectic-I/C Density. Comparison of the electron density, $\rho(z)$, for the seven-layer smectic-I/C film for (a) Forward Model, (b) Direct Inversion.

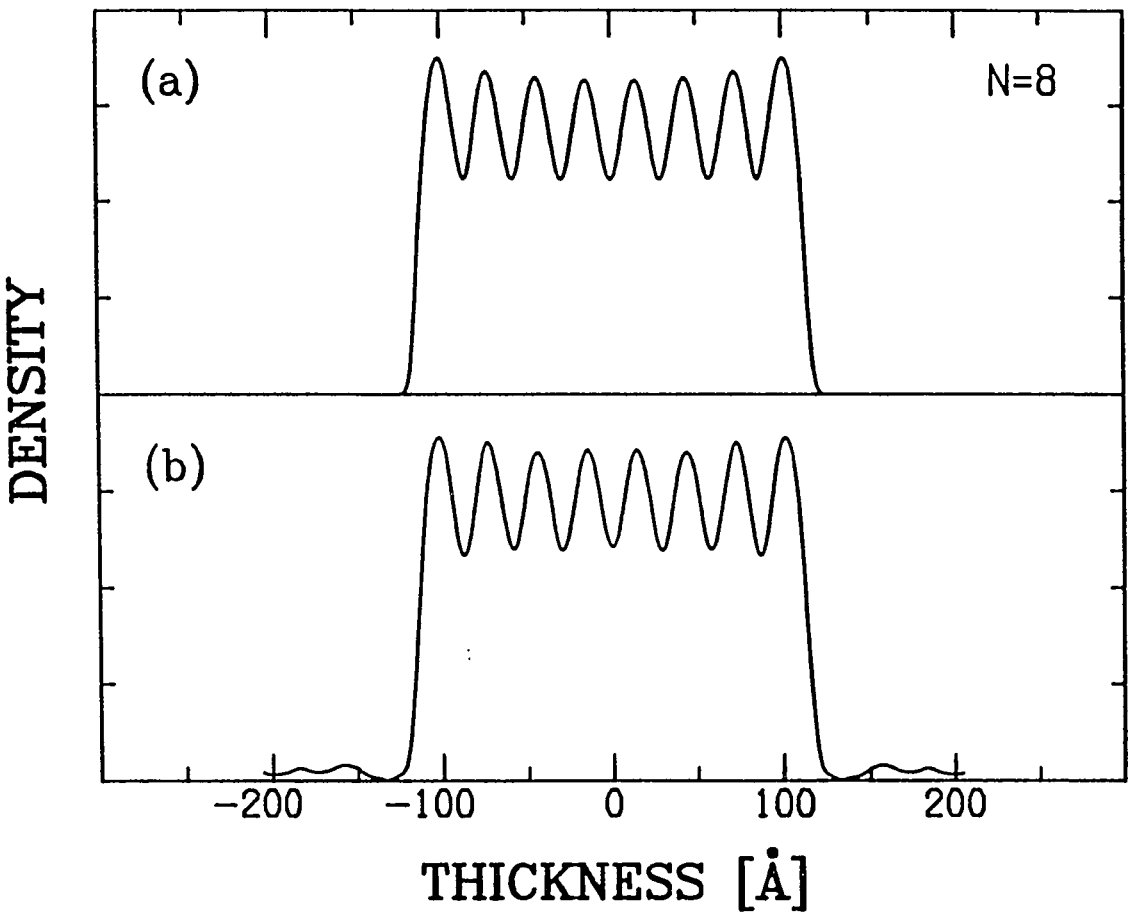

Figure 3.49: 8-Layer Smectic-I/C Density. Comparison of the electron density, $\rho(z)$, for the eight-layer smectic-I/C film for (a) Forward Model, (b) Direct Inversion.

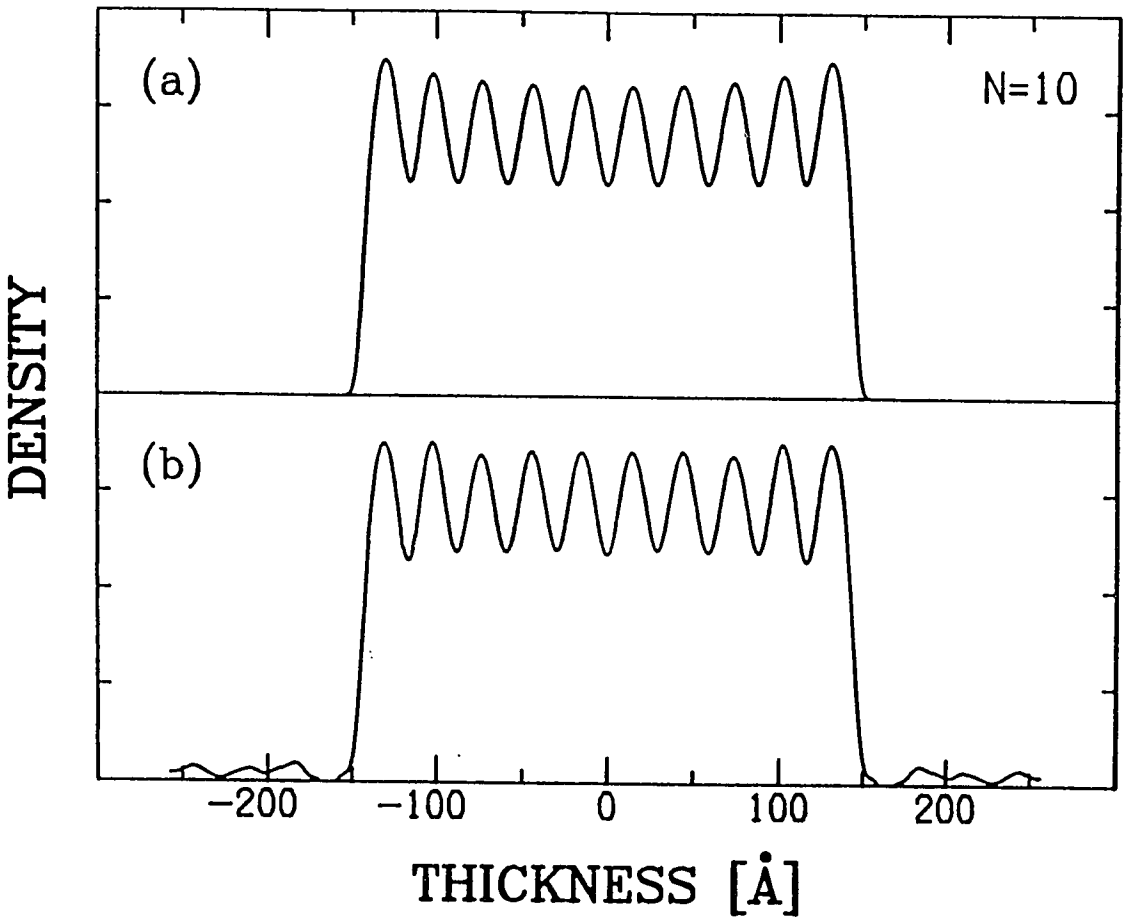

Figure 3.50: 10-Layer Smectic-I/C Density. Comparison of the electron density, $\rho(z)$, for the ten-layer smectic-I/C film for (a) Forward Model, (b) Direct Inversion.

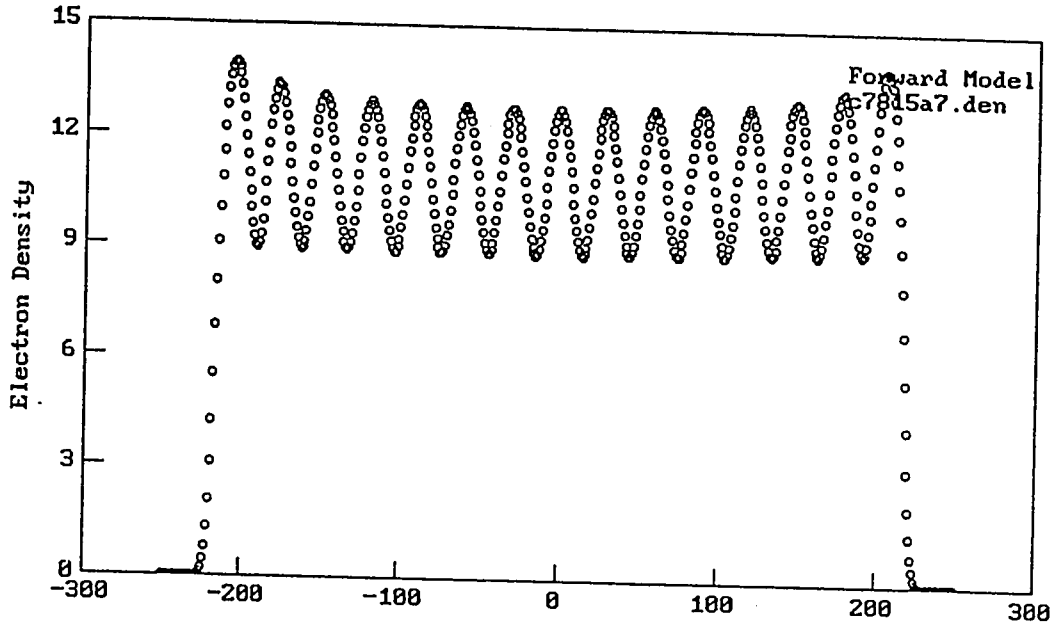

Figure 3.51: 15-Layer Smectic-I/C Density. Comparison of the electron density, $\rho(z)$, for the 15-layer smectic-I/C film for (a) Forward Model

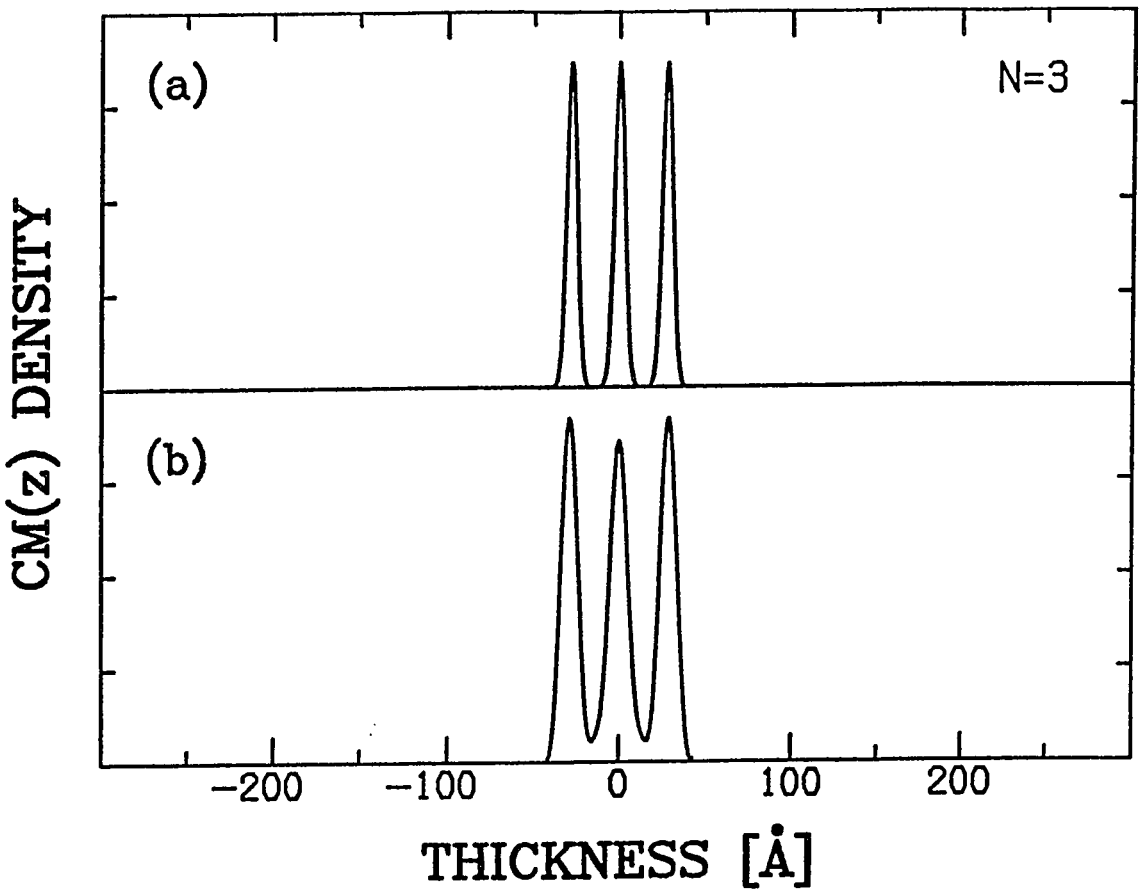

Figure 3.52: 3-Layer Smectic-G Center-of-Mass Density. Comparison of the center-of-mass density for the three-layer smectic-G film for (a) Forward Model, (b) Direct Inversion.

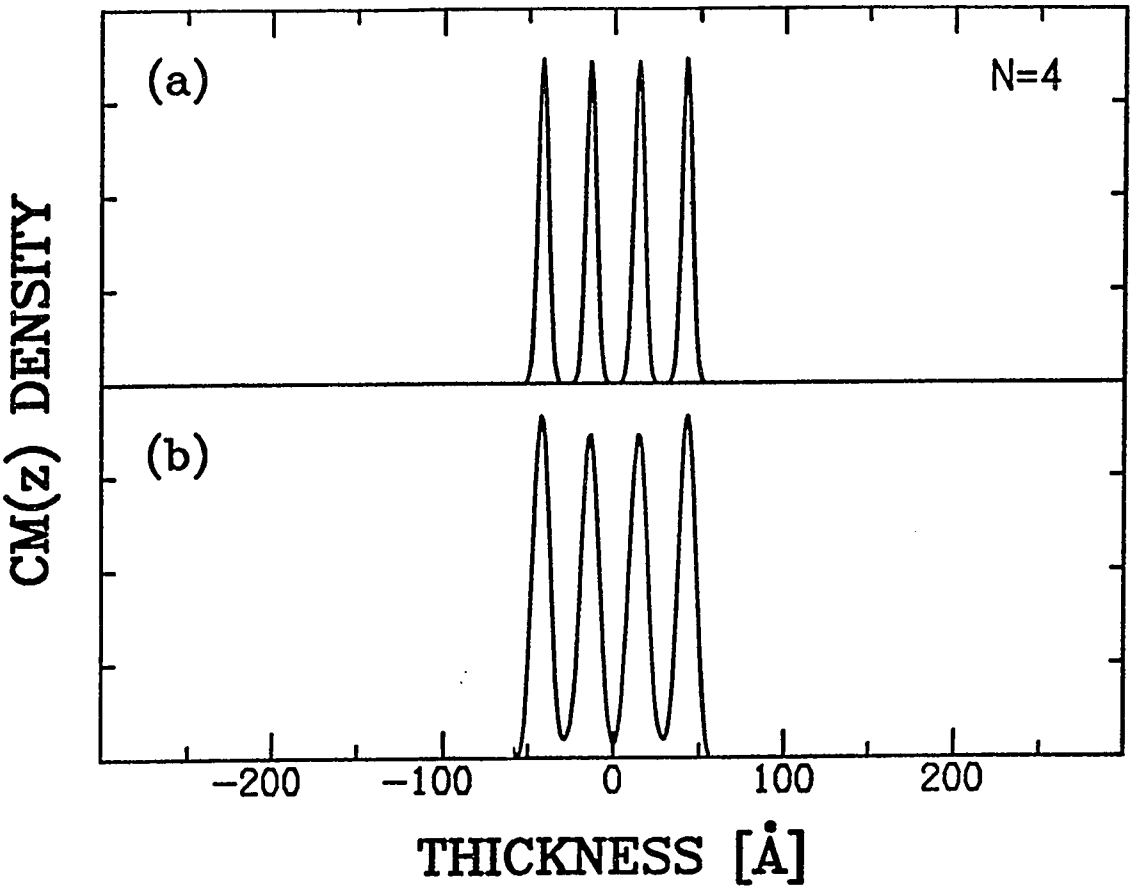

Figure 3.53: 4-Layer Smectic-G Center-of-Mass Density. Comparison of the center-of-mass density for the four-layer smectic-G film for (a) Forward Model, (b) Direct Inversion.

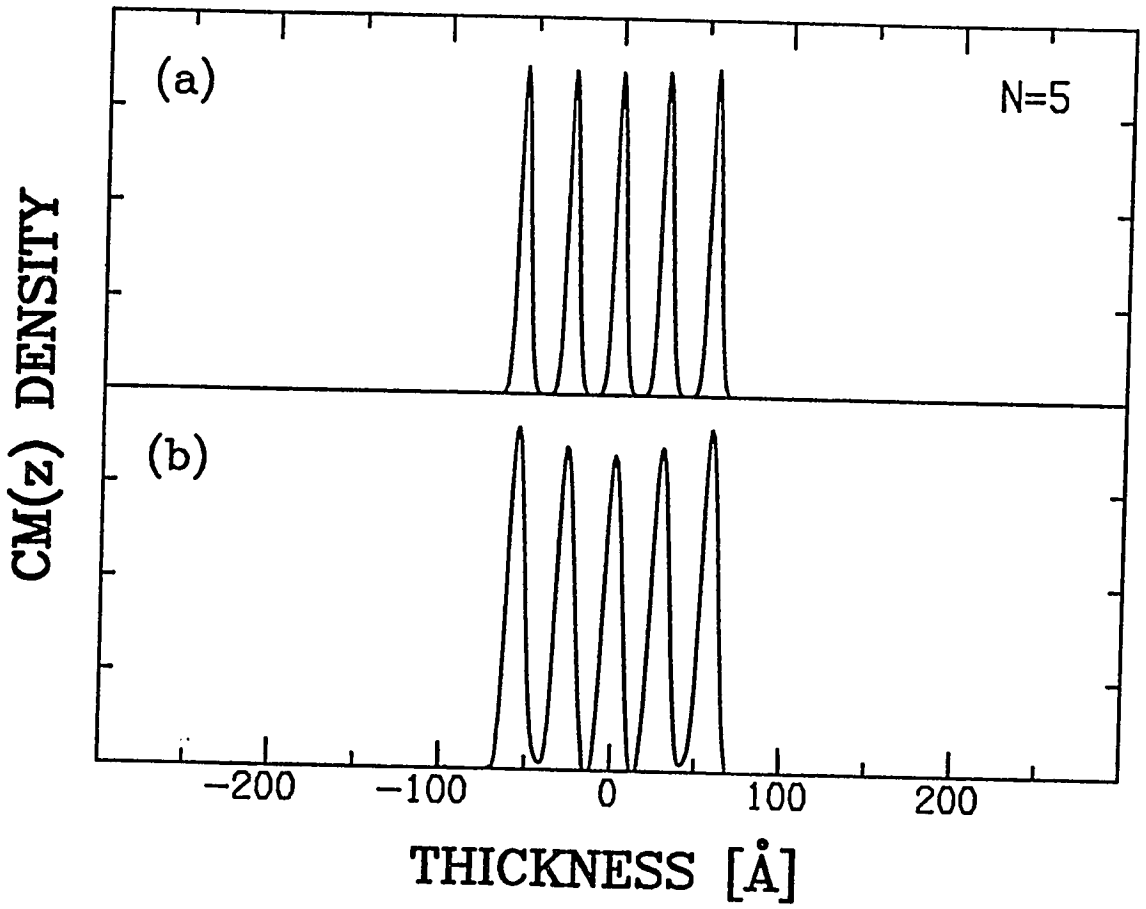

Figure 3.54: 5-Layer Smectic-G Center-of-Mass Density. Comparison of the center-of-mass density for the five-layer smectic-G film for (a) Forward Model, (b) Direct Inversion.

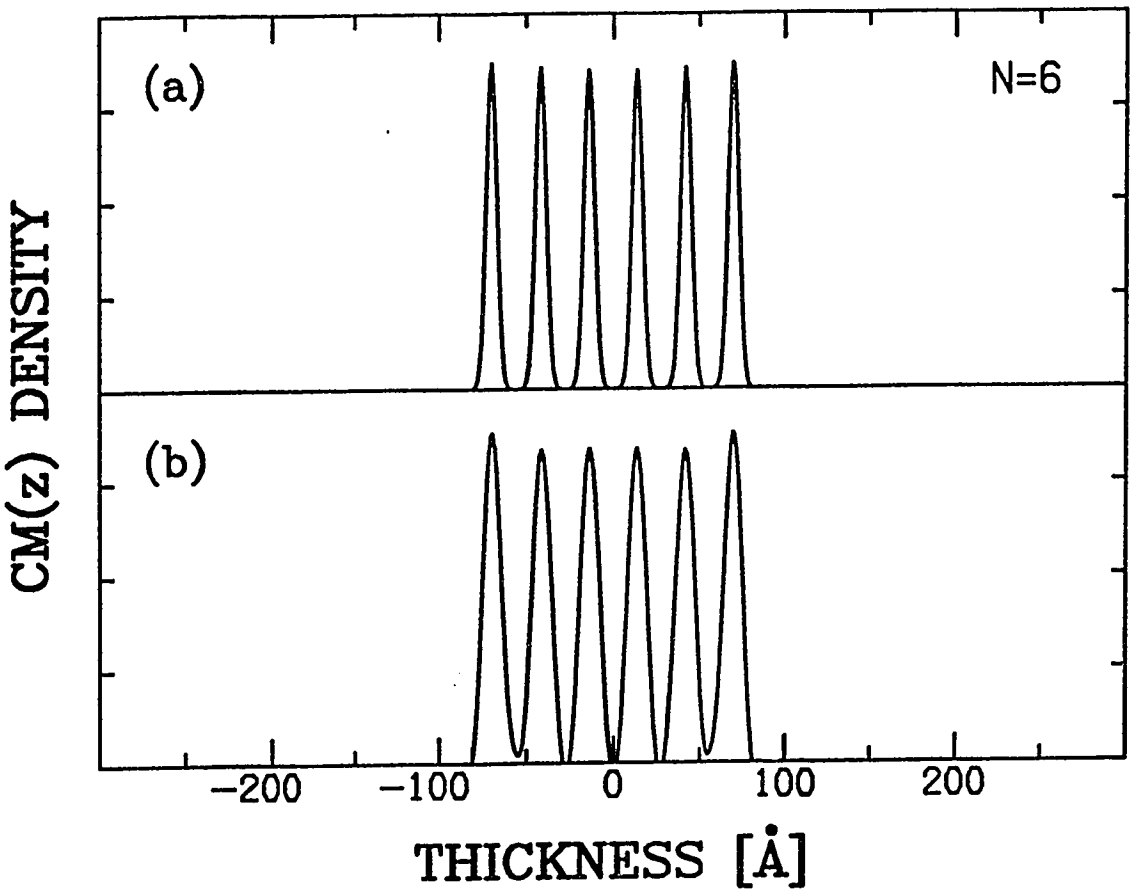

Figure 3.55: 6-Layer Smectic-G Center-of-Mass Density. Comparison of the center-of-mass density for the six-layer smectic-G film for (a) Forward Model, (b) Direct Inversion.

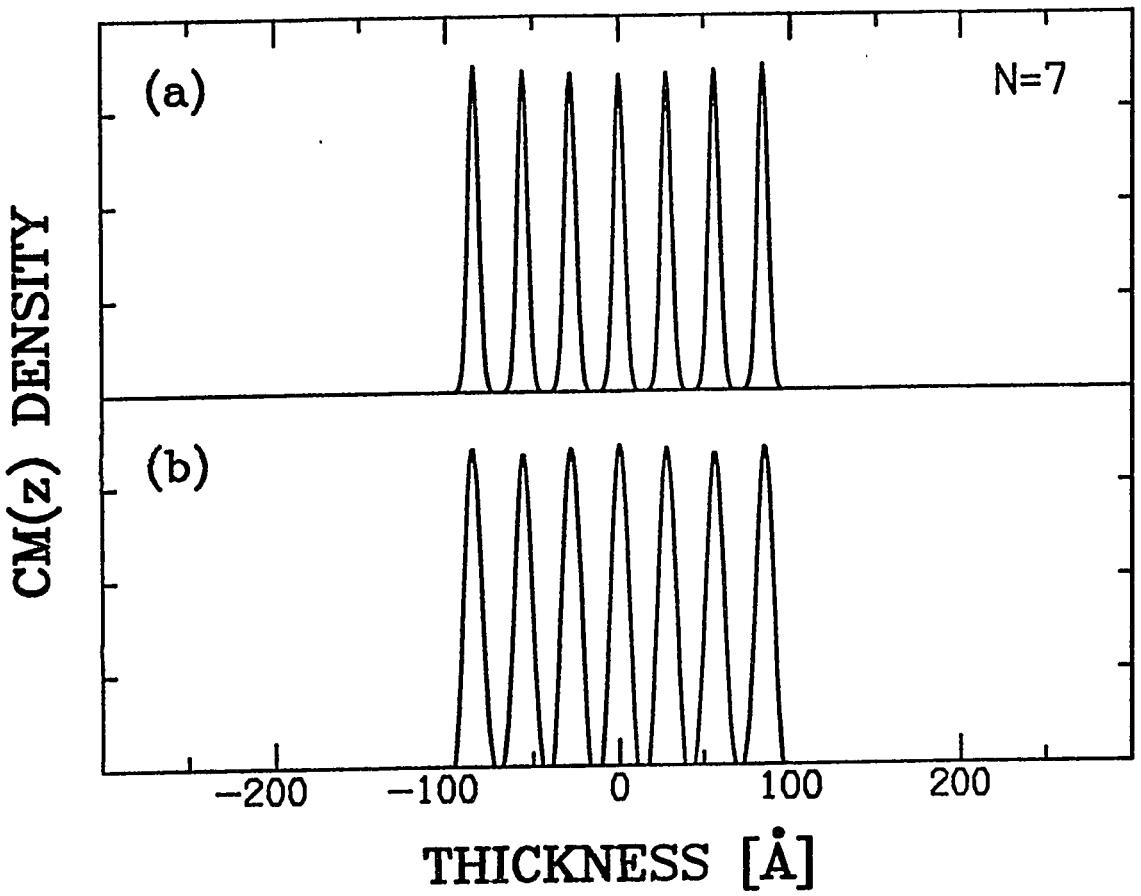

Figure 3.56: 7-Layer Smectic-G Center-of-Mass Density. Comparison of the center-of-mass density for the seven-layer smectic-G film for (a) Forward Model, (b) Direct Inversion.

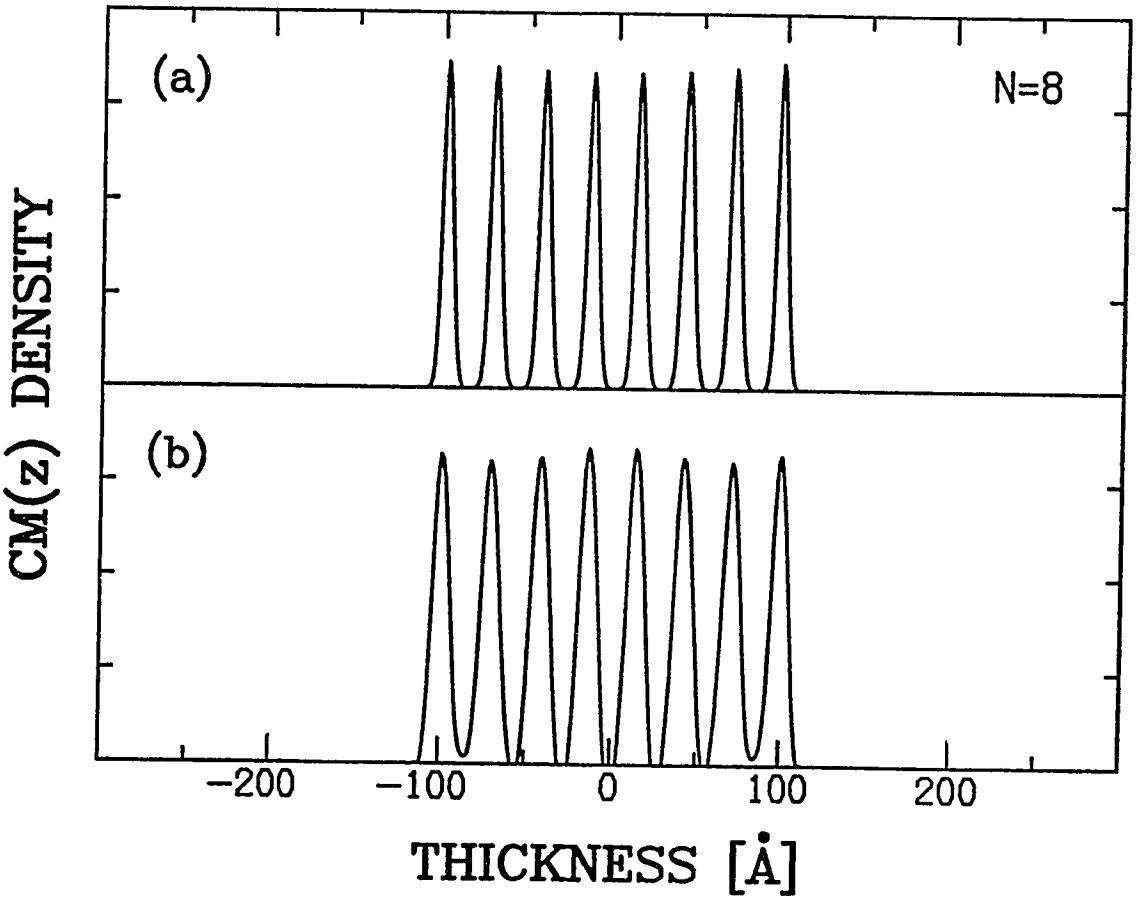

Figure 3.57: 8-Layer Smectic-G Center-of-Mass Density. Comparison of the center-of-mass density for the eight-layer smectic-G film for (a) Forward Model, (b) Direct Inversion.

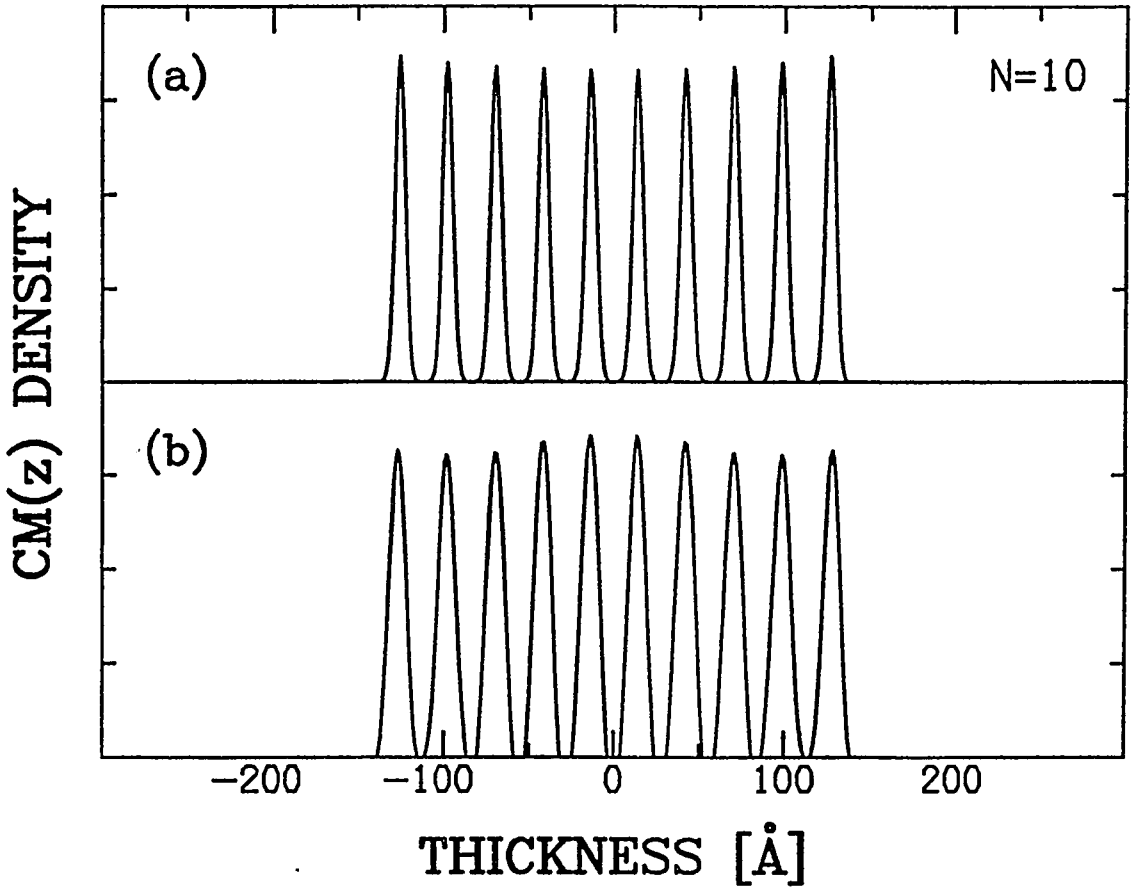

Figure 3.58: 10-Layer Smectic-G Center-of-Mass Density. Comparison of the center-of-mass density for the ten-layer smectic-G film for (a) Forward Model, (b) Direct Inversion.

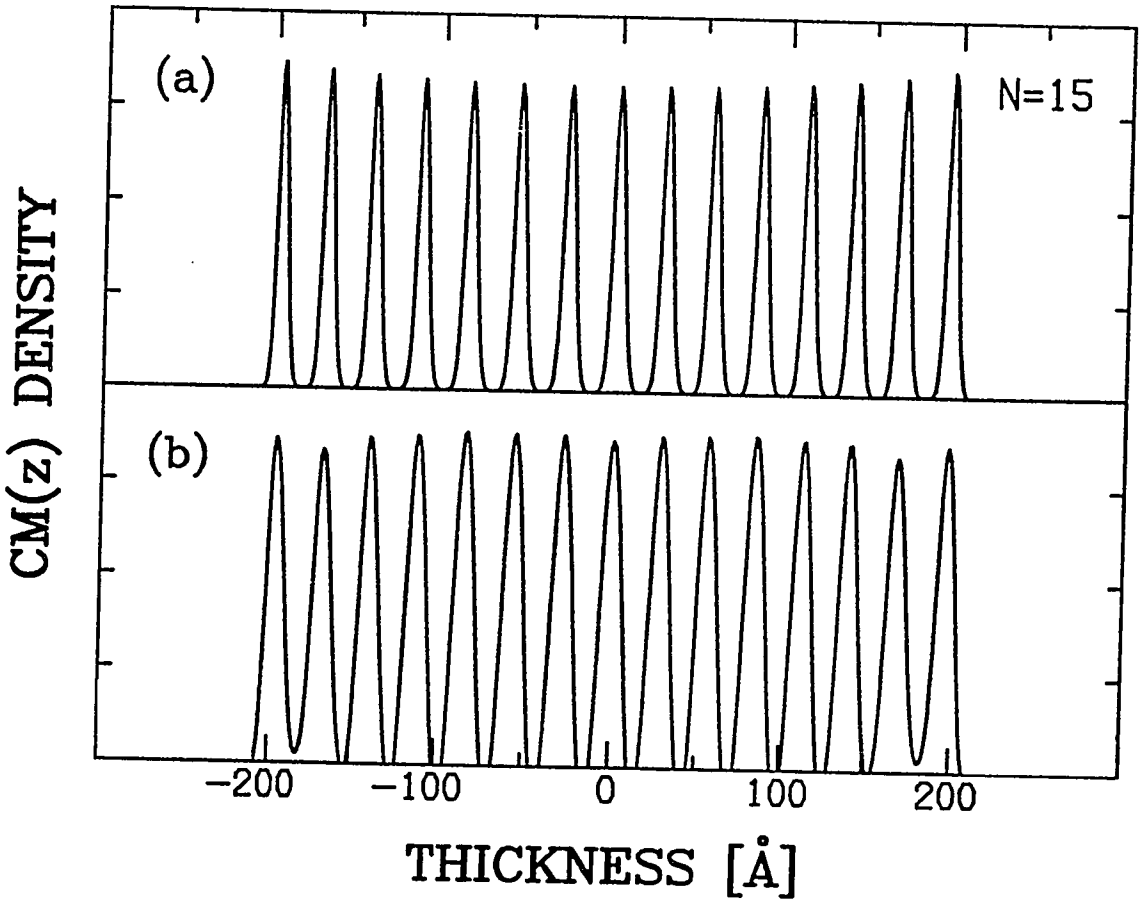

Figure 3.59: 15-Layer Smectic-G Center-of-Mass Density. Comparison of the center-of-mass density for the 15-layer smectic-G film for (a) Forward Model, (b) Direct Inversion.

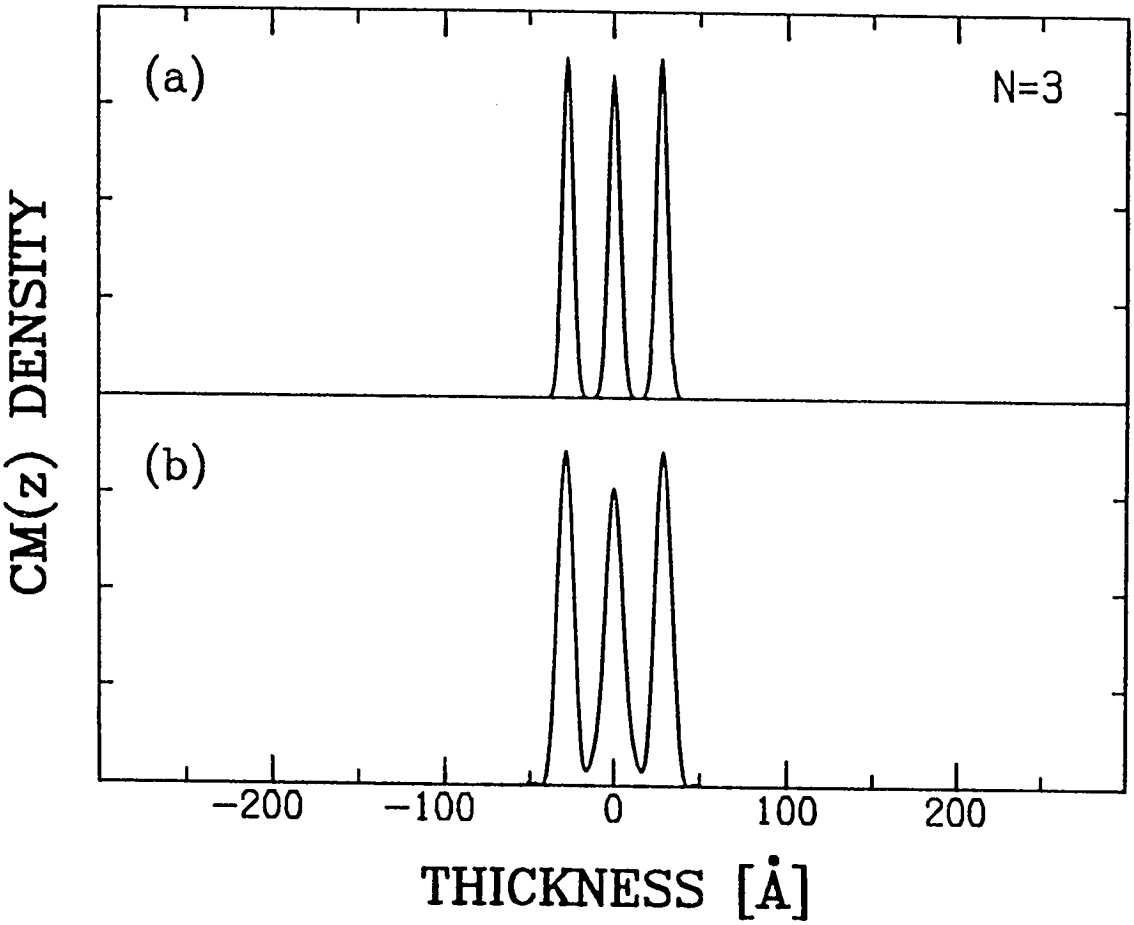

Figure 3.60: 3-Layer Smectic-I/C Center-of-Mass Density. Comparison of the center-of-mass density for the three-layer smectic-I/C film for (a) Forward Model, (b) Direct Inversion.

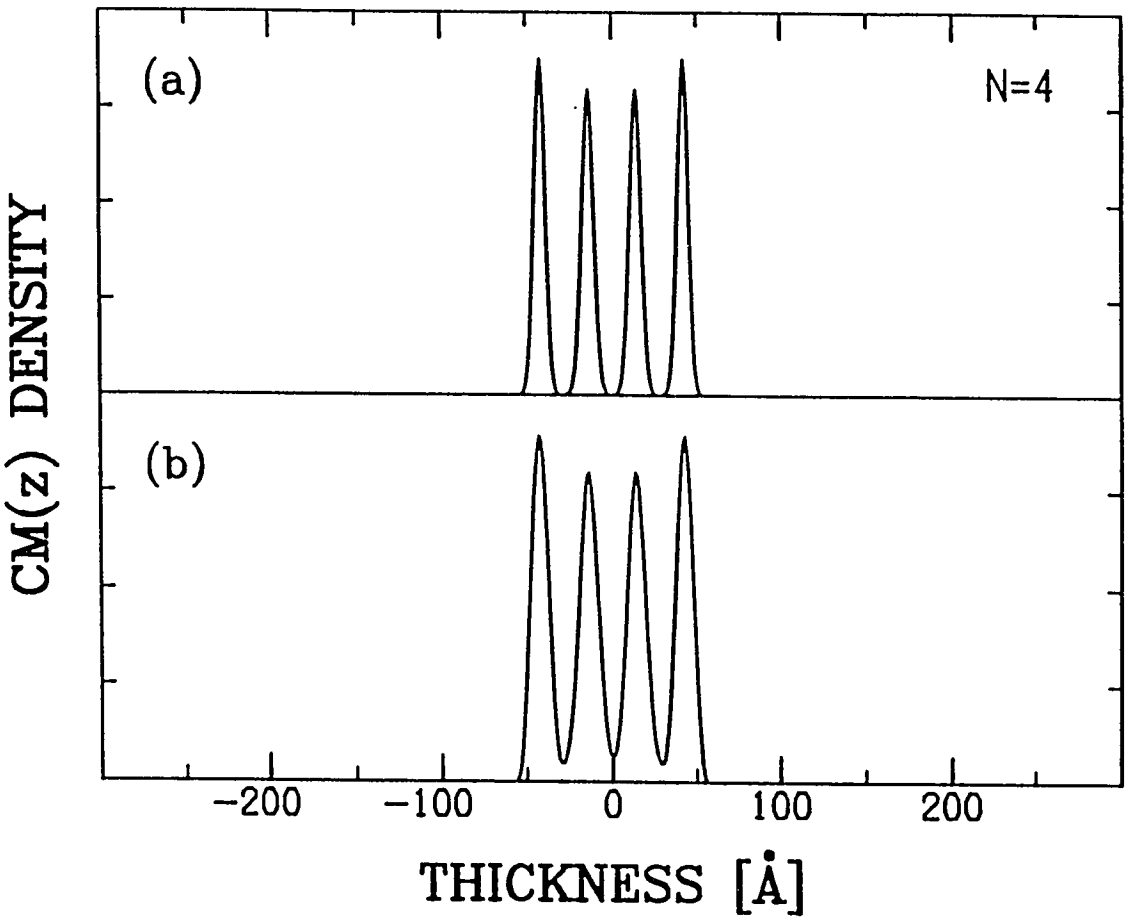

Figure 3.61: 4-Layer Smectic-I/C Center-of-Mass Density. Comparison of the center-of-mass density for the four-layer smectic-I/C film for (a) Forward Model, (b) Direct Inversion.

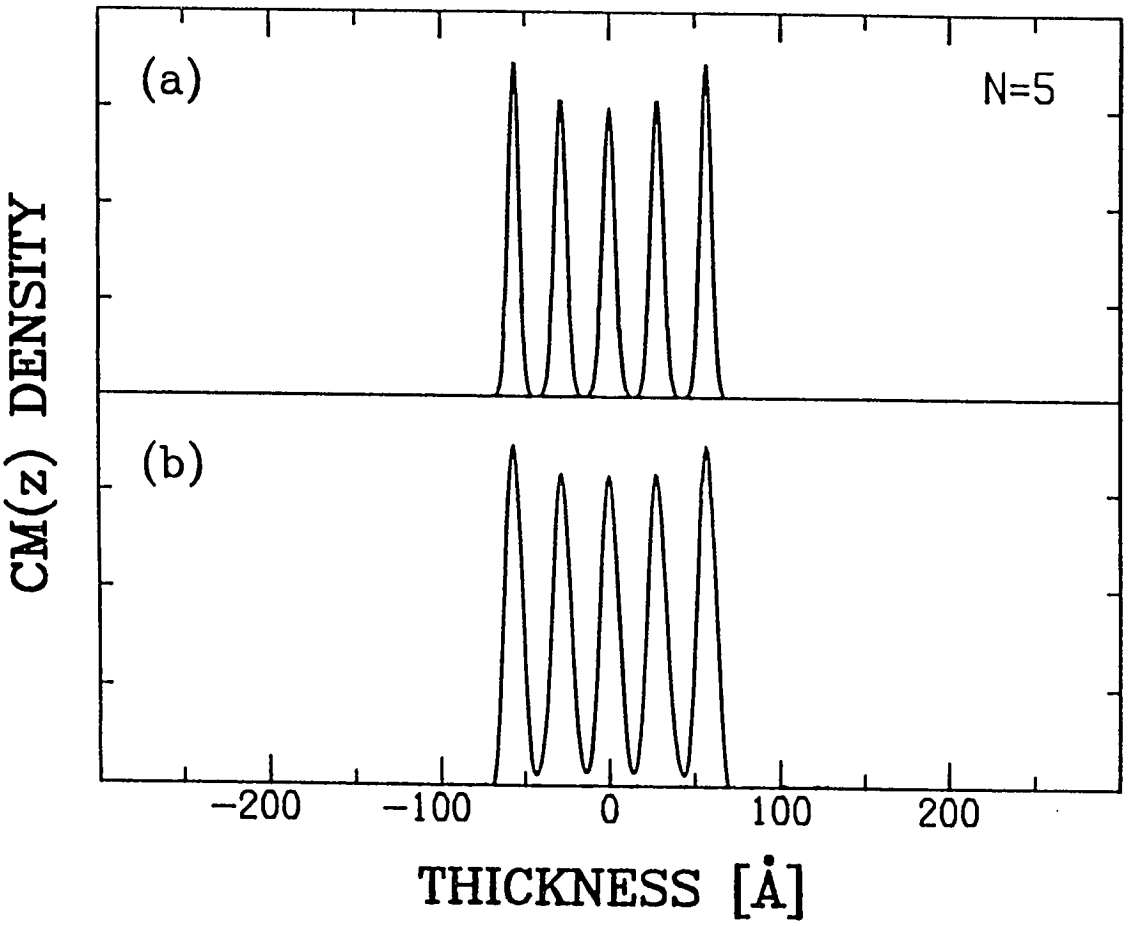

Figure 3.62: 5-Layer Smectic-I/C Center-of-Mass Density. Comparison of the center-of-mass density for the five-layer smectic-I/C film for (a) Forward Model, (b) Direct Inversion.

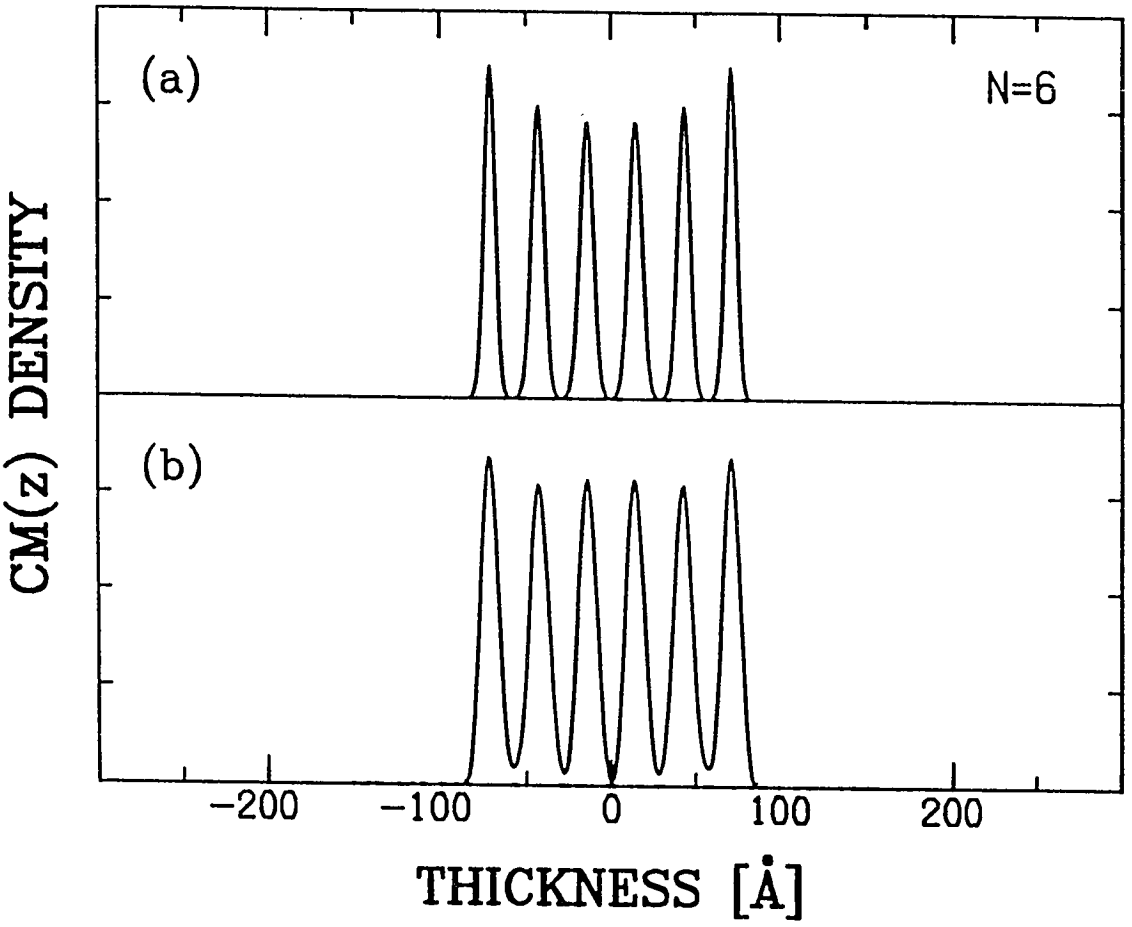

Figure 3.63: 6-Layer Smectic-I/C Center-of-Mass Density. Comparison of the center-of-mass density for the six-layer smectic-I/C film for (a) Forward Model, (b) Direct Inversion.

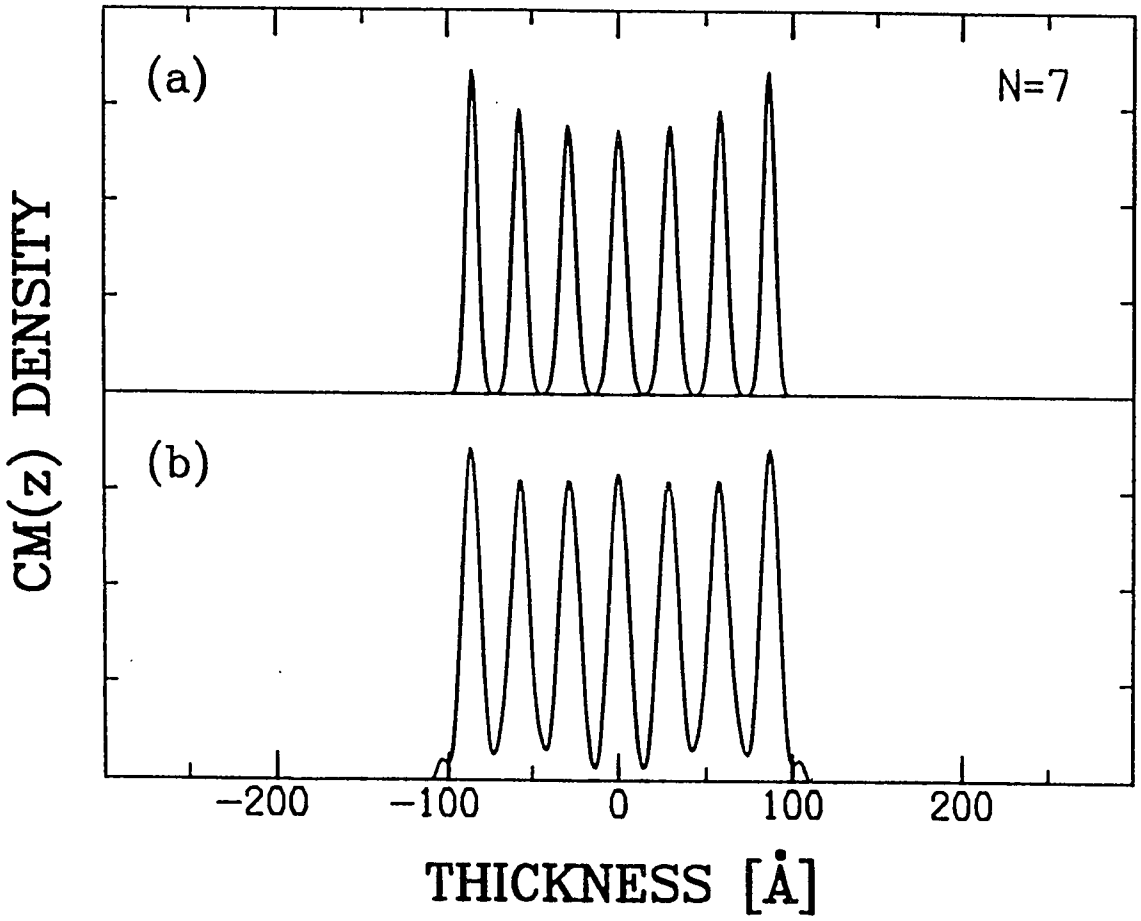

Figure 3.64: 7-Layer Smectic-I/C Center-of-Mass Density. Comparison of the center-of-mass density for the seven-layer smectic-I/C film for (a) Forward Model, (b) Direct Inversion.

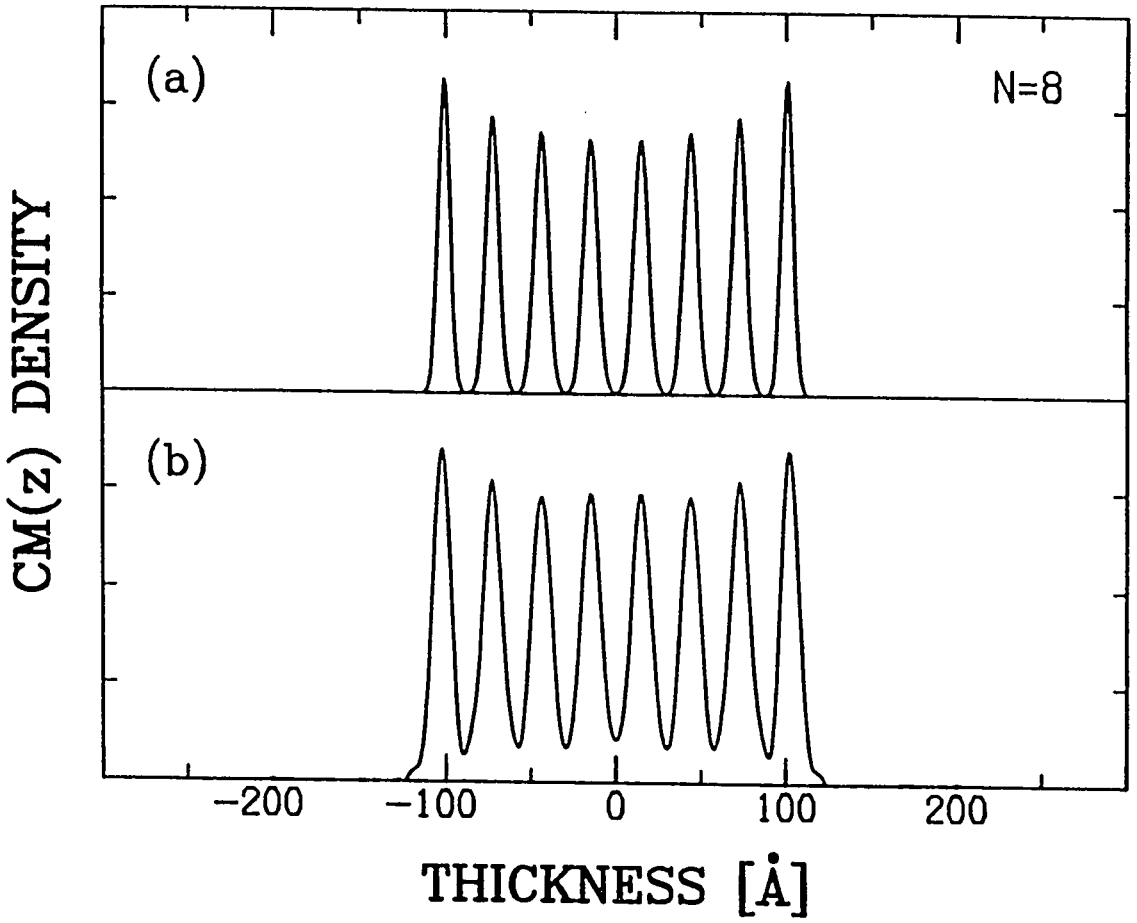

Figure 3.65: 8-Layer Smectic-I/C Center-of-Mass Density. Comparison of the center-of-mass density for the eight-layer smectic-I/C film for (a) Forward Model, (b) Direct Inversion.

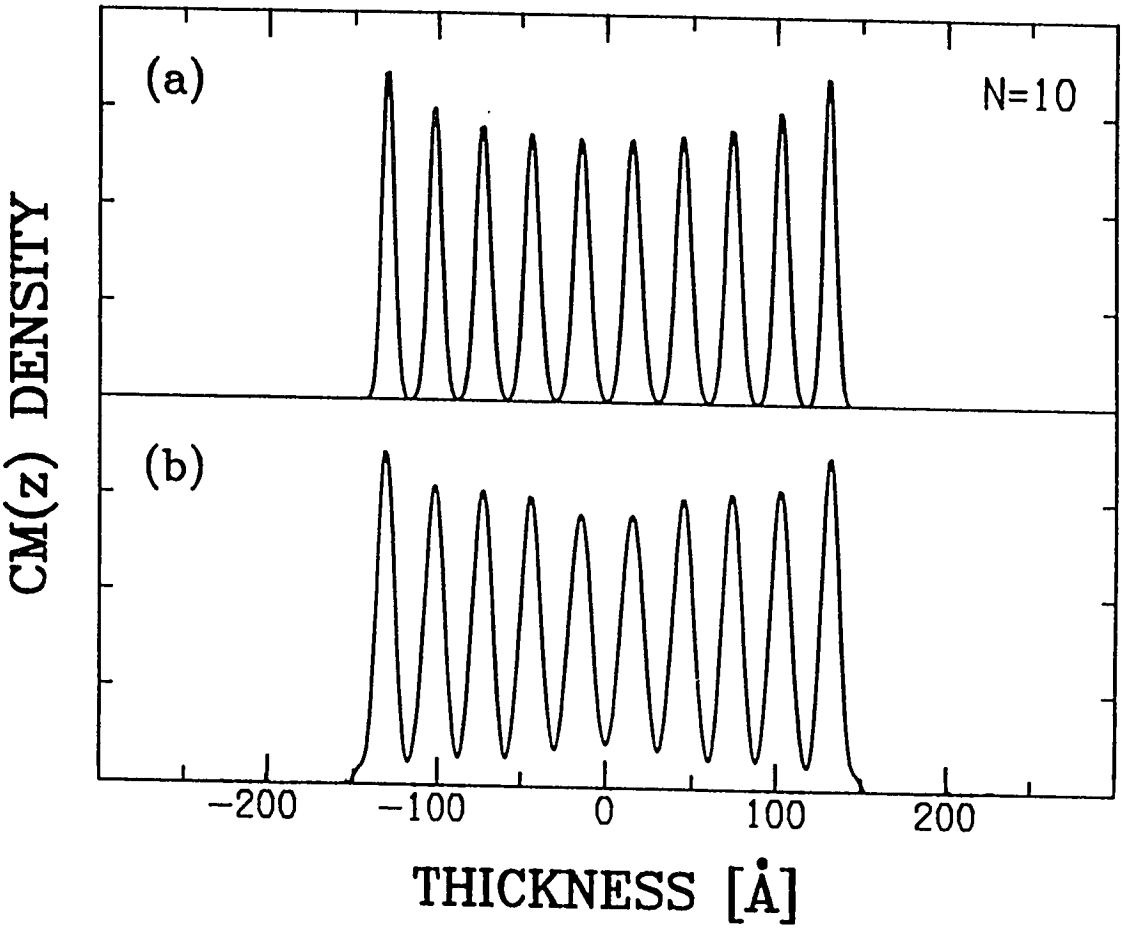

Figure 3.66: 10-Layer Smectic-I/C Center-of-Mass Density. Comparison of the center-of-mass density for the ten-layer smectic-I/C film for (a) Forward Model, (b) Direct Inversion.

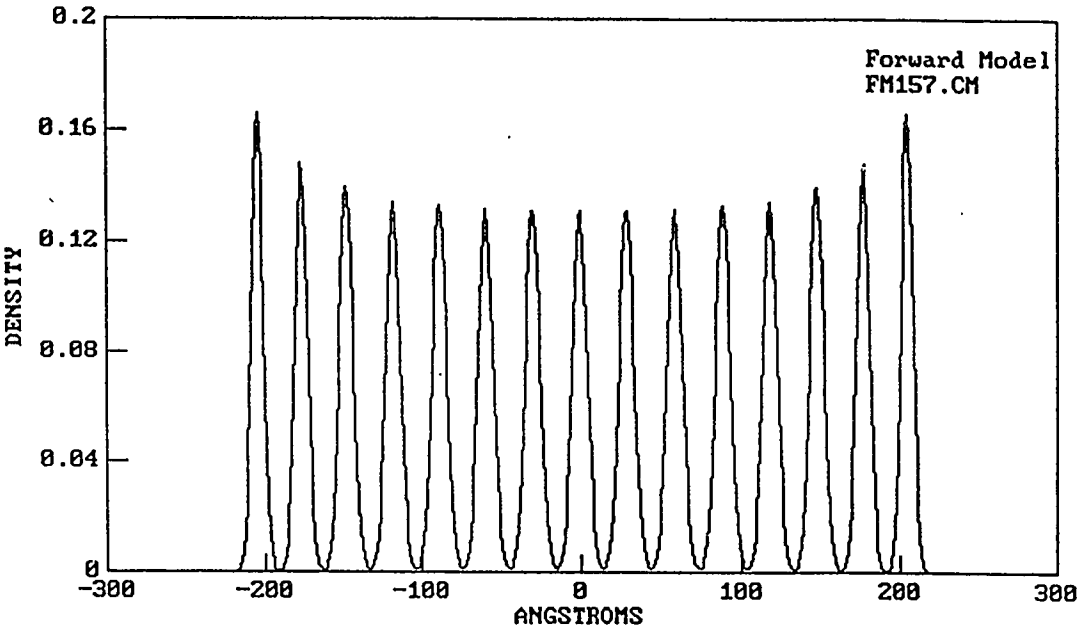

Figure 3.67: 15-Layer Smectic-I/C Center-of-Mass Density. Comparison of the center-of-mass density for the 15-layer smectic-I/C film for (a) Forward Model

Chapter 4

SURFACE FREEZING, FLUCTUATIONS, AND INTERLAYER STRUCTURE

...In order to examine into the truth, it is necessary once in one's life to doubt of all things, so far as this is possible.

- Descartes

4.1 Introduction

This chapter describes the relationship between the surface freezing results presented in Chapter 2 and the layer fluctuation profile results described in Chapter 3. They are related in several direct and indirect ways: a) At the microscopic level, the layer fluctuations could directly affect the surface freezing. When the layer fluctuations are too large, the in-plane order is disturbed and the layer cannot freeze. This simple idea is explored in Sections 4.3 – 4.6. While the simple quenched-fluctuation-induced surface freezing (QFISF) models that are described in these sections agree qualitatively with the observed surface freezing transitions, they do not agree quantitatively and it is not clear yet whether this mechanism is important or not. b) As the surface freezing transitions proceed, the in-plane structure of each layer is altered. This produces the subtle, but clearly observable, changes in the interlayer density profiles described in Chapter 3. The relationship between the thickness of the frozen surface layer, l(t), and the surface order parameter profile, $M_1(t)$, in terms of the standard microscopic theory of surface melting/freezing is described in Section 4.7.

4.2 LC Film Structure: Fluctuation Profiles and Surface Induced Order

The structures of the smectic-I/C 7O.7 films are quite interesting since these films are in the process of surface freezing. An expanded explanation of the forward model density is provided here since the fluctuation profile extracted from the forward model center-of-mass density will be used to make predictions of the temperature dependence of surface freezing transitions in Sec. 4.3 and 4.5.

4.2.1 Forward Model and Direct Inversion Results

The interlayer structure of freely suspended liquid crystal (FSLC) films has been extracted from the measured x-ray diffraction intensity using two complementary approaches: direct inversion and forward modeling methods. While the direct inversion technique results in a model-independent determination of the densities, the forward model gives very well determined tilt and layer fluctuation profiles consistent with simple physical models of the tilt and fluctuation physics. Both approaches reveal modulated densities exhibiting the localization of the smectic layers throughout the film. For thin 7O.7 smectic-I/C films, both methods provide structural determinations showing narrower center-of-mass peaks for the surface layers of the film – the widths of the center-of-mass distributions of the surface layers are 10 - 25 % less than those for interior film layers. The resulting electron and center-of-mass densities for the smectic-I/C films extracted using both techniques were shown in Chapter 3 Figs. 3.44 to 3.51 and 3.60 to 3.67.

In the forward model, the width of the Gaussian center-of-mass distribution for each layer is identified with the layer fluctuation amplitudes and provides a quantitative measure of the fluctuations within the film. The resulting widths of the Gaussian center-of-mass density peaks have been extracted from the center-of-mass density and are illustrated for the 10 layer smectic-I/C film in Fig. 4.1. These widths indicate a fluctuation profile throughout the film and that the surface layer fluctuations are less than the interior layer fluctuations. Fig. 4.2 shows fluctuation profiles for films with thicknesses $L = 3, 4, 5, 6, 7, 8, 10, 15, 35$, and 60 layers. For all these smectic-I/C films the surface fluctuations are suppressed by $\sim 1 - 2$ Å relative to fluctuations at the center of the film and the fluctuations increase rapidly over the first few layers away from each free surface. The fluctuation profiles appear flat near the center of the

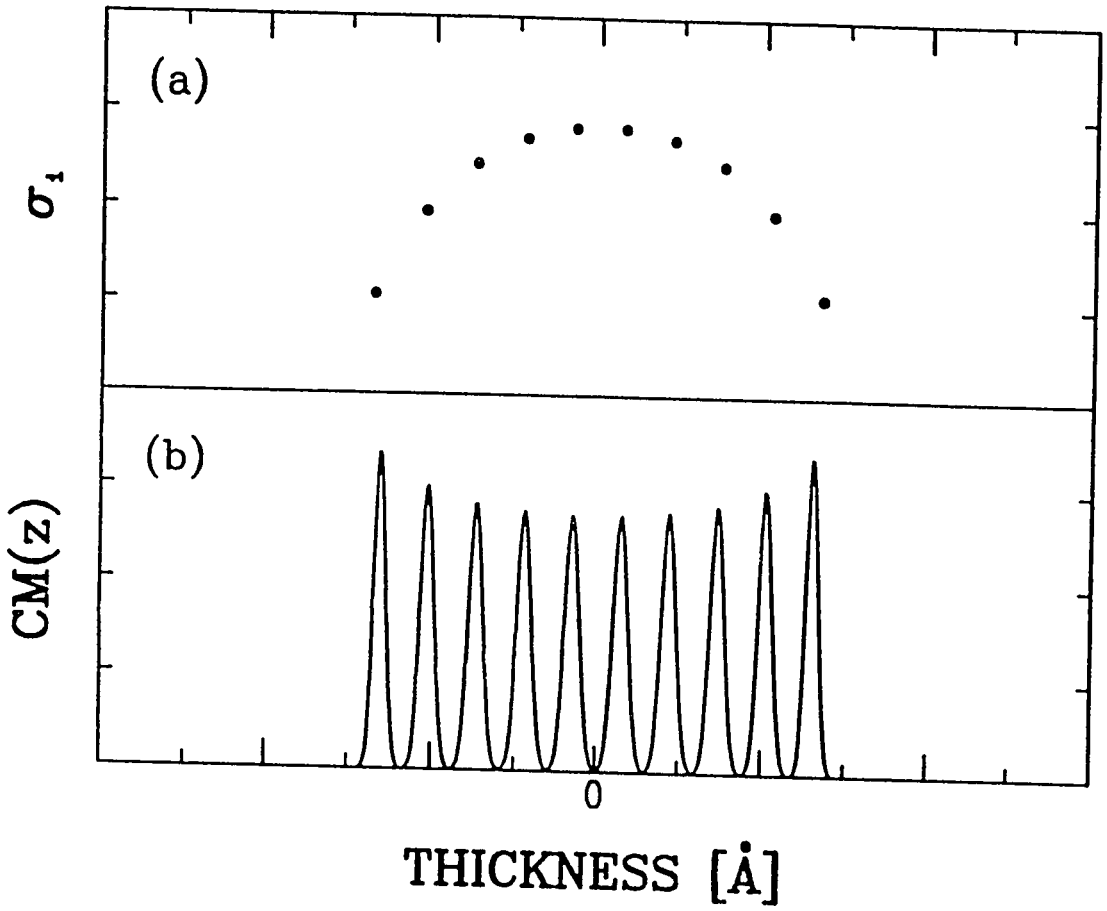

Figure 4.1: 10 Layer Film Fluctuation Profile. The fluctuation profile for the 10 layer smectic-I/C film. The profile is the width of the forward model center-of-mass density peaks extracted from the measured x-ray scattering intensity.

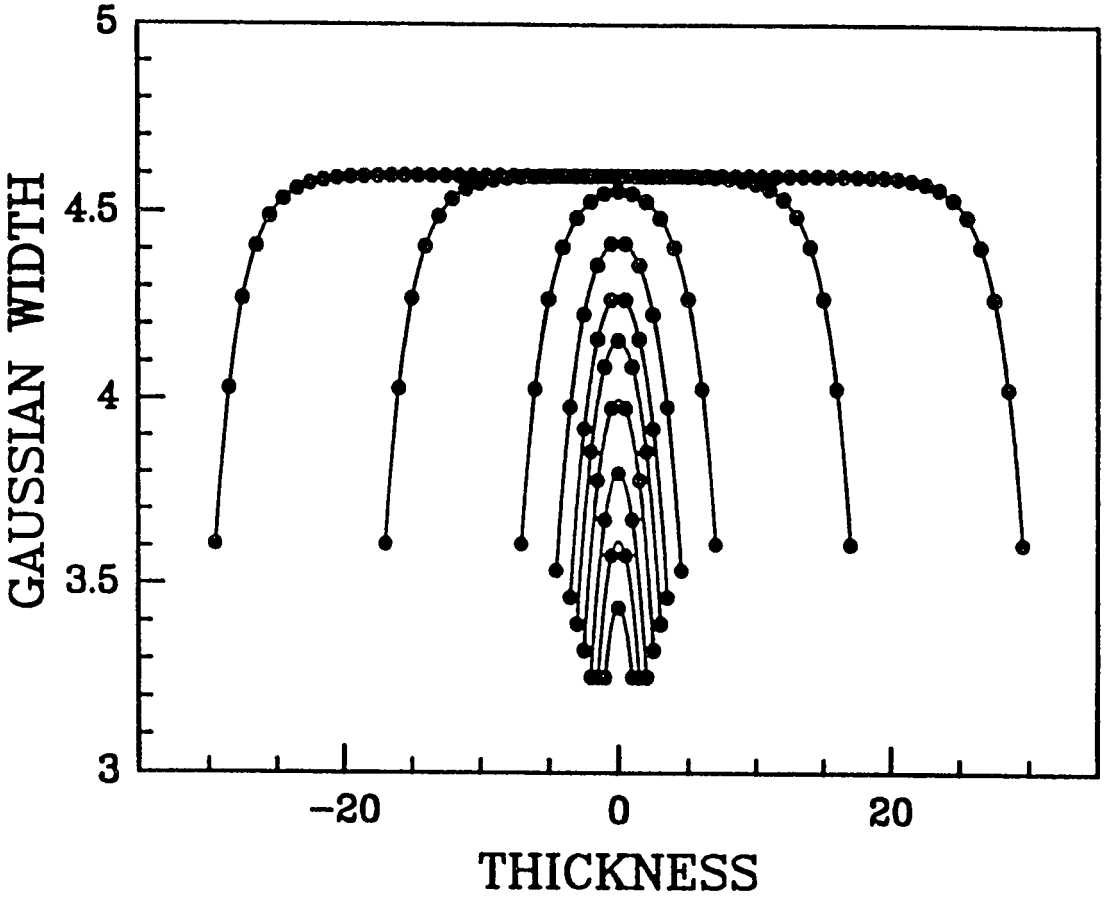

Figure 4.2: 7O.7 Smectic-I/C Fluctuation Profiles. The fluctuation profiles for the smectic-I/C films for thicknesses L = 3, 4, 5, 6, 7, 8, 10, 15, 35, and 60. The center-of-mass densities obtained using the direct inversion analysis are in qualitative agreement with these results.

film where the fluctuations eventually saturate to a constant value. The instrument resolution which determines the long-wavelength cutoff of the spectrometer modifies the shape and saturation value near the center of thick films [26]. The fluctuation profile determined for the 60 layer film shown in Fig. 4.2 will be used in Sec. 4.3 to make comparisons between the fluctuation profiles and the surface freezing of 64-layer 7O.7 films.

The forward model density assumes each layer has the same areal density and that the narrow widths of the surface layer center-of-mass density peaks are due to quenched fluctuations. Both the direct inversion and forward modeling analyses show that these films exhibit narrower center-of-mass peaks for the surface layers of the film, but the interpretation of this profile as either quenched fluctuations or enhanced areal density at the surface of the film remains an open experimental question. In either case, the width of the center-of-mass peaks provides a convenient quantitative measure of each layer's density distribution due to static disorder, thermal fluctuations, and/or the presence of more-dense surface layers. If the fluctuations of the surface layers are indeed quenched, what is the cause of these fluctuation profiles – surface tension, finite-size effects, stiffer surface layer couplings, or the presence of surface frozen monolayers of smectic-I on each surface of the film? To determine whether the presence of frozen smectic-I surface layers affect the fluctuation profile of the film, experiments are planned to measure the structure of films in the smectic-A phase, with and without frozen surface layers.

Does the surface tension cause the quenched interlayer fluctuations seen at the surface of the film? A theory by R. Holyst et al.[26, 119] predicts fluctuation profiles similar to those seen in 7O.7 smectic-I/C films and attributes the cause of the quenched fluctuations to the effect of surface tension. In this theory, the Gaussian form for center-of-mass positions of each layer is a consequence of the Hamiltonian used to calculate the fluctuations. The layer fluctuations, dominated by hydrodynamic, long-wavelength fluctuations, were calculated using a Landau-de Gennes smectic-A free energy modified to include the surface tension. The profiles obtained from the Landau-de Gennes smectic-A free energy calculation closely resemble the fluctuation profiles of Eq. 4.1 but the free parameters in the theory, the smectic elastic constants, B and K, and the surface tension, γ, have not been independently measured for 7O.7. One troubling aspect of the Holyst et al. theory which includes the

effects of the surface layer B_S and K_S in addition to the interior layer B and D and the surface tension, γ, is that the fitted value of the surface tension, $\gamma = 6 \pm 3$ dyn/cm [26, 128], is much smaller than the measured value, $\gamma = 27 \pm 2$ dyn/cm, for other similar LC materials [129]; the value of γ is extremely sensitive to the real-space cutoff of the fluctuation amplitudes. The simplest cosh model for the fluctuation profile will be compared here with the surface freezing data since the Landau-de Gennes with surface tension model is too complicated to fit directly to the measured data.

The enhanced strength of the surface layer couplings is another possible cause of the fluctuation profiles seen in smectic-I/C films. Li et al. [50] describe a model for the incomplete surface freezing seen in thin hexatic FSLC films which predicts an ordering of the surface layers before the bulk. The temperature dependence of the surface layer coupling strengths are calculated using mean-field theory and a 2D Ising model. This theory claims that the interlayer couplings near the surface of films are stronger and that the decay of this surface order into the film controls the temperature difference between the ordering of the surface and interior layers. This theory will not be discussed further except to note that it also describes some aspects of the incomplete wetting behavior seen in heat capacity studies of very thin FSLC films [81, 82]. In these experiments, bond-orientational order appears to develop at the surface of the film before the bulk.

4.2.2 The Forward Model Analysis

In the forward model analysis, a mathematical model is made of the electron density from which the intensity is calculated and fit to the measured x-ray scattering intensity [22, 26]. The electron density for the i^{th} layer of a film is given by the center-of-mass Gaussians for each layer, $G_i(z)$, convolved with the molecular density, $MD_i(z, \phi_i)$. The molecular center-of-mass distribution for each layer i is parameterized by a normalized Gaussian distribution, $G_i(z)$, centered at z_i with width σ_i. The width, σ_i, represents the degree of disorder or the amplitude of the fluctuations of each layer. In the forward model density, the fluctuation profile is parameterized for all films with thickness Z by,

$$\sigma_i = \sigma_{Center} + (\sigma_{Surface} - \sigma_{Center}) \frac{\cosh(z_i/\lambda)}{\cosh((Z-1)/2\lambda)}. \qquad (4.1)$$

with free parameters, $\sigma_{Surface}$ and σ_{Center}, the Gaussian width at the surface and center of the film respectively, and λ, the characteristic elastic decay length. In the model density for smectic-I/C films, both $MD_i(z, \phi_i)$ and the layer position, z_i, depend on each layer's molecular tilt angle, ϕ_i, with respect to the layer normal direction, $\hat{z}$. The molecular tilt angle profile is calculated using a simple phenomenological free energy which results in $\phi_i = \phi_{Interior} + (\phi_{Surface} - \phi_{Interior})\cosh(z_i/\xi)/\cosh((Z-1)/2\xi)$, where $\phi_{Surface}$ and ϕ_{Center} are the tilt of the surface and center layers respectively, and ξ is the tilt decay length. The molecular density, $\mathrm{MD}_i(z, \phi_i)$, for each layer is calculated from the known atomic structure of the molecule and symmetrized since the molecules have equal probabilities of orientation along and opposite to the director. The contributions from each layer are added together and the scattering intensity was calculated by Fourier transforming the electron density, convolving with the instrument resolution, and correcting for the scattering geometry factors[26, 126]. The best-fit model density for all thickness films results from a non-linear least square fit to the measured intensity with a single set of parameters, σ_{Center}, $\sigma_{Surface}$, λ, $\phi_{Surface}$, ϕ_{Center}, and ξ.

4.3 Simple Quenched-Fluctuation-Induced Surface Freezing Model

As described in Chapter 2, the standard surface freezing theory is based on thermodynamics: the wetting of the interior liquid phase by its own surface frozen phase with the interfacial energy gain balancing the phase conversion cost. A second completely different approach, would be to construct a detailed microscopic theory based, for example, on the idea that the system can only freeze when the fluctuations are small enough; the physical idea is that large fluctuations prevent the system from freezing. In the case of FSLC films, the layer fluctuations are quenched at the surface of the film so freezing should begin there. A detailed microscopic theory of this type has been constructed by Holyst and is described in Sec. 4.5. In this section a simple version is described which directly relates the layer fluctuation profiles presented in Chapter 3 with the surface freezing results presented in Chapter 2. This model will be call the "quenched-fluctuation-induced surface freezing (QFISF) model.

4.3.1 Simple QFISF Model: 7O.7 Results

The simplest possible QFISF model is just to postulate that each layer freezes when its layer fluctuations fall below a specific fluctuation amplitude for freezing. Since the fluctuation profiles (Chapter 3) for the smectic-I on smectic-C phase of 7O.7 and the surface freezing transitions (Chapter 2) of 7O.7 have both been measured, the simple QFISF model will be explored for this system.

Fig. 4.3a shows the surface freezing profile predicted by the simple QFISF model from the measured 60 layer 7O.7 smectic-I/C film fluctuation profile, σ_l, overplotted on the measured 64 layer 7O.7 surface freezing transitions assuming that the surface freezing transition of the l^{th} layer, T_l, is given by $T_l = 73.4 - \sigma_l$. Remarkably, this simple scaling qualitatively describes the 7O.7 surface freezing data and describes it about as well as the detailed Holyst QFISF model presented in Section 4.5. Fig. 4.3b shows the surface freezing profile predicted by a second QFISF model overplotted on the measured 64 layer 7O.7 surface freezing transitions assuming that $T_l = 68.8 + 10(4.6 - \sigma_l)^2$. This model with $T_l \propto \sigma_l^2$ better represents the temperature difference between the first and second layer transitions, but as described in detail in Chapter 2, because the surface freezing measurements are quite precise, this quantitative agreement is not consistent with the measurements in detail, although the trend is clearly correct. The measured surface freezing transitions for 7O.7 can also be used to predict the qualitative shape of the layer fluctuation profile via the simple QFISF model. These predicted layer fluctuation profiles are shown in Fig. 4.4. Again, they are qualitatively correct.

4.3.2 Simple QFISF Model: 4O.7 Results

In addition, since careful film thickness dependence measurements were made for 4O.7, the simple QFISF model will also be applied to 4O.7. In this case the fluctuation profile has not been measured, but for the purposes of the comparison, the fluctuation profile is assumed to have the same cosh form as 7O.7 given by Eq. 4.1. Fig. 4.5a, shows an overplot of the 60 layer 4O.7 surface freezing results with the fluctuation profile rescaled as $T_l = 49.3 + 1.4(4.6 - \sigma_l)^2$. This phenomenological scaling compares well with the data up to point 10 but the transitions deviate, as illustrated in Fig. 4.5b, as did the logarithmic form presented in Chapter 2. The measured surface freezing transitions for 4O.7 can also be used to predict the qualitative shape of the layer

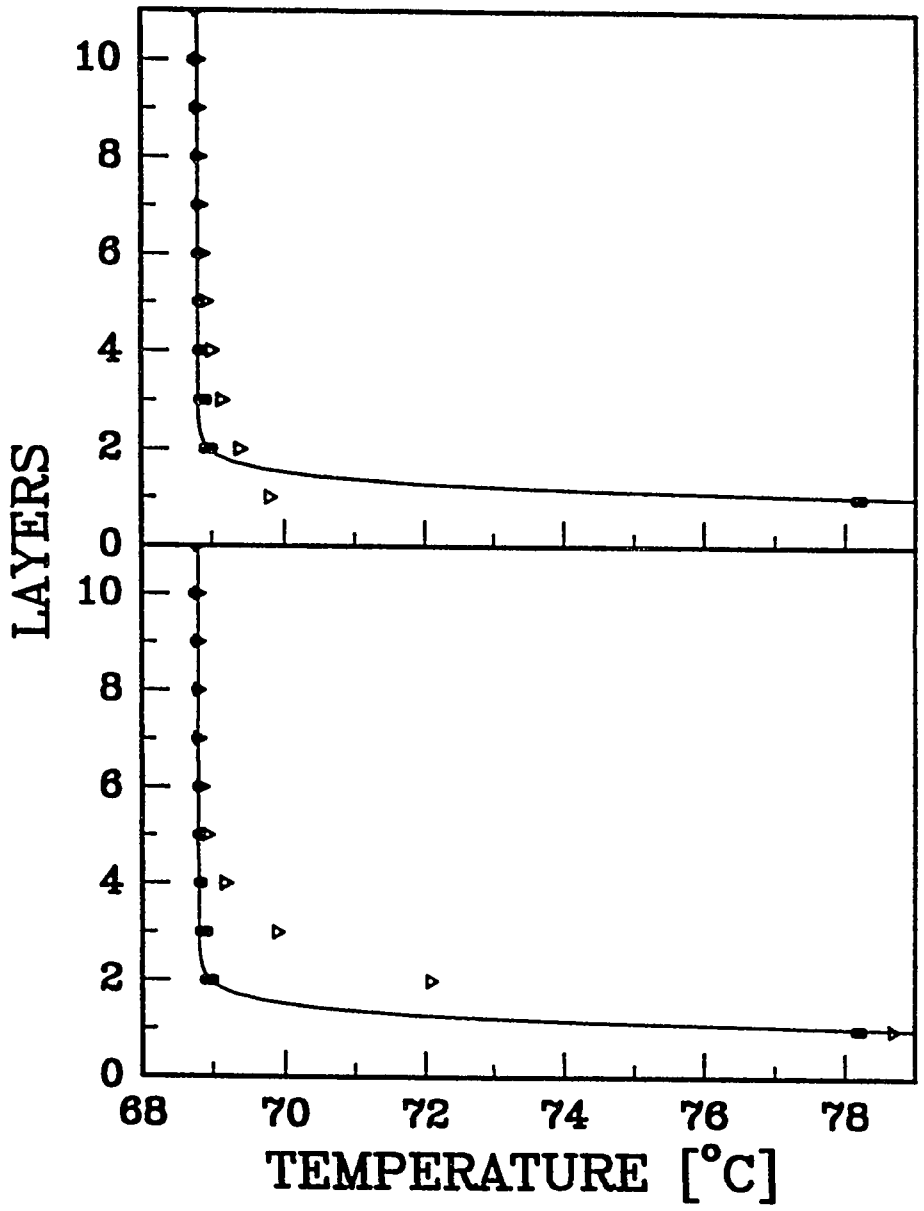

Figure 4.3: Simple Model Results For Quenched-Fluctuation-Induced Surface Freezing: 7O.7. Comparison of surface freezing results with simple models for quenched-fluctuation-induced surface freezing using the fluctuation profile σ_l for the l^{th} layer obtained from the 60 layer 7O.7 smectic-I/C film. Shown is an overplot of the 64 layer 7O.7 surface freezing results (Circles) with the fluctuation profile (Triangles) rescaled as $T_l = 73.4 - \sigma_l$ (Top Panel) and $T_l = 68.8 + 10(4.6 - \sigma_l)^2$ (Bottom Panel). Neither of these models is in quantitative agreement with the precise measurements of the surface freezing transition temperatures but the trends are correct.

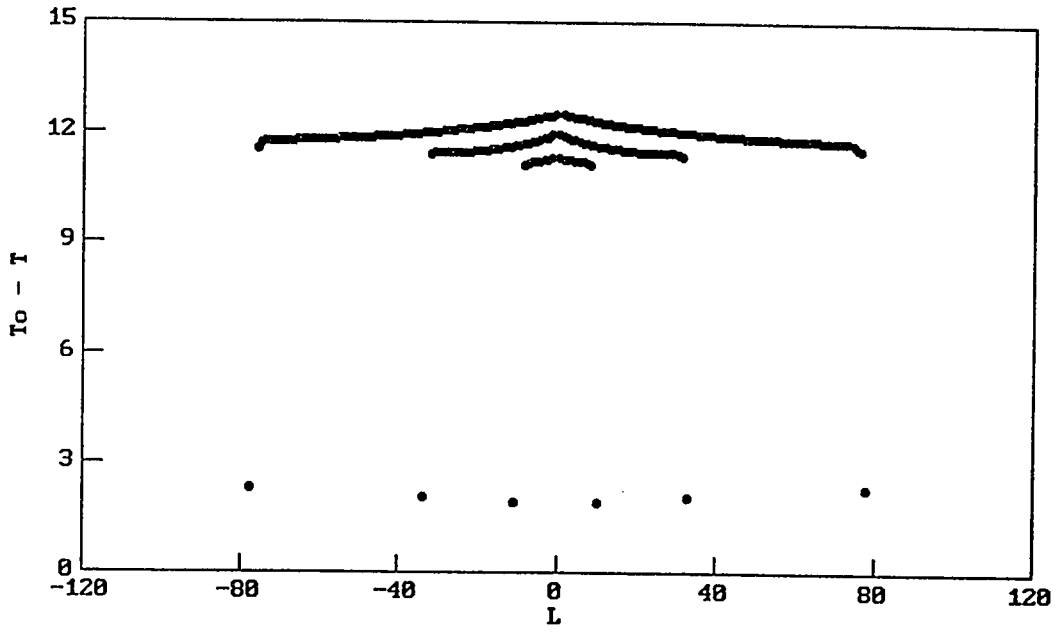

Figure 4.4: Simple QFISF Model: Prediction of the 7O.7 Fluctuation Profiles. The layer fluctuation profiles predicted by the QFISF model for 7O.7 from the measured surface freezing transitions.

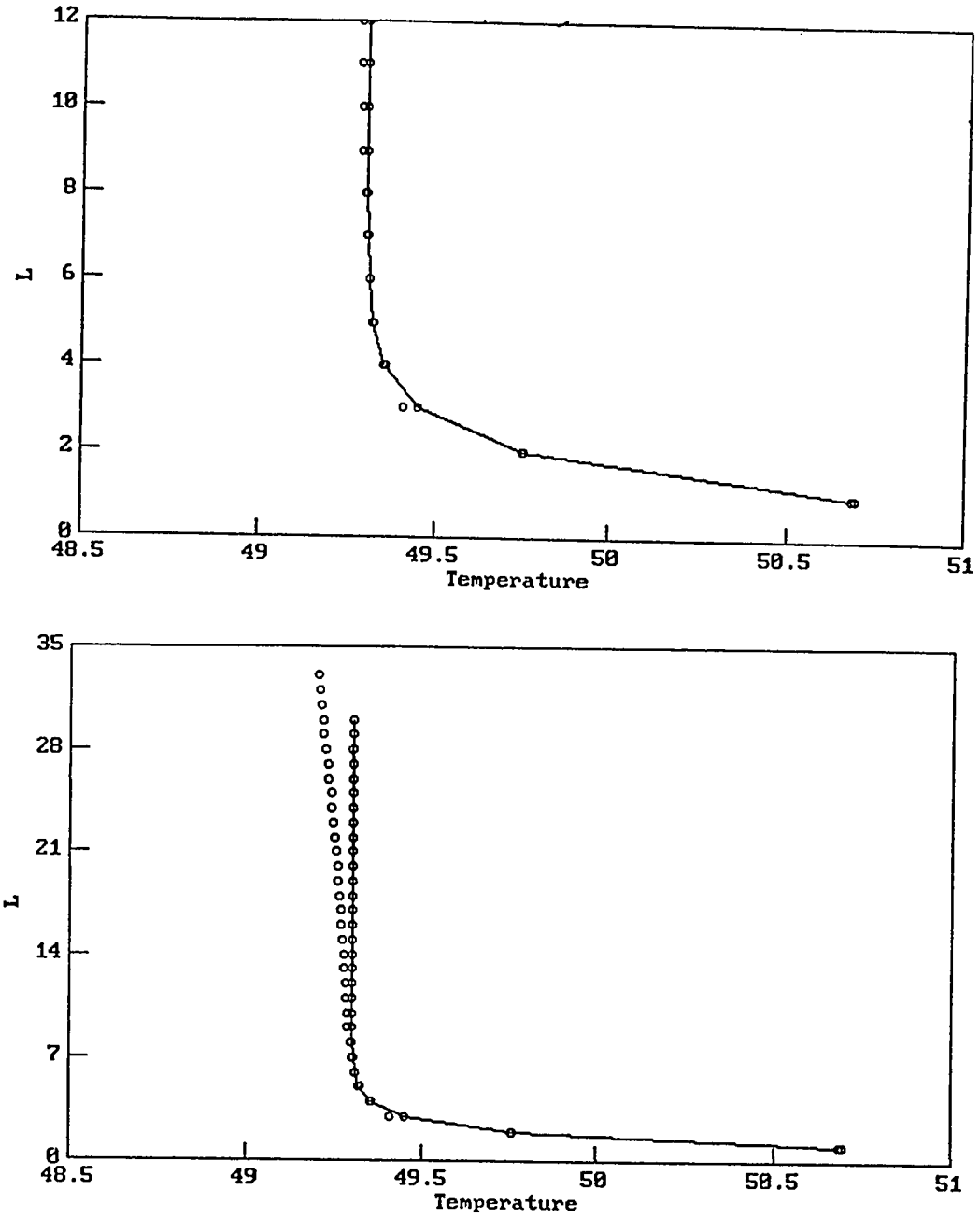

Figure 4.5: Simple Model Results For Quenched-Fluctuation-Induced Surface Freezing: 4O.7. Comparison of surface freezing results with simple models for quenched-fluctuation-induced surface freezing using the fluctuation profile σ_l for the lth layer obtained from the 60 layer 7O.7 smectic-I/C film. (a) An overplot of the 60 layer 4O.7 surface freezing results (Circles) with the fluctuation profile rescaled as $T_l = 49.3 + 1.4(4.6 - \sigma_l)^2$ (Circles and Line). This re-scaling fit compares well with the data up to point 10. (b) The same model plotted for all the data.

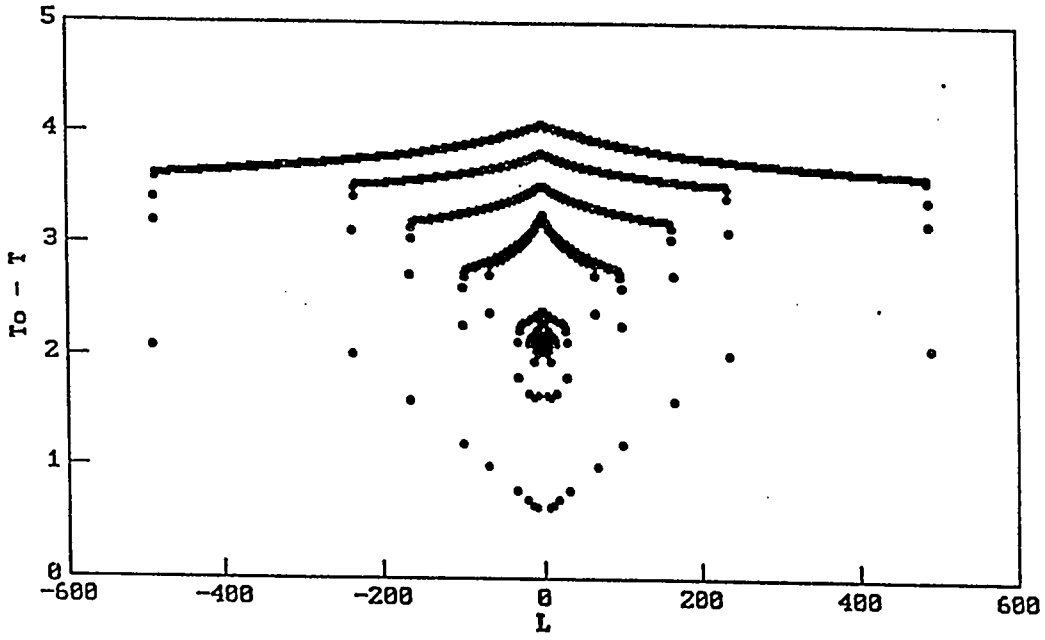

Figure 4.6: QFISF Model Prediction: 4O.7 Surface Freezing Fluctuation Profiles. The layer fluctuation profiles predicted by the QFISF model for 4O.7 from the measured surface freezing transitions.

fluctuation profile via the simple QFISF model. These predicted layer fluctuation profiles are shown in Fig. 4.6.

4.4 Fluctuations and the Landau-Peierls Instability

The degree of long-range order in low dimensional solids and smectic-A materials depends on their dimensionality. In these systems the effect of thermal fluctuations is quite different from the effects displayed on 3D crystals where crystallinity and long-range order is preserved in the thermodynamic limit since the amplitude of thermal fluctuations remains finite. For three-dimensional solids, periodic in only one or two dimensions, with characteristic size L, the famous argument of Landau and Peierls [101, 102] showed that, in the thermodynamic limit, divergent thermal fluctuations destroy the long-range order: for one- and two-dimensional solids, the thermal averaged squared displacement, $\langle |u(\mathbf{r})|^2 \rangle$, diverges as L and $\ln(L)$, respectively. For bulk smectic-A materials with smectic layers perpendicular to $\hat{z}$, there are two fundamental long-wavelength modes: layer compression parallel to $\hat{z}$ with elastic constant B, and layer bending perpendicular to $\hat{z}$ with elastic constant K. The bulk free energy, F_{Bulk}, for layer displacement from the equilibrium position, $u(\mathbf{r})$, is given by [4]

$$F_{Bulk} = \frac{1}{2} \int d\mathbf{r} \left[B \left(\frac{\partial u(\mathbf{r})}{\partial z} \right)^2 + K \left(\frac{\partial^2 u(\mathbf{r})}{\partial x^2} + \frac{\partial^2 u(\mathbf{r})}{\partial y^2} \right)^2 \right]. \tag{4.2}$$

Applying the equipartition theorem, each mode has on average $\frac{1}{2} k_B T$ of energy [1], so

$$\langle |u(\mathbf{q})|^2 \rangle = \frac{k_B T}{B q_z^2 + K q_\perp^4}. \tag{4.3}$$

Fourier transforming this expression for the case of an infinite thickness sample with a finite transverse width W, the thermally averaged fluctuations are given by

$$\langle u(\mathbf{r})^2 \rangle = \frac{k_B T}{4\pi \sqrt{KB}} \ln \left(\frac{W}{a_0} \right), \tag{4.4}$$

---

[1] The following relation is obtained using $u(\mathbf{r}) = (2\pi)^{-3/2} \int d\mathbf{q}\ u(\mathbf{q})\ e^{i\mathbf{q}\cdot\mathbf{r}}$ and by decomposing $F_{Bulk} = \int d\mathbf{q}\ F_{Bulk}(\mathbf{q})$ into independent normal modes where $\langle F_{Bulk}(\mathbf{q}) \rangle = \frac{1}{2} k_B T$.

where a_0 is the molecular width. For an infinite transverse width sample with a finite thickness, D, the fluctuations are given by

$$\langle u(\mathbf{r})^2 \rangle = \frac{k_B T}{4\pi\sqrt{KB}} \ln\left(\frac{\sqrt{\lambda D}}{a_0}\right), \tag{4.5}$$

where $\lambda = \sqrt{K/B}$ is the characteristic smectic length. In both cases, the fluctuations grow logarithmically with the system 'size' and the long-range order is destroyed in the thermodynamic limit. This characteristic logarithmic divergence of the fluctuations means that the smectic-A phase is always at its critical point and has fluctuations on all length scales. As a consequence of smectic-A LC's quasi-long-range order, the quasi-Bragg peaks have algebraic singularities instead of the delta function Bragg peaks of 3D crystals. For finite thickness samples, the layer fluctuations are limited by the size of the sample and the algebraic singularities in the x-ray scattering pattern are cut-off [108]. Even though the smectic-A phase is at lower-marginal dimensionality, the logarithmic growth of the fluctuations with the size of the system is so slow that the breakdown of long-range order has been difficult to observe experimentally [103]. The magnitude of the mean-square fluctuations for a very thick (1 cm) sample with typical values of the LC parameters [125] is only $\sqrt{\langle u(\mathbf{r})^2 \rangle} = 8.1$ Å which is smaller than the typical 30 Å smectic layer spacing. However for the 7O.7 films studied here, which are at least 10^5 times thinner, the measured fluctuation amplitudes at the center of the film, σ_i are still about 1/2 this bulk value [22].

The importance of these smectic fluctuations on the structure of thin FSLC films has been outlined by Holyst et al. [26, 119]. The question addressed here is: What is the effect of these divergent fluctuations on the surface freezing transition?

The applicability of mean-field theory to phase transitions in low dimensional systems depends on the dimensionality of the system and the effects of thermal fluctuations [134]. If the dimension of the system, d, is larger than d^*, the upper marginal dimension, then mean-field results will apply. The surface freezing transitions in 7O.7 are described quite well by a simple mean-field theory, which ignores the effects of thermal fluctuations. The fact that both the smectic-A and smectic-C phase are at lower-marginal dimensionality, $d^* = 3 = d$, and have divergent fluctuations in the thermodynamic limit apparently is not important in these FSLC films where the finite-size and surface tension of the film limits the amplitude of the fluctuations. Although the layer fluctuation amplitudes are found to be quite large, $\sim 15\%$ of the

smectic periodicity, mean-field theory still describes the surface freezing very well. For simple 3D fluids, fluctuations are not important in the traditional theory of surface melting or freezing since for these wetting transitions, the upper marginal dimension, $d^* = 2$, for long-range van der Waals forces [35] and $d^* = 3$ for short-range exponential forces [41]. Consequently, mean-field exponents are correct far away from T_o in both cases and logarithmic corrections to the exponents are expected very close to T_o in the case of short-range exponential forces. A search for these logarithmic corrections in the short-range exponential force LC systems is planned.

Surface freezing transitions will be layer-by-layer if the effective interface profile retains the periodicity of the film. If the layer fluctuations are too large, the thermal fluctuations will remove this intrinsic periodicity of the effective interface profile and the surface freezing transition will become continuous. Turning this around, the fact that the surface freezing transitions occur layer-by-layer in these systems implies that the fluctuations are not large enough to destroy the smectic layer order. This agrees with the x-ray measurements. How large can the fluctuations be and still have layer-by-layer surface freezing transitions? In the case of 60-layer 7O.7 films, the fluctuation amplitudes are reasonably large. The mean-squared displacement is about 4 Å at the center of the film compared to the smectic layer-spacing of about 30 Å, yet these films still exhibit layer-by-layer surface freezing transitions. The magnitude of the layer fluctuations is limited by the characteristic 'size' of the system, and as argued above, even for macroscopic smectic-A samples the fluctuations are small enough that the interfaces are still well defined.

4.5 The Holyst Quenched-Fluctuation-Induced Surface Freezing Model

In a very recent preprint R. Holyst [19] constructs a detailed QFISF model. In his model, the surface tension inhibits the out-of-plane fluctuations of the surface layers. The values of the bend elasticity and the surface tension determine the fluctuation profile in the film and consequently the surface freezing transition temperatures.

The theory is based on the Kosterlitz-Thouless mechanism [20, 21] which predicts that the solid to liquid phase transition in very thin (2D) films proceeds in a two stage process involving the separate unbinding transitions of two different topological defects, dislocations and disclinations. Holyst considers the first stage of this process in which disclination pairs unbind at the liquid-hexatic transition. The calculation is

an extension of the results of Nelson and Peliti [131] for the coupling within a single layer of the in-plane bond angle and the out-of-plane displacement of the smectic layers and of the work by Selinger [132] for the smectic-A to hexatic-B phase transition. In Holyst's theory, the elastic properties of a $N+1$ layer smectic film is described by in-plane bond angles $\theta_n(\mathbf{r}_\perp)$, and out-of-plane displacements, $u_n(\mathbf{r}_\perp)$, for layers $n = 0, 1, ..., N$, where $\mathbf{r}_\perp$ is the in-plane position vector and $\hat{z}$ is normal to the layers. The elastic Hamiltonian is given by,

$$\begin{aligned}\beta H[u,\theta] = \; & \beta H_0[u] + \tfrac{1}{2}\int d\mathbf{r}_\perp \textstyle\sum_{n=0}^{N} \beta K_A(\nabla_\perp \theta_n + \mathbf{A}_{\perp n})^2 - \\ & \int d\mathbf{r}_\perp \textstyle\sum_{n=1}^{N} \beta K_H \cos 6(\theta_n - \theta_{n-1} + A_{n,n-1})\end{aligned} \tag{4.6}$$

where K_A and K_H are hexatic elastic constants and β is the Boltzmann factor. The interaction energy results from the competition between the bond-angle field which attempts to maintain hexatic order and the fluctuation induced curvature of the smectic layers which attempts to destroy it. The terms which couple the layer fluctuations with the in-plane hexatic order are given by,

$$\mathbf{A}_\perp = \frac{1}{2}\varepsilon_{\alpha\beta}\nabla_\perp \partial_\alpha u_n(\mathbf{r}_\perp)\partial_\beta u_n(\mathbf{r}_\perp) \tag{4.7}$$

and

$$A_{n,n-1} = \frac{1}{2}\varepsilon_{\alpha\beta}\partial_\alpha u_n(\mathbf{r}_\perp)\partial_\beta u_{n-1}(\mathbf{r}_\perp), \tag{4.8}$$

where $\varepsilon_{\alpha\beta}$ is the 2D antisymmetric tensor. The thin film smectic layer fluctuation Hamiltonian is given by,

$$\begin{aligned}H_0[u] = \frac{1}{2}\int d\mathbf{r}_\perp \Big(\sum_{n=0}^{N-1} \frac{B}{d}(u_{n+1}(\mathbf{r}_\perp) - u_n(\mathbf{r}_\perp))^2 + \\ \sum_{n=0}^{N} Kd(\Delta_\perp u_n(\mathbf{r}_\perp))^2 + \gamma|\nabla_\perp u_0(\mathbf{r}_\perp)|^2 + \gamma|\nabla_\perp u_N(\mathbf{r}_\perp)|^2\Big)\end{aligned} \tag{4.9}$$

where B and K are the compression and bending smectic elastic constants respectively, and γ is the vapor-smectic-A surface tension. After a perturbation expansion and renormalization group calculation [19], the transition temperature $T_n = k_B/\beta_n$, for the n^{th} layer is given by,

$$\exp(-\beta_n E_n^{eff}) = \frac{\beta_n K_A}{144} - \frac{1}{2\pi} \tag{4.10}$$

where

$$E_n^{eff} = \frac{\pi C K_A}{36} - \beta \left(\frac{K_A}{12}\right)^2 \int \frac{d\mathbf{q}}{(2\pi)^2} \int \frac{d\mathbf{p}}{(2\pi)^2} |\mathbf{q} \times \mathbf{p}|^4 |G(\mathbf{q}+\mathbf{p})|^2 \langle u_n(\mathbf{q}) u_n(-\mathbf{q}) \rangle \langle u_n(\mathbf{p}) u_n(-\mathbf{p}) \rangle \qquad (4.11)$$

and $G(\mathbf{q}) = -\frac{2\pi}{q^2}$. Although this model for surface freezing proposes that this specific microscopic mechanism is responsible for both surface melting and surface freezing, the detailed connection with the thermodynamic wetting formalism is unclear.

A comparison of Holyst's predictions using Eq. 4.10 with the measured surface freezing data from the 64-layer 7O.7 films is shown in Fig. 4.7. Holyst's model calculations were done for an 11 layer film for two values of the smectic bend elastic constant K = 0.5 and 1 $\times 10^{-6}$ dyn. The other parameters were chosen to be close to the smectic-I constants used in the forward model fits the smectic-I/C x-ray diffraction data [26]. Holyst's predicted freezing temperatures depend only very weakly on film thickness. The best fit forward model value for the smectic-I/C data was $K = 3.1 \times 10^{-6}$ dyne. As can be seen, a larger value of K results in an asymptotic transition temperature that is too high and the difference between the first and second transition is too small. Intermediate values of K result in a family of curves with decreasing asymptotic transition temperatures. The asymptotic transition temperature of the model can be made equal to that of the data for some intermediate value of K, but the temperature difference between the first and second transition is then too small.

4.6 Comparison of Simple QFISF Model and Holyst QFISF Model

Although the 7O.7 and 4O.7 data is fit qualitatively by the simple QFISF model, neither the simple QFISF model nor the more detailed Holyst QFISF model agrees in detail with the measured surface freezing data. The simple QFISF model assumes the layers freeze when their fluctuation amplitude falls below a fixed 'critical' value. Both the QFISF models need the layer fluctuation profile to calculate the surface freezing transitions and both models assume that the fluctuation profile remains fixed throughout the surface freezing process. This may not be a good assumption since the fluctuation amplitude of the interior layers may certainly change as the frozen surface layer becomes thicker and the frozen interface approaches them. So far, the

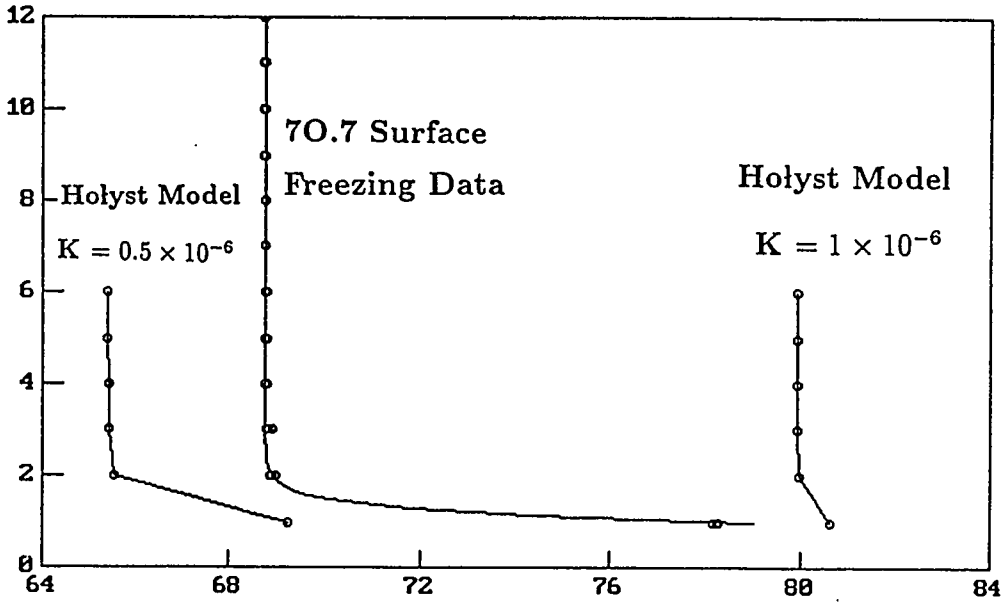

Figure 4.7: Holyst Quenched-Fluctuation-Induced Surface Freezing Model Results. Comparison of 7O.7 surface freezing results by R. Holyst for quenched-fluctuation-induced surface freezing. Overplot of the model calculations and the 64 layer 7O.7 surface freezing data. The model calculations were done for an 11 layer film for two values of the smectic bend elastic constant K = 0.5 and 1 $\times 10^{-6}$ dyne with the other parameters chosen to be close to the smectic-I constants used to fit the forward model to the 60 layer 7O.7 smectic-I/C x-ray diffraction data. Intermediate values of K result in a family of curves, none of which give both the correct transition temperature and the correct temperature difference between the first and second layer transitions.

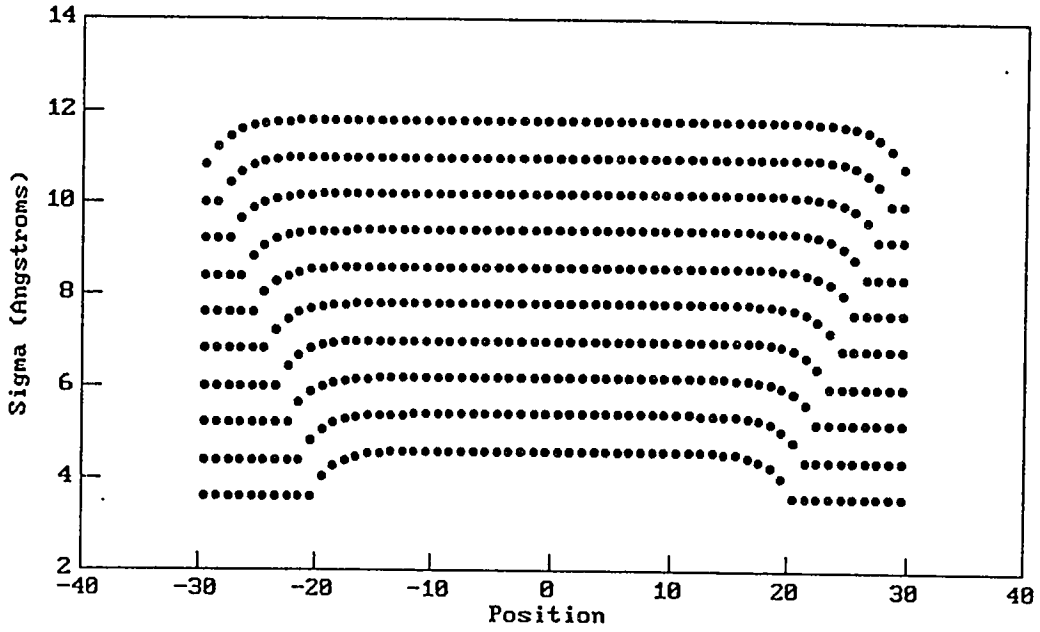

Figure 4.8: Changing Fluctuation Profiles During Surface Freezing. To correctly account for the changing fluctuation profile during the surface freezing, new intermediate profiles must be calculated which account for the quenching of outside layer fluctuations by additional surface-frozen layers. This is illustrated for the 60-layer fluctuation profile with the assumption that the internal fluctuation profiles retain the same shape and that the surface-frozen layers have the same fluctuation amplitudes.

experimental work, described in Chapter 3, and the theoretical work [19, 26, 119] have only considered single frozen surface layers. To properly connect the layer fluctuation profiles and the surface freezing transitions, the layer fluctuation profiles with multiple frozen surface layers present are needed. A possible series of profiles for the 60-layer 7O.7 film, assuming that all frozen layers have the same fluctuation amplitude, are illustrated in Fig. 4.8 . X-ray experiments are planned to measure the fluctuation profiles versus the number of 9O.4 surface frozen layers to determine how the layer fluctuation profile depends on the number of frozen surface layers. This can also be studied theoretically, but is difficult to evaluate numerically [133].

It would also be interesting to produce a new detailed QFISF model based on a first-order transition instead of on the infinite-order Kosterlitz-Thouless transition. The actual surface freezing transitions in these films are almost surely first-order and are not Kosterlitz-Thouless transitions.

4.7 The Interlayer Structure and the Order Parameter

This section describes the relationship between the order parameter profile, which is measured indirectly by the x-ray profiles, and the surface freezing transitions. The relationship between the order parameter profiles and the surface freezing has been worked out in detail by Lipowsky [10] and others [36, 75, 85, 87, 136, 137].

The standard mean-field formulation of surface melting theory is the Landau-Ginzburg theory developed by Lipowsky [10] and others [135]. It predicts the same temperature dependence of the frozen surface layer thickness as the simple phenomenological theory presented in Chapter 2. In the mean-field description, a d-dimensional semi-infinite system with a (d-1)-dimensional surface is considered. The order parameter profile, $M(z)$, of the system is connected explicitly to the effective interfacial potential, δF. A brief summary of part of this description is given here so that the order parameter profile information contained in the x-ray measurements can be compared to the order parameter profile predictions of the theory. The Landau free-energy functional for a system described by a scalar order parameter, ϕ, has the form,

$$F[\phi] = \int d^{d-1}\rho \int_0^\infty dz \, [\frac{1}{2}(\nabla\phi)^2 + f(\phi) + \delta(z) f_1(\phi)]. \qquad (4.12)$$

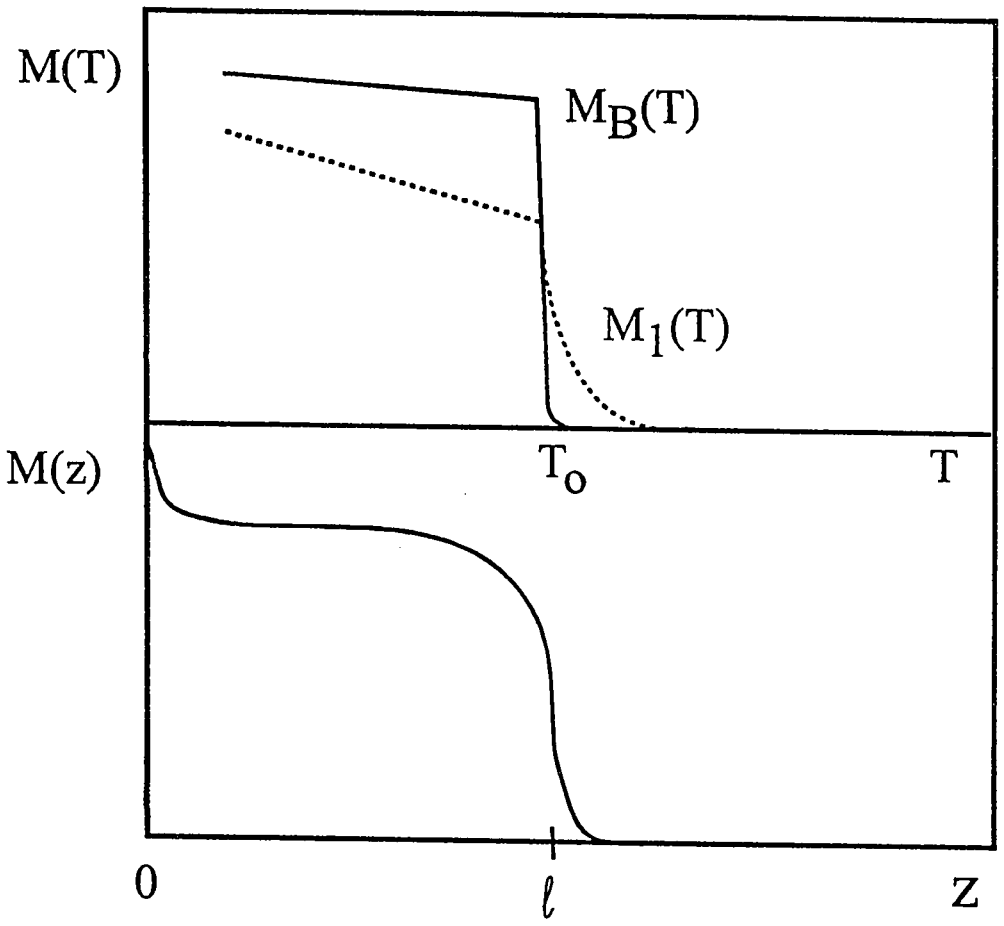

Figure 4.9: Surface Freezing Order Parameters for a Semi-Infinite System. The bulk, $M_B(T)$, and surface, $M_1(T)$, order-parameters, are shown (Top Panel) for a surface freezing transition in a semi-infinite system. The order-parameter profile for a semi-infinite sample is illustrated (Lower Panel) with the vapor-solid interface at $z = 0$ and the solid-liquid interface at l which is also the thickness of the surface-frozen layer.

The bulk properties are described by $f(\phi)$, which must have a form leading to a first-order bulk transition at temperature T^*. The global minimum of $f(\phi)$ describes the bulk order parameter $\phi = M_B$. For $T > T^*$, the system is in the disordered state with $\phi = M_B = 0$ and for $T < T^*$, the system is in its ordered state with $M_B > 0$. The term $\delta(z)f_1(\phi)$ includes the surface interactions. Minimizing, $\frac{\delta F}{\delta \phi} = 0$, subject to the two boundary conditions,

$$\left.\frac{dM}{dz}\right|_{z=0} = \left.\frac{\partial f_1(M)}{\partial M}\right|_{M=M(z=0)} \tag{4.13}$$

$$\lim_{z\to\infty} M(z) = M_{Bulk} \tag{4.14}$$

gives a set of coupled equations

$$\frac{1}{2}\left(\frac{dM}{dz}\right)^2 = f(M) - f(M_B) \tag{4.15}$$

$$\frac{1}{2}\left(\frac{\partial f_1(M_1)}{\partial M_1}\right)^2 = f(M_1) - f(M_B) \tag{4.16}$$

where $M(z=0) \equiv M_1$. These coupled equations provide a profile $M(z)$ for each solution M_1. The simplest model for a system with short-range exponential interactions which can be solved analytically is given by,

$$\begin{aligned} f(\phi) &= -h\phi + \frac{1}{2}a\phi^2 - \frac{b}{x}\phi^x + \frac{c}{y}\phi^y \\ f_1(\phi) &= h_1\phi + \frac{1}{2}a_1\phi^2 \end{aligned} \tag{4.17}$$

where x is equal to 3 or 4 and y is equal to 4 or 6. As illustrated in Fig. 4.9, the results show that while the bulk order parameter, M_B, jumps to zero at the transition temperature T^*, the surface order parameter, M_1, decreases as $|T - T^*|^{\beta_S}$ with a new universal surface exponent β_S. Therefore the surface starts to disorder below T^* and this disorder moves inward with increasing temperature. The overall system is described by the order parameter profile $M(z)$. The characteristic distance l, from the surface to the inflection point of the order parameter profile specifies the thickness

of the disordered layer and the location of the interface. As $T \rightarrow T^*$, the interface becomes unbound from $z = 0$ and $l \propto |\ln(M_1)| \propto |\ln(|T - T^*|)|$. This is the same result obtained from the simple thermodynamic arguments outlined in Chapter 2.

An effective interfacial potential can be derived [13] from the order parameter profile, $M(z)$, and this effective interfacial potential has the same l dependence as Eq. 2.4 for a system with short-range exponential interactions. For short-range interactions with $h = h_1 = 0$,

$$l = -\frac{1}{\sqrt{a^*}} \ln(M_1/M_B), \tag{4.18}$$

and the divergence of l is related to that of the surface order parameter M_1. For the van der Waals system, the effective interface potential has been derived [136], but the order parameter profile and surface order parameter cannot be obtained analytically. In Chapter 2, the complete effective interfacial potential for a liquid crystal film with short-range exponential interactions is calculated explicitly from measurements of the temperature dependence of the surface freezing transitions using the simple thermodynamic theory.

Lipowsky et al. [10, 13] showed that the effective interface potential can be derived from the order-parameter profile $M(z)$ and that the l(t) dependence obtained from the Landau-Ginzburg theory is the same as that given by Eq. 2.4 for short-range interactions. The model in Eq. 4.17 gives analytic results for the order-parameter profile $M(z)$ and the surface order-parameter $M_1(T)$. Eq. 4.18 shows that $\ln(M_1)$ is proportional to the layer thickness, l, so that in principle $M_1(t)$ can be determined from the surface freezing l(t) measurements. The reconstruction of $M_1(t)$ from $l(t)$ is illustrated qualitatively in Fig. 4.10. Fig. 4.10a shows a sketch of the order parameter profile for a film with a single frozen monolayer on each surface. Solid layers are present at both LC-vapor surfaces of the film and the order-parameter profile $M(z)$ has two inflection points. In this illustration, the order-parameter has been taken to be zero in the vapor and decays rapidly to zero in the liquid interior phase of the film. Since it is difficult analytically to use the full spatially dependent order parameter profile, and since the asymptotic dependence does not require it, most of the theoretical results use the sharp-kink approximation. This approximation is shown as the solid line in Fig. 4.10a. The order parameter profiles in the sharp kink approximation for the first few layer freezing transitions are shown in Fig. 4.10b through d. Fig. 4.10e shows the measured electron density which only indirectly

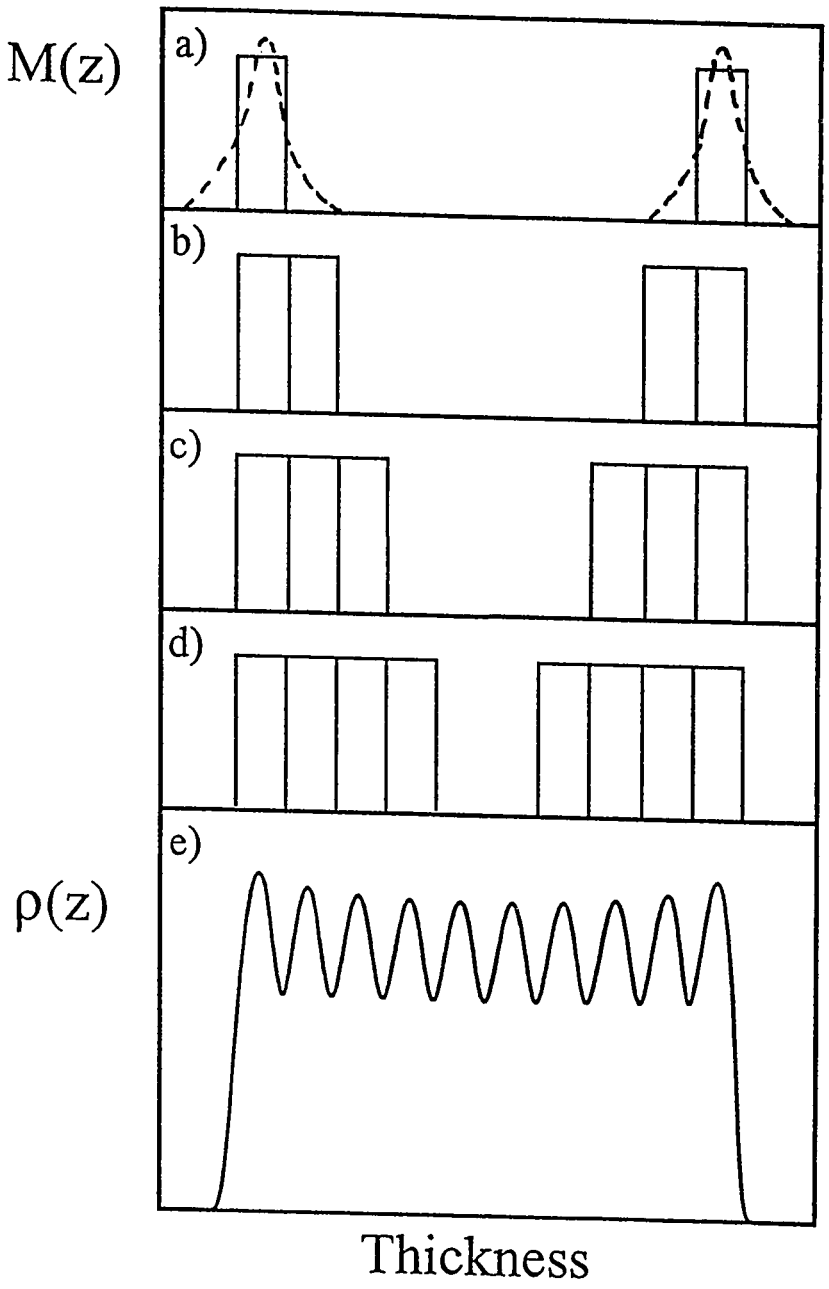

Figure 4.10: Surface Freezing Order Parameters for a FSLC Film. (a) The dashed line is an illustration of the order-parameter profile M(z) for a FSLC film with a monolayer surface frozen layer on each surface. The solid line indicates the order-parameter profile resulting from the sharp-kink approximation. (b)–(d) Order-parameter profile with 2, 3, and 4 layers frozen on each surface of the film. (e) The measured electron density for a 10 layer 7O.7 smectic-I/C film. This film has a monolayer surface-frozen layer on both surfaces. The electron density is indirectly related to the in-plane hexatic order parameter, M(z), illustrated in (a).

reveals the in-plane hexatic order parameter of the monolayer smectic-I surface phase.

4.8 Conclusions

The enhanced order exhibited at the film surfaces of 7O.7 smectic-I/C films is quite interesting and a microscopic theory, based on surface tension quenched fluctuations, predicts very similar behavior [26]. Intuitively, this enhanced ordering should be related to the surface freezing seen in these systems: If the enhanced order indicates quenched thermal fluctuations at the surfaces of the film, the film should begin freezing spatially at the film surface first once the fluctuation amplitudes drop below some critical value. This simple idea is the basis of the QFISF models described in Sections 4.3 – 4.6. The various QFISF models predict qualitative 'surface freezing like' behavior but the thermodynamic theory presented in Chapter 2 quantitatively describes the surface freezing measurements much better than any version of QFISF models. The effect of thermal fluctuations on these quasi-two-dimensional systems does not appear to destroy the mean-field behavior of the surface freezing transitions but the enhanced order displayed in the electron densities of the films may indirectly exhibit the order parameter of the hexatic smectic-I surface layers.

BIBLIOGRAPHY

[1] Katherine J. Strandburg, Rev. Mod. Phys. **60**, 161 (1988).

[2] J.G. Dash, Phys. Today **38**:12, 26 (1985).

[3] P.S. Pershan, *Structure of Liquid Crystal Phases*, (World Scientific, Singapore, 1988).

[4] P.G. de Gennes, J. Phys. (Paris) **30**, Colloq. C4, Suppt. to No. 11-12, 65 (1969); *The Physics of Liquid Crystals*, (Oxford University Press, London 1974).

[5] An early suggestion for LC films occurs in G. Friedel, Ann. Phys. (Paris), **18**, 273 (1922).

[6] E.B. Sirota, P.S.Pershan, L.B. Sorensen, and J. Collett, Phys. Rev. A **36**, 2890 (1987); J. Collett, P.S. Pershan, E.B. Sirota, and L.B. Sorensen, Phys. Rev. Lett **52**, 356 (1984).

[7] S.A. Amador, Ph.D. thesis, Harvard University, (1989).

[8] Optical studies of the thickness dependence of the phase diagram of 7O.7, performed by H. Stragier and C. Bitz, private communication.

[9] S. Amador, P.S. Pershan, H. Stragier, B.D. Swanson, D.J. Tweet, L.B. Sorensen, E.B. Sirota, G.E. Ice, and A. Habenschuss, Phys. Rev. A **39**, 2703 (1989); E.B. Sirota, P.S. Pershan, S. Amador, and L.B. Sorensen, Phys. Rev. A **35**, 2283 (1987).

[10] R. Lipowsky, Phys. Rev. Lett. **49**, 1575 (1982); R. Lipowsky and W. Speth. Phys. Rev. B **28**, 3983 (1983).

[11] F.A. Lindemann, Z. Physik, **11**, 609 (1910).

[12] H.H. Farrell and G.A. Somorjai, Adv. Chem. Phys. **20**, 215 (1971).

[13] R. Lipowsky, D.M. Kroll, and R.P. Zia, Phys. Rev. B **27**, 4499 (1983).

[14] L. Pietronero and E. Tosatti, Sol. State Comm. **32**, 255 (1979).

[15] R. Lipowsky, J. Appl. Phys. **55**, 2485 (1984); Ferroelectrics, **73**, 69 (1987).

[16] G. An and M. Schick, Phys. Rev. B **37**, 7534 (1988); *ibid.* **39**, 9722 (1989).

[17] I.N. Stranski, Z. Phys. **119**, 22 (1942); J. Frenkel, *Kinetic Theory of Liquids*, (Oxford, Clarendon Press, (1946)). J.K. Kristensen and R.M.J. Cotterill, Phil. Mag. **36**, 437 (1977).

[18] J.Q. Broughton and G.H. Gilmer, J. Chem. Phys. **79**, 5119 (1983); **84**, 5759 (1986); A. Trayanov and E. Tosatti, Phys. Rev. Lett. **59**, 2207 (1987), and references therein.

[19] R. Holyst, Phys. Rev. B **46** (Dec. 1992).

[20] J.M. Kosterlitz and D.J. Thouless, J. Phys. C **6**, 1181 (1973); J.M. Kosterlitz and D.J. Thouless, J. Phys. C **5**, L124 (1972).

[21] B.I. Halperin and D.R. Nelson, Phys. Rev. Lett. **41**, 121 and 519(E) (1978); D.R. Nelson and B.I. Halperin, Phys. Rev. B **19**, 2457 (1979); D.R. Nelson and B.I. Halperin, Phys. Rev. B **21**, 5312 (1980); D.R. Nelson in *Phase Transitions and Critical Phenomena Vol. 7*, edited by C. Domb and J.L. Lebowitz, (Academic Press, London, 1983).

[22] Douglas J. Tweet, Robert Holyst, Brian D. Swanson, Hans Stragier, and Larry B. Sorensen, Phys. Rev. Lett. **65**, 2157 (1990).

[23] S. Gierlotka, P. Lambooy, and W.H. de Jeu, Europhys. Lett. **12**, 341 (1990).

[24] S. M. Amador and P.S. Pershan, Phys. Rev. A **41**, 4326 (1990); C. Rosenblatt, R. Pindak, N.A. Clark, and R.B. Meyer, Phys. Rev. Lett. **42**, 1220 (1979).

[25] S. Heinekamp, R.A. Pelcovits, E. Fontes, E.Y.Chen, R.Pindak and R.B. Meyer, Phys. Rev. Lett. **52**, 1017 (1984).

[26] Douglas J. Tweet, Robert Holyst, Brian D. Swanson, Hans Stragier and Larry B. Sorensen, (in preparation).

[27] M. Rigby, E.B. Smith, W.A. Wakeham, and G.C. Maitland, *The Forces Between Molecules* (Claredon Press, Oxford (1986).

[28] A.J. Stone in *The Molecular Physics of Liquid Crystals*, edited by G.W. Luckhurst and G.W. Gray, (Academic Press, London, 1979).

[29] Brian D. Swanson, Hans Stragier, Douglas J. Tweet, and Larry B. Sorensen, Phys. Rev. Lett. **62**, 909 (1989).

[30] Brian D. Swanson, Cecilia Bitz, and Larry B. Sorensen, (in preparation).

[31] An introduction to surface melting has been given by J.G. Dash, in *Proceedings of the Nineteenth Solvay Conference*, edited by F.W. Dewitte (Springer-Verlag, New York, 1988) and Contemp. Phys. **30**, 89 (1989).

[32] K. Binder in *Phase Transitions and Critical Phenomena* Vol. 8, edited by C. Domb and J. Lebowitz (Academic, New York, 1984).

[33] Michael Elbaum and M. Schick, Phys. Rev. Lett. **66**, 1713 (1991).

[34] Dzyaloshinskii, Lifshitz and Pitaevskii, Prog. in Phys. **10**, 156 (1961); Dzyaloshinskii, Lifshitz and Pitaevskii, J. Exptl. Theoret. Phys **37**, 229, (1959) and JEPT **37**, 161 (1960).

[35] M. Schick, in Les Houches, Session XLVIII, 1988–*Liquides aux interfaces/Liquids at interfaces*, edited by J. Charvolin, J.F. Joanny, and J. ZinnJustin (Elsevier, Amsterdam, 1990).

[36] H. Löwen, T. Beier and Wagner, Europhys. Lett. **9**, 791 (1989).

[37] R. Ohnesorge, H. Löwen and H. Wagner, Phys. Rev. A. **43**, 2870 (1991).

[38] R. Lipowsky, U. Breuer, K.C. Prince and H.P. Bonzel, Phys. Rev. Lett. **62**, 913 (1989).

[39] D.A. Huse, Phys. Rev. B **30**, 1371 (1984).

[40] D. M. Kroll, R. Lipowsky and R. K. P. Zia, Phys. Rev. B, **32**, 1862 (1985).

[41] R. Lipowsky, Phys. Rev. Lett. **52**, 1429 (1984).

[42] Two reviews on wetting are provided by D.E. Sullivan and M.M. Telo da Gama, in *Fluid Interfacial Phenomena* edited by C. A. Croxton (Wiley, New York, 1986); S. Dietrich, in *Phase Transitions and Critical Phenomena*, edited by C. Domb and J. Lebowitz (Academic, London, 1988), Vol. 12.

[43] D.J. Bishop, W.O. Sprenger, R. Pindak, and M.E. Neubert, Phys. Rev. Lett. **49**, 1861 (1982).

[44] D.E. Moncton, R. Pindak, S.C. Davey, and G.S. Brown, *ibid.* **49**, 1865 (1982).

[45] A good review of multilayer physisorbed films is given by George B. Hess, preprint, (1991).

[46] R. Pandit, M.Schick, and M. Wortis, Phys. Rev. B **26**, 5112 (1982).

[47] D.M. Kroll and G. Gompper, Phys. Rev. B **39**, 433 (1989); D.M. Kroll, J. Appl, Phys. **61**, 3595 (1987).

[48] G. Gompper and D.M. Kroll, Phys. Rev. B **40**, 7221 (1989).

[49] M.N. Barber, in *Phase Transitions and Critical Phenomena*, edited by C. Domb and J. Lebowitz (Academic, New York, 1984), Vol. 8.

[50] H. Li, M. Paczuski, M. Kardar, and K. Huang, Phys. Rev. B **44**, 8274 (1991).

[51] D.E. Moncton and R. Pindak, Phys. Rev. Lett. **43**, 701 (1979).

[52] Guozhong An and M. Schick, J. Phys. A: Math. Gen. **21**, L213 (1988).

[53] M.E. Fisher, Rev. Mod. Phys. **46**, 597 (1974).

[54] R. Evans and U. Marini Bettolo Marconi, J. Chem Phys. **86**, 7138 (1987); R. Evans, U. Marini Bettolo Marconi and P. Tarazona, *ibid* **84**, 2376 (1986); R. Evans and P. Tarazona, Phys. Rev. A **28**, 1864 (1983).

[55] A. Poniewierski and T.J. Sluckin, Liq. Cryst. **2**, 281 (1987).

[56] R. Lipowsky and G. Gompper, Phys. Rev. B. **29**, 5213 (1984); D. Sornette, Phys. Rev. B **31**, 4672 (1985).

[57] D. Armitage and F.P. Price, Chem. Phys, Lett. **44**, 305 (1976); F.M. Aliev and M.N. Breganov Sov. Phys. JETP **68**, 70 (1987).

[58] M. Kuzma and M.M. Labes, Mol. Cryst. Liq. Cryst. **100**, 103 (1983).

[59] V.S. Sundaram, B. Farrell, R.S. Alben, and W.D. Robertson, Phys. Rev. Lett. **31**, 1136 (1973).

[60] Douglas Sluis and Stuart A. Rice, J. Chem. Phys. **79**, 5658 (1983); M.P. D'Evelyn and S.A. Rice, Phys. Rev. Lett. **47**, 1844 (1981).

[61] J. Daeges, H.Gleitner and J.H. Perepezko, Phys. Lett. A **119**, 79 (1986); L. Grabaek, J. Bohr, E. Johnson, A. Johansen, L. Sarholt-Kristensen and H.H. Anderson, Phys. Rev. Lett. **64**, 934 (1990).

[62] D. Beaglehole and D. Nason, Surf. Sci. **96**, 357 (1980); Y. Furukawa, M. Yamamoto, and T. Kurado, J. Cryst. Growth **82**, 665 (1987).

[63] R.R. Gilpin, J. Colloid Interface Sci. **77**, 435 (1980).

[64] J. W. M. Frenken, J.P. Toennies, and C. Woll, Phys. Rev. Lett. **60**, 1727 (1988), and references therein.

[65] P.H. Fuoss, L.J. Norton, and S. Brennan, Phys. Rev. Lett. **60**, 2046 (1988).

[66] G. Devaud and R. H. Willens, Phys. Rev. Lett. **57**, 2683 (1986).

[67] K.C. Prince, U. Breuer, and H.P. Bonzel, Phys. Rev. Lett. **60**, 1146 (1988).

[68] Da-Ming Zhu and J. G. Dash, Phys. Rev. Lett. **57**, 2959 (1986); **60**, 432 (1988).

[69] J. Krim, J.P. Coulomb, and J. Bouzidi, Phys Rev. Lett. **58** 583 (1987).

[70] M. Bienfait, Europhys. Lett. **4**, 79 (1987).

[71] B. Pluis, A.W. Denier van der Gon, J.W.M. Frenken and J.F. van der Veen, Phys. Rev. Lett. **59**, 2678 (1987).

[72] H.S. Nham and G.B. Hess, Langmuir **5**, 575 (1989); H.S. Youn and G.B. Hess, Phys. Rev. Lett. **64**, 918 (1990).

[73] A review of surface induced order in liquid crystals is given by B. Jérôme, Rep. Prog. Phys. **54**, 391 (1991).

[74] For a review see T.J. Sluckin and A. Pondiewierski, in Fluid Interfacial Phenomena, edited by C. A. Croxton (Wiley, New York, 1986).

[75] Clive A. Croxton, *Statistical Mechanics of Liquid Surfaces*, (John Wiley & Sons, 1980).

[76] For example, J. Cognard, *Alignment of Nematic Liquid Crystals and Their Mixtures*, (Gordon and Breach, London, 1982).

[77] H. Hsiung, T. Rasing, and Y.R. Shen, Phys. Rev. Lett. **57**, 3065 (1986); **59**, 1983(E) (1987).

[78] B. M. Ocho, A. Braslau, P.S. Pershan, J. Als-Nielsen, and M. Deutsch, Phys. Rev. Lett. **57**, 94 (1986); B.M. Ocho, R.J. Birgeneau, and J.D. Litster, Z. Phys. B **62**, 487 (1986).

[79] B.M. Ocho, Phys. Rev. Lett. **64**, 2160 (1990).

[80] Y. Galerne, Phys. Rev. Lett. **64**, 906 (1990).

[81] T. Pitchford, C.C. Huang, R. Pindak, J.W. Goodby, Phys. Rev. Lett. **57**, 1239 (1986); R. Geer, C.C. Huang, R. Pindak and J.W. Goodby, Phys. Rev. Lett. **63**, 540 (1989); R. Geer, T. Stoebe, C.C. Huang, R. Pindak, G. Srajer, J.W. Goodby, M. Cheng, J.T. Ho, and S.W. Hui, Phys. Rev. Lett. **66**, 1322 (1991).

[82] T. Stoebe, R. Greer, C.C. Huang, and J.W. Goodby, Phys. Rev. Lett. **69**, 2090 (1992).

[83] K. Miyano, Phys. Rev. Lett. **43**, 51 (1979), and J. Chem. Phys. **71**, 4108 (1979); J.C. Tarczon and K. Miyano, J. Chem. Phys. **73**, 1994 (1980); H. A. van Sprang, J. Phys. (Paris) **44**, 421 (1983); and Mol. Cryst. Liq. Cryst. **97**, 255 (1983).

[84] W. Chen, L.J. Martinez-Maranda, H.Hsiung, and Y.R. Shen, Phys. Rev. Lett. **62**, 1860 (1989).

[85] Z. Pawlowska, G.F. Kventsel, and T. J. Stuckin, Phys. Rev. A **36**, 992 (1987).

[86] See the review by J. Als-Nielsen, in *Structure and Dynamics of Surfaces II*, edited by W. Schommers and P. Blanckenhagen (Springer-Verlag, New York, 1987), and references therein.

[87] J. V. Selinger and D.R. Nelson, Phys. Rev. A **37**, 1736 (1988).

[88] L. Mederos and D.E. Sullivan, Phys. Rev. A **39**, 854 (1989).

[89] D. Beaglehole, Mol. Cryst. Liq. Cryst. **89**, 319 (1982).

[90] A. Braslau, Ph.D. Thesis, Harvard University (1988); P.S. Pershan, J. Physique Coll. **50**, C7 1 (1989).

[91] B. Rapp and H. Gruler, Phys. Rev. A. **42**, 2215 (1990).

[92] M. Born and E. Wolf, *Principles of Optics*, (Pergamon Press, Oxford, 1970).

[93] E.B. Sirota, Ph.D. thesis, Harvard University (1986).

[94] We have developed a visual dictionary of LC film textures associated with the different phases. For bulk samples, some of these distinctive LC textures are illustrated in: Dietrich Demus and Lothar Richter, *Textures of Liquid Crystals*, (Verlag Chimie, 1978).

[95] Smith, J. Chem. Phys. **59**, 3214 (1973).

[96] Mary E. Neubert, R.E. Cline, M.J. Zawaski, Arun Ekachai, Mol. Cryst. Liq. Cryst. **76**, 43 (1981).

[97] A. Ajdari, L. Peliti, and J. Prost, Phy. Rev. Lett. **66**, 1481 (1991).

[98] Hao Li and Mehran Kardar, *ibid.* **67**, 3275 (1991).

[99] P.E. Cladis, Wim van Saarloos, David A. Huse, J.S. Patel, J.W. Goodby, and P.L. Finn, Phys. Rev. Lett. **62**, 1764 (1989); M.A. Anisimov, P.E. Cladis, E.E. Gorodetskii, David A. Huse, V.E. Podneks, V.G. Taratuta, Wim van Saarloos, and V.P. Voronov, Phys. Rev. A **41**, 6749 (1990).

[100] Hong Yan, David Kessler, and L.M. Sander, Phys. Rev. Lett. **64**, 926 (1990); *ibid* **65**, 661 (1990); Joachim Krug and Herbert Spohn in *Solids Far From Equilibrium: Growth, Morphology and Defects*, edited by Claude Godrèche (1990).

[101] L.D. Landau, *Collected Papers of L.D. Landau*, edited by D. Ter Haar, (Gordon and Breach, New York, 1965), p. 209; R.E. Peierls, Helv. Phys. Acta. **7**, Suppl. 81 (1934).

[102] A. Caille, C.R. Acad. Sci. Ser. B **274**, 891 (1972).

[103] J. Als-Nielsen, J.D. Litster, R.J. Birgeneau, M. Kaplan, C.R. Safinya, A. Lindegaard-Andersen and S. Mathiesen, Phys. Rev. B **22**, 312 (1980).

[104] E.N. Keller, R. Halfon, E. Nachaliel, D. Davidov, and H. Zimmermann, Phys. Rev. Lett. **61**, 1206 (1988); K.K. Chan, P.S. Pershan, L.B. Sorensen, and F. Hardouin, Phys. Rev. A **34**, 1420 (1986); B.M. Ocko, A.R. Kortan, R.J. Birgeneau, and J.W. Goodby, J. Phys. (Paris) **45**, 113, (1984); R.J. Birgeneau, C.W.

Garland, G.B. Kasting, and B.M. Ocko, Phys. Rev. A **24**, 2624 (1981); J.D. Litster, J. Als-Nielsen, R.J. Birgeneau, S.S. Dana, D. Davidov, F. Garcia-Golding, M. Kaplan, C.R. Safinya, and R. Schaetzing, J. Phys. Colloq. C3, suppl. **4**, 339 (1979).

[105] R. Pindak and D.E. Moncton, Physics Today **35**:5, 57 (1982).

[106] J.D. Litster and R.J. Birgeneau, Physics Today **35**:5, 26 (1982).

[107] F. Christensen, Ph.D. thesis, Technical University of Denmark, (1981).

[108] L. Gunther, Y. Imry and J. Lajzerowicz, Phys. Rev. B **22**, 1733 (1980).

[109] W.H. Bragg, Phil. Trans. R. Soc. A **215**, 253 (1915).

[110] H. Ott, Z. Kristallogr. **66**, 136 (1928).

[111] A.L. Patterson, Phys. Rev. **46**, 372 (1934).

[112] M.M. Woolfson, Acta Cryst. A **43**, 593 (1987).

[113] D. Harker and J.S. Kasper, Acta Cryst. **1**, 70 (1948).

[114] I.L. Karle and J. Karle, Acta Cryst. **17**, 835 (1964).

[115] Jerome Karle, Science **232**, 837 (1986); Herbert Hauptmann, *ibid* **233**, 178 (1986).

[116] W. Swindell and H.H. Barrett, Physics Today **30**:12, 32 (1977).

[117] R.W. James, *The Optical Principles of the Diffraction of X-Rays*, (Bell, London, 1950).

[118] I.K. Robinson, Phys. Rev. B **33**, 3830 (1986).

[119] R. Hołyst, D.J. Tweet, and L.B. Sorensen, Phys. Rev. Lett. **65**, 2153 (1990).

[120] H. Lipson, *Optical Transforms*, (Academic Press, New York, 1972).

[121] John M. Crowley, *Diffraction Physics*, (Elasevier, Amsterdam, 1984).

[122] Turbo Pascal Numerical Numerical Methods Toolbox FFT Routine V. 4.0, (Borland International Inc., Scotts Valley, CA.).

[123] N. Wiener, *The Extrapolation, Interpolation and Smoothing of Stationary Time Series*, (John Wiley, New York, 1949).

[124] L.B. Sorensen, A.B. thesis, Princeton University, (1972); W.H. Press, B.P. Flannery, S.A. Teukolsky, and W.T. Vetterling, *Numerical Recipes*, (Cambridge University Press, New York, 1986).

[125] D. Tweet, Ph.D. thesis, University of Washington, (1990).

[126] B.E. Warren, *X-ray Diffraction*, (Dover, New York, 1990).

[127] J. Doucet and A.M. Levelut, J. Phys. (Paris), **38**, 1163 (1977).

[128] R. Holyst, Phys. Rev. A **44**, 3692 (1991).

[129] K. Miyano, Phys Rev. A **26**, 1820 (1982).

[130] P.S. Pershan and J. Als-Nielsen, Phys. Rev. Lett. **52**, 759 (1984); J. Als-Nielsen and P.S. Pershan, Nucl. Instrum. Methods **208**, 545 (1983); J. Als-Nielsen, F. Christensen, and P.S. Pershan, Phys. Rev. Lett. **48**, 1107 (1982).

[131] D.R. Nelson and L. Peliti, J. Phys. (France) **48**, 1095 (1987).

[132] J.V. Selinger, J. Phys. (Paris) **49**, 1387 (1988).

[133] R. Holyst, private communication.

[134] E. Brézin, B.I. Halperin and S. Leibler, J. Physique **44**, 775 (1983).

[135] A.K. Sen and D.E. Sullivan, Phys. Rev. A **35**, 1391 (1987).

[136] D.M. Kroll and T.F. Meister, Phys. Rev. B **31**, 392 (1985); M. Napiórkowski and S. Dietrich, *ibid* **34**, 6469 (1986).

[137] G. Barbero and G. Durand, J. Appl Phys. **69**, 6968 (1991).

Appendix A

VIDEO-MICROSCOPY TEMPERATURE RECORDING CIRCUIT

A new scientific truth does not triumph by convincing its opponents and making them see the light, but rather because its opponents eventually die, and a new generation grows up that is familiar with it.

-Max Planck

A.1 Introduction

This appendix describes a simple electronic circuit for recording computer readable text and numerical information onto the two audio channels of a video tape. It is often very useful to be able to label the video information with additional experimental parameters such as the time, date, sample temperature and sample ID. There are several ways to display this information on the video field but then the parameters cannot be directly accessed by a computer. For experiments involving quantities which change quickly with time, analysis involving computers is essential. The 20 khz bandwidth of stereo audio tracks provides two extra data channels that can be easily used to encode computer readable information simultaneously with the video signal.

A.2 Circuit Description

The circuit shown in Fig. A.1 consists of two channels which can encode or decode information simultaneously from the two stereo channels of a VCR. This circuit is

operational during both record and playback: During recording, the computer transmits data serially at 1200 baud via RS-232 from the output of 2 serial/parallel cards COM 1 OUT and COM 2 OUT. Consider the input from the computer via COM 1 OUT. Since the modem accepts TTL signals, the MC1489 line receiver converts the RS-232 to TTL. This TTL signal, a group of 8 pulses signifying the 8 bit numerical equivalent of each ASCII letter, number or symbol to be recorded on the tape, enters the Tx Data input of the MC6860 digital modem labeled Modem 1. The modem operates in full duplex mode using frequency shift key (FSK) modulation, which shifts the continuous-running carrier between two closely spaced frequencies according to the 1's and 0's being transmitted. Both the answer and the originate signals are encoded within the 3khz telephone bandwidth, by using separate answer and originator frequencies. In this circuit, Modem 1 is set in "answer mode" and transmits at 2025 and 2225 Hz, while Modem 2 is set in "originate mode" transmits at 1070 and 1270 Hz. The FSK signal from the two Tx Carrier outputs of the modems is buffered and inverted by two unity gain 741 inverting amplifiers and this analog FSK encoded data is recorded on the audio channels of the video recorder. Pots R1 and R8 are 10 kΩ potentiometers which are used to zero the DC offsets of the FSK signals from each 741 buffer.

During playback, the recorded signal coming from the video recorder left channel (CH L OUT), is buffered and inverted by another unity gain 741 amplifier. The signal is then filtered and converted into a square wave by a 741 comparator before it is converted to RS-232 by the MC1489L. Pots R13 and R14 are 10 kΩ potentiometers which set the DC level of the 741's which convert the signals into a square wave format. The signal then enters the Rx Carrier input of Modem 2 for demodulation back to TTL pulses. The data leaves modem 2 through the Rx Data output and is converted back to RS-232 by the MC1488 line driver. The RS-232 signal, input via COM 1 IN, returns to the computer through the RS-232 serial input port of the serial/parallel card. The right channel operation is similar. The two modems are used for two channel capability and so that no change is necessary in the circuit between record and play. If only one channel output is available, the input and output of the other channel must be connected together. The modem pin connections are listed in Table A.1.

A.3 Application

In this application, monolayer surface freezing transitions can be observed in freely suspended liquid crystal films because the tilted surface-frozen phase is very birefringent. By illuminating a film with polarized white light and viewing the specularly reflected light through a crossed polarizer, waves of slightly increased contrast appear near the center of the film and spread radially outward as the temperature of the film is lowered using an oven with a small radial temperature gradient. Since the optical contrast change corresponding to these freezing transitions of single molecular layers is very small, the video images are computer-contrast enhanced to increase visibility. Two thermistors are attached to a temperature regulated liquid crystal film oven. The two thermistors are monitored by digital voltmeters which are interfaced via IEEE488 to a IBM AT computer. The contrast-enhanced images were recorded on video tape and the temperature of the film oven was simultaneously recorded onto the audio channels using the modem circuit. The computer outputs the two temperatures to the modem circuit using two RS-232 serial ports. The experiment consists of slowly lowering the oven temperature and simultaneously recording the film image and the film temperature. After the film has been cooled sufficiently so that the entire film is frozen, the video tape is replayed and the video image is monitored to determine the exact temperature when each surface freezing transition has occurred. When a transition occurs on the screen, a key on the computer keyboard is struck, and the computer program records the oven temperature read back from the RS-232 inputs via the modem circuit.

I wish to acknowledge and thank P. Felis for assistance in building the first prototype of this circuit.

Table A.1: MC-6860 Modem Connections. The MC-6860 connections are listed here with Modem 1 set in answer mode and Modem 2 set in originate mode.

	Modem 1 Answer mode	Modem 2 Originate mode
0V:	1 5 7 9 14 18 19 20 22	1 5 7 9 14 18 20 21 22
+5V:	6 8 12 16 21	6 8 12 16 19
N.C	3 4 11 15 23	3 4 11 15 23

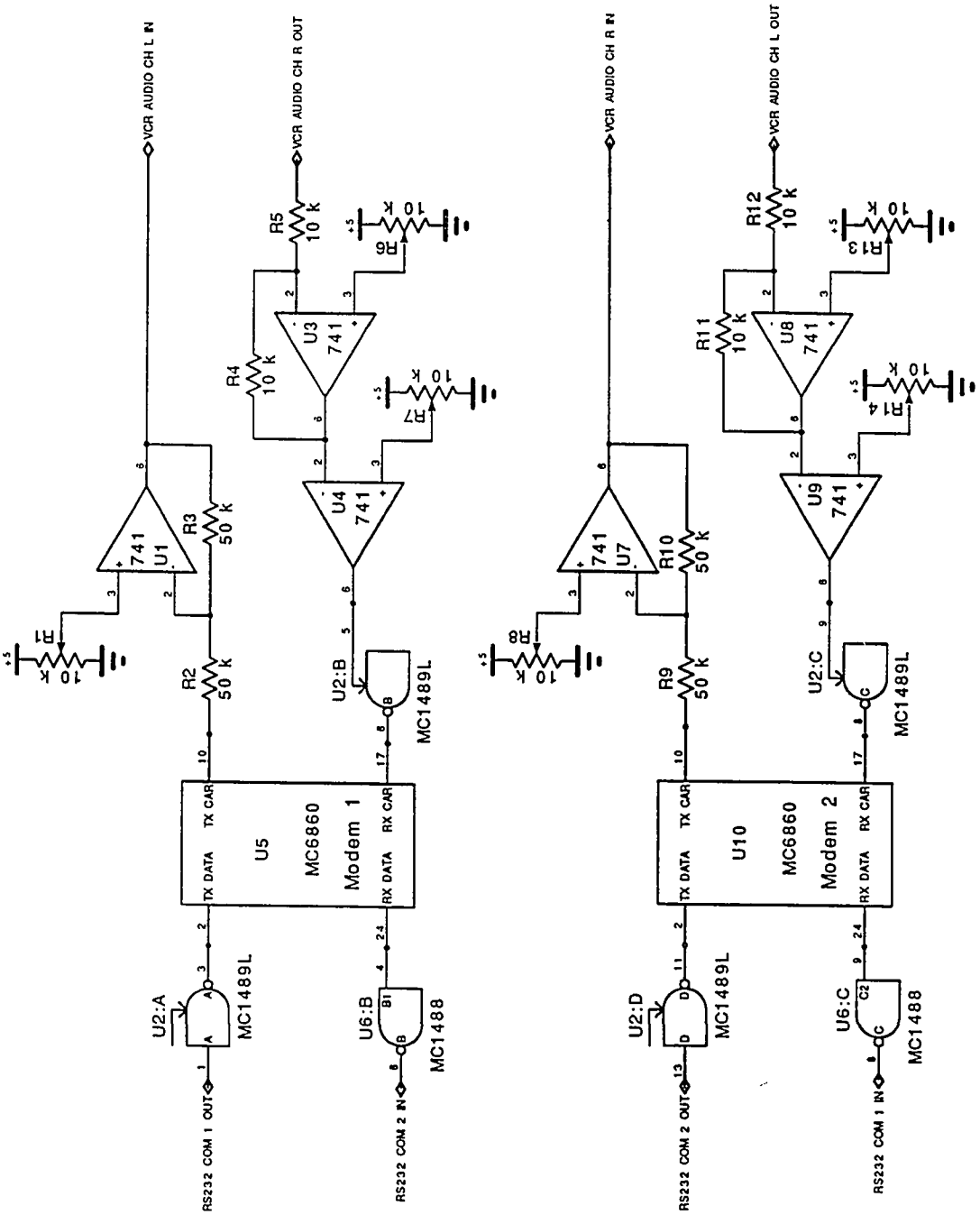

Figure A.1: Modem Circuit Diagram

Appendix B

CONTENTS OF VIDEO TAPE

Except I shall see ... I will not believe.

- John 20:25

A video tape is included which contains six illustrations of the surface freezing observations described in Chapter 2. The contents of the tape and corresponding times are:

I. Initial Surface Freezing Observations (0:00 to 2:00)

Initial observations of the surface freezing were recorded in color without image enhancement. The edge of the 7 mm diameter film is visible in the upper portion of the screen. The film has a radial temperature gradient with the center of the film cooler than the edge. In this segment, a 9O.4 film is cooled quite quickly and the smectic-A to smectic-I surface freezing transition appears as a 'burst' of texture appearing near the center of the film and moving radially outward. The transition is unusual since the interface appears quite broad unlike other first-order transitions in FSLC films. As the film is cooled further, a second transition to the smectic-F phase is also shown. The experiment is repeated at a slower cooling rate where the surface freezing appears as 'flashes' of transitions throughout the central region of the film. The transition to the smectic-F phase and finally to the smectic-G phase is also visible.

II. 9O.4 Surface Freezing: Contrast-Enhanced (2:00 to 3:00)

This segment displays a magnified and contrast-enhanced image of a 9O.4 film undergoing surface freezing starting after the second pair of SF transitions. The cooling rate here is slower than that displayed in the first segment but still much faster than

the cooling rate used during a standard data run. The nucleation point for the surface freezing is off screen to the upper right. The surface freezing transitions from the top and bottom surfaces of the film appear as pairs of transitions moving radially across the film. The image is becoming lighter then darker due to rotation of the nearly crossed polarizers and the stripes are the characteristic smectic-I texture. The surface freezing transitions continue until the entire film is frozen to the smectic-I phase. The smectic-I to smectic-F transition is also visible here, note the turbulence at the smectic-I—smectic-F interface.

III. 9O.4 Surface Freezing: Slower Cooling Rate (3:00 to 4:00)

This segment contains a magnified and contrast-enhanced image of a thick 9O.4 film undergoing surface freezing after about 20 layers have surface frozen. The image is of the center 5 mm the film and the cooling rate is still faster than the usual experimental rate of about 0.5 m°/sec. In these films, the layer-by-layer surface freezing transitions continue a single layer at a time until the entire film is smectic-I.

IV. 4O.7 Surface Freezing (4:00 to 5:00)

This segment shows a magnified and computer-contrast-enhanced image of a very thick 4O.7 film surface freezing after about 30 layers have frozen. The cooling rate is relatively fast but this illustrates the many SF transitions seen in these thick 4O.7 films.

V. 7O.7 Film (5:00 to 9:00)

This portion has a color image of a $\sim$ 64 layer thick 7O.7 film first making the smectic-I/A to smectic-I/C transition at about 72° and then at about 69° surface freezing to the smectic-I phase just before making the transition to the smectic-B phase.

VI. 9O.4 Data Runs (10:00 to 70:00)

The remainder of the tape contains a few typical data runs from 64-layer 9O.4 films. The surface freezing transitions appear infrequently at first and eventually the time interval between transitions becomes shorter.

VITA

Brian Douglas Swanson, the eldest child of Florice and Allan Swanson was born in Seattle, Washington. He grew up on a dairy farm near Bothell and attended Bothell High School and then the University of Washington where he received a B.A. in philosophy before joining the Peace Corps. He spent three years in the Philippines organizing and managing a sewing co-op for the Philippine Rural Electrification Administration. When he returned to the U.S. he reentered the University of Washington and in 1981 he received a B.S. in physics and a B.A. in mathematics. In 1985 he obtained a M.S. in Physics. He has been married to Mary Laucks since June 1986.

PLEASE NOTE

The video tape is not included in this material. It is available for consultation at the author's graduate school library.

University Microfilms International